DESIGN AND DEVELOPMENT OF A HIGH-SPEED MOTOR FOR A VACUUM PUMP

Ulrike Martina Hoefer

A thesis submitted for the degree of

Engineering Doctorate

University of Newcastle upon Tyne
School of Electrical, Electronic and Computer Engineering

Abstract

Turbomolecular pumps require a motor to drive them at speeds of up to 90,000 rpm. These high-speed motors are typically brushless permanent magnet motors that are specifically designed for the application. Intellectual property rights over the design lock the company into one single supplier. Also low manufacturing volumes make the motor expensive to produce. To stay competitive continuous cost reductions or product improvements are necessary. This can only be achieved by looking at new materials, alternative manufacturing methods and simplified assembly processes.

The aim of this project is to replace an existing laminated, high-speed (60,000rpm) motor with a new low-cost design. Special considerations need to be given to the motor design with regards to minimising losses due to the high operating speed and the fact that the motor operates in a vacuum. A machine design employing a simple, 3-tooth segmented stator made from soft magnetic composites (SMC) and using non-overlapping coils, and a 'deep' plastic bonded magnet on the rotor is proposed to deliver low rotor losses and low manufacturing costs.

Four SMC prototype motors have been built, which have led to the following discoveries: (1) Bulk eddy currents in the SMC material cannot be neglected and need to be taken into account separately as a function of the actual component size and shape. (2) A process is suggested to improve the iron loss calculation in SMC, which is evaluated against the prototypes built. (3) SMC material properties are adversely affected by prototype machining, leading to higher iron losses than initially expected. (4) The segmented SMC design has proven to be commercially very attractive.

During testing a large sensitivity of the magnetically supported pump shaft to the inherent unbalanced magnetic pull (UMP) force of the 3-tooth, 2-pole design was discovered. This led to a practical and theoretical study into the effects of UMP in this application. An alternative design that avoided the inherent UMP was required, and a 6-tooth, 4-pole motor has been designed and built. For reasons of minimising risks laminations were chosen as the stator material rather than SMC. Test results of this motor in the pump have been successful and the motor has been selected to go into the next generation of turbomolecular pumps.

Table of Contents

List of Figures

List of Tables

Acknowledgements

Without the help, support and encouragement of so many people along the way, I would not have made it to the end, and this thesis would not be what it is now.

Firstly I want to thank Edwards Ltd. for allowing me to enrol on the EngD Scheme, and giving me time off work to attend the lectures. Without their support it would not have been possible to work and study at the same time. I also thank Edwards for the funding of the project, especially to cover the cost of building and testing the five prototype machines. With regards to covering costs I also thank the EPSRC in funding the EngD Scheme at the University of Newcastle by paying for the fees.

Many thanks are due to my academic supervisors, Professors Alan Jack and Barrie Mecrow, for their advice and guidance throughout this EngD project. Especially I want to thank Alan Jack for sharing his expertise and experience with SMC, which was invaluable for the project, and for his help, feedback and encouragement throughout the years, especially for believing in me, when things were tough and I doubted myself.

Thanks also to my industrial supervisor Mark Gardiner, who gave me the freedom in managing the project, and to my colleague Jim Haylock, for always being available to discuss results and exchange ideas.

The project could not have happened without the support of Höganäs. They supplied the SMC material over the duration of the project and gave access to their latest development material, which was greatly appreciated. Especially I like to thank Patricia Jansson and Lars-Olov Pennander for their technical advice with SMC and its properties.

This project also involved a lot of testing, building and stripping of test rigs and pumps which would not be possible without the dedication and help of the technicians at Edwards: Dick Ottway, and Ray Hucklesby.

I am especially grateful to my proofreaders, Jim Haylock and Jennifer Schooling, for taking the time to read this thesis (or parts of it) despite their own busy lives and for providing invaluable feedback.

The biggest 'Thank You', however, belongs to my sister Monika and her family, for just being there, and for cooking countless meals, when I was too tired and exhausted to look after myself; also for providing a healthy balance to my work-study-life. What would I have done without the smiles of my (now two-year old) nephew Luke!

List of Symbols

Below is a list of symbols, subscripts and abbreviations that are widely used throughout this thesis. Wherever possible the meaning of each symbol is given in the text when the symbol is first used. Note that the use of italic print in certain circumstances is not intended to imply any difference in meaning.

a	Strands in parallel
a	Radius of grain (spherical part)
A	Area
$A_{cu,turn}$	Copper cross section area per turn
A_{slot}	Slot area
A_{wire}	Wire cross section area
$\overline{A}$, A_z	Magnetic vector potential
α	Phase advance angle
α	Slot pitch angle
α_{cu}	Temperature coefficient of resistivity for copper
B	Magnetic flux density
B_r	Residual flux density
β	Torque angle
β	Coil pitch angle
c	Constant in non-linear μ_r equation
c	Viscous damping factor
C_1	Constants
C_2	Constants
$c_{material}$	Specific heat capacity of 'material'
d	Diameter
d_{wire}	Wire diameter
δ	Skin depth
e	Instantaneous back-EMF
E	Back-EMF (open circuit voltage)
ε_0	Permittivity of free space
ε_r	Relative permittivity
f	Frequency
Φ	Flux
F	Mechanical force
g	Slots per pole per phase
γ	Slot opening angle
h'	Heat transfer coefficient
H	Magnetic field strength
H_c	Coercive force
η_G	Efficiency of the generator
η_M	Efficiency of the motor
i	Instantaneous current
I	Current
I_{dc}	DC-Drive input current
J	Current density
J_e	External applied current density
J_i	Induced current density
k	Bearing stiffness
k	Constant in Fourier series
k_a	Anomalous loss constant
k_d	Winding distribution factor
k_e	Eddy current loss constant
k_{fill}	Slot fill factor
k_h	Hysteresis loss constant
k_p	Winding pitch factor
k_w	Winding factor (general)
l	Constant in Fourier series
l	Length
l_a	Axial active stack length
l_{gap}	Length of air gap
l_{mag}	Magnet length in direction of magnetisation
l_{turn}	Average length of one turn
L	Inductance
λ	Tooth pitch
m	Mass
m	Constant
M	Molecular weight
μ_0	Permeability of free space
μ_{max}	Constant in non-linear μ_r equation
μ_{min}	Constant in non-linear μ_r equation
μ_r	Relative permeability
n	Constant
n	Harmonic number
$N_{effslots\_ph}$	Number of effective slots per phase
NI	Ampere-turns
N_{ph}	Number of series turns per phase
N_{slot}	Number of slots
N_{teeth}	Number of teeth
p	Constant in non-linear μ_r equation
p	Pole pairs
p_1	Inlet pressure
p_2	Backing pressure
P	Power, Power loss
$P_{controller}$	Controller loss
P_{cu}	Copper loss
P_e	(Bulk) Eddy current loss
P_g	In-grain eddy current loss
$P_{G,loss}$	Generator loss
$P_{G,out}$	Generator output power
P_h	Hysteresis loss
$P_{M,in}$	Motor input power
$P_{M,loss}$	Motor loss
P_{Rig}	Rig losses
P_{shaft}	Shaft power
P_{system}	System input power
θ	Angular coordinate; rotor position
r	Radius
$r_{i,stator}$	Stator inner radius
$r_{o,mag}$	Magnet outer radius
R	Resistance
ρ	Resistivity
ρ	Density

sf	Space-factor
σ	Conductivity
σ	Magnetic stress in air gap
t	Time
T	Torque
T	Temperature
τ	Time constant
v	Linear velocity
V_{dc}	DC-Supply voltage
w_{slot}	Slot opening
w_{tooth}	Tooth width
ω	Angular velocity
ω_n	Natural frequency of system
x	Displacement
$\dot{x}$	First derivative of displacement
$\ddot{x}$	Second derivative of displacement
X	Steady-state amplitude of oscillation
Ψ	Flux linkage

Commonly Used Subscripts

a, b, c	Phase a, b, c
ab, bc, ca	Line-to-line values between phases a-b, b-c, c-a
ac	Alternating current
coil	Armature winding (coils)
dc	Direct current
e	(Bulk) Eddy current
elec	Electrical
gap	Air gap
h	Hysteresis
i	Inner
lam	Lamination
LL	Line-to-line
mag	Magnet
max	Maximum
mech	Mechanical
min	Minimum
n	Normal component
n	n^{th} harmonic component
o	Outer
ph	Phase
pk	Peak value
r, φ, z	Polar coordinates
t	Tangential component
x, y, z	Cartesian components x, y, z
0	Base or reference value

Abbreviations

AC	Alternating Current
CFRE	Carbon Fibre Reinforced Epoxy
DC	Direct Current
EDM	Electrical Discharge Machining
EMF	Electromotive force
EngD	Engineering Doctorate
EPSRC	Engineering and Physical Sciences Research Council
FE	Finite Elements
ID	Inner Diameter
Mk1,2,...	Mark1,2,...(as in design variants)
MMF	Magnetomotive force
MS	Mass Spectrometer
NdFeB	Neodymium Iron Boron
OD	Outer Diameter
PM	Permanent Magnet
PWM	Pulse Width Modulation
R&D	Research and Development
SMC	Soft Magnetic Composites
SmCo	Samarium Cobalt
St-St	Stainless Steel
TMP	Turbomolecular Pump
UMP	Unbalanced Magnetic Pull

Chapter 1

Introduction

1.1 Thesis Overview

1.1.1 The Engineering Doctorate

The Engineering Doctorate is a PhD that combines academic research and innovation with real industrial projects. The aim is to innovate and implement new ideas in practice, by putting the research into a business context working on real commercially relevant projects.

The sponsoring company for the work presented here is Edwards Ltd., a leading supplier of vacuum technology to the semiconductor, chemical, pharmaceutical and scientific industries. It specialises in the design and manufacture of a comprehensive range of vacuum pumps and controls, and vacuum accessories. To stay competitive in an increasingly cost sensitive market, the main focus of the company's industrial R&D is continuous product development and improvements as well as cost reductions, which also form the basis and main drivers for this project.

1.1.2 Structure of the Thesis

This Engineering Doctorate Thesis is a portfolio of five motors in total, the design of which evolved as performance issues were identified and understood at each stage of the research.

Chapter 1 gives an introduction to turbomolecular pumps, which are the target application of the new motor, highlighting the requirements and challenges faced by the motor design for such an application. It also presents the existing motor, pointing out the areas which are to be addressed, and summarises the aims and objectives of the thesis.

Chapter 2 to Chapter 4 describe the design, development and testing of the first three motors using Soft Magnetic Composites as the stator material (Chapter 2: SMC Mk1 Motor, Chapter 3: SMC Mk2 Motor, Chapter 4: SMC Mk3 Motor). The design calculations and measured performance of these early motors have provided valuable information and experience in designing with SMC and the use of plastic bonded magnets.

Chapter 5 and Chapter 6 take a step back and focus on the loss calculations in these motors. Stator iron loss calculations, especially when using SMC as the stator material, are analysed in Chapter 5, highlighting the issue of bulk eddy currents. Their impact is determined and a process to more accurately estimate the iron losses in SMC parts is described. Chapter 6 deals with the different sources of rotor iron losses, analysing their contributions to rotor heating.

Chapter 7 describes the fourth and last SMC motor, an improved design incorporating the experience gained from the earlier SMC motors and using the methods developed to predict the iron losses more accurately. A new SMC material with lower loss characteristic was also used. This resulted in a motor with acceptable performance and iron losses close to the existing motor.

However, during testing of the motor in a real turbomolecular pump, serious rotor dynamic run-up problems caused by unbalanced magnetic pull (UMP) were discovered. An analytical and experimental investigation followed, which is described in Chapter 8, to quantify the effect of UMP in this particular application, providing a better understanding of UMP effects in permanent magnet machines in general.

The design and development of a motor (Mk5) that has no intrinsic UMP is described in Chapter 9. The requirements of the physical space envelope had changed in the mean time, and a new smaller motor was required. Test results show there are no issues with UMP for this motor and successful performance in terms of losses and thermal behaviour is demonstrated.

The final chapter, Chapter 10, evaluates the project as a whole and reviews the objectives. It summarises the major achievements and shortcomings of the SMC motors in terms of their design and performance in vacuum pump applications, reviews the methods for the iron loss calculations and provides some suggestions for further work.

1.2 The Turbomolecular Pump

1.2.1 History of the Molecular Pump

The turbomolecular pump is a molecular drag pump that is designed to operate in the pressure range of 10^{-3}mbar down to 10^{-8}mbar (molecular flow conditions). The initial idea of the molecular pump was developed by Gaede [1] in 1913 (Fig. 1.1), using a fast (12000rpm) rotating cylinder to create a vacuum. The concept of the molecular drag pump is based on the principle that gas molecules, which strike a fast moving surface, have a directional velocity imparted. Molecular drag pumps were not much used until many years later due to their low pumping speed and their poor reliability as a result of the requirement for very tight clearances of only tens of microns between rotor and stator [2, 3]. In 1958 Becker [2] came up with a new concept of using blades on the rotor and stator like a turbine, which allowed clearances of 1mm and more. This was the breakthrough for the 'new' molecular pump, the turbomolecular pump (TMP).

Today many industrial processes and research labs are using vacuum. The fact that TMPs are able to produce a clean, high-vacuum makes them invaluable in many applications [4]. Examples are electron microscopy, mass-spectrometry, leak detection, some semiconductor processes like etching, sputtering, and vapour deposition, TV tube manufacturing, high-energy physics and ultra-high vacuum generation in research labs.

1.2.2 Basic Principle of Operation

The operating principle of a TMP [4-6] is based on the physics of momentum exchange between a molecule and a moving surface. The short but finite residence time occurring when a molecule strikes a surface results in the molecule acquiring an additional velocity component in the direction of the moving surface. The orientation of the moving (rotor) blades and stationary (stator) blades to the axial direction in a TMP is shown in Fig. 1.2. Overall performance is optimised by varying the blade geometry throughout the pump. For the blades to be effective with the rapidly moving molecules, the blade speed must approach the molecule speed; otherwise the molecules will pass through the rotor without being struck [4].

The average air molecule with a molecular weight of M=29 at a temperature of T=300K has a velocity of about 470 m/s [6]. Heavier molecules will be slower, lighter molecules will be faster. This means that the impeller needs to rotate at high speeds for the blade

tips to reach speeds of similar order. For example, with an impeller diameter of 100mm and a rotational speed of 60,000 rotations per minute the blade tips move with a speed of about 314 m/s. This means turbomolecular pumps require a high-speed motor.

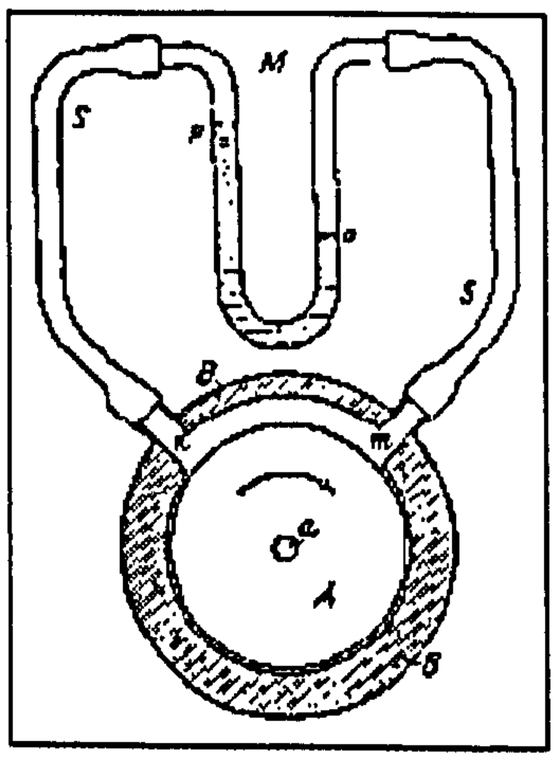

Fig. 1.1 W. Gaede's first experiment on molecular drag pumping, 1912 [7]

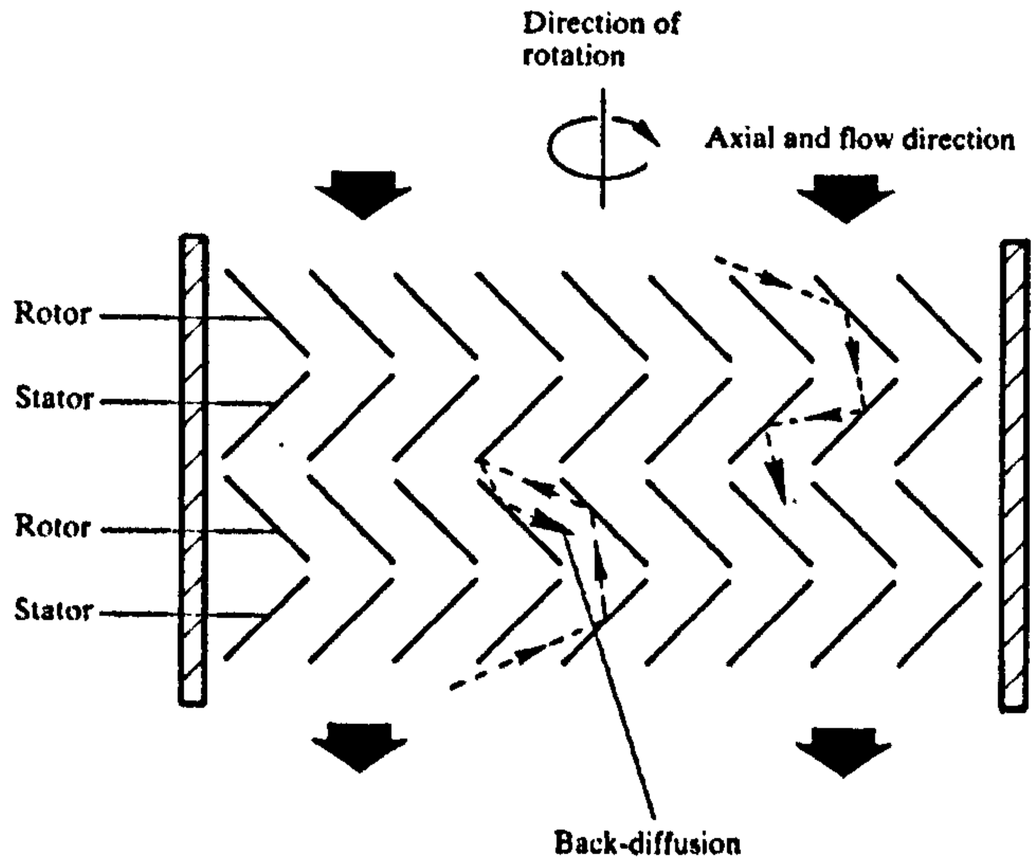

Fig. 1.2 Orientation of rotors and stators in a TMP [4]

1.2.3 Construction of a Turbomolecular Pump

Fig. 1.3a shows a cross section of a typical TMP. The turbine-like bladed impeller is mounted onto a shaft, which is held in position by a passive permanent magnet bearing at the top and an oil-lubricated ceramic ball bearing at the bottom of the shaft. One emergency mechanical bearing at the top protects the impeller against serious damage from external vibrations and shocks which can overcome the stiffness of the magnetic bearing. The motor is located inside the pump envelope and therefore exposed to a vacuum.

To reduce transmitted vibration (important for applications like electron microscopes) and to keep the vacuum free from any out-gassing of oil or grease lubrication in the bearings (important for applications like mass spectrometers or to reach ultra high vacuum), some turbomolecular pumps support the impeller entirely on magnetic bearings. Fig. 1.3b shows a cross section of a typical 'magnetically levitated' pump. In this design there are two passive permanent magnet bearings, one at the top and one at the bottom, providing radial support, and one active magnetic bearing controlling the axial position. Such a bearing arrangement has a very low radial stiffness compared to

standard ball bearings, and is very sensitive to unbalanced forces. To protect the pump there are two emergency ball bearings.

Both pumps are the target application for the design and development of a new motor, which is the subject of this thesis.

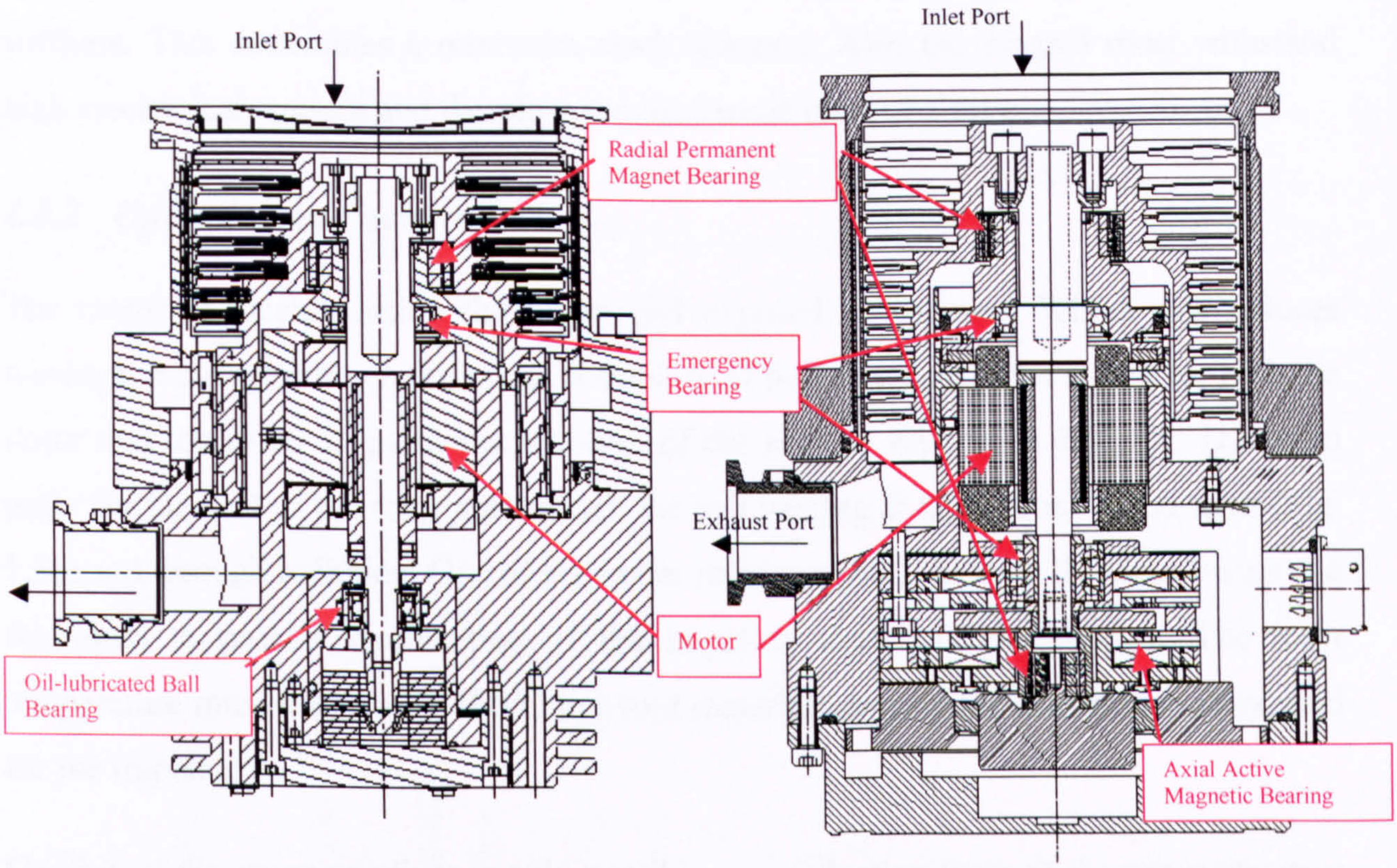

Fig. 1.3 Cross-section of a turbomolecular pump with a) hybrid bearings, b) magnetic bearings [8]

1.3 Specific Motor Requirements for a Turbomolecular Pump

It has been shown that turbomolecular pumps (TMPs) require a motor to drive the impeller at speeds of up to 90,000rpm (depending on impeller diameter) for the pumping mechanism to work. Therefore the motor of a TMP faces three challenging design requirements: (1) operating at high speed, (2) operating in vacuum, and (3) being cost effective to manufacture. Additional requirements become apparent through the course of this thesis.

1.3.1 Operating at High-Speed

High speeds of 60,000rpm are a challenge to the life of the ball bearing in terms of friction and heat removal. Running in vacuum reduces the windage, but unfortunately also reduces the cooling, and as a result one of the major paths for the heat out of the

rotor is through the bearing. Hysteresis and Eddy current losses are roughly proportional to frequency and frequency squared respectively. Hence a major requirement for high-speed operation is to keep the stator and rotor losses under control and to a minimum to avoid damage to the bearing and / or excessive heating of the impeller.

High speed is also a challenge to the rotor with respect to rotor dynamics and shaft stiffness. This determines a minimum shaft diameter. Also the magnet must withstand high mechanical stresses and therefore requires some form of sleeve.

1.3.2 Operating in Vacuum

The motor is located inside the pump and exposed to vacuum. Whilst this reduces windage, it also severely reduces the possibility of heat removal. This is true for both the stator and the rotor. In particular, cooling of the rotor is especially difficult. The main paths for the heat of the rotor are through the ball bearing at the bottom of the shaft (Fig. 1.3a) and through radiation. One of the major requirements is to keep the rotor losses at a minimum to prevent overheating of the impeller, shaft and the bearing. The rotor temperature must not exceed 100°C to avoid material creep in the aluminium alloy used for the impeller.

Cooling of the stator windings is only possible by conduction through the stator structure itself into the body of the pump, and by radiation from the windings. For the stator to conduct heat into the body effectively, a good thermal contact between stator and pump body is required because in vacuum even a gap of a couple of hundred microns acts as an insulation barrier. Potting the stator windings in epoxy can improve the situation.

Out-gassing is another problem in a vacuum and therefore only materials with a low vapour pressure suitable for vacuum applications can be used.

1.3.3 Cheap to Manufacture

There is a strong commercial pressure, especially for the semiconductor industry, to reduce the cost year by year. To stay competitive in the market the price of a turbomolecular pump has to follow this trend.

The motors are specially designed for Edwards and due to a high content of manual labour and relatively low annual volumes the existing motors are expensive. Looking at the relative costs of the parts of an existing turbomolecular pump (Fig. 1.4), the motor

stator stands out as the second most expensive item, and if considered together with the rotor, it becomes the most expensive component. This makes the motor (stator and rotor) a prime target for a cost reduction project.

The aim of this thesis is therefore to design and develop a motor with a low manufacturing cost but with comparable performance to the existing motor. It is intended to achieve this through the use of new materials (SMC, plastic bonded magnets), alternative manufacturing methods (powder metallurgy rather than lamination stamping, or alternative laminated structure e.g. tooth segments and non-overlapped windings), simplified assembly processes (simpler rotor construction, simpler coil insertion by segmented designs and non-overlapped coils).

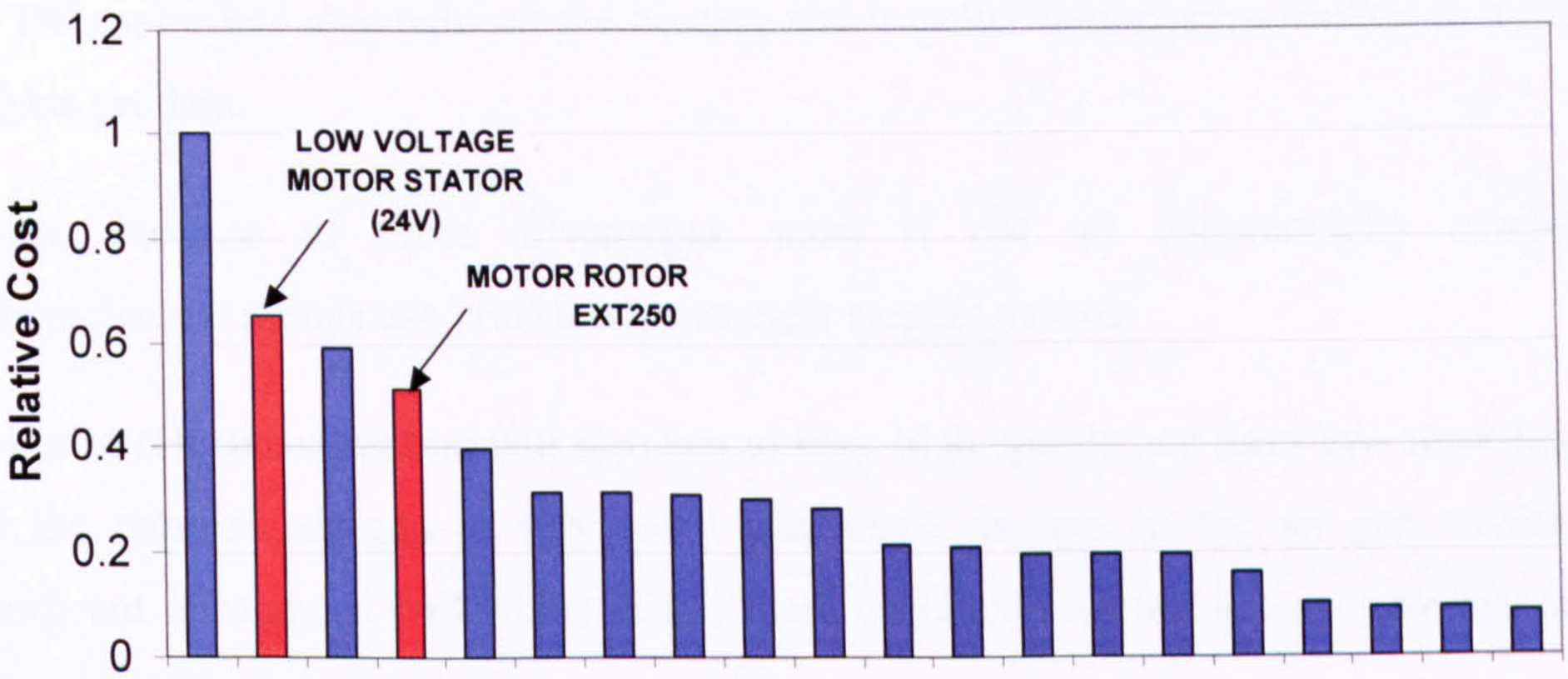

Fig. 1.4 Cost breakdown of a turbomolecular pump – the 20 most expensive individual items excluding in-house labour (due to commercial sensitivity individual items other than the motor can't be identified)

1.4 Choice of Motor

Due to the high speed requirement of TMPs, brushed motors (DC or AC synchronous) are not suitable, because of wear of the brushes and friction losses at the high speeds.

In the early years of the development of TMPs induction motors were used to drive the pumps. They were the most advanced and developed motors at that time, and easily available. However, one of their biggest problems was the induction heating of the rotor leading to high rotor and impeller temperatures. Another disadvantage of the induction motor was the small air gap. With the move to magnetic bearings to create a clean, lubricant free vacuum, the stiffness of the bearing system reduced, and the small air gap

between stator and rotor became problematic. UMP may also have been an issue with induction motors and passive magnetic bearings.

In the mid 1980's there was a move to use brushless permanent magnet DC motors rather than induction motors. In 1988 three different types of motor systems were used [3, 9]: the AC induction motor, the brushless DC permanent magnet motor and the hysteresis motor. Conrad and Gutperlet [9] showed in their comparison of the three different types, that the hysteresis motor has by far the largest losses (33W, mainly iron losses), followed by the AC motor with 22W, and the brushless DC motor with only 15W (all for a torque of 2Ncm at f=720Hz, equivalent to 90W output power). The DC motor not only has the lowest power consumption and losses of the three motors, it also has the largest air gap between rotor and stator, which made it mechanically more reliable. The low losses of the DC motor had also reduced the bearing and impeller temperature leading to a more reliable product.

Today, because of these advantages, most if not all commercially available turbomolecular pumps use brushless permanent magnet motors.

Switched reluctance motors will also run to very high speeds and have low rotor losses but the required air gap is very small and small changes in the air gap results in significant unbalanced pull which makes them unsuitable for use in a passive magnetic bearing application.

1.5 The Existing Motor

1.5.1 The Stator

The existing motor is a brushless DC permanent magnet motor. The lamination stack is made of 0.35mm fully-processed, non-oriented lamination steel (M330-35-A5). A cross section of the motor and the lamination is shown in Fig. 1.5. The stator has six teeth and the three-phase winding uses fully overlapped coils with a coil pitch angle of 180°. Each phase consists of two coils, wound in a double layer arrangement. The coils are wound separately, but inserted by hand into the stator. This process is very labour intensive and time consuming and contributes significantly to the cost of the motor. (For a summary of the machine details of the existing motor and all new motors discussed in this thesis see Appendix A).

1.5.2 The Rotor

There are currently two very similar rotor designs, which work with the same stator. Ideally both designs should be replaced with one generic rotor.

One rotor design has the rotor as a separate item, which is shrunk onto a stainless steel shaft. It consists of a mild steel magnetic carrier, rare earth Samarium-Cobalt (SmCo) magnets and a stainless steel sleeve. The rotor has two poles with a magnet arc length of 127°. Each magnet arc consists of five rectangular slab magnets, which are glued onto the mild steel carrier (see Fig. 1.5), giving a radially magnetised field. An aluminium spacer is glued between each magnet arc. Finally the stainless steel sleeve is added.

The other variant combines the shaft and rotor in one assembly. This was necessary because the impeller of this pump variant was longer and the shaft would have been too thin if a "shrunk on rotor" was to be used. To avoid bending due to rotor dynamics, this rotor consists of a thicker magnetic steel shaft (combining the magnet carrier and shaft in one) onto which the five slab magnets per pole are glued directly. The magnet material is identical (SmCo), but the sleeve is made of carbon fibre reinforced epoxy (CFRE) in an attempt to reduce rotor losses and reduce cost.

The motor (stator and rotor) has been specifically developed by one supplier for Edwards. This makes Edwards very dependent on this supplier and takes out any competitive price negotiation. The company is looking for an alternative motor design for this reason even without any improvement in the design.

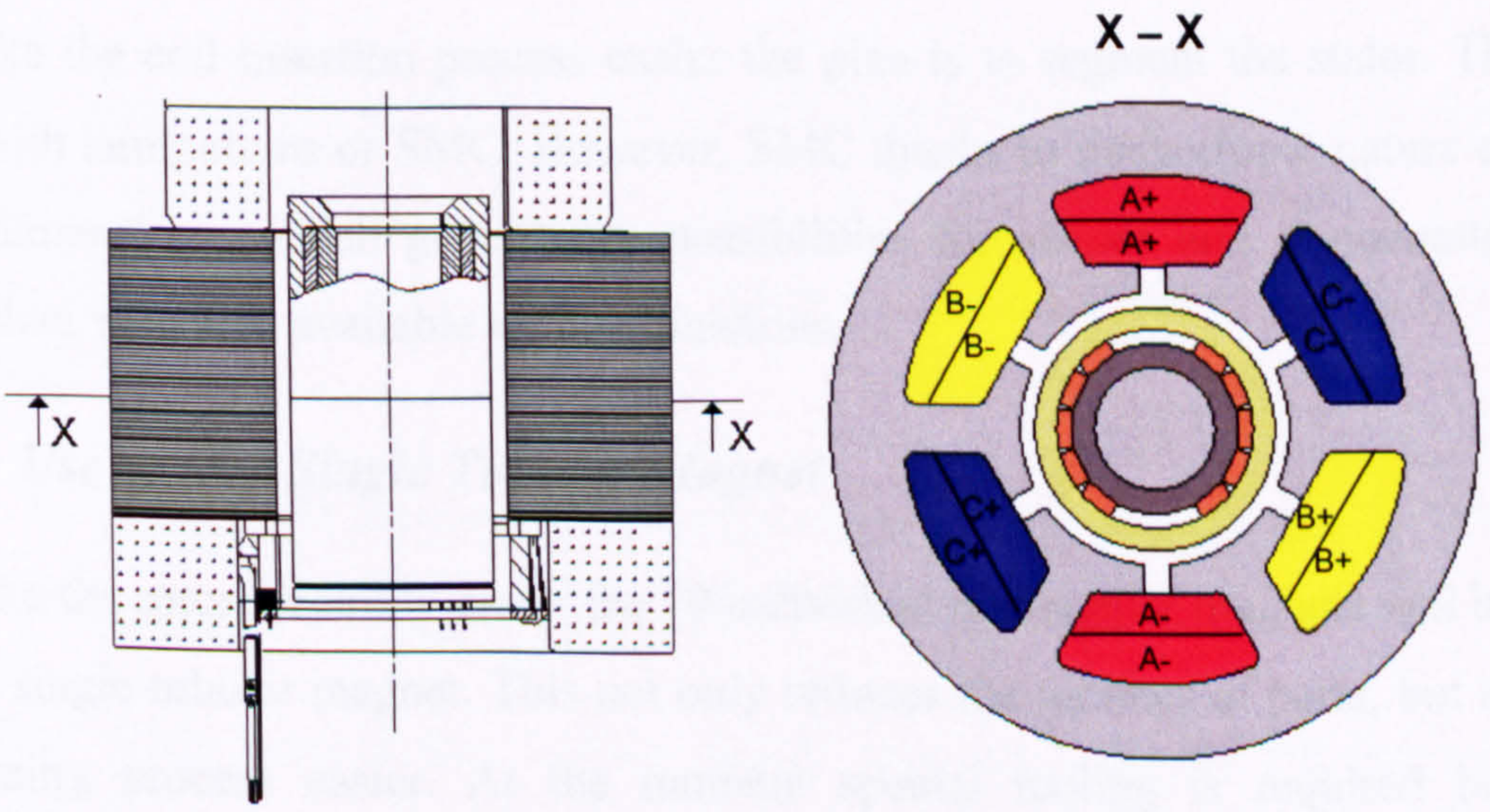

Fig. 1.5 Cross-section of existing turbomolecular pump motor – stator and rotor

1.6 Low-Cost Motor Design Suggestions

Based on a brushless DC permanent magnet motor, the following ideas will be the initial starting point for the new motor design and will be evaluated and tested in this thesis.

1.6.1 Use of Soft Magnetic Composites (SMC) for the Stator

The aim is to reduce the stator iron losses in the high-speed motor, especially the eddy current losses, through the use of soft magnetic composites. The average grain size of SMC is less than the thickness of laminations and hence SMCs might be expected to have lower iron losses at higher frequencies. However, in practice the particle insulation is not perfect and the material possesses some bulk conductivity. Another advantage of SMC is that the net shape parts and smooth surface finish enable concepts in which the core is assembled from sub-components, which allow simpler windings. Simplifying the windings might help to overcome the single-supplier problem faced by the company.

1.6.2 Use of Non-Overlapping, Concentrated Coils

The existing fully-pitched, overlapped winding is difficult to insert, either by hand or automatically. Using a design with non-overlapping coils gives more opportunities for simple coil arrangements. To maintain compatibility with the existing controller, the motor has to be a three-phase motor, which means that the minimum number of coils is three, suggesting a three-tooth design.

1.6.3 Segmenting the Stator

To make the coil insertion process easier the plan is to segment the stator. This can be done with laminations or SMC. However, SMC thanks to its isotropic nature can use all three dimensions, which gives more possibilities for shapes and segmentation of the stator than would be available with laminations.

1.6.4 Use of One Single Tubular Magnet

To make the rotor assembly easier the 10 individual rectangular magnets will be replaced with a single tubular magnet. This not only reduces the number of parts, but also makes the gluing process easier. At the moment special tooling is required because the individual slab magnets repel each other when glued next to each other. A single piece magnet should make the assembly process much easier, and reduce the possibility for errors by gluing on a magnet the wrong way round.

1.6.5 Use of Plastic Bonded Rare Earth Magnets

Plastic bonded rare earth magnets have a lower electrical conductivity than pure sintered rare earth magnets, which should help to reduce the rotor losses. Plastic bonded magnets are generally understood to have a lower energy product per unit cost but in these machines the high speed necessitates a relatively low air gap flux density, which makes sintered magnets very thin and hence expensive, and renders plastic bonded magnets competitive.

1.7 Objectives

The thesis describes the progress of the work and to some extent reflects the changing directions as the research revealed performance problems and issues and additional requirements. The aim at the outset of the work can be summarised as follows:

- **To investigate the suitability of a 3-tooth, 2-pole SMC design, with a single piece plastic bonded rotor magnet as a low-cost alternative solution of similar performance to the existing motor.**

Constraints: The new motor is intended to be a direct replacement for the existing motor. It should be possible for it to be retrofitted into the existing pump variants without requiring an absolute minimum of modification to other parts of the pump. Therefore the new motor must fit in the existing space envelope and must work with the existing drive, ideally without any modifications of the drive, as this would require a full product re-qualification.

An initial assumption that UMP in this 3-tooth, 2-pole motor would be low enough not to be an issue proved to be wrong, and a series of theoretical and practical investigations into the magnitude of the UMP force followed. Hence, a second objective could be formulated as:

- **To quantify theoretically and experimentally the magnitude of UMP in a 3-tooth, 2-pole machine, which is supported by magnetic bearings.**

The UMP study showed that 3-tooth, 2-pole was not viable in the passive magnetic bearings currently employed and the consequence was a third objective:

- **To design, prototype and test a motor with sufficiently low UMP, that is as simple as possible to construct.**

Constraints: Instead of being a retrofit, projects in the company have moved on and the target for the new motor is the next generation of pumps. Due to a change in pumping mechanism, a motor with a significantly shorter axial length than the existing motor is required, but an increase in outer diameter can be tolerated. There is no requirement with respect to existing drive compatibility, as a new sinusoidal, sensorless drive will be developed for this new generation of pumps. The drive is not part of this thesis.

Chapter 2

The First 3-Tooth, 2-Pole SMC Machine (Mk1)

2.1 Introduction

There has been a desire to move away from the current overlapped winding machine because of the cost in manufacturing of such a specialist motor at such low annual volumes.

The move towards a non-overlapped three-tooth concept had been shown to be promising in a previous study by Edwards and the University of Newcastle [10]. Another major change of that design was the move to using SMC for the armature, mostly for the possible benefits in simplicity of construction – simple sub-contracted components available from a wide range of suppliers with very simple bobbin wound coils which could easily be sourced from multiple suppliers. That particular machine was designed to be capable of producing 1.0Nm at 18,000 rpm and operating at speeds of up to 36,000 rpm. The results demonstrated that a three-tooth brushless permanent magnet design made from SMC can deliver comparable performance to a laminated design [11].

Extending the use of SMC and the three-tooth concept to a permanent magnet motor operating at 60,000 rpm, and delivering about 100W is the challenge of this part of the research. This chapter describes the background, the design constraints and process in obtaining the first high-speed machine made from SMC for this application, as well as the results of this first prototype SMC motor.

2.2 Background

The first prototype machine (Mk1) was a first try at using the three-tooth concept and SMC in a real turbomolecular pump application. The chosen application was the 250 l/s family of turbomolecular pumps as these represented the largest percentage of the TMP production at Edwards and hence promised the greatest cost savings.

The initial requirements were for proof of concept for the higher speed application rather than very fine optimisation and it was always expected that further refinement would be necessary. In the absence of any experience of designing with SMC or any knowledge of how accurate the data sheet values for SMC and the plastic bonded magnets are, a first prototype was necessary to evaluate the design calculations. Hence it was faster to do a quick initial design and build and test the motor, than to spend lots of time in trying to optimise the design without knowing how accurate the simulation was. The main aim was to gain experience and start to learn the key issues for this new style of machine and for designing high-speed machines with SMC.

The design, construction and testing of this first prototype fell in the period of the first year of the Engineering Doctorate program, where the majority of the time was spent at the University of Newcastle attending the taught modules. Therefore staff at Edwards carried out the assembly and testing of the motor, in order to provide the results for analysis.

2.3 SMC - Advantages and Challenges

One of the main technical research interests was to evaluate the use of SMC for this particular high-speed application. Therefore a brief overview over the properties of SMC will be given here.

SMC materials have been around since the earliest electrical machines. Fritts's patent of an apparatus for the production, transmission and distribution of electric currents [12], filed in 1886, had more or less all of the principles found in modern SMC: cores of finely divided magnetic material (fine iron filings), which are covered in a suitable non-conducting substance, which will both insulate the particles and cement them together in a compact mass. His aim was to minimise eddy currents and reduce waste energy in heating when using high frequency currents.

The key to good SMC properties is the grain insulation system. It must be very thin, continuous around the particle and be capable of surviving high temperatures during processing. Over the past 20 years there has been renewed interest in SMC due to advances in the insulation material and in grain coating [13-15]. The latest materials are becoming a viable alternative to steel laminations. Their AC properties and performance for the use in electrical machines has been demonstrated in several prototypes providing new design concepts are followed to allow a successful performance [16-21]. The following SMC properties need to be considered for an optimum design [22]:

3D flux and 3D geometries: The main features of SMCs, which make them a viable alternative, are the isotropic magnetic properties and the powder metallurgy process. This allows complex 3D-geometries in the tooth design allowing flux concentration and simple windings leading to an easier assembly process. For example the tooth tip and the core back can be axially extended while the tooth body is made shorter reducing the end windings and copper loss.

Losses: Despite high loses at low frequencies (hysteresis losses) SMCs potentially have a better dynamic behaviour than laminated steels at high frequencies because the average grain size is less than the thickness of laminations. Care needs to be taken here because the grain insulation is not perfect and therefore there is a finite conductivity, which leads to what might be described as 'bulk eddy currents'. These eddy currents and hence losses are related to the size and shape of the SMC component and to the electrical frequency at which they operate. Hence no generic statement on the balance of loss between SMC and laminations can be made. The rather complicated issue of iron loss in these SMC prototypes is covered in more detail in Chapter 5. For now let it suffice to show typical measured loss curves on a 5x5mm cross-section ring sample (Fig. 2.1).

Permeability and Magnetic Induction: SMC has a significantly lower maximum relative permeability than typical lamination steels (figures of greater than 500 are good) mostly because the compaction can never be perfect. It also saturates earlier than the pure iron from which its particles are made because of local variations of porosity around a particle. In permanent magnet machines, where the maximum permeability of the stator is less important due to the large air gaps, SMC can be competitive. The low saturation levels can be overcome by using more iron in critical regions. Also in these high-speed machines flux densities near saturation need to be avoided to control iron loss. The B-H curve for a ring sample of the material used in the first prototype is shown in Fig. 2.2.

Strength: Compared to laminations SMC has a lower strength as it cannot be sintered. Sintering would destroy the insulation layer between the iron particles leading to an increase in eddy current losses. The lower strength allows use in a stator but may not be appropriate for a rotor due to the high rotational forces. The centrifugal load depends on diameter and speed and is proportional to the square of the rotational speed. The material is much weaker in tension than it is in compression. The ultimate tensile strength (UTS) depends on the heat treatment but for the material used in the first prototype the UTS is around 19MPa (compared to 430 MPa for M330-35A lamination steel).

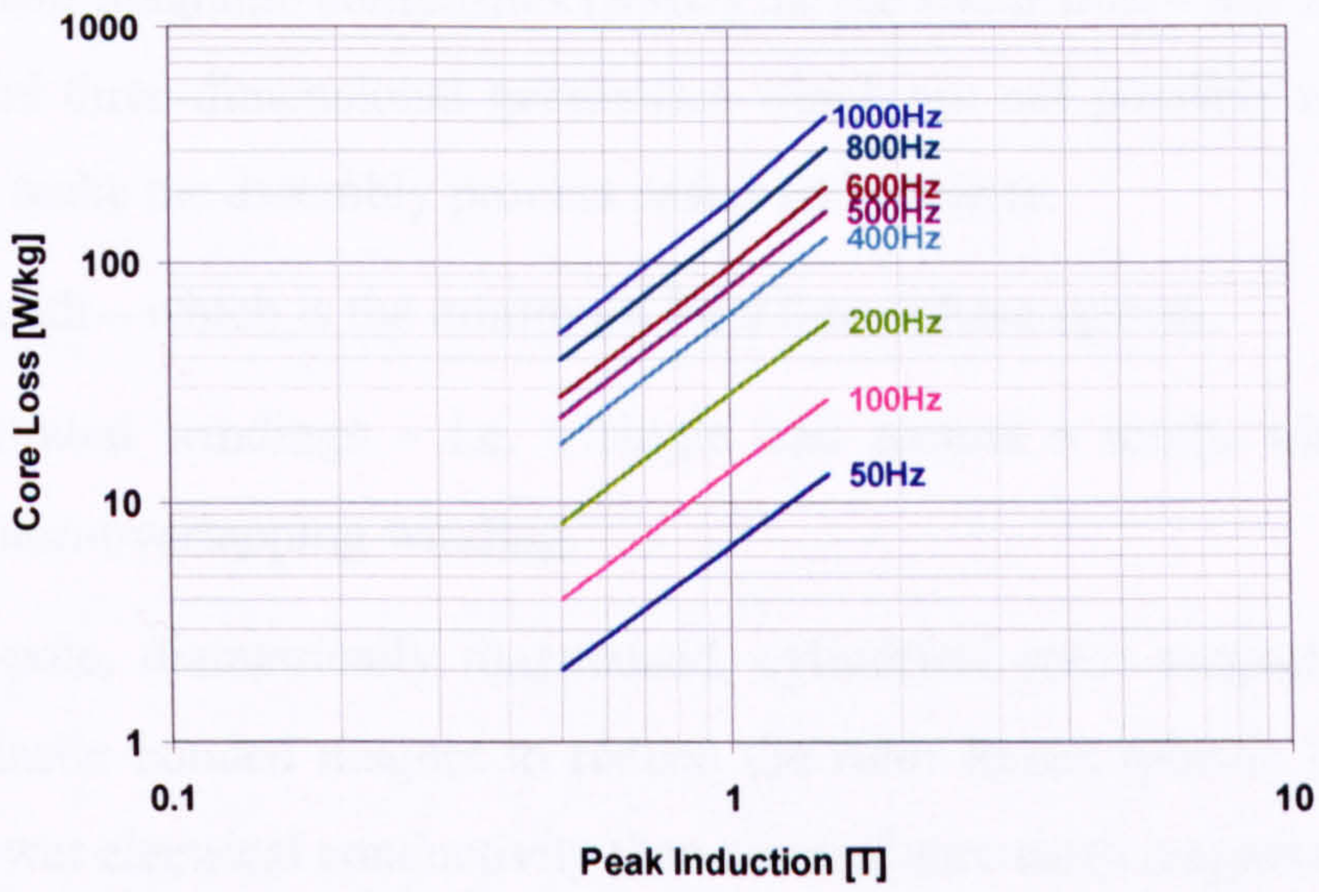

Fig. 2.1 Core loss for Somaloy 500+0.5%Kenolube compacted at 600MPa, heat treated at 500°C for 30minutes in air [23]

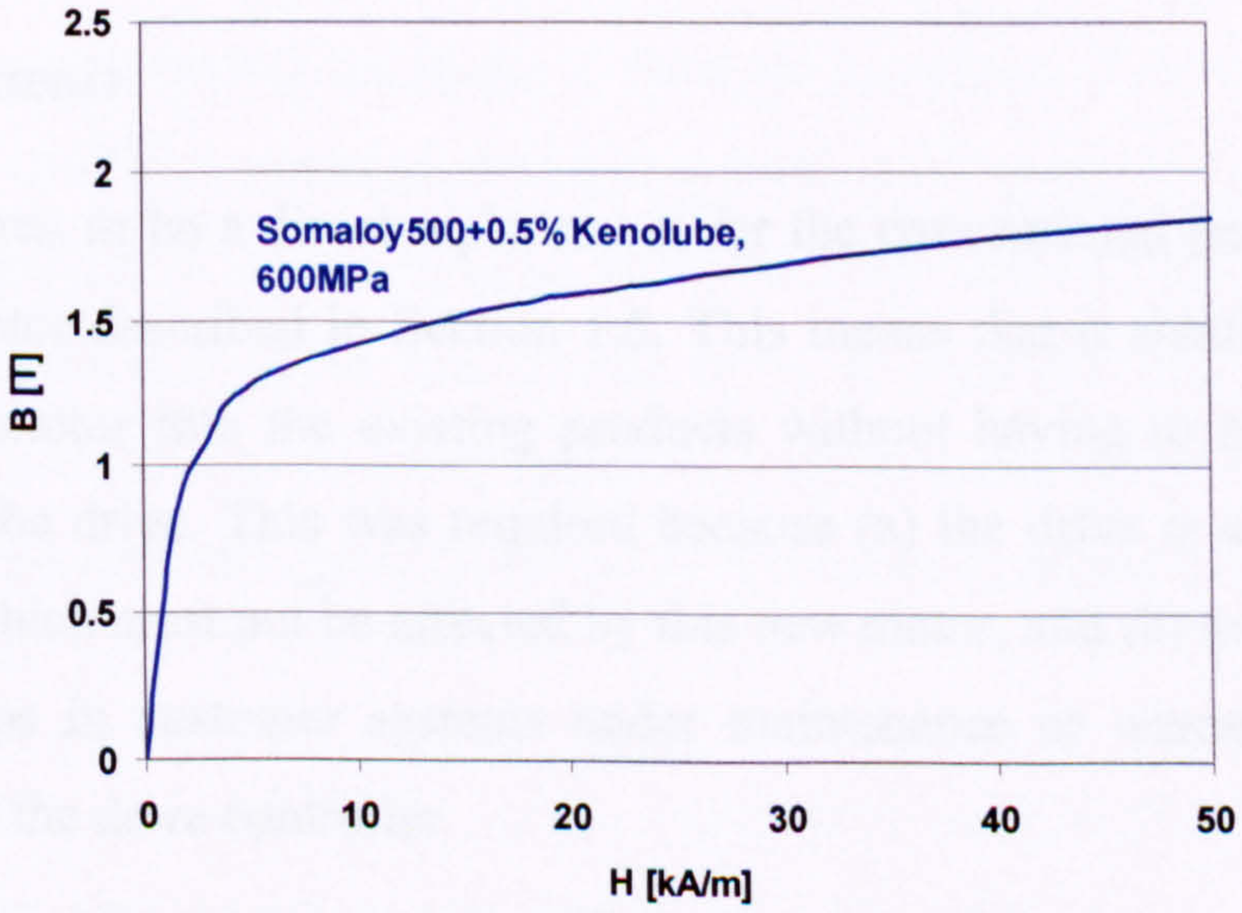

Fig. 2.2 B-H curve of Somaloy500+0.5%Kenolube, compacted at 600MPa, heat treated at 500°C for 30minutes in air [23]

2.4 Design Concept and Dimensions

2.4.1 Design Concept

The main objective was to design and develop a simple motor with a low manufacturing cost, with comparable performance to the existing motor. Only a significant change in the design, the materials and the manufacturing and assembly methods used could reduce the cost.

The design concept for the new motor was:

- Use of soft magnetic composites (SMC) for the stator iron – this allows net shape parts and three-dimensional geometries which are not possible with laminations but can make the assembly process easier and cheaper.
- Three teeth – which is the minimum for a three-phase system.
- Concentrated windings – i.e. a single coil around a tooth, which produces a simple non-overlapping winding.
- A two-pole, diametrically magnetised, cylindrical rotor magnet – preferably a deep plastic bonded magnet to reduce the rotor losses (plastic bonded magnets have lower electrical conductivity than sintered rare earth magnets)
- A non-conductive sleeve – e.g. carbon fibre to protect and strengthen the magnets against centrifugal forces.

2.4.2 Requirements

The new motor was to be a direct replacement for the conventional permanent magnet, brushless DC motor described in Section 1.5. This means that it should be possible to retrofit the new motor into the existing products without having to modify any other parts, including the drive. This was required because (a) the drive is universal to other pump variants, which must not be affected by this new motor, and (b) to allow individual retrofits of pumps in customer systems under maintenance or warranty without also having to replace the drive controller.

This can be translated into the following specific design requirements for the new motor:

- The new motor was to fit into the physical space envelope of the old motor, i.e. having an outside diameter not larger than the old one, and an overall axial height including end windings and Hall board not exceeding the existing height.

- The motor was to work with the existing drives, which require the line resistance, inductance and back EMF to be of similar value.
- The new motor was to be cheaper and easier to make without (any) significant negative impact on the performance.

2.4.3 Choice of Materials for Mk1

Stator

The main aim of this part of the project was to test the use of soft magnetic composites as the material for the stator. It was hoped that SMC would help to reduce the overall stator iron losses in this high-speed machine, and also reduce the cost of assembly by having a segmented design (see Section 2.5). The material used for the stator was Somaloy^{TM}500 +0.5% Kenolube from Höganäs AB, Sweden [23]. This was one of the main 'standard' materials available from Höganäs at the time of this first prototype.

Magnet

The rotor/shaft construction has a great influence on the total rotor losses, which are of high importance for turbomolecular pumps. To keep the eddy current losses in the rotor to a minimum, a plastic bonded NdFeB magnet was chosen because of its lower electrical conductivity compared to sintered rare earth magnets. The magnet material used was VACOBOND NC 76/64 from Vacuumschmelze GmbH [24].

Sleeve

A sleeve is required to protect the magnets from the centrifugal forces, against damage during assembly, and from corrosion during operation in the pump. It was decided to use the same non-conductive sleeve material as is used on several other turbomolecular pumps. A non-conductive sleeve was chosen to try to minimise the rotor losses, and using existing parts helped to keep the impact of a replacement motor low. The material was a carbon fibre reinforced epoxy from Hardy Advanced Composites.

Shaft

The shaft material was chosen as carbon (magnetic) steel, 817-M40-T (previously EN24T), due to its common use on other turbomolecular pumps.

2.4.4 Physical Dimensions

Stator Overall Dimensions

As this motor was a direct replacement the physical design envelope was given by the space in the pump. The outer diameter was chosen to allow the motor to fit into the existing bore, and the maximum axial length including end winding and Hall position sensor board had to be equal or smaller than the existing motor.

→ outer diameter (OD) of new SMC motor (same as before): 54 mm

→ overall axial height including endwindings and Hall board: 40 mm

The stator inner diameter (ID) was chosen to be similar to that of the existing laminations (ID=22.43mm) to give a similar mechanical air gap (the rotor uses an existing sleeve and therefore has same OD).

→ inner diameter of new SMC motor: 22 mm

The rest of the stator dimensions were chosen to accommodate the three-tooth design and allow enough space for the windings. For more details on the SMC design see Section 2.5.

Rotating Assembly – Magnet, Shaft and Sleeve Diameters

For reasons of stiffness and rotor dynamics an absolute minimum shaft diameter of 10mm was recommended based on Edwards' experience. This defined the magnet inner diameter. Trying to use as many existing parts as possible and to keep the number of changes to current parts to a minimum it was decided to use the existing carbon fibre sleeve. This defined the magnet outer diameter.

→ minimum magnet inner diameter: 10.1 mm

→ fixed magnet outer diameter: 16.32 mm

As one of the design concepts was to use a 'deep' plastic bonded magnet to minimise rotor eddy current losses, the whole available space was used for the magnet. Hence the above dimensions became the magnet dimensions, which gave a radial magnet thickness of 3.11mm.

The carbon fibre sleeve is an existing part with the following dimensions:

→ CFRE sleeve inner diameter: 16.45mm

→ CFRE sleeve outer diameter: 18.95mm

The preferred assembly process on the production line for the rotor assembly is glueing of the magnet and sleeve onto the shaft. This reduces the risk of putting the magnet under tension and avoids any press fits or shrink fits, which would require the handling of liquid N_2 on the shop floor. The chosen dimensions take account of the glue gaps.

Winding configuration

It was decided to use a delta configuration for the coils, as the coils are already in a delta arrangement in a 3-tooth design.

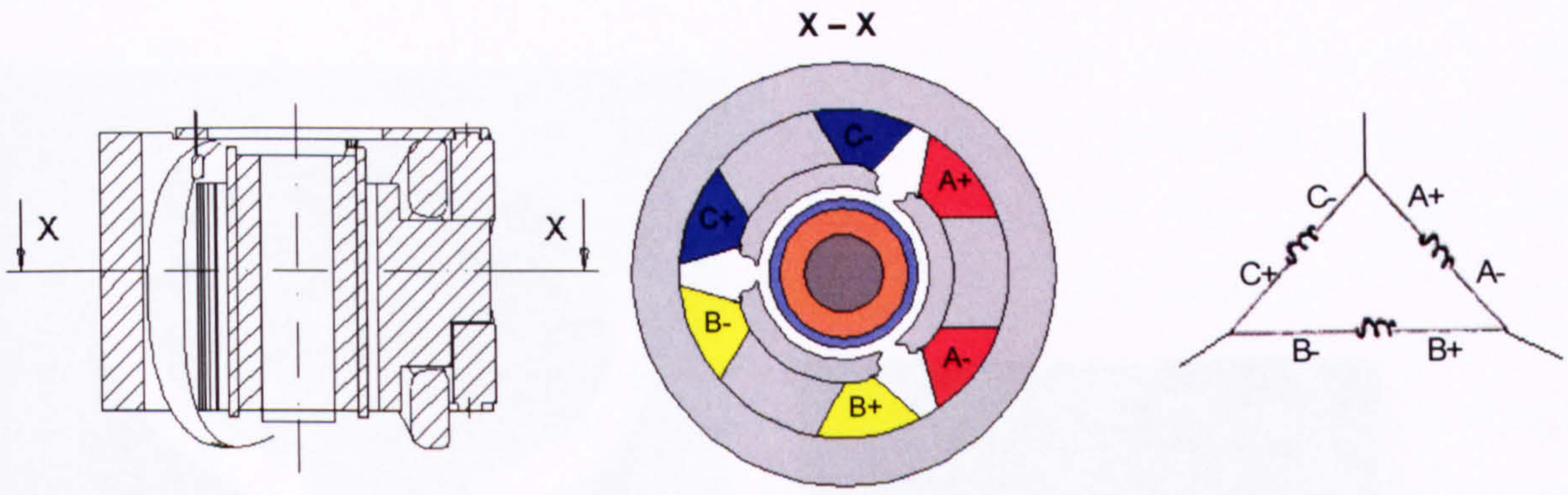

Fig. 2.3 Cross-section of first SMC motor Mk1 with delta-winding arrangement

2.5 The SMC Parts in Detail

2.5.1 Three-Dimensional Shaped Parts

One of the biggest advantages in using SMC is the possibility to produce complex shaped parts, which can make the assembly process easier and cheaper. Due to the powder metallurgy compaction process these three-dimensional geometries can be produced in a single compaction process.

The machine was constructed from 5 parts: three teeth and a two-piece back-iron ring, which holds and clamps the three teeth together. Fig. 2.4 shows a model of the parts, and Fig. 2.5 and Fig. 2.6 show photos of the real SMC components.

This segmented design allowed the coils to be wound and preformed (Fig. 2.7) independently and then inserted onto the teeth, or the coils could be wound directly onto the teeth. This process is much easier than to insert a fully pitched, overlapped winding, as is currently the case on the existing motor.

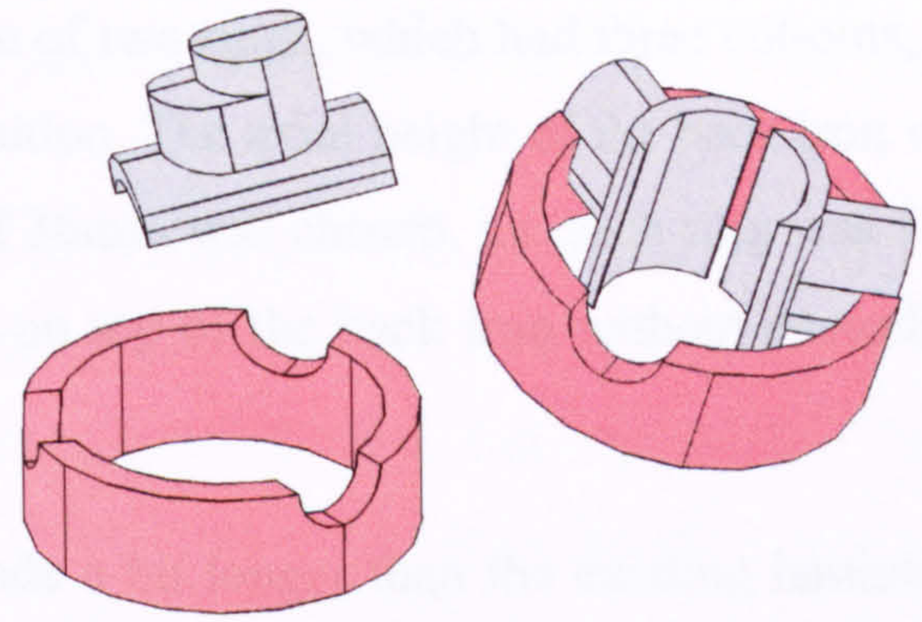

Fig. 2.4 The SMC stator parts: two back iron rings and three teeth.

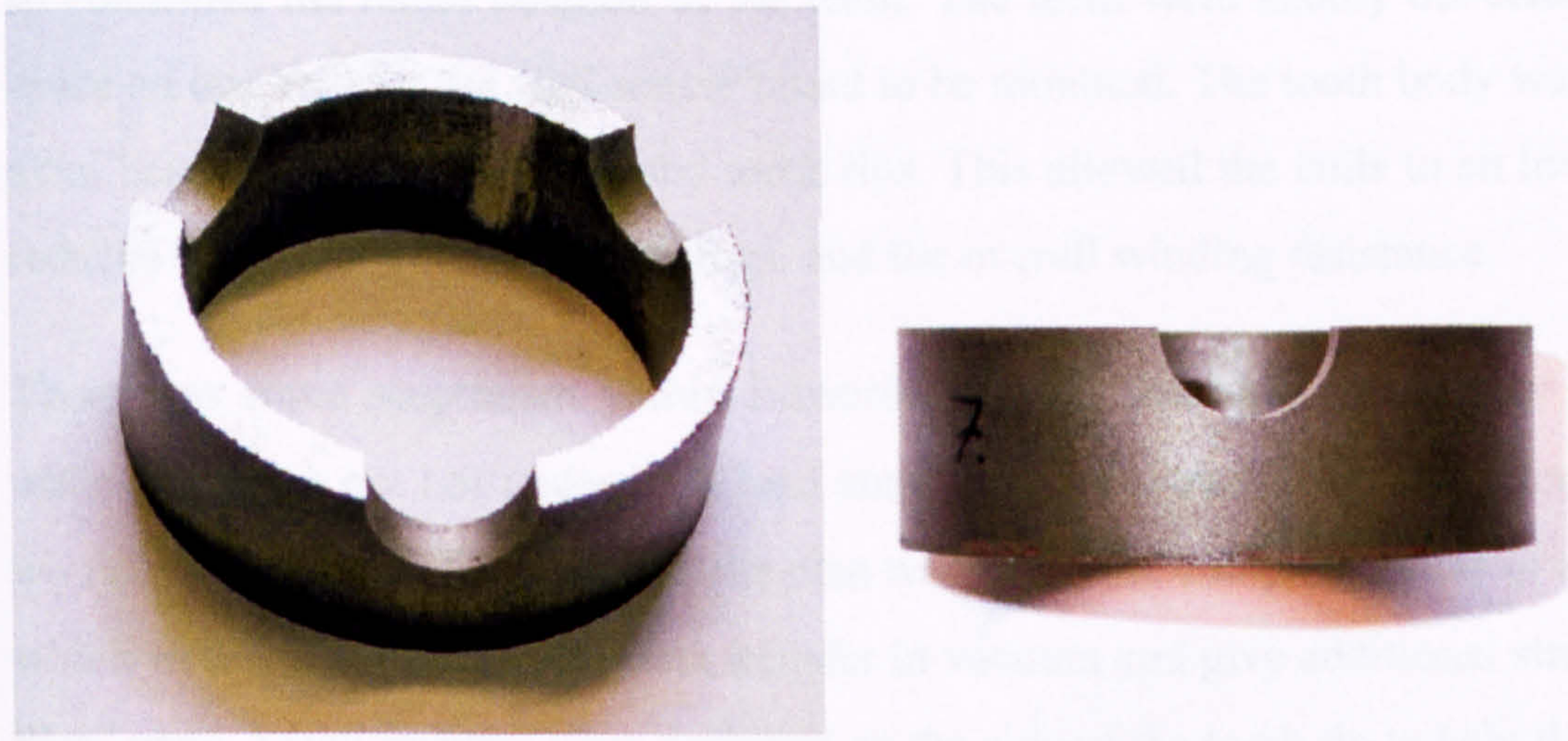

Fig. 2.5 The two-piece SMC back iron ring

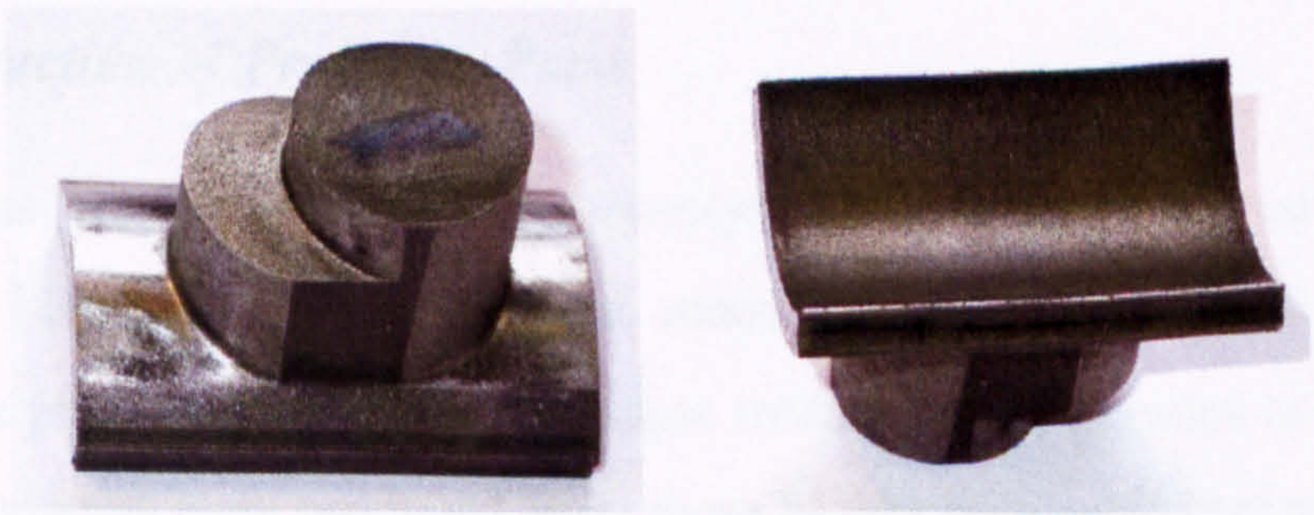

Fig. 2.6 The SMC tooth

Fig. 2.7 The wound and preformed coil

The back iron was made of two rings, which had three cut-outs, 120° apart, to locate and clamp the teeth into position. The axial height of the back iron was longer than the teeth, and an overall height of 36mm was chosen, i.e. each ring was 18mm high, so that a Hall board could be located on top of the back iron without exceeding the maximum height requirement.

The tooth tips were made a bit longer than the existing lamination stack (31mm versus 27mm) to collect as much flux as possible from the weaker plastic bonded magnet. The teeth were shaped with a step that located them in the cut outs of the back iron rings and so controlled the radial position of the teeth. The teeth were axially off-centre to allow space on one side for the Hall sensor board to be mounted. The tooth body was shorter in axial height than the back iron and tooth tips. This allowed the coils to sit lower, and so reduced the height of the end windings, and the overall winding resistance.

There was some scepticism within Edwards whether the teeth would stay in position when the motor got hot under high load conditions, or if the force of the magnetic field would pull them out. To avoid this the plan was to pot the complete motor in epoxy resin, which would also improve the heat transfer in vacuum and give additional strength to the SMC parts. Small features were designed on the side of the tooth tip to help the potting to retain the teeth.

2.5.2 Construction of Prototype Parts

A cheap and fast way to produce SMC prototypes is to machine the components out of pre-fabricated blanks. The blanks were made from Somaloy^{TM}500+0.5%Kenolube, compacted at a pressure of 600MPa, and heat treated for 30 minutes at 500°C. The ring and teeth components were produced from these blanks by a combination of wire erosion and machining.

The wound and preformed coils were then inserted onto the teeth, which were covered with a slot liner. The two back iron rings and the three teeth were all glued together. This assembly process was outsourced to North Devon Electronics Ltd., a traditional coil and transformer manufacturer. The process of inserting and connecting the coils is simple and does not require any specialised motor skills, giving the possibility of finding several potential suppliers.

2.6 The Motor Parameters of the First SMC Motor

This first SMC motor was always understood to be more a proof of concept rather than an optimised design. Hence, only very basic modelling was done to determine the main motor parameters: resistance, inductance, and back EMF. The main emphasis was on testing and subsequent modelling, rather than the other way round. The iron losses of Mk1 are discussed separately in Section 2.7 and in more detail in Chapter 5.

2.6.1 The Basic Finite-Element Model

A simple linear two-dimensional FE model was constructed (Fig. 2.8). To account for the 3D effects (different axial length of the tooth body and back iron) the dimensions of the 2D model were adjusted to give the same cross sectional area when using the active axial length of the tooth tips, i.e. the back iron was modelled thicker and the tooth body thinner than in reality.

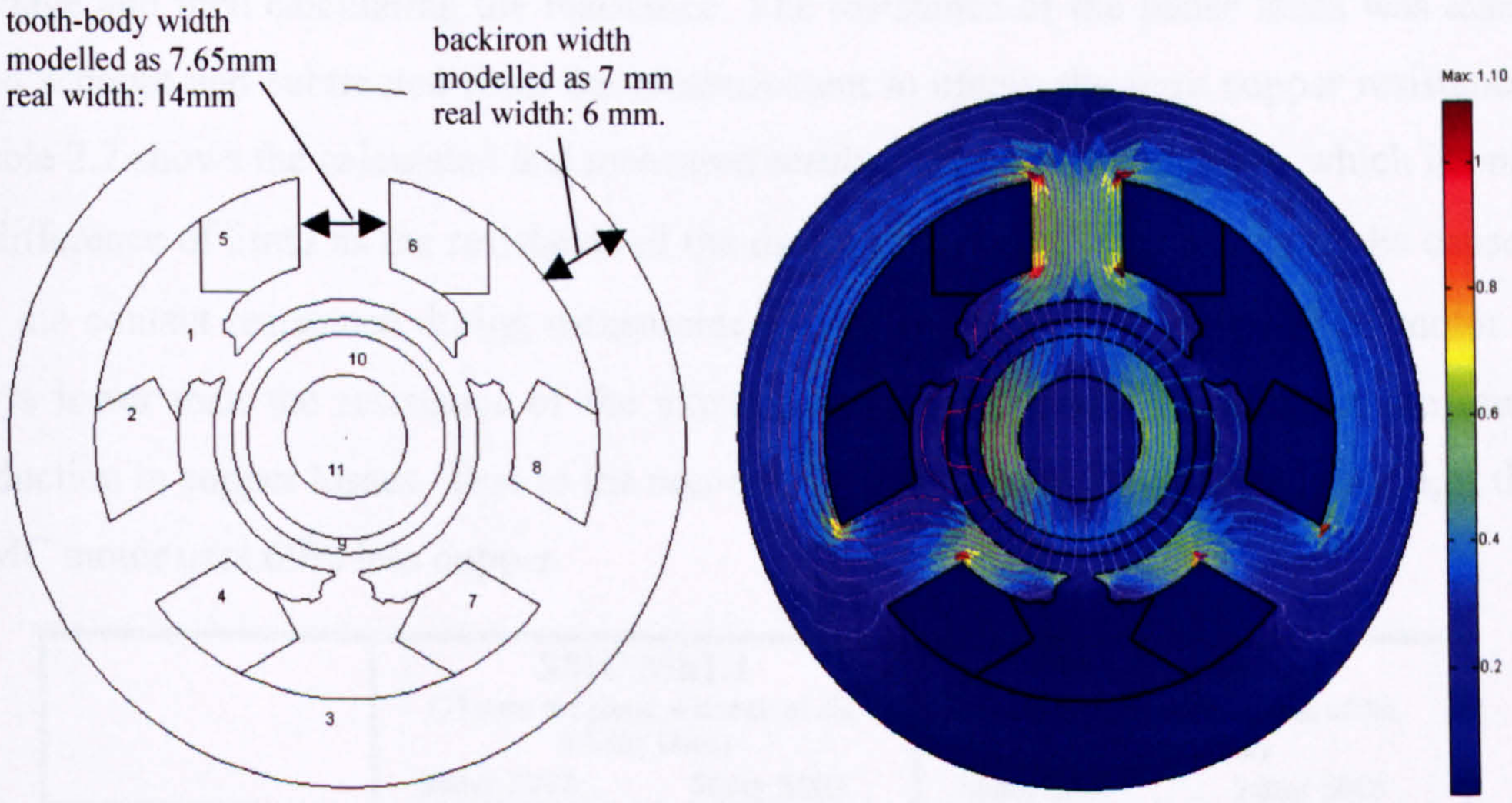

Fig. 2.8 2D-FE model of SMC Mk1 motor (axial length of model taken as tooth tip length of 31mm)

The data sheet values, which were used for the magnet and SMC, are given in Table 2.1. Later experience showed that a constant permeability of 500 was optimistic for SMC that had been cut after compaction and heat treatment (see Chapter 5).

Magnet	**SMC**
Vacobond NC 76/64 B_r: 0.68T, H_c: 410 kA/m, μ_r: 1.32 data at room temperature	Somaloy 500+0.5% Kenolube compacted at 600MPa, heat treated at 500°C for 30min, μ_r: 500

Table 2.1 Properties of the magnet [24] and SMC [23] used in the FE model of Mk1

2.6.2 Resistance & Copper Loss of SMC Mk1

The phase resistance depends on the average length per turn l_{turn}, the number of turns per phase N_{ph}, the cross sectional area per turn $A_{cu,turn}$ (wire cross section times the number of strands in parallel), and on the winding temperature T and can be calculated relatively accurately analytically using equation (2.1), where ρ is the resistivity of copper (ρ_{cu}=1.78·10^{-8} Ωm) and α_{cu} the temperature coefficient of the resistivity (α_{cu}=0.0039 1/°C). The DC copper loss is calculated according to (2.2) for a three-phase winding.

$$R_{ph,T_0} = \rho \cdot \frac{l_{turn} \cdot N_{ph}}{A_{cu,turn}} \quad \text{and} \quad R_{ph,T} = R_{ph,T_0} \cdot \left(1 + \alpha_{cu}\left(T - T_0\right)\right)$$

$$\text{STAR: } R_{LL} = 2 \cdot R_{ph} \qquad \text{DELTA: } R_{LL} = \tfrac{2}{3} \cdot R_{ph} \tag{2.1}$$

$$P_{cu} = 3 \cdot I_{ph,rms}^2 \cdot R_{ph} = 1.5 \cdot I_{LL,rms}^2 \cdot R_{LL} \tag{2.2}$$

The DC resistance was measured using the 4-wire method, measuring current and voltage and then calculating the resistance. The resistance of the phase leads was taken into account and subtracted from the measurement to obtain the pure copper resistance. Table 2.2 shows the calculated and measured results. They are within 10%, which is only a difference of 3mΩ as the resistance of the motor is so small. This can easily be caused by the contact resistance during measurement. The DC resistance of the SMC motor is 39% lower than the resistance of the existing motor, potentially resulting in the same reduction in copper losses. Due to the non-overlapped coils and shorter endwindings, the SMC motor uses 69% less copper.

	SMC Mk1.1 (27 turns per phase, 4 strands of dia. 0.5mm, Delta)		**Existing Motor** (14turns per phase, 9 strands of dia. 0.5mm, Star)	
	Stator S002	Stator S003	Stator S004	Stator S005
DC Line-Line Resistance				
Predicted	**30 mΩ**		**55 mΩ**	
Measured	35 mΩ	32 mΩ	54.2 mΩ	54.7 mΩ
Average	**33.5 mΩ** 39% less than current motor		**54.5 mΩ**	
Copper Loss				
with rated current of $5A_{rms}$, $T_{winding}$=60°C	**1.44W** 39% less than current motor		**2.35 W**	
Copper Volume & Mass				
Slotfill	**27.3%**		**24.4%**	
Volume	**4.46 cm^3**		**14.32 cm^3**	
Mass	**40.0 g** 69% less than current motor		**128.3 g**	

Table 2.2 DC resistance, copper loss and copper volume for SMC Mk1.1 motor

2.6.3 Inductance of SMC Mk1

The steady-state inductance given by (2.3) is defined as the flux linkage of the coil, Ψ, divided by the current in the coil. The same basic 2D-FE model was used, this time with a current density of J_0 and +/- $0.5J_0$ applied to the coils respectively according to a delta–winding. To model the inductance for the stator on its own (no rotor) the magnetic properties of the rotor were all set equivalent to air. The difficulty in the inductance calculation lies in the right choice of the axial length to be used to determine the flux linkage of the coil. This is especially true in this three-dimensional SMC tooth, as the tooth tips are much longer than the tooth body where the coil is located. The most consistent results were obtained by using the tooth body height, as this represented the coil length more closely (ignoring end effects).

$$L_{ph} = \frac{\Psi}{I} = \frac{N_{ph} \cdot \Phi}{I} \quad \text{with} \quad \Phi = \oint A_t \cdot dl \ \text{(from FE)} \quad \text{and} \quad J_0 = \frac{N_{ph} \cdot I}{coil\ area_{FE}} \ \text{applied}$$

$$\text{STAR: } L_{LL} = 2 \cdot L_{ph} \qquad \text{DELTA: } L_{LL} = \tfrac{2}{3} \cdot L_{ph} \tag{2.3}$$

The inductance was measured using an Inductance Analyzer (Wayne Kerr IA3255). Results are shown in Table 2.3. The calculated inductance underestimates the real inductance by 31% (Mk1.1) and 28% (existing motor). This is most likely due to the 2D model which neglects the endwinding inductance, and the three dimensional features of the SMC stator. Accurate inductance calculation is complex and only a 3D-FE model could take account of these effects.

	SMC Mk1.1 (27 turns per phase, Delta) Stator S002	Stator S003	**Existing Motor** for reference (14 turns per phase, Star) Stator S004	Stator S005
Line-Line Inductance (stator only)				
Predicted	**99 µH**		**85 µH**	
Measured	131.7 µH	128.0 µH	108.7 µH	109.4 µH
Average	**130 µH**		**109 µH**	

Table 2.3 Line-line inductance for SMC Mk1.1 motor – predicted and measured

2.6.4 Back EMF of SMC Mk1

The induced voltage in the windings, the back EMF E, is defined as the rate of change of flux linkage with time. This would require a time-stepping model unless the flux linkage, Ψ, varies with a constant rotational frequency, ω. In this case the time variation can be

replaced with a space variation, $d\Psi/d\theta$. The diametrically magnetised magnet produces a near enough sinusoidal magnetic flux distribution in the air gap, so that the EMF can be easily calculated using (2.4), with the flux per unit length obtained from FE.

$$E_{ph} = \frac{d\Psi}{dt} = \frac{N \cdot d\Phi}{dt} = N \cdot \frac{d\Phi}{d\theta} \cdot \frac{d\theta}{dt} = N \cdot \frac{d\Phi}{d\theta} \cdot \omega \quad \text{with} \quad \Phi = \hat{\Phi}_0 \cdot \sin(\theta) = \oint A_t \cdot dl$$

$$\text{STAR: } E_{LL} = \sqrt{3} \cdot E_{ph} \qquad \text{DELTA: } E_{LL} = E_{ph} \tag{2.4}$$

The first stator (Mk1.0) was wound with 21 turns per phase, which was calculated using the data sheet values and a simple 2D FE model. In practice this produced a below target back EMF and to get a similar back EMF to the existing motor the number of turns was increased to 27 (Mk1.1). Two motors with 27 turns per phase were then built, and tested in a back-to-back rig. The back EMF or open-circuit voltage between each of the phases was measured with a true-rms multimeter (Fluke III) on the generating end of the back-to-back rig. Table 2.4 shows the results.

	SMC Mk1.1 (27 turns per phase, Delta)		**Existing Motor** for reference (14 turns per phase, Star)	
	Stator S002	Stator S003	Stator S004	Stator S005
Back EMF Line-Line @ 1000Hz				
Predicted	**16.96 V_{rms}**		**14.21 V_{rms}**	
Measured	(13.33 V_{rms})	**14.42 V_{rms}**	14.21 V_{rms}	14.07 V_{rms}
Average	Rotor of S002 was demagnetised and the value of S003 is more representative		**14.14 V_{rms}**	

Table 2.4 Back EMF for SMC Mk1.1 motor

There was also a significant difference (8%) measured between the two Mk1.1 motors in the back-to-back rig. Both stators were known to have the same number of turns, as the resistance and inductance measurements were the same for both motors. Initially it was not clear if this difference was due to underperforming SMC, i.e. variation in material properties after machining, or due to an underperforming magnet. After a couple of tests (i.e. swapping shafts between existing motors and SMC motors) it was confirmed that it was due to the magnet. Unfortunately, there was not enough hardware and time available to make a new shaft for the back-to-back rig. Hence, all the performance tests (section 2.7) were carried out using this shaft, but the results for S003 are taken rather than those for S002 were possible.

Considering the results for S003, S004 and S005 in Table 2.4, good agreement between measured and predicted back EMF was achieved for the existing laminated motor, but not for the SMC Mk1.1 motor. The difference there was about 15%. Reasons for the error are:

- a too optimistic set of data for magnet and SMC,
- a simple 2D-FE model of the SMC not representing 3D effects appropriately and
- ignoring end region effects altogether in 2D.

2.7 Performance of the First SMC Motor

2.7.1 Estimation of Iron Losses

The design of the first SMC stator was driven by decisions about the physical size rather than the actual performance. Therefore iron loss modelling was only done in retrospect and not as part of a design and optimisation process.

The initial iron loss estimation for the SMC stator was very basic, using peak flux densities from the FE model and core loss data specified by the supplier. The stator was divided into three areas: the back iron ring, the tooth body, and the tooth tip. For each area a peak flux density value was taken from FE. For these values the specific loss values in W/kg were looked up from the data sheet curves and multiplied by the component mass.

Iron loss estimation for the existing laminated motor uses data sheet values for the lamination steel multiplied by an empirical lamination built factor of 1.5. This factor takes account of performance variation caused by [25]:

- mechanical stress and strain within the laminations due to manufacturing processes like stamping or cutting,
- non-annealed or improper annealed laminations,
- insulation breakdowns between laminations due to stamping burrs,
- air gaps due to stacking,
- and the difference between the ideal test conditions, in which the data sheet values were obtained (pure sinusoidal excitation), and the conditions in the real machine (non-sinusoidal / rotating excitation).

From the data sheet curves it is clear that replacing the existing laminated core with SMC will result in increased iron losses. However, this can be minimised by an optimised design of the SMC stator (see Chapter 7, SMC motor Mk4). The modelled iron losses for the SMC Mk1 motor are estimated at about 14W (see Table 2.5), compared to the modelled iron losses of the existing motor between 5.4W and 8W (past measurements have confirmed the motor losses to be around 6.5W to 7W, measured in a fully levitated turbomolecular pump with no mechanical losses). This means that the iron losses in the SMC machine are double those in the standard machine at no load, which is not ideal. But it is a starting point for further optimisations.

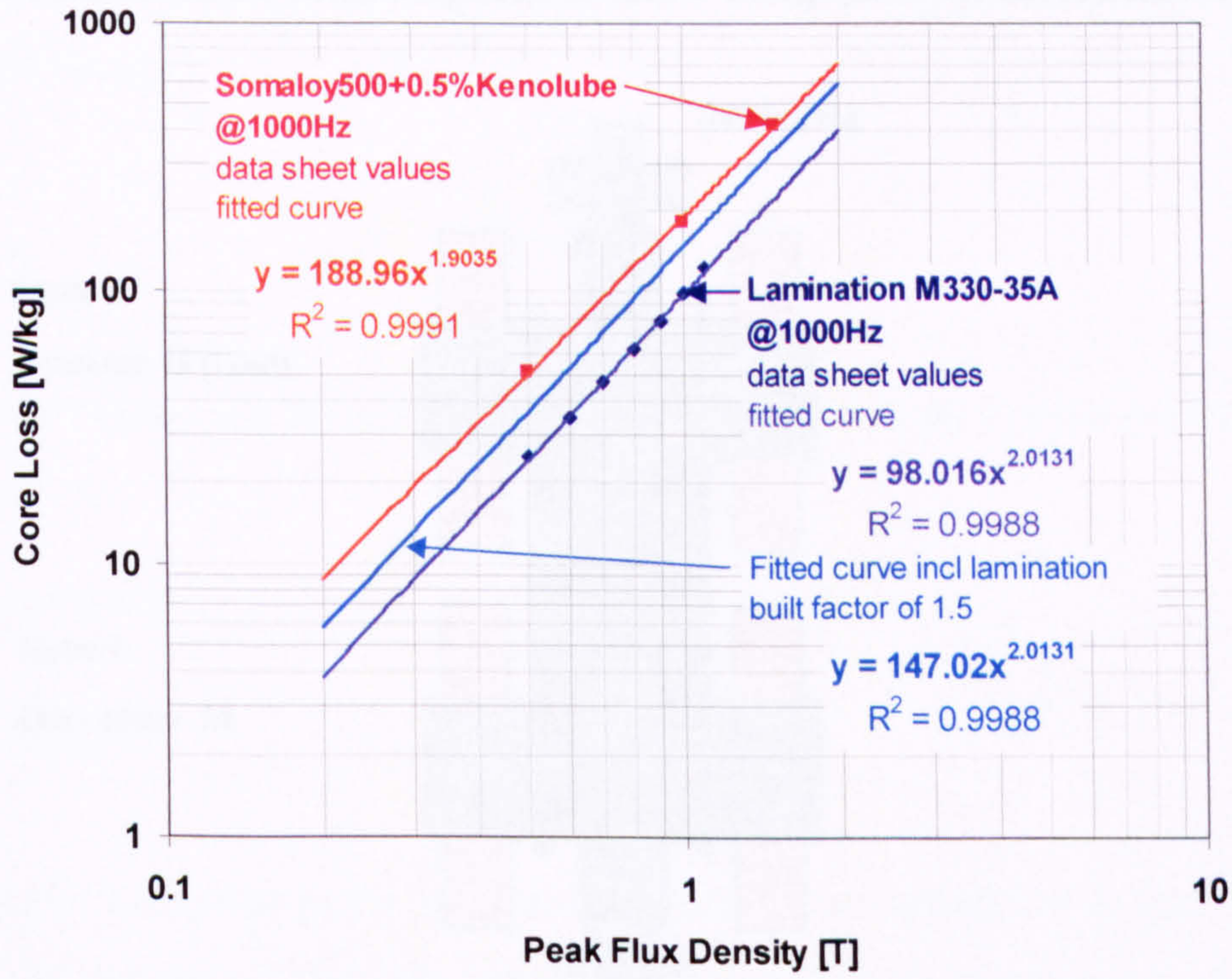

Fig. 2.9 Core loss data for Somaloy500+0.5%Kenolube and lamination steel M330-35A at 1000Hz [23, 26]

Modelled Stator Iron Losses (Open-Circuit)		
	SMC Mk1.1	**Existing Motor**
Peak flux density – back iron	0.44 T	0.45 T
Peak flux density – tooth body	0.61 T	0.58 T
Peak flux density – tooth tip	0.50 T	0.38 T
Core loss – back iron	9.255 W	3.684 W
Core loss – one tooth body	0.882 W x 3	0.200 W x 6
Core loss – one tooth tip	0.731 W x 3	0.084 W x 6
Total Stator Iron Loss	**14.1 W**	**5.4 W**
Incl. lam built factor of 1.5		**8.1 W**

Table 2.5 Estimated stator iron loss for no-load operation for SMC Mk1 and the existing motor

2.7.2 The Back-to-Back Test Rig

SMC motor Mk1.1 (and subsequent Mk2) were tested in a purpose built back-to-back rig. The rig (Fig. 2.10) consisted of two motors facing each other. The motor rotors were mounted onto one common shaft, which was supported by two ball bearings. One of the machines was driven and acted as a motor, while the other acted as a generator or load. Two power analyzers were connected to the rig measuring the input power to the motor and the output power of the generator (Fig. 2.11). The supply voltage V_{dc} and current I_{dc} to the controller were also measured. Two different shafts were available for each motor design: a single rotor shaft with only one permanent magnet rotor mounted, and a double rotor shaft with two motor rotor magnets, to allow comparative measurements.

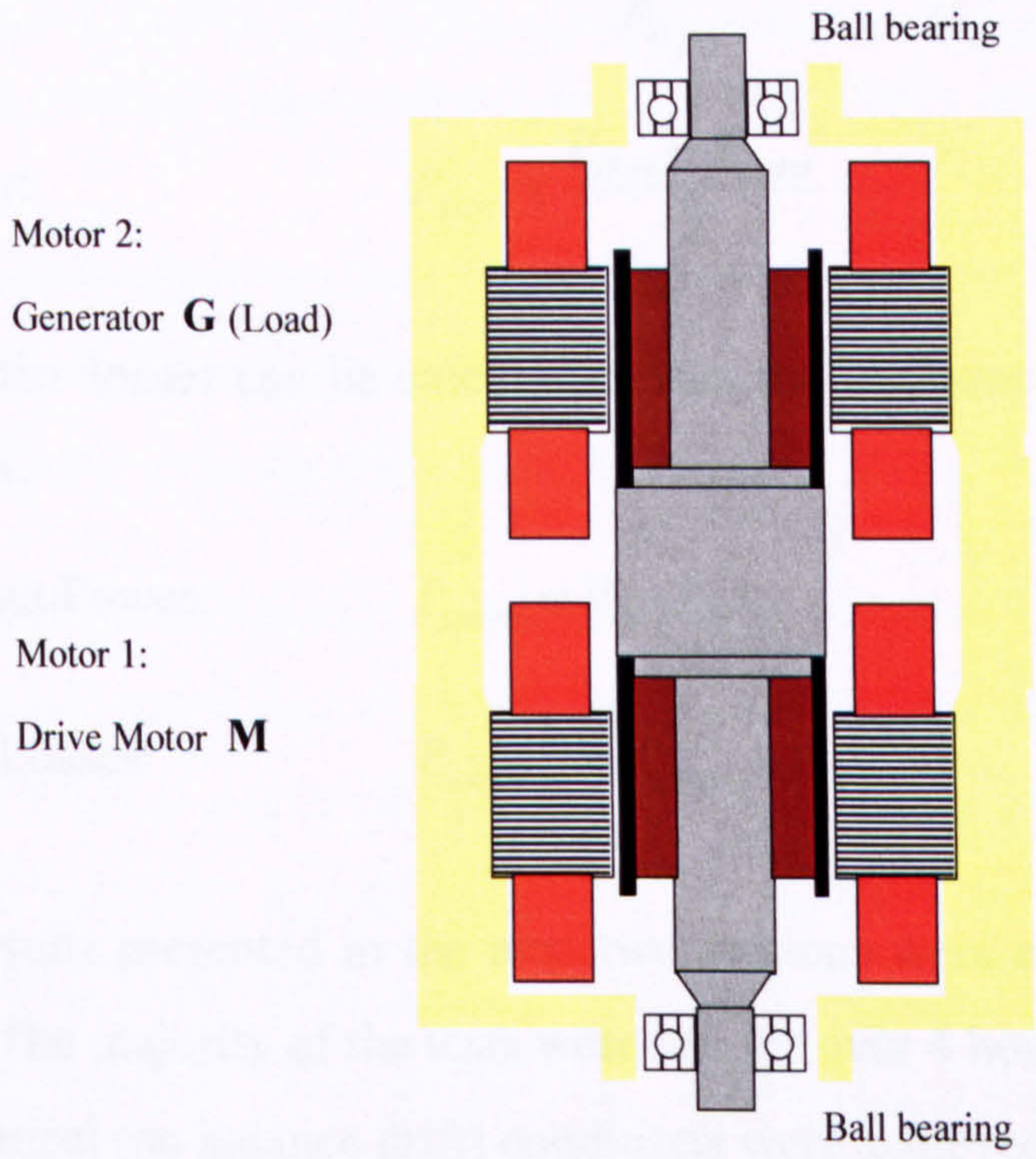

Fig. 2.10 Schematic of the back-to-back motor test rig

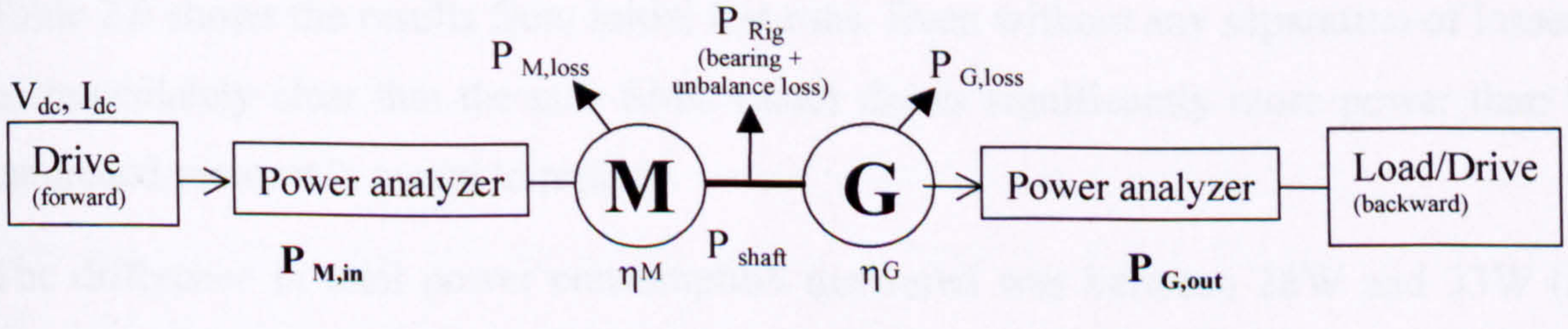

Fig. 2.11 Configuration of the back-to-back rig with two power analyzers for motor testing

The total losses of the rig were calculated from the difference between the electrical input to one machine and the electrical output of the other machine. These total losses included the rig losses (i.e. the mechanical bearing losses, windage and friction), as well as all the

motor losses for the two machines (active and passive iron losses, rotor losses, copper losses). Under the assumption that the two identical machines are run at essentially the same load conditions, the losses are equally distributed. When the rig losses P_{Rig} are known the motor losses $P_{M,loss}$ (for one machine) and motor efficiency η_M can be calculated as follows (2.5)-(2.8) [27], where $P_{M,in}$ is the motor input power, and $P_{G,out}$ the output power of the generating motor:

Single ended rotor:
$$P_{M,loss} = (P_{M,in} - P_{G,out} - P_{Rig}) \tag{2.5}$$

Double ended rotor:
$$P_{M,loss} = \frac{(P_{M,in} - P_{G,out} - P_{Rig})}{2} \tag{2.6}$$

Efficiency of motor:
$$\eta_M = \frac{P_{M,in} - P_{M,loss}}{P_{M,in}} \tag{2.7}$$

Shaft power:
$$P_{shaft} = \frac{P_{M,in} + P_{G,out}}{2} \tag{2.8}$$

The controller losses can be calculated from the difference in system power and motor input power:

System Input Power:
$$P_{system} = V_{dc} \cdot I_{dc} \tag{2.9}$$

Controller Losses:
$$P_{controller} = P_{system} - P_{M,in} \tag{2.10}$$

The test results presented in the next two sections were carried out in the laboratory at Edwards. The majority of the tests were run for over 4 hours to make sure stable thermal and mechanical (no balance drift) conditions were achieved.

2.7.3 No-Load Test Results

Table 2.6 shows the results from initial test runs. Even without any separation of losses it is immediately clear that the new SMC motor draws significantly more power than the laminated motor it is meant to replace.

The difference in total power consumption measured was between 28W and 33W (see test 2 & 3 with respect to 1). This difference would be purely the additional losses in the SMC motor, if the rig losses could be assumed to be the same, which would bring the SMC motor losses to 35W to 40W. However, taking the difference from the single ended and double ended rotor tests (test 2 & 3 with 4), which accounts for the additional iron losses in the generator, then the losses for one SMC motor came only to around 18W to

23W. This was a significant difference in measurement results and further tests were carried out to identify the cause. It was suspected that different levels of windage and shaft out-of-balance were the reason.

Measured Performance SMC Mk1.1 – Initial No-Load Tests – Total Input Power								
N°	**Stators**	**Rotors**	**Condition**	**$P_{M,in}$**	**$P_{G,out}$**		**Out of Balance [mg]†**	**Comment**
1	EXT250	EXT250 single	No load	22.4 W	-		375 42	
2	SMC Mk1.0	SMC Mk1 single	No load	50.5 W	-		No number, but suspected to be approx. 600-700	
3	SMC Mk1.0	SMC Mk1 single	No load	55.5 W	-			Repeat of 2
4	SMC Mk1.1	SMC Mk1 *double*	No load	73.6 W	-		667 690	

†Out of balance measured in milli'g' peak (acceleration g=9.81m/s²); first number is the out-of-balance value for the top of the shaft (generator end), and the second for the bottom of the shaft (motor end).

Table 2.6 Initial input power measurements for SMC Mk1 compared to the existing motor

The effect of windage was tested by increasing the pressure in the back-to-back rig, from a good vacuum of $1 \cdot 10^{-1}$mbar to 11mbar. The difference in power drawn was only 0.5W, which was found to be insignificant (Table 2.7, Test 5 & 6).

The effect of out-of-balance was investigated measuring loss for a well balanced rotor and then adding unbalance to the rotor and repeating the test. The SMC rotor proved very difficult to balance and it was impossible to achieve low and consistent out-of-balance readings. In hindsight, the difficulty of balancing the SMC shaft might have been the first indication of an unbalanced magnetic pull issue (see Chapter 8). In any case the difficulty of balancing the SMC rotor for the SMC stator-rotor combination made it unsuitable for this test. Therefore the tests were carried out using the existing stator and rotor. A shaft with low out-of-balance was purposely made worse, and the difference in motor input power measured (Table 2.7, Test 7 & 8).

The measurements show an increase of nearly 15W, resulting purely from the increased shaft imbalance. Basically, the shaft's out-of-balance adds additional forces onto the bearing, increasing the bearing losses, and so the total rig losses. For the existing motor the total rig losses can be estimated for the different levels of unbalance on the basis of known motor losses. Fig. 2.12 shows the different measurements and a fitted curve. The rig losses vary approximately linear with the level of shaft unbalance. This can be used to estimate the total rig losses for the SMC motors depending on the measured level of unbalance.

After taking into account the varying rig losses depending on the measured shaft unbalance, the average losses for the SMC motor came to 22.4W (Table 2.9). This was 60% more than the modelled losses of 14W, and 3.2 times more than the existing motor losses of 7W. Investigations into the difference between modelled and measured iron losses continued over a long period and are summarised in Chapter 5.

Measured Performance SMC Mk1.1 – Effect of Windage and Out-of-balance							
N°	**Stators**	**Rotors**	**Condition**	**$P_{M,in}$**	**$P_{G,out}$**	**Unbalance**	**Comment**
Effect of Windage							
5	SMC Mk1.1	SMC Mk1 single	No load	57.6 W	-	No number, but suspected to be approx. 600-700	10^{-1}mbar vacuum
6	SMC Mk1.1	SMC Mk1 single	No load	58.1 W	-	No number, but suspected to be approx. 600-700	Increased pressure to 11mbar
Effect of Out-of-Balance							
7	EXT250	EXT250 single	No load	20.6 W	-	221 267	
8	EXT250	EXT250 single	No load	35.0 W	-	490 798	Made balance purposely worse

Table 2.7 Effect of windage and out-of-balance on the input power to the back-to-back rig

Total Rig Losses as a function of Out-of-balance							
N°	**Stators**	**Rotors**	**$P_{M,in}$**	**$P_{G,out}$**	**P_{Rig}**	**$P_{M,loss}$**	**Unbalance**	**Comment**
Existing Motor EXT250 – used to estimate rig losses (bearing and unbalance) based on motor loss=7W)							
1	EXT250	EXT250 single	22.4 W	-	15.4 W	7 W	375 42	
7	EXT250	EXT250 single	20.6 W	-	13.6 W	7 W	221 267	
8	EXT250	EXT250 single	35.0 W	-	28.0 W	7 W	490 798	
9	EXT250	EXT250 *double*	32.0 W	-	18.0 W	7 W	255 370	
10	EXT250	EXT250 *double*	24.1 W	-	10.1 W	7 W	185 345	
11	EXT250	EXT250 *double*	35.1 W	-	21.1 W	7 W	500 260	

Table 2.8 Total back-to-back rig losses as a function of out-of-balance

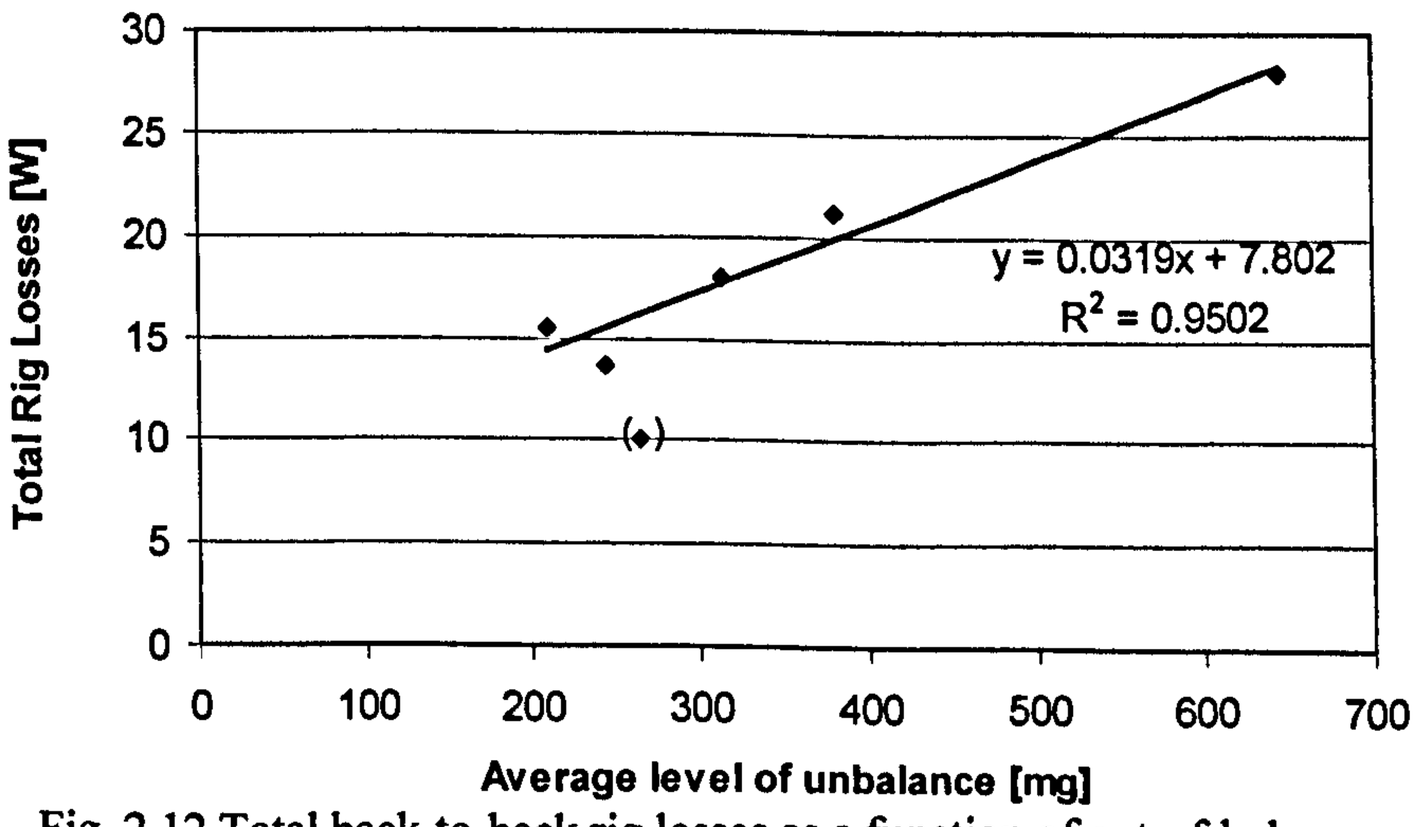

Fig. 2.12 Total back-to-back rig losses as a function of out-of-balance

Measured Performance SMC Mk1.1 – Motor Loss @ No-load								
N°	**Stators**	**Rotors**	**$P_{M,in}$**	**$P_{G,out}$**	**P_{Rig}**	**$P_{M,loss}$**	**Unbalance**	**Comment**
SMC Motor Mk1.1 – rig losses based on fitted curve								
2	SMC Mk1.0	SMC Mk1 single	50.5 W	-	29.0 W	21.5 W	No number, but suspected to be very high	
3	SMC Mk1.0	SMC Mk1 single	55.5 W	-	30.0 W	25.5 W	No number, but suspected to be very high	
4	SMC Mk1.1	SMC Mk1 *double*	73.6 W	-	29.4 W	22.1 W	667 690	
5	SMC Mk1.1	SMC Mk1 single	57.6 W	-	30.0 W	27.6 W	No number, but suspected to be very high	
12	SMC Mk1.1	SMC Mk1 *double*	62.0 W	-	23.7 W	19.2 W	405 590	
13	SMC Mk1.1	SMC Mk1 *double*	66.4 W	-	29.2 W	18.6 W	805 534	
Average SMC Mk1.1 Motor Losses:						**22.4 W**		

Table 2.9 Determination of no-load SMC Mk1.1 losses through measurement

2.7.4 Load Tests

To test the motor under load, resistors were connected between the lines of the generating machine and the input power and output power were measured. The results are listed in Table 2.10 and Table 2.11. Fig. 2.13 shows the total motor losses as a function of shaft power. The SMC motor has more losses overall than the existing laminated motor. However, the slope, which is a measure for the dynamic performance, is smaller in the SMC machine than in the laminated one. This indicates that SMC material has lower eddy current losses. The large no-load losses are dominated by hysteresis losses, which are inherent in the material. It might be possible to optimise the SMC motor so that the full-load losses are equal to or less than the existing motor, despite having higher no-load losses.

The SMC motor is about 5% less efficient than the laminated motor with a peak efficiency of 87% versus 92% (see Fig. 2.14). The difference is much more noticeable at light loads, but less at high loads. However, efficiency is not really an important criteria for turbopump applications. More important is that the motor and pump (i.e. impeller) does not overheat. But thermal measurements in the back-to-back rig are not representative of the situation in a real pump (the shaft has no blades and therefore negligible windage loss), so thermal results cannot be read across. Therefore thermal measurements have not been the focus of the testing here, and will be investigated at a later stage when the motor is built into a real turbomolecular pump.

Measured Performance under Load:									
N°	**Stators & Rotors**	**$P_{M,in}$ [W]**	**$P_{G,out}$ [W]**	**P_{shaft} [W]**	**ΔP [W]**	**P_{Rig} [W]**	**$P_{M,loss}$ [W]**	**Efficiency η**	**Unbalance [mg]**
Existing Motor EXT250									
14	EXT250	32.0	0	16.0	32.0	17.8	**7.1**	77.8%	255
	double	77.0	42.0	59.5	35.0	17.8	**8.6**	88.8%	370
		90.0	50.0	70.0	40.0	17.8	**11.1**	87.7%	
		108.0	67.0	87.5	41.0	17.8	**11.6**	89.2%	
		121.0	77.0	99.0	44.0	17.8	**13.1**	89.2%	
		169.0	126.0	147.5	43.0	17.8	**12.6**	92.5%	
		185.0	134.0	159.5	51.0	17.8	**16.6**	91.0%	
15	EXT250	121.4	75.0	98.2	46.4	20.2	**13.1**	89.2%	530
	double	120.0	73.5	96.8	46.5	20.2	**13.2**	89.0%	245

Table 2.10 Performance measurement under load: existing laminated motor

Measured Performance under Load:									
N°	**Stators & Rotors**	**$P_{M,in}$ [W]**	**$P_{G,out}$ [W]**	**P_{shaft} [W]**	**ΔP [W]**	**P_{Rig} [W]**	**$P_{M,loss}$ [W]**	**Efficiency η**	**Unbalance [mg]**
SMC Motor Mk1.1									
16	SMC Mk1.1	60	0	30	60	23.7	**18.2**	69.7%	405
	double	61	0	31	61	23.7	**18.7**	69.4%	590
		99	37	68	62	23.7	**19.2**	80.6%	
		108	46	77	62	23.7	**19.2**	82.3%	
		122	58	90	64	23.7	**20.2**	83.5%	
		128	65	97	63	23.7	**19.7**	84.6%	
17	SMC Mk1.1	60	0	30	60	23.7	**18.2**	69.7%	405
	double	64	0	32	64	23.7	**20.2**	68.5%	590
	(repeat of 16)	100	37	69	63	23.7	**19.7**	80.3%	
		113	45	79	68	23.7	**22.2**	80.4%	
		126	57	92	69	23.7	**22.7**	82.0%	
		121	56	89	65	23.7	**20.7**	82.9%	
		129	63	96	66	23.7	**21.2**	83.6%	
		165	99	132	66	23.7	**21.2**	87.2%	
		183	111	147	72	23.7	**24.2**	86.8%	
18	SMC Mk1.1	132	60	96	72	28.1	**21.9**	83.4%	738
	double								536

Table 2.11 Performance measurement under load: SMC Mk1 motor

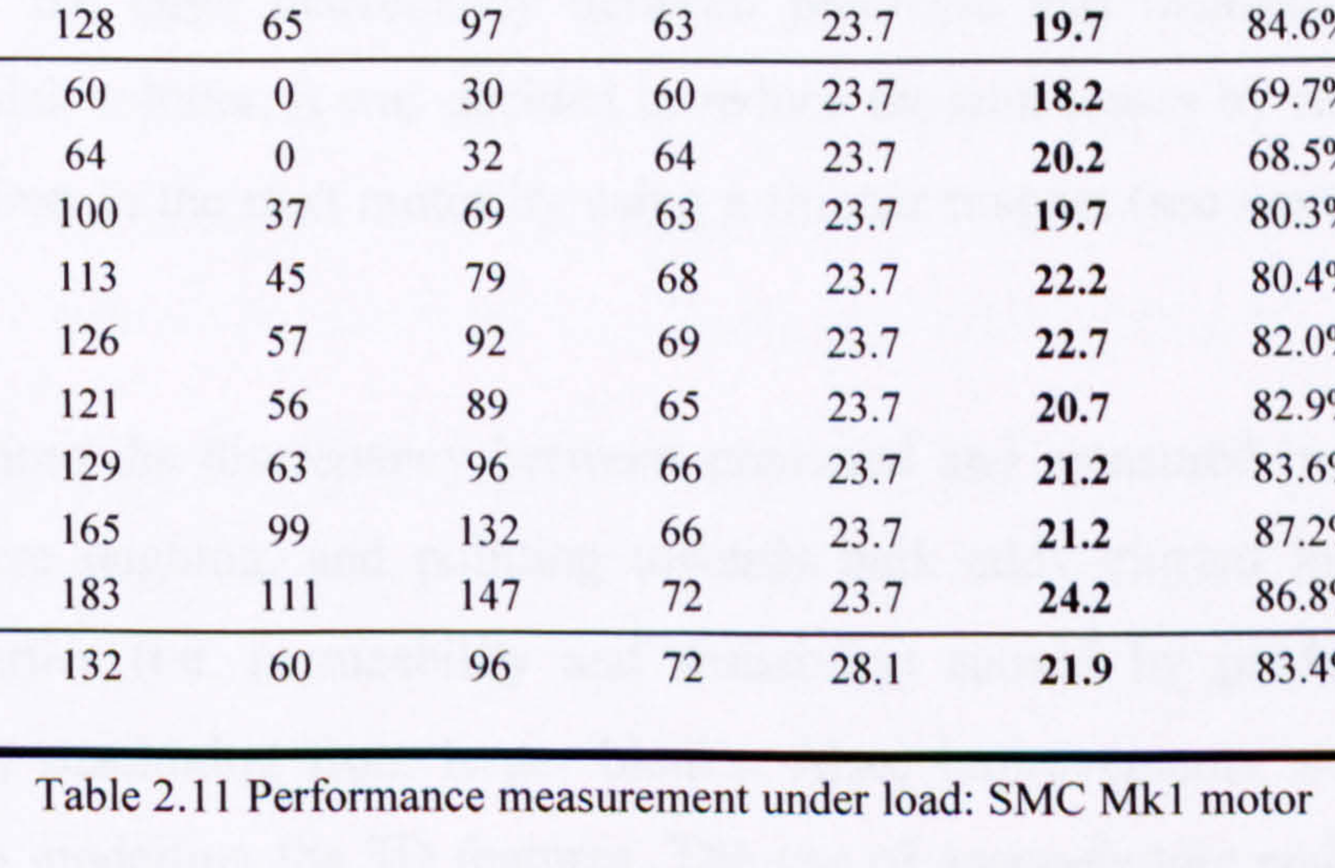

Fig. 2.13 Motor losses as a function of shaft power for the SMC Mk1 motor and the existing motor

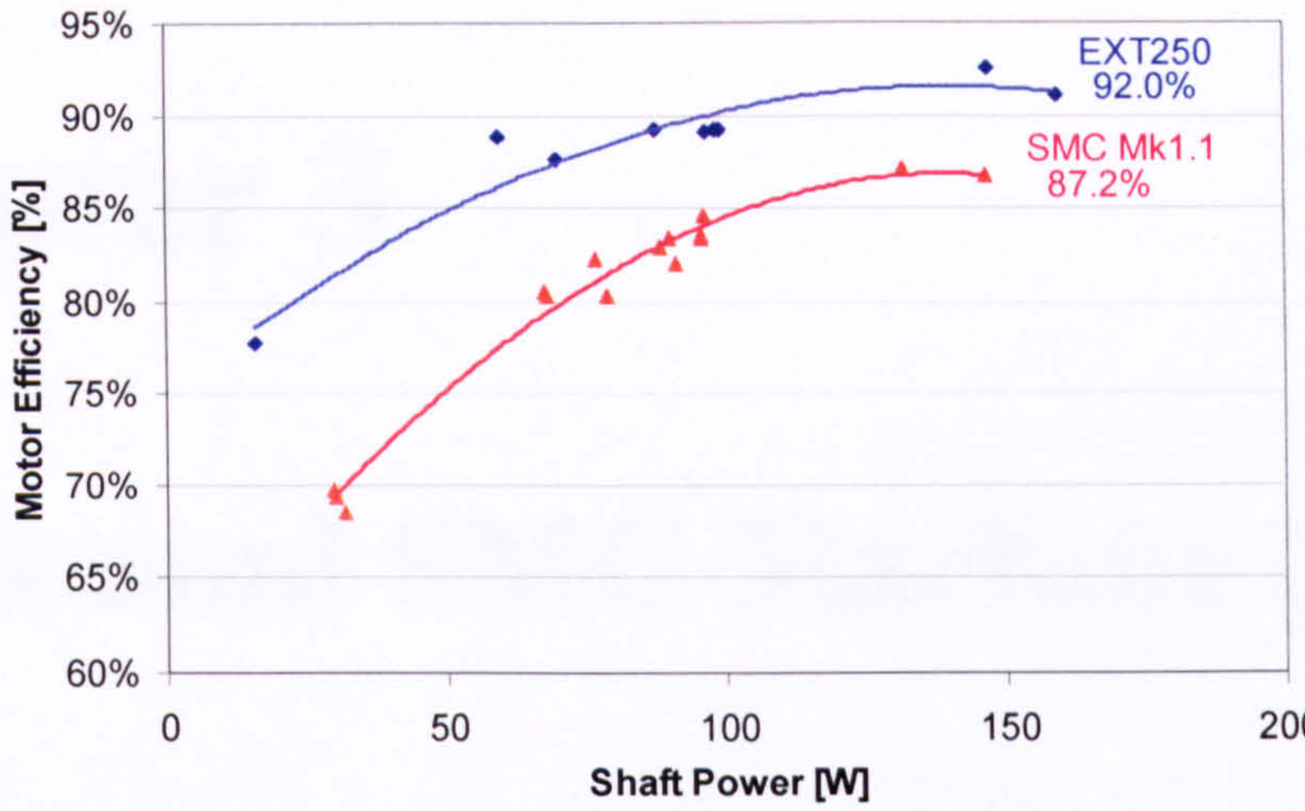

Fig. 2.14 Motor efficiency as a function of shaft power for SMC Mk1 motor and existing motor

2.8 The Next Step

It was clear from the test results, especially the no-load measurements, that the SMC motor Mk1.1 cannot compete with the existing motor with regard to the motor losses. This was in some way expected, as it was only a rough initial design. What was more surprising was the large discrepancy between predicted and measured no-load iron losses. As a quick solution it was decided to reduce the iron losses by reducing the flux density in the iron in the next motor by using a thinner magnet (see next Chapter: SMC Mk2).

Investigations into the discrepancy between predicted and measured iron losses in the SMC parts were ongoing, and pointing towards bulk eddy current losses and lower material properties (i.e. permeability and resistivity) caused by producing the SMC components by machining from larger blanks. Also, improvements were being made with respect to modelling the 3D features. The use of space-factors and different (non-linear) BH curves to model the regions with different axial length in 2D was introduced next.

Chapter 3

The Second SMC Machine (Mk2):

Thin Plastic Bonded Magnets

3.1 Introduction

During the testing of the first SMC motor (Mk1) much higher input powers than expected were measured. The no-load iron losses came to about 22W, which is three times more than the losses in the existing motor and 60% more than predicted. To be able to compete with the existing motor the iron losses needed to be reduced.

The solution proposed was to reduce the flux density in the iron by using a thinner magnet. The drop in flux needed to be compensated by an increase in the number of turns to achieve a similar back EMF. This chapter describes the design and test results of the second SMC motor (Mk2).

3.2 Design and Construction of the Second SMC Motor

3.2.1 Design Differences Compared to Mk1

The most significant change to Mk1 was the use of a thinner magnet to reduce the flux density in the iron in an attempt to reduce the iron losses. A thinner magnet meant a thicker shaft, which was also encouraged by Edwards for reasons of shaft stiffness and rotor dynamics. There was concern (based on one bad experience with the existing rotor) that a shaft diameter of 10mm as used in Mk1 could bend under the rotating force in

certain larger 'split-flow' pumps. For this reason the shaft diameter was increased to 12.5mm.

This meant that the magnet inner diameter increased to 12.6mm, whereas the outer diameter stayed the same at 16.32mm to allow continued use of the existing carbon fibre sleeve. As a result the magnet thickness was reduced to 1.86mm, compared to 3.11mm in Mk1. The magnet material was kept the same (plastic bonded NdFeB magnets).

A thinner magnet meant a reduction in flux linking the stator windings. To compensate for this reduction in flux the number of turns per phase was increased from 27 to 49 turns to keep a similar back EMF. To allow more room for the windings the slot area was increased by reducing the back iron width from 6mm to 5mm.

Everything else stayed the same: the axial length of the teeth, tooth body and back iron, the tooth shape, and the SMC material Somaloy500+0.5%Kenolube (compacted at 600MPa and heat treated at 500°C for 30 minutes).

3.2.2 Construction of Mk2

The same manufacturing and assembly processes were used as on the first motor. The SMC parts were machined and wire eroded from pre-fabricated blanks, the coils pre-wound and then inserted onto the teeth. The slot fill on Mk1 was relatively low (27.3%), and was increased in Mk2 (41.3%). Feedback from the subcontractor showed that this time it was tight to fit the windings into the available space and to maintain short endwindings to fit the hall sensor board within the given overall axial height. Optimising the winding process and possibly pre-pressing the coils should overcome this and allow even higher fill factors [18, 21].

On Mk1 it was noted that after assembling the back-to-back rig several times, i.e. taking the shaft in and out of the stator, the SMC stator teeth started to show cracks. It is nearly impossible to avoid contact between the shaft and the stator teeth when inserting or removing the shaft due to the magnetic attraction. If the SMC can be damaged as easily as this the risk of damaging the stator in production is very high. A solution for this is potting the motor stator to give additional strength and protection to the 'brittle' SMC. Hence Mk2 was potted using a clear epoxy resin to avoid damaging the stator teeth during testing. Fig. 3.1 shows the motor stator before and after potting.

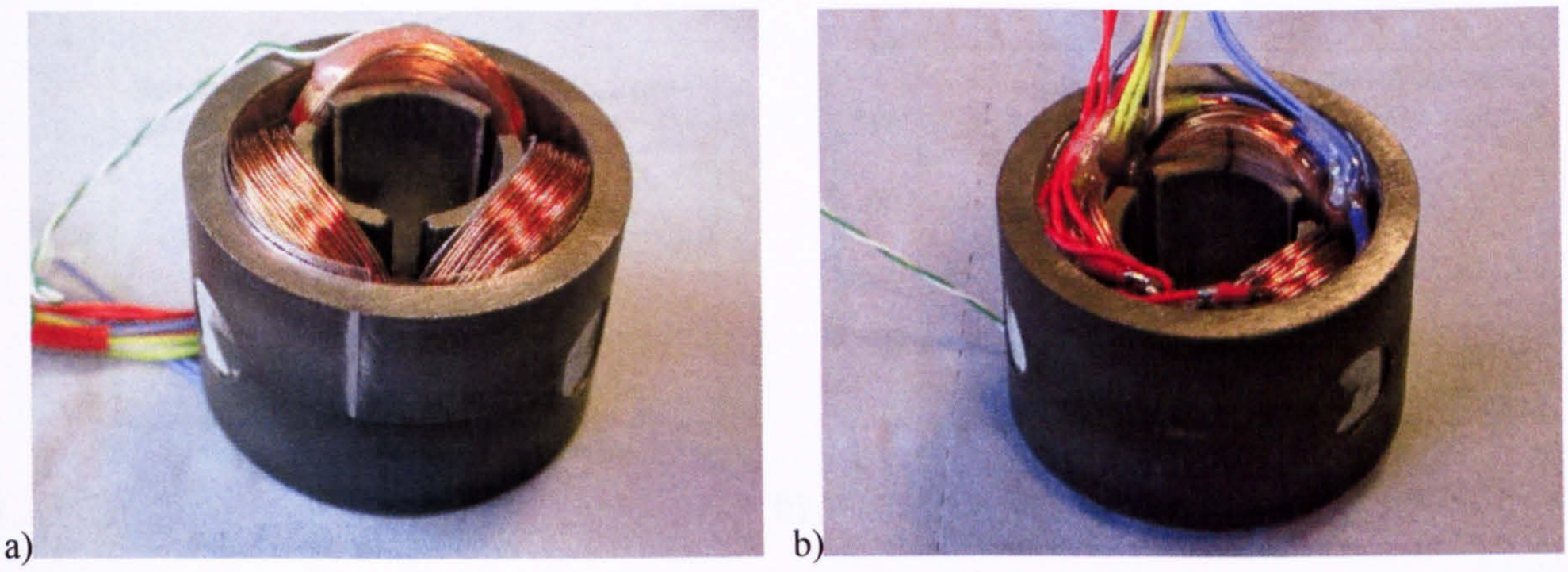

Fig. 3.1 Photos of second SMC motor (Mk2): a-b) before potting, c) after potting

3.3 Improved Finite-Element Model

3.3.1 Non-Linear Permeability

This time a non-linear 2D FE model was used, replacing the constant permeability of the SMC with a more realistic non-linear function. The FE model requires the relative permeability μ_r as a function of the flux density B to avoid circular dependency of the magnetic field strength H. The following function was used to represent μ_r [28]:

$$\mu_r = \frac{\mu_{\max}}{1 + c \cdot |B|^p} + \mu_{\min} \tag{3.1}$$

with $\mu_{\max}, \mu_{\min}, c, p$ being constants, determined to give the best fit with given data sheet values. Fig. 3.2 shows the original curve and the fitted function with the constants used.

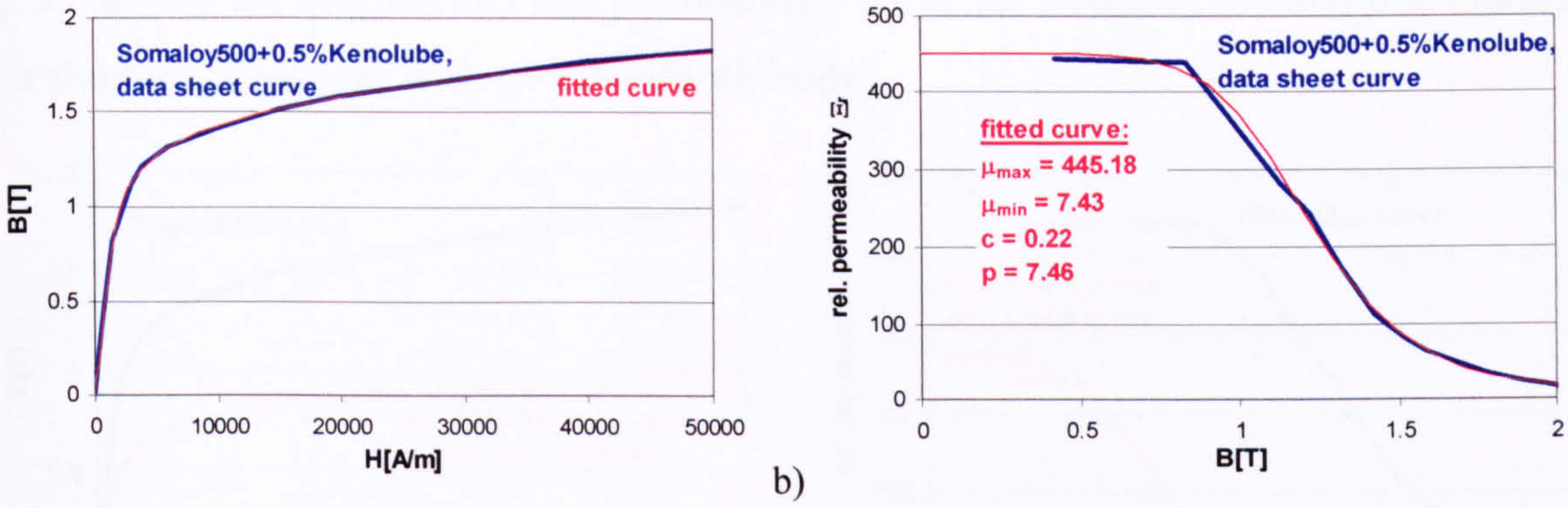

Fig. 3.2 Data sheet and fitted curve for Somaloy500: a) non-linear BH-curve and b) permeability as a function of flux density

3.3.2 Concept of a Space-Factor, sf

The second major difference is the way the 3D effects of the tooth body and back iron were taken into account in the 2D model. Adjusting the geometry as done in Mk1 to model the true cross section area by adjusting the width for a given length has its problems. It can produce very thin components in the 2D plane, distorting the geometry and resulting flux lines. In addition it can lead to saturation in other components (i.e. tooth tips) because of modified, unrealistic flux paths.

To avoid this a space-factor, *sf*, is introduced. This factor is defined as the ratio of the actual component area to the modelled area, and modifies the material properties in such a way as to simulate the different saturation characteristics, i.e. shorter parts saturate earlier than longer ones. This means that the dimensions are kept in the 2D plane giving a more realistic representation of the geometry, but the components are stretched over the full length, modelled as components with new material properties. The new material is basically a compound material consisting of the original material (SMC) and air. The BH curve is adjusted in the following way to represent the new, modified material properties:

$$B_{modified} = B_{original} \cdot sf \quad \text{, hence} \quad B_{original} = \frac{B_{modified}}{sf} \tag{3.2}$$

i.e. for a shorter component (sf<1) the BH curve saturates earlier. The relative permeability μ_r now also becomes a function of $B_{modified}$ and the space-factor.

$$\mu_r = f(B_{original}) = f\left(\frac{B_{modified}}{sf}\right) = \frac{\mu_{\max} \cdot sf}{1 + c \cdot \left|\frac{B}{sf}\right|^{p+(1-sf)}} + \mu_{\min} \cdot sf \tag{3.3}$$

Fig. 3.3 shows the original BH and permeability curve for Somaloy500 and one modified for a shorter component with *sf*=0.55 (tooth body).

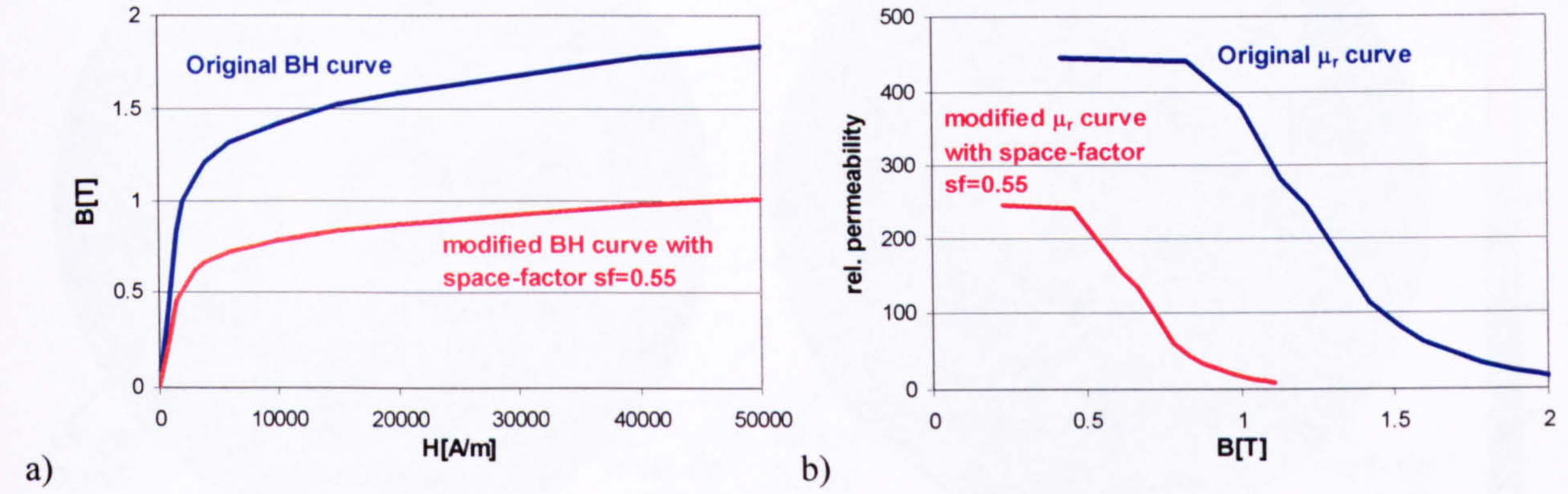

Fig. 3.3 Applying space-factor *sf* to BH curve and μ_r to model 3D-effects in 2D-FE model

For the Mk2 motor the reference axial length was the tooth tip length of 31mm. The space-factor for the tooth body was 0.55 as it is shorter in length and for the back iron sf is 1.16 as it is longer. Fig. 3.4 shows the 2D cross section of the tooth from the FE model and the corresponding 3D axial cross section of the motor stator including space-factors.

The FE program now calculates and plots $B_{modified}$ in the components where a space-factor has been applied. To get a plot of the true magnetic flux density in the original material, this flux density value needs to be divided by the space-factor *sf* according to equation (3.2). Fig. 3.5a shows the open circuit flux density plot as obtained directly from the FE program using the modified BH curve, whereas Fig. 3.5b shows the same flux density distribution corrected for the space-factors to reflect the true flux density in the 3D parts, hence the discontinuity in flux density between the back iron, tooth body and tooth tip. This improved 2D FE model was used to analyse the back EMF, the inductance and the stator iron losses.

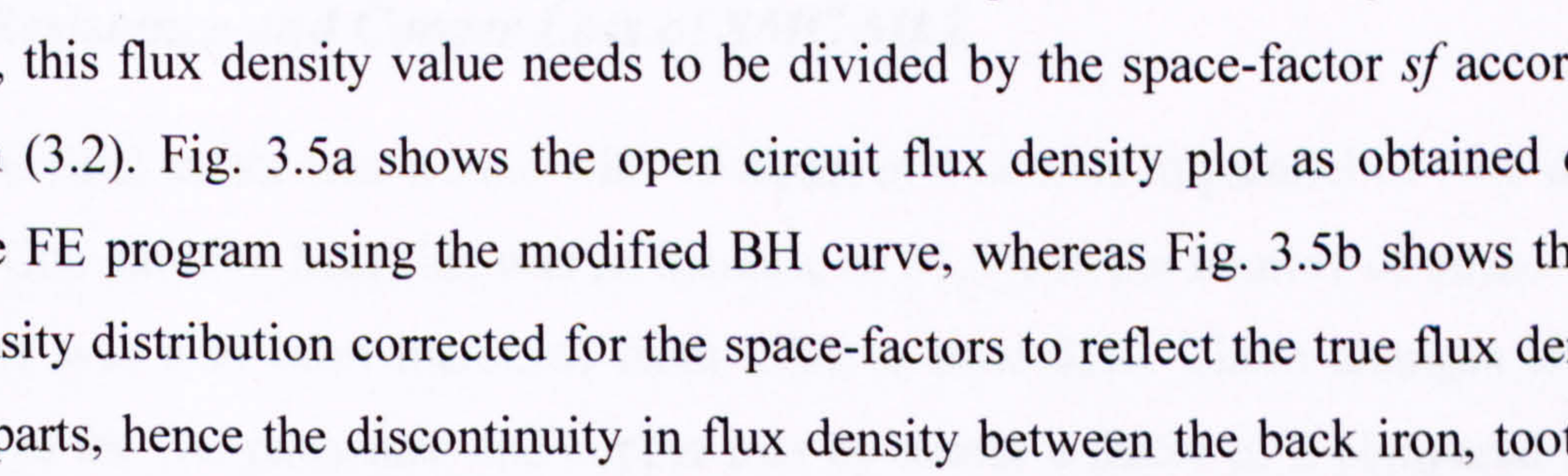

Fig. 3.4 2D FE cross section and corresponding axial cross section of SMC stator showing space-factors to model 3D geometry in 2D

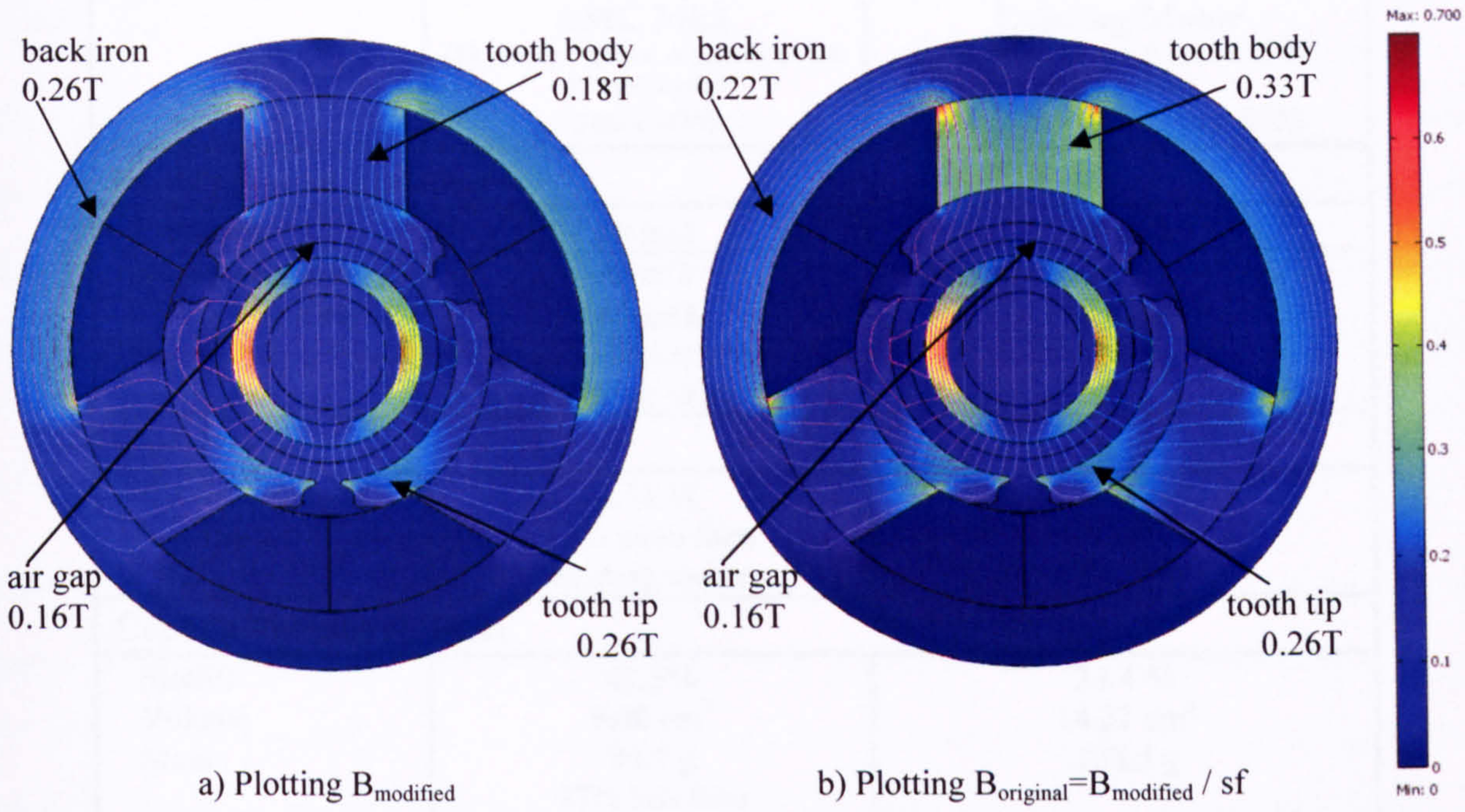

a) Plotting $B_{modified}$ b) Plotting $B_{original}=B_{modified}$ / sf

Fig. 3.5 Open-circuit flux density plot of SMC Mk2 using improved FE model and space-factors a) plotting $B_{modified}$, b) corrected for space-factors to obtain true flux density in 3D parts, $B_{original}$

3.4 Motor Parameter of the SMC Mk2 Motor

3.4.1 Resistance and Copper Loss of SMC Mk2

The SMC Mk2 motor was wound with 49 turns, of 4 strands in parallel of wire diameter 0.5mm. Compared to Mk1 this was an increase of 81.5% in the number of turns. The slot fill factor was also been increased from 27% to now 41%. These changes led to an increase in the DC resistance and copper loss by nearly a factor of 2 compared to Mk1. The total copper loss (at rated current of $5A_{rms}$ and $60^{o}C$ winding temperature) was now 2.71W, which was slightly higher than the existing motor, i.e. 0.4W or 15% more copper loss. Overall 0.4W is a very small increase on a 100W machine, and it was decided that this was not an issue. Even with the increase in copper over that in the Mk1 design, the total copper volume in the Mk2 machine was still 37% less than in the existing motor due to the non-overlapped coils and shorter endwindings.

	SMC Mk2 (49 turns per phase, 4 strands of dia. 0.5mm, Delta) Stator S006	**Existing Motor** (14 turns per phase, 9 strands of dia. 0.5mm, Star) Stator S004	Stator S005
DC Line-Line Resistance			
Predicted	**60 mΩ**	**55 mΩ**	
Measured (@25°C)	63 mΩ	54.2 mΩ	54.7 mΩ
Average	**63 mΩ** 15 % higher than existing motor	**54.5 mΩ**	
Copper Loss			
with rated current of $5A_{rms}$, $T_{winding}$=60°C	**2.71 W** 15% more than existing motor	**2.35 W**	
Copper Volume & Mass			
Slotfill	**41.3%**	**24.4 %**	
Volume	**9.00 cm^3**	**14.32 cm^3**	
Mass	**80.7 g** 37% less than existing motor	**128.3 g**	

Table 3.1 DC resistance, Copper Loss and Copper Volume for SMC Mk2

3.4.2 Inductance of SMC Mk2

Due to the large increase in the number of turns per phase the inductance of the Mk2 motor is very high. Because the inductance is proportional to N^2, an increase of a factor of $49^2/27^2 = 3.3$ was expected. The measured inductance on Mk1 (with and without rotor) was around 130μH, hence an inductance of around 429μH was expected for Mk2.

The measured inductance came to 379μH for the stator only, and to 428μH with the rotor. The modelled inductance using the improved 2D FE model came to 279μH for the stator only and to 345μH with the rotor. The predicted inductance value still underestimates the measured inductance by between 23% and 36%. This error is similar to the values reported for Mk1 and is believed to be caused by neglecting the endwinding leakage inductance in the 2D model.

Line-Line Inductance			
	SMC Mk2 Stator S006	**Existing Motor** Stator S004	Stator S005
Stator Only			
Predicted (FE)	279 μH	85 μH	
Measured Average	x 1.355 → **379 μH**	x 1.282 → **109 μH**	
With Rotor			
Predicted (FE)	345 μH	112 μH	
Measured Average	x 1.231 → **425 μH**	x 1.188 → **133 μH**	

Table 3.2 Line-Line Inductance for SMC Mk2 motor in comparison with the existing motor

3.4.3 Back EMF of SMC Mk2

The number of turns required per phase was determined by winding some test turns around a spare set of SMC stator parts, and measuring the induced voltage with the new thin rotor magnet at low speed. As a result of this test the number of turns per phase was specified as 49. This was expected to give a back EMF of around $14.4V_{rms}$ at full speed with the magnets at room temperature (see Table 3.3 for measured and predicted back EMF values).

However, when testing the motor in the back-to-back rig at full speed a back EMF of only $12.6V_{rms}$ was measured (Fig. 3.6). This was 12.5% or 1.8V lower than the expected $14.4V_{rms}$ from the initial measurement. A small variation can be caused by extrapolation errors from low speed and small voltage values with the few test turns, but this is typically not more than 5%. It is more likely that the magnet had been demagnetised during run up of the machine.

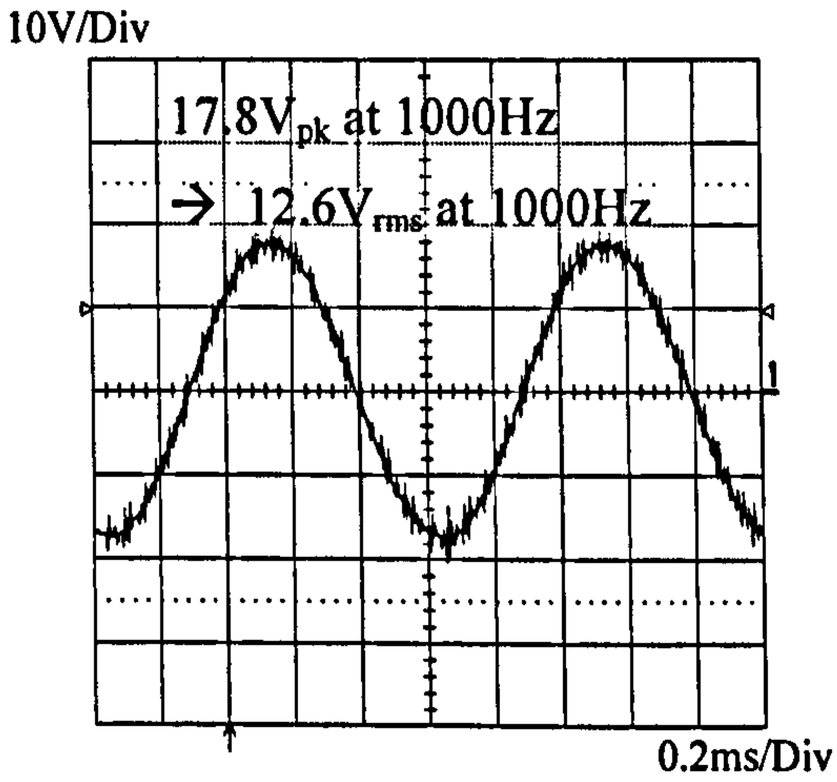

Fig. 3.6 Measured back EMF waveform of SMC Mk2 motor

The whole shaft assembly was eventually re-magnetised and re-tested. A different drive was used to limit the start-up current and avoid demagnetisation again. The measured back EMF was $14.0V_{rms}$, which is close to the expected value from the initial test (3% less), and confirms that the low back EMF of 12.6V was caused by demagnetisation.

Using the improved FE model with space-factors and non-linear properties for the SMC material as well as data sheet values for the magnet, the theoretical back EMF with 49 turns is $22.6V_{rms}$ (Table 3.3). Compared to a measured value of 14.0V this is an overestimation of 38%. This error is unusually high for back EMF modelling, and much larger than the 15% error reported on the SMC Mk1 (Section 2.6.4).

	SMC Mk2 (49turns per phase, Delta) Stator S006	**Existing Motor** (14turns per phase, Star)
Initial Test (to determine number of turns)		
	3 turns @ 28.4Hz → 0.071 V_{pk-pk} (0.0251V_{rms})	
	48 turns @ 1000Hz → 14.142 V_{rms} **49 turns @ 1000Hz → 14.437 V_{rms}** 50 turns @ 1000Hz → 14.731 V_{rms}	
Back EMF Line-Line @ 1000Hz		
Predicted	**22.58 V_{rms}**	**14.21 V_{rms}**
Measured	**12.58 V_{rms}**	**14.14 V_{rms}**
Repeat: Back EMF Line-Line @ 1000Hz SMC Mk2 **shaft remagnetised** by the supplier		
Measured	**14.03 V_{rms}** Some of the performance has been regained and back EMF has reached level of initial test, but not closed the gap to the predicted value	

Table 3.3 Back EMF for SMC Mk2 motor

Despite the demagnetisation issue, there was a large discrepancy between the modelled and measured back EMF. The following possible causes of the lower than expected back EMF were investigated:

Magnet too thin

The first thoughts were focused around the magnetisation of the rotor magnet: Are the data sheet values too optimistic? Is the magnet with 1.86 mm thickness too thin for plastic bonded magnets? Typically data sheet values are obtained from magnet samples, whose minimum thickness is 5mm in the direction of magnetisation. Smaller dimensions may deviate from these values [29]. Unfortunately no information was available from the supplier as to how much the strength of the plastic bonded magnets could vary with thickness. The effect of thickness might be more noticeable on plastic bonded magnets than on pure rare earth magnets, because of the ratio of magnet to bonding material, which might be different in thinner components than in thicker ones. To fully investigate the dependency of magnet strength on thickness further investigations and testing would be required, which is outside the scope of this thesis. The performance of plastic bonded magnets thinner than 5mm needs to be treated with caution, and a 5% to 10% reduction allowed in future modelling.

Axial end effects neglected in the 2D FE model

The construction of the rotor assembly could be another reason for a low back EMF. The cylindrical rotor magnet is glued onto a carbon steel shaft and located axially on a step in the shaft. This creates a magnetic short circuit on the end where the magnet is touching

the shaft, and leads to a reduction in the field density towards that end. At the other end the magnet extends beyond the stator tooth to trigger the Hall sensors. Fig. 3.7a shows a model of the axial fringing flux when the rotor is assembled into the stator, and Fig. 3.7b shows the flux density distribution in the air gap axially along a tooth. The flux density reduces significantly where the magnet touches the shaft, but increases at the end where the magnet extends beyond the stator tooth. When calculating the back EMF the active length of the machine was taken as the tooth tip length, but as Fig. 3.7b shows, the left part does not collect much flux leading to an overestimation of the back EMF. This axial leakage flux can reduce the total flux linkage by around 10% to 15%.

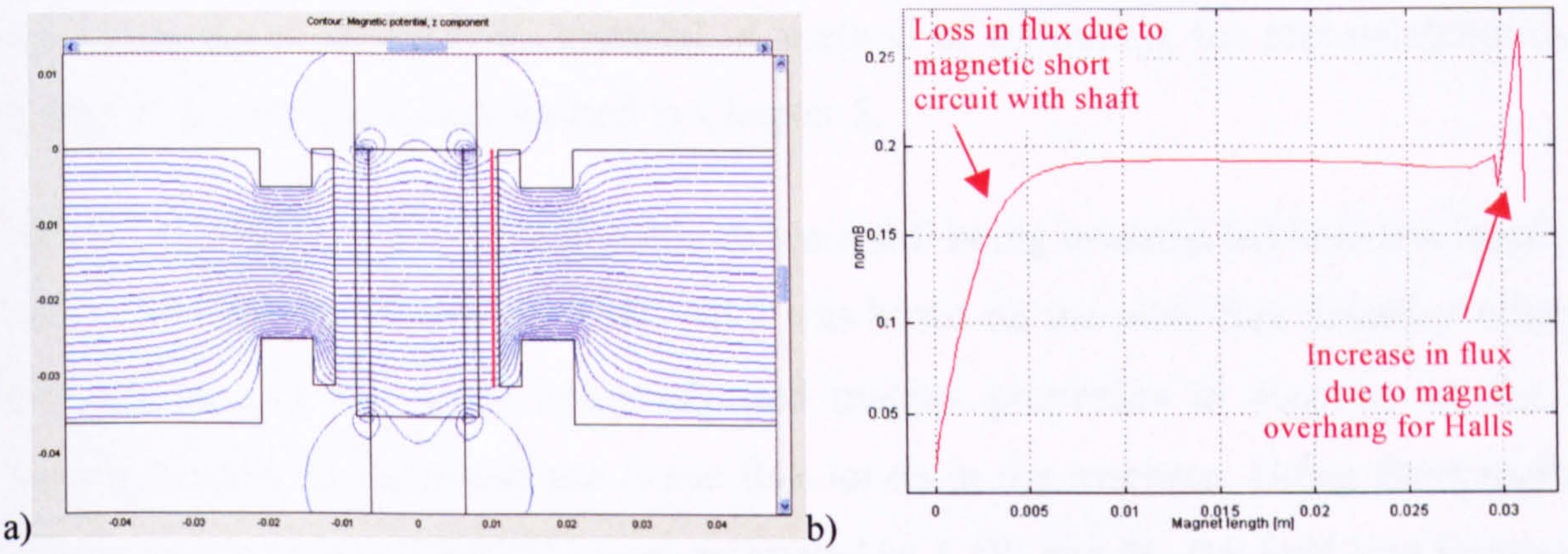

Fig. 3.7 Axial fringing flux and magnetic short circuit between magnet and shaft: a) FE flux plot, b) flux density plot in air gap axially along tooth

Underperforming SMC

All of the above effects contribute to a lower back EMF, and might account for 15% to 25%, but that is still not enough to explain the nearly 40% difference observed between measured and predicted back EMF in this machine.

Some other mechanism must be present to account for such serious performance degradation, and for the first time it was suspected that the SMC material might be damaged by machining. This was supported by the observation that some damaged, or broken-off tooth tips did not affect the back EMF much. Is the SMC material damaged especially when it is machined thin?

Recalculating the back EMF with a very low permeability for the SMC (150 instead of 445) the back EMF dropped by 12%. This goes in the right direction, and discussions with the supplier were initiated to investigate whether the SMC properties may be adversely affected during prototype machining, i.e. wire erosion, or mechanical machining. The results of this investigation are discussed further in Chapter 5 on iron loss modelling in SMC.

3.5 Performance of the SMC Mk2 Motor

3.5.1 Estimation of Iron Losses – Ongoing Improvements

Investigations into the cause of the large discrepancy between measured and predicted iron losses on the SMC Mk1 machine were still ongoing. It was suspected that bulk eddy currents play a much bigger role than initially anticipated, and that the dimensions of the components need to be taken into account in the calculation of eddy current losses. A method for separating the iron losses into hysteresis and eddy current loss was subsequently developed and is presented in Chapter 5. There was also some doubt about the conductivity of the SMC material. A method of estimating the real conductivity of the SMC material is also described in Chapter 5.

While these improved analytical methods were still being investigated and developed, the initial iron loss estimation for SMC Mk2 was based on the peak flux densities obtained through the 2D FE model using adjusted magnet properties to account for the low measured back EMF, and hence lower flux levels in the machine. Using these methods the no-load iron losses for Mk2 were estimated as 3.7W and the full load iron losses with rated current of 5A at 9.2W. Table 3.4 summarises the data. The no-load (open-circuit) flux density plot is shown in Fig. 3.5 presented earlier in the chapter.

Modelled Stator Iron Losses: SMC Mk2		
	No-load	**Rated Load** ($5A_{rms}$ line current)
Peak flux density – back iron	0.22 T	0.37 T
Peak flux density – tooth body	0.33 T	0.58 T
Peak flux density – tooth tip	0.26 T	0.30 T
Core loss – back iron	2.112 W	5.681 W
Core loss – one tooth body	0.314 W x 3	0.918 W x 3
Core loss – one tooth tip	0.205 W x 3	0.269 W x 3
Total Stator Iron Loss	**3.7 W**	**9.2 W**

Table 3.4 Estimated stator iron loss for SMC Mk2

3.5.2 Measurement of Losses – the Set-Up

The SMC motor Mk2 was tested in the purpose built back-to-back rig, described in the previous chapter. No rotor dynamic problems were noticed, with the shaft supported by two ball bearings. This time only one SMC Mk2 stator was built, which meant that the testing was carried out using one of the SMC Mk1 stators. The rotor was a new double-ended shaft with one of the new thinner plastic bonded magnets on each end. Because the

SMC parts are very similar in Mk1 and Mk2, i.e. identical tooth shape and dimension, but slightly smaller back iron thickness in Mk2, the machines are treated as similar enough to split the losses equally. It is believed that this should be accurate enough to demonstrate the effect of having reduced the magnetic flux density in the machine. Below are test results for the initial demagnetised shaft (less flux in the machine), and results obtained from measurements after the shaft was re-magnetised.

3.5.3 No-Load Test Results

Table 3.5 shows the measured no-load power consumptions and derived losses for the SMC Mk2 motor. The initially measured no-load losses came to about 4.7W. This was low due to the demagnetised shaft. Measurements with a re-magnetised shaft gave no-load losses in the order of 6.4W. Compared to the SMC Mk1 motor with 22.4W this is a significant reduction in the no-load losses, achieving similar maybe even slightly lower losses than the existing motor with 7W. This shows that the reduction of flux density in the iron by employing a thinner magnet was successful in reducing iron losses.

Measured Performance SMC Mk2 – Motor Loss @ No-load
(rig losses based on fitted curve – see Fig. 2.12, page 32)

N°	Stator	Rotors	$P_{M,in}$ [W]	$P_{G,out}$	P_{Rig} [W]	$P_{M,loss}$ [W]	Unbalance [mg]	Comment
Results with initial demagnetised shaft:								
19	SMC Mk2	SMC Mk2 *double*	23.5 W	-	14.3 W	4.6 W	127 278	V_{dc}= 24.1 V
20	SMC Mk2	SMC Mk2 *double*	22.8 W	-	13.5 W	4.7 W	126 234	V_{dc}= 24.1 V
Results with re-magnetised shaft:								
26	SMC Mk2	SMC Mk2 *double*	25.6 W	-	12.8 W	**6.4 W**	118 196	V_{dc}= 24.0 V

Table 3.5 Measured no-load losses for the SMC Mk2 motor

3.5.4 Load Tests

Due to the large inductance the motor was unable to operate under load from its nominal DC link voltage of 24V. The supply voltage had to be increased to 27-28V. It was also necessary to connect capacitors in parallel to the load resistors to improve the rig's load capability by compensating the phase shift of the inductance.

The total motor loss for a shaft power of 86W and 92W are estimated as 11.4W and 13.0W respectively (see Table 3.6). This is comparable with the measured losses in the existing motor, which are about 11.6W at a shaft power of 88W (see previous chapter,

Table 2.11). Compared to the SMC Mk1 motor this motor is acceptable with respect to the motor losses, but unfortunately suffers from the large inductance.

Measured Performance SMC Mk2 – Motor Loss @ Load:										
N°	**Stators & Rotors**	**$P_{M,in}$ [W]**	**$P_{G,out}$ [W]**	**P_{shaft} [W]**	**ΔP [W]**	**P_{Rig} [W]**	**$P_{M,loss}$ [W]**	**η**	**Un-balance [mg]**	**Comment**
Results with initial demagnetised shaft:										
21	SMC Mk2 *double*	103	68	86	35	12.3	**11.4**	83.5%	118 167	V_{dc}= 27 V
22	SMC Mk2 *double*	111	72	92	39	12.8	**13.0**	82.3%	130 182	V_{dc}= 28 V
Results with re-magnetised shaft:										
27	SMC Mk2 *double*	115	75	95	40	12.8	**13.6**	82.6%		

Table 3.6 Performance measurement under load for the SMC Mk2 motor

Fig. 3.8 shows the measured motor losses of the Mk2 motor with increasing load using the re-magnetised shaft. The losses are in the order of 6.4W at no-load, rising to 13.6W at rated load. The error between predicted and measured iron loss is very large, with 73% for no-load (3.7W versus 6.4W) and about 48% error under load (9.2W versus 13.6W). Reason for this discrepancy will be investigated in Chapter 5.

The motor losses show also a stronger non-linear behaviour with load than observed on Mk1 (see Fig. 2.13). This is due to the fact that the electric loading is much larger in the Mk2 motor, giving the armature magnetic field B_{coil} a stronger influence over the magnetic field from the magnet B_{mag}, as the losses are roughly proportional to $(B_{mag}+B_{coil})^2$. Overall, the motor losses of the SMC Mk2 motor were comparable with the existing motor, an improvement over Mk1.

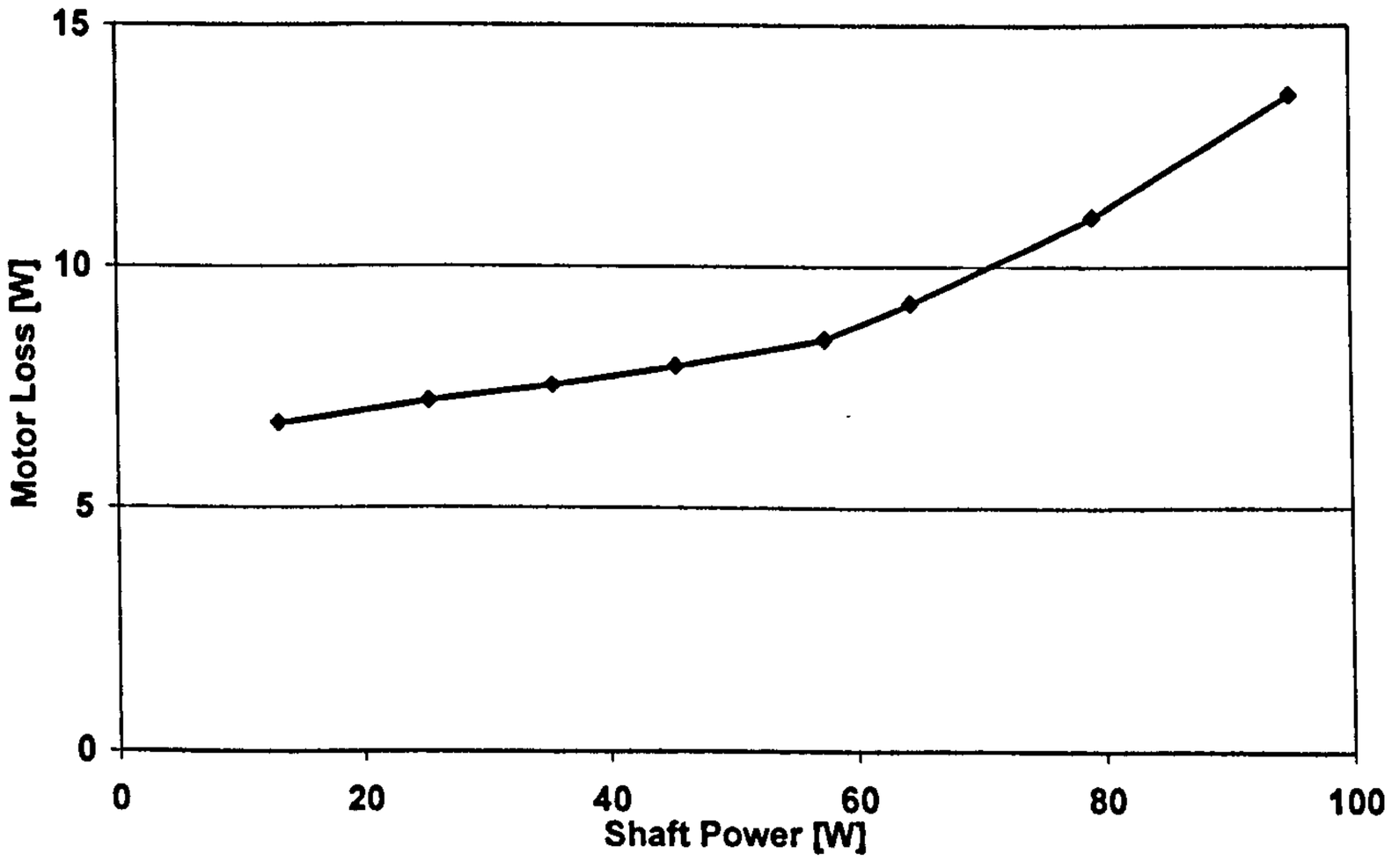

Fig. 3.8 Motor loss with increasing load for the SMC Mk2 motor (DC supply voltage: 30V)

3.6 Applying Phase Advance to Compensate for High Inductance

In the long run it became clear that the best compromise might be to allow a bit higher inductance than the existing motor and apply some phase advance to enable operation from a 24V DC-supply. This section investigates the effect of phase advance applied to the SMC Mk2 motor with a view using it on future SMC motors. The work is mainly based on experimental results, but also develops a simulation program, which can be used as a tool for future machine designs.

3.6.1 Principle of Phase Advance

Phase advance, also referred to as field weakening, is a control method commonly used to increase a machine's operating range [30-33], which either means to increase the speed range beyond base speed or to maximise the available torque at rated speed. In the conventional separately excited DC machine field weakening is easily implemented by reducing the field current in the separate field winding and reducing so the flux in the machine. This is not possible in brushless DC machines where the field source is a permanent magnet. Here the main principle of field weakening control consists of time shifting the turn-on points of the stator phase currents with respect to the corresponding back EMFs [31].

Machine Operating Range: Current Control versus Voltage Limited Current

Base speed is the maximum speed the machine can reach before it runs out of current control, i.e. when the applied DC-supply voltage equals the induced back EMF plus the voltage drop across the winding inductance and resistance. For a square-wave brushless DC motor operating in current control, i.e. not being voltage limited, the optimum operating point is when the back EMF and current are in phase as this requires the minimum current (only q-axis current), and keeps the copper losses in the motor and the switching and conduction losses in the drive to a minimum. However, at high speeds the inductive reactance of the windings can result in a significant motor electrical time constant, and as a consequence the current requires some time to reach its steady state level. Where the applied voltage is in phase with the back EMF, the current appears out-of phase, lagging the back EMF, and as a result the torque output decreases. To align

current and back EMF again a small amount of phase advance is typically applied to the drive output voltage (in the existing turbo pump motor this is around 4^{o}).

If on the other hand the motor is voltage limited, as is the case for the Mk2 motor above a certain load, then the speed starts to decrease as the load torque increases. This decrease in speed can be prevented by phase advancing the current even more, so the voltage is applied while the back EMF is still rising. The current rise is faster as the back EMF is lower at turn on. This allows the motor to reach rated torque at rated speed again, but as a consequence the current required will increase, leading to higher copper losses in the motor and higher switching and conduction losses in the drive. The larger the inductance is, the more phase advance is required.

3.6.2 Initial Condition and Example Waveforms

The SMC Mk2 motor with its re-magnetised shaft was run in the back-to-back rig, instrumented as described in 2.7.2, but with a different drive, where an offset could be applied to the Hall phasing. The Hall offset angle is a parameter in software that adjusts the current switching position with reference to the falling edge of Hall 1. The relationship of the falling edge of Hall 1 to the back EMF depends on the physical position of the hall board on the motor stator itself, and hence can vary slightly from motor to motor.

Fig. 3.9 shows the relationship between the Hall 1 signal and the back EMF signal of Phase AC. The controller uses only the falling edge of Hall 1 as reference and then calculates the other five switching positions in equal steps of 60^{o} in software. In the SMC Mk2 motor the Hall board is mounted in a position where the Hall signal leads the voltage signal by 2^{o}.

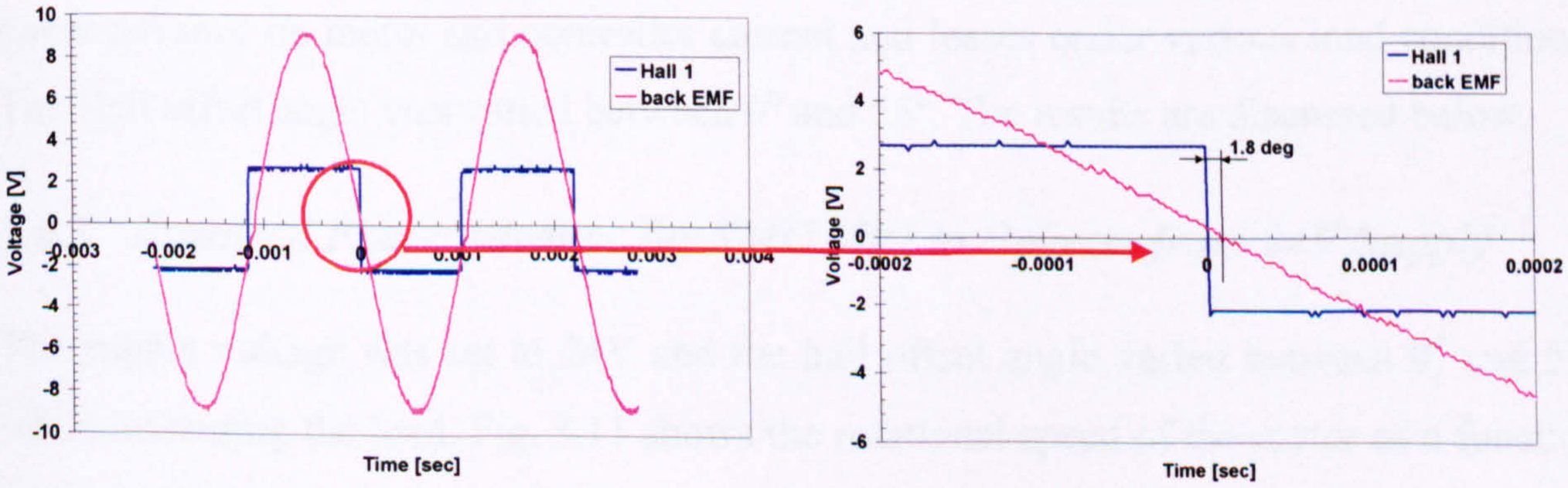

Fig. 3.9 Relationship between Hall 1 and back EMF of phase AC in the SMC Mk2 motor

Fig. 3.10a and b show two measured current waveforms with reference to Hall 1, one at the default Hall angle with zero offset in software, and one with the Hall offset set to 30°. The offset causes a relative change in the current switching position equal to ~30° (3° lagging to 23° leading: shift of 26°, 6° lagging to 23° leading: shift of 32°. Small differences are caused by non-equal Hall on/off periods.) The increase in current magnitude due to phase advance is also clearly visible (Fig. 3.10c).

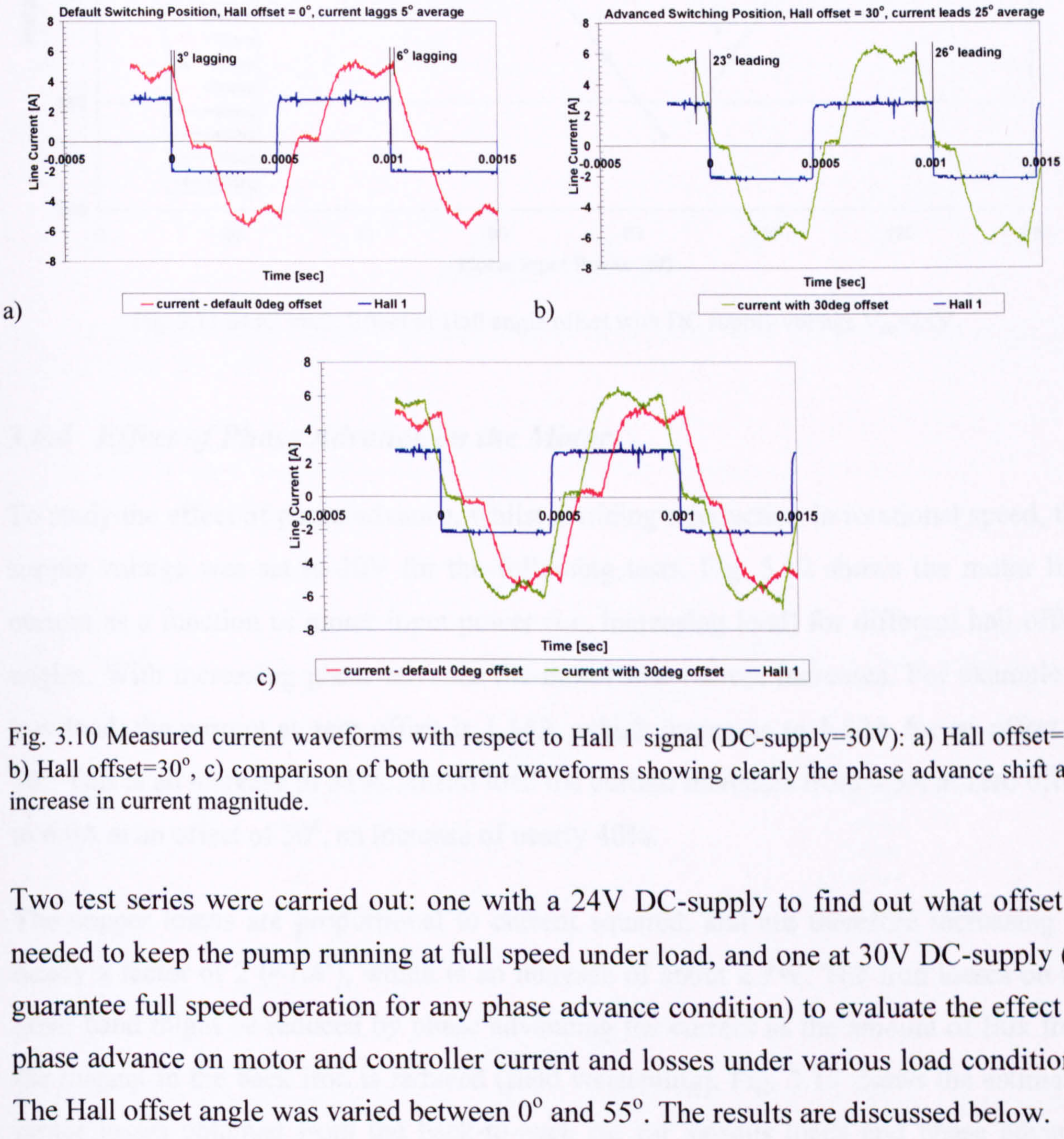

Fig. 3.10 Measured current waveforms with respect to Hall 1 signal (DC-supply=30V): a) Hall offset=0°, b) Hall offset=30°, c) comparison of both current waveforms showing clearly the phase advance shift and increase in current magnitude.

Two test series were carried out: one with a 24V DC-supply to find out what offset is needed to keep the pump running at full speed under load, and one at 30V DC-supply (to guarantee full speed operation for any phase advance condition) to evaluate the effect of phase advance on motor and controller current and losses under various load conditions. The Hall offset angle was varied between 0° and 55°. The results are discussed below.

3.6.3 Required Phase Advance for SMC Mk2 to Operate from 24V Supply

The supply voltage was set to 24V and the hall offset angle varied between 0° and 55° while increasing the load. Fig. 3.11 shows the rotational speed of the motor as a function of motor input power for the various hall offset angles. An offset angle of 50° or more allows the SMC Mk2 motor to run at full speed under rated load from a 24V supply.

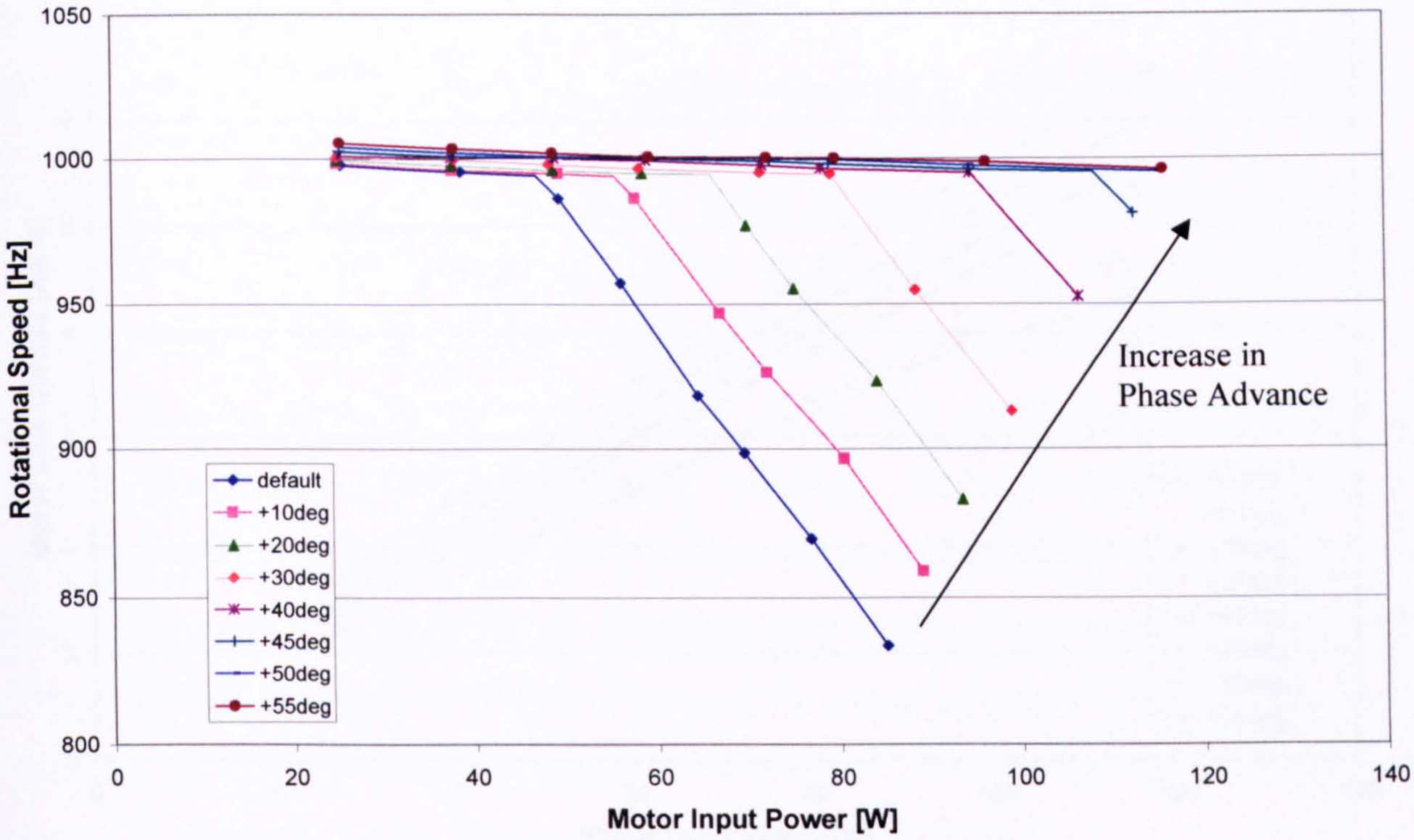

Fig. 3.11 SMC Mk2: Effect of Hall angle offset with DC supply voltage V_{dc}=24V.

3.6.4 Effect of Phase Advance on the Motor

To study the effect of phase advance, whilst avoiding a reduction in rotational speed, the supply voltage was set to 30V for the following tests. Fig. 3.12 shows the motor line current as a function of motor input power (i.e. increasing load) for different hall offset angles. With increasing phase advance the motor line current increases. For example at low load, the current at zero offset is 1.14A, which increases to 1.50A for an offset of 50°. This is an increase of 31%. At full load the current increases from 4.3A at zero offset to 6.0A at an offset of 50°, an increase of nearly 40%.

The copper losses are proportional to current squared, and are therefore increasing by nearly a factor of 2 (=1.4^2), which is an increase of about 2.7W. The iron losses on the other hand might be reduced by phase advancing the current as the amount of flux from the magnet in the back iron is reduced (field weakening). Fig. 3.13 shows the estimated motor losses obtained from the back-to-back rig for various loads and phase advance settings. The increase in current is large and the increase in copper loss also, but the motor loss is dominated by iron loss, so the total motor loss increases only a little. Under high load the variation in motor loss due to phase advance is in the order of 2.5W.

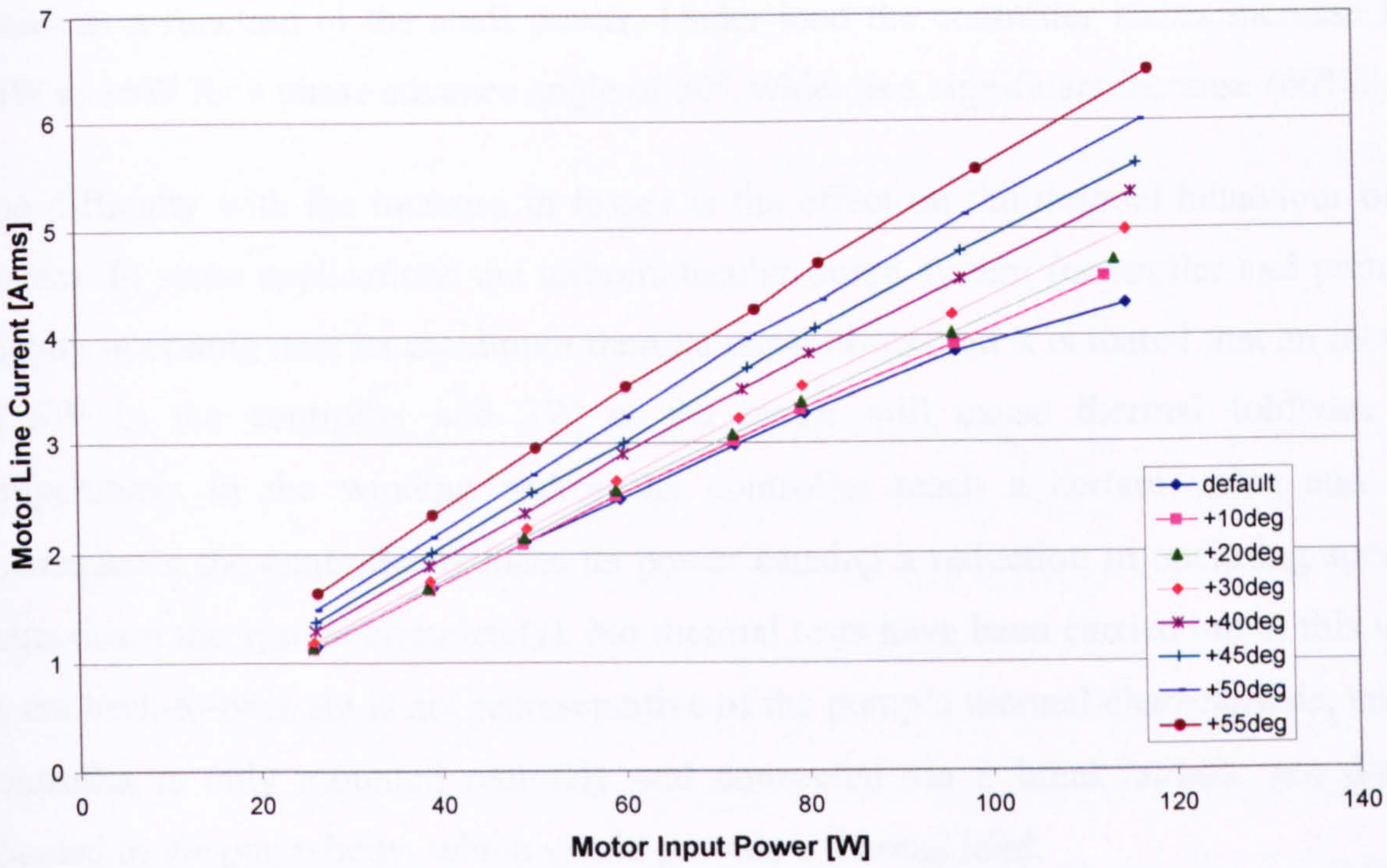

Fig. 3.12 SMC Mk2 motor current as function of motor input power with varying Hall offset angles (DC supply Voltage: V_{dc}=30V)

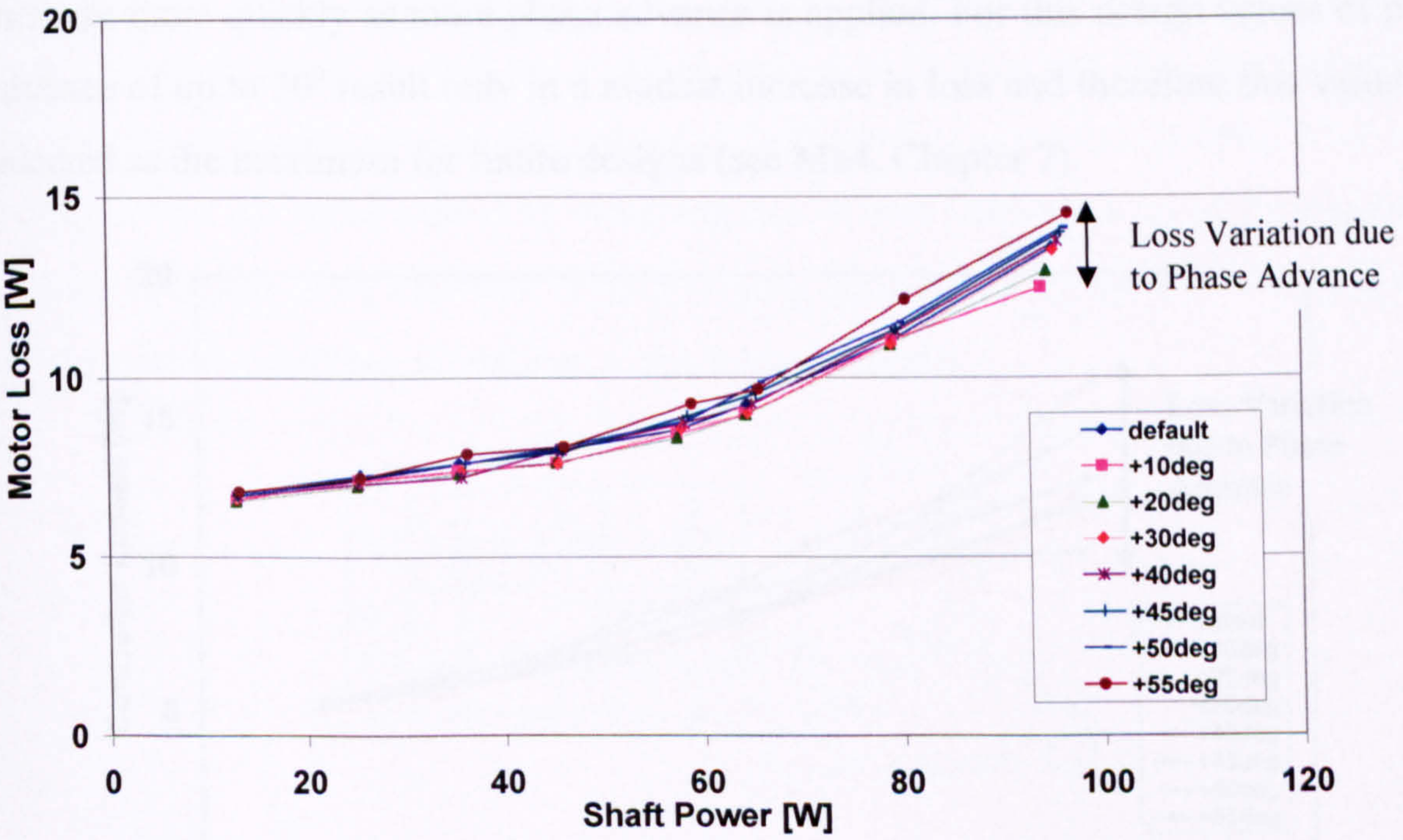

Fig. 3.13 Motor loss as a function of shaft power for the SMC Mk2 motor with different phase advance angle (V_{dc}=30V)

3.6.5 Effect of Phase Advance on the Controller

Phase advance not only increases the motor current and hence motor losses, it also increases the switching and conduction losses in the drive. The drive has to work harder to deliver the increased current requirement to the motor. Fig. 3.14 shows the controller

losses as a function of the shaft power. Under load the controller losses increase from 10W to 16W for a phase advance angle of 50°, which is a significant increase (60%).

The difficulty with the increase in losses is the effect on the thermal behaviour of the system. In some applications the turbomolecular pump system (controller and pump) is already operating near its maximum thermal capabilities, and it is feared that an increase of 6W in the controller and 3W in the motor will cause thermal foldback (i.e. temperatures in the winding and/or the controller reach a certain value and as a consequence the controller reduces its power causing a reduction in operating speed or shuts down the system completely). No thermal tests have been carried out at this stage, as the back-to-back rig is not representative of the pump's thermal characteristic, and the controller is only mounted remotely and connected via a breakout-box, not directly coupled to the pump body, which would provide a thermal load.

From Fig. 3.14 it can be seen that the larger the phase advance the more the losses increase under load. At first the losses increase slowly with phase advance but begin to increase more quickly as more phase advance is applied. For this design values of phase advance of up to 30° result only in a modest increase in loss and therefore this value was selected as the maximum for future designs (see Mk4, Chapter 7).

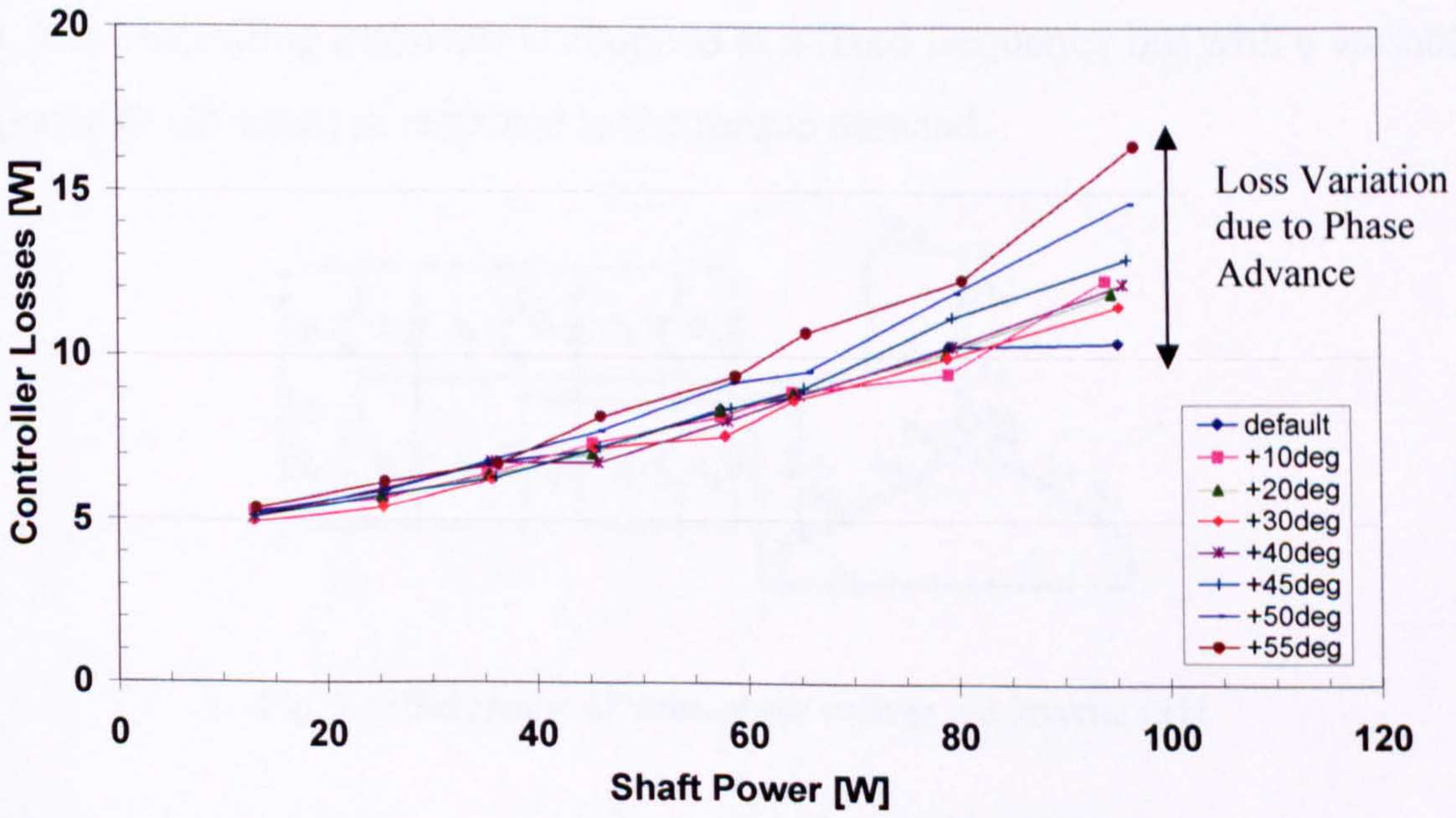

Fig. 3.14 Controller loss as a function of shaft power for the SMC Mk2 motor with different phase advance angle (V_{dc}=30V)

3.6.6 Computer Simulation

It would be useful as part of the design process to simulate the performance of the brushless DC motor and drive, to determine in advance the values of back EMF, and

inductance for which the drive would run out of volts, or to determine the required phase advance to deliver full torque at rated speed. To assist in future motor designs a Matlab program was written to simulate the current waveform of a brushless DC drive and predict the average torque.

Brushless DC Drive Operation and Voltage equation

The brushless DC motor is driven by a pulse-width-modulated three-phase voltage source inverter. Fig. 3.15 shows the basic schematic of the voltage-fed inverter with a star-connected motor. The form of control used is feed forward in nature, setting a voltage to be applied (via PWM) for a given speed and load. This makes the performance of the motor essentially of a voltage control type. During one cycle the current gets commutated six times between the three phases. In between commutations the current flows in two phases, while the third phase is off. However, during the commutation event, current flows in all three phases. The current in the phase that is being switched off free-wheels through the diode against the supply voltage and drops rapidly. At the same time the current in the phase that is being switched on rises at a slower rate. The third phase that stays on, will see a dip in current to balance out the other two phases. Between commutation events the current is controlled to a current demand level using voltage PWM (as noted above) by switching one or both transistors off in the conducting phases. The controlling transistor is chopped at a fixed frequency but with a variable duty cycle (variable off-time) in response to the torque demand.

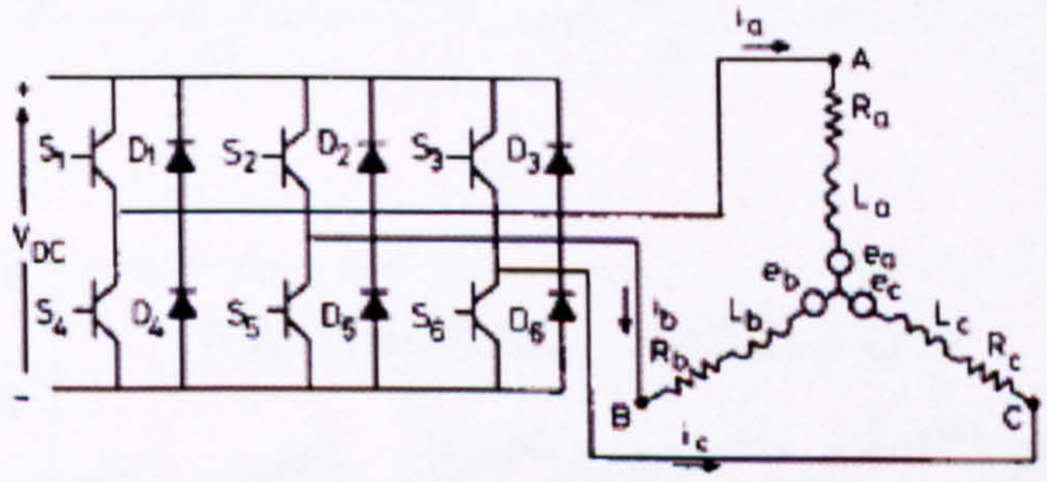

Fig. 3.15 Schematic of three-phase voltage fed inverter [31]

Assuming a non-saturated motor and neglecting the voltage drop in the switching devices (which can be taken into account by reducing V_{dc}), the governing voltage equations are [30, 31]:

a) In between commutations: Two phases on, one off (zero):

$$V_{dc} = 2Ri + 2L\frac{di}{dt} + e_a - e_b \text{, with } i = i_a = -i_b \tag{3.4}$$

Hence the rate of current change (rise) with time is $\frac{di}{dt} = \frac{V_{dc} - 2Ri - (e_a - e_b)}{2L}$ (3.5)

This is true for the PWM on-period. In the PWM off-period, when two transistors are switched off (as implemented in the model), the current free-wheels through two diodes, and the following equations apply:

$$-V_{dc} = 2Ri + 2L\frac{di}{dt} + e_a - e_b, \text{ with } i = i_a = -i_b \quad (3.6)$$

Hence the rate of current change (fall) with time is $\frac{di}{dt} = \frac{-V_{dc} - 2Ri - (e_a - e_b)}{2L}$ (3.7)

i.e. the slope of the current rise and fall during a PWM controlled period are not the same (Fig. 3.16).

b) During commutations: current flows in all three phases – requires two voltage equations:

$$V_{dc} = Ri_a + L\frac{di_a}{dt} + e_a - Ri_c - L\frac{di_c}{dt} - e_c \quad (3.8)$$

$$0 = Ri_a + L\frac{di_a}{dt} + e_a - Ri_b - L\frac{di_b}{dt} - e_b, \quad (3.9)$$

With the condition $\frac{di_a}{dt} + \frac{di_b}{dt} + \frac{di_c}{dt} = 0$, the rate of change of current is

$$\frac{di_a}{dt} = \frac{2V_{dc} - 2e_{ab} + e_{cb} - 3Ri_a}{3L}, \text{ and } \frac{di_c}{dt} = \frac{-V_{dc} - 2e_{cb} + e_{ab} - 3Ri_c}{3L} \quad (3.10)$$

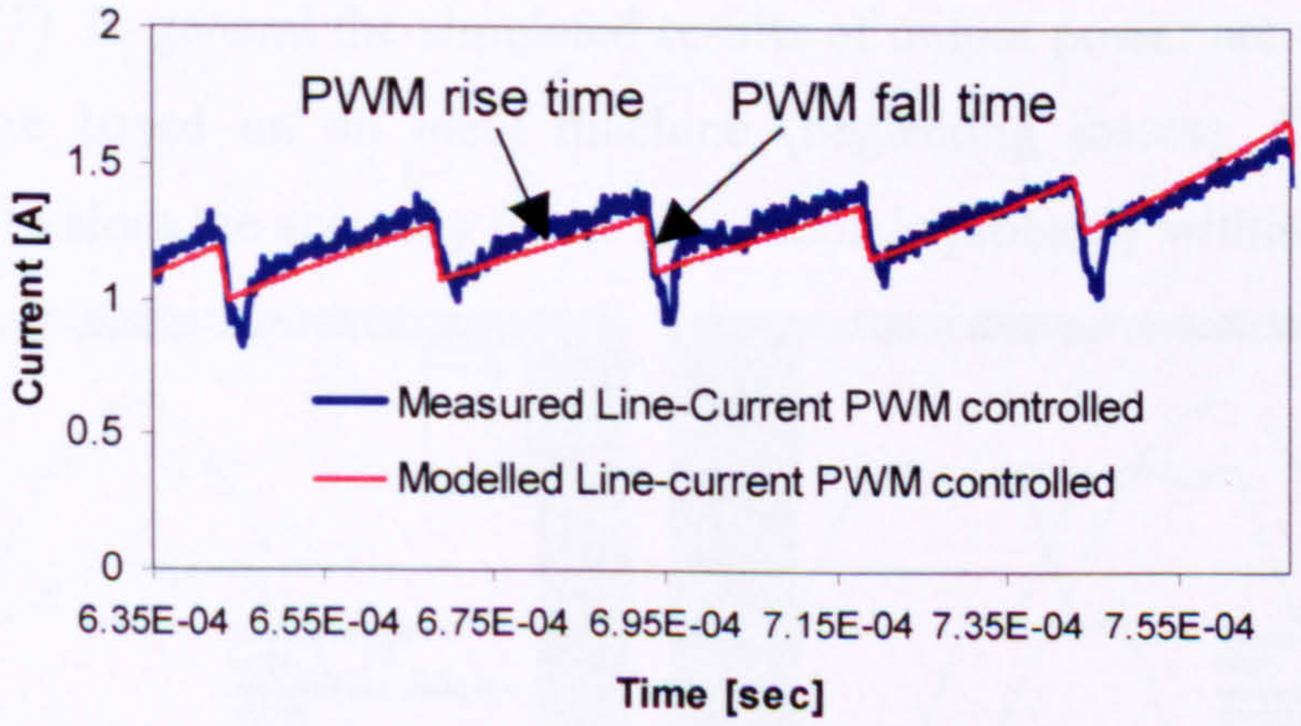

Fig. 3.16 Sample of PWM controlled current

MATLAB-Program: Current Waveform Simulation

The current equations have been implemented as a numerical time-stepping routine in Matlab. This allows simulation of the current waveform for a PWM controlled square-wave drive with sinusoidal back EMF and calculates the average torque and power. The input parameters are supply voltage V_{dc}, line resistance R_{LL}, line inductance L_{LL}, line back EMF e_{LL}, phase advance angel α, PWM-index *pwm* (controls the duty-cycle on-time, in the absence of a current control routine) and frequency *f*. As an example Fig. 3.17 shows a section of the measured current waveforms from Fig. 3.10 and the simulated waveforms using the Matlab program.

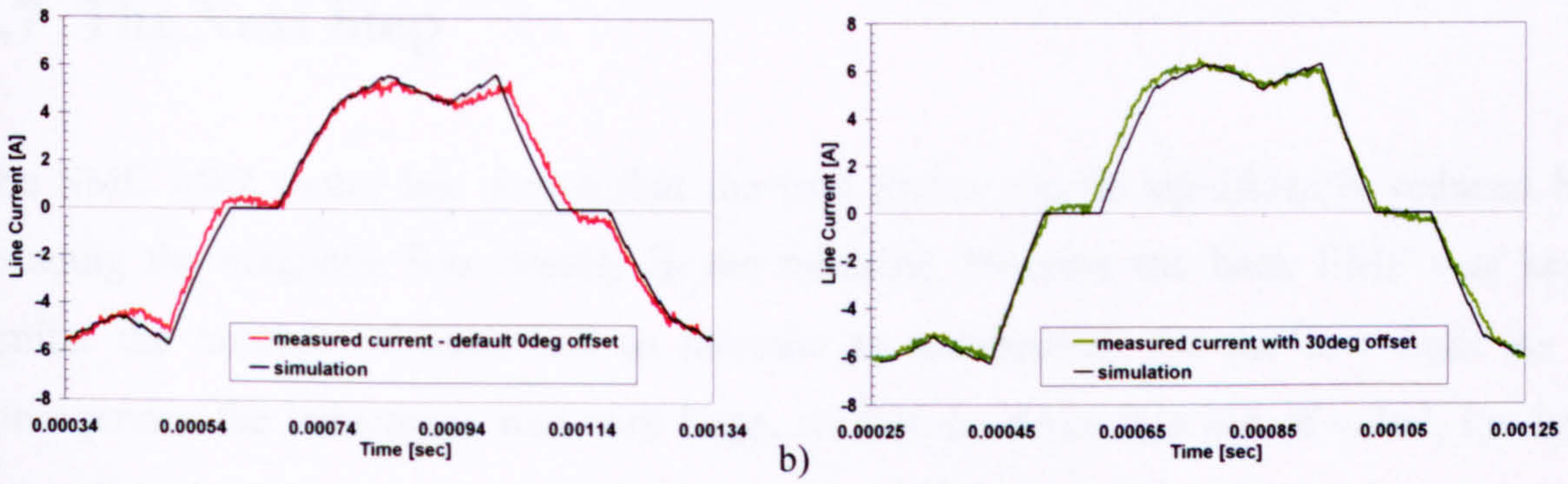

a) b)

Fig. 3.17 Comparison between measured and simulated current waveforms using time-stepping routine for the SMC Mk2 motor: a) 0° phase advance, b) 30° phase advance

To validate the program the output power from a 24V supply for different phase advance angles for the SMC Mk2 was calculated and compared with measurements. Fig. 3.18 shows an example of the current waveforms relative to the back EMF for an offset angle of 0° and 50°, and Table 3.7 summarises the results. To deliver 110W to 120W output power, a phase advance angle of 50° is required. This agrees well with the experimental results (Fig. 3.11). In general the simulated results of output power are on the optimistic side as they are based on an ideal machine (neglecting losses). Compared to the measured power values the accuracy of the simulation is probably within 10-15%.

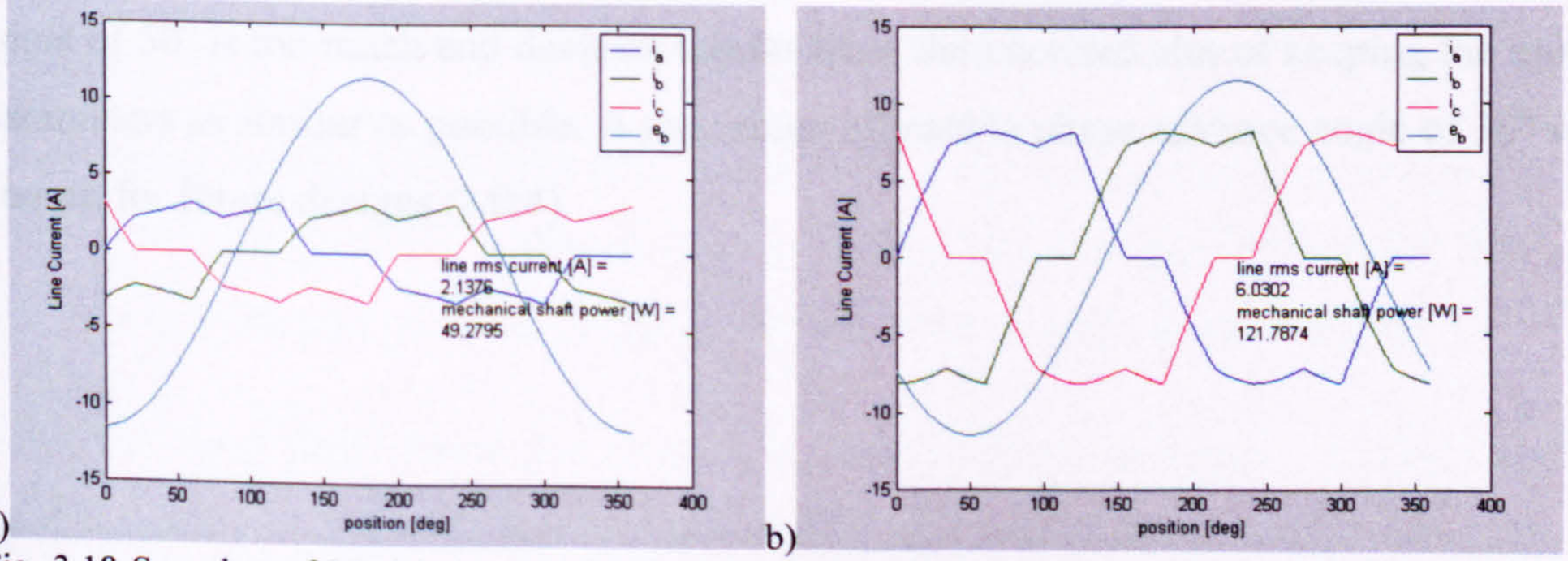

a) b)

Fig. 3.18 Snapshot of Matlab current-simulation output for SMC Mk2 motor (input values according to Table 3.7): a) zero phase advance, b) 50° phase advance

Input Values:	Results from the Simulation: Phase Advance [deg]	Line Current [A_{rms}]	Output Power [W]
V_{dc}=23.5V (accounts for voltage drop in controller)	0	2.14	**49.3**
	10	2.35	**55.5**
	20	2.86	**66.9**
R_{LL}=0.11Ω	30	3.65	**82.7**
L_{LL}=425μH	40	4.71	**101.7**
e_{LL}=14.0V_{rms}	45	5.34	**111.7**
pwm =0.995 (limit to stay in current control)	50	6.03	**121.8**
	55	6.78	**131.6**
f=1000Hz			

Table 3.7 Results from the simulation program: Output power as a function of phase advance angle

3.7 The Next Step

The SMC Mk2 motor has shown that the iron losses can be significantly reduced by reducing the magnetic flux density in the machine. Because the back EMF was kept similar the number of turns had to increase to compensate for the low flux. As a consequence the inductance was very large, so that the drive 'ran out of volts', i.e. had less voltage headroom and was unable to provide sufficient torque under load.

It was decided to build another SMC motor Mk3, reducing the inductance again to values similar to those in Mk1 and the existing motor, and to reduce the iron losses by reducing the axial length of the machine, rather than by reducing the flux density so much. Because of the large discrepancy between predicted and actual back EMF of Mk1 and Mk2, which was attributed mainly to the plastic bonded magnets not performing well, it was decided to use sintered rare earth magnets in the next motor rotor.

It has been demonstrated that applying phase advance to the current can extend the drive's full load capability, despite a large inductance, but it would increase the losses, especially in the drive. However, the perception at this point was that a phase advance angle of 50° is too much and deviates too far from the intended aim of keeping the motor parameters as similar as possible. A maximum allowable phase advance angle of 30° was chosen for future designs (Mk4).

Chapter 4

The Third SMC Machine (Mk3): Axially Shorter & Thin Sintered Rare Earth Magnets

4.1 Introduction

The first two SMC machines built both had their own shortcomings. Mk1 had very high iron losses. To reduce the iron losses the flux density was reduced in the second machine (Mk2) by using thinner plastic bonded magnets. This was successful in reducing iron loss, but to compensate the reduction in flux the number of turns was increased, which made the inductance too high resulting in the drive running out of volts. As the initial specification was to design a replacement motor, that keeps the impact on the drive to a minimum, Mk2 was also found not to be an acceptable solution. The aim of this third SMC machine is to find a compromise between the two designs.

After having built and tested the previous motors in the back-to-back rig, which was not without its difficulties due to the variation of bearing loss, the SMC Mk3 motor was built into a turbomolecular pump, allowing for the first time realistic thermal testing.

With this third SMC motor the project reached a critical milestone. A major review meeting was planned after the testing of Mk3, to examine the results to date, discuss

what is acceptable, and to decide whether or not to continue pursuing the SMC technology.

This chapter presents the Mk3 design and test results and summarises the outcome of the review meeting.

4.2 Design Changes in Mk3

4.2.1 Change of Magnet Material

After the discrepancy between the measured and predicted back EMF, especially in the Mk2 design, the plastic bonded magnets were considered a performance risk. Therefore it was decided to use sintered rare earth NdFeB magnets on Mk3. Still driven by the requirement of a stiff shaft, the shaft diameter was kept at 12.5mm (same as Mk2), which meant the magnets had the same radial dimensions as Mk2 (i.e. 1.86mm).

4.2.2 Change in Active Axial Length

Rather than changing the flux density to reduce the iron losses as in Mk2 the plan was to reduce the axial length of the machine. To achieve this the extended tooth tips on both sides of the existing teeth were cut off (see Fig. 4.1) (unused SMC parts from Mk2 were used). The axial tooth length was thus reduced from 31mm to 14mm.

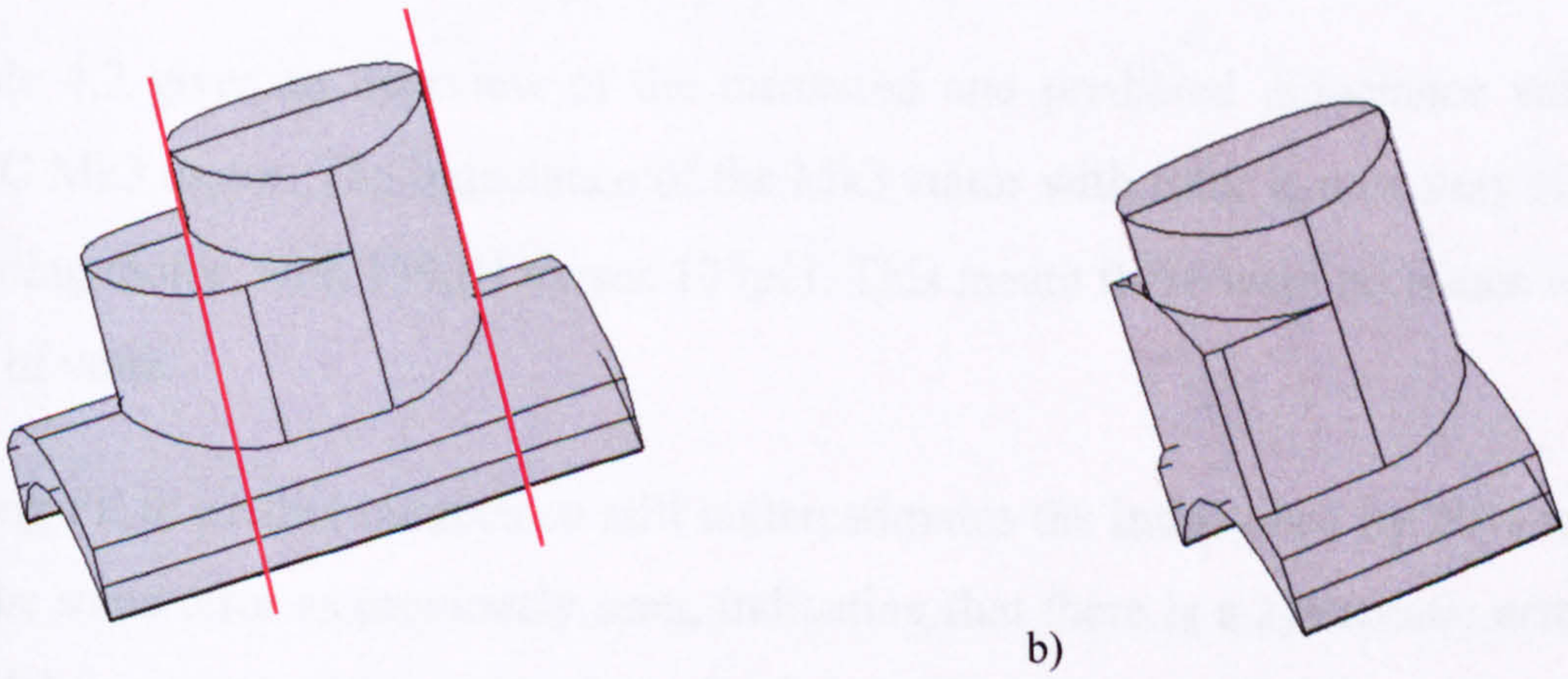

Fig. 4.1 a) Modifications to the 'long' tooth of Mk2, b) the 'short' tooth used for SMC Mk3 motor

4.3 SMC Mk3 Motor Parameters and Performance

4.3.1 Resistance and Inductance of SMC Mk3

The SMC Mk3 motor was wound with 34 turns of 5 strands in parallel of wire diameter 0.5mm. The coils were wound using the existing large coil former despite the shorter SMC teeth to keep things simple and reduce lead time. Therefore the resistance is a bit higher than it ideally could have been with the shorter teeth and tight coils. Nevertheless the resistance of the Mk3 motor is 27% lower compared to the existing motor, reducing the predicted copper loss from 2.35W to 1.71W (Table 4.1). Due to the non-overlapped windings the copper volume is only half of that of the existing motor, despite the larger coils.

The inductance is significantly lower than in the Mk2 motor, as the number of turns N_{ph} has been reduced from 49 to 34 (inductance proportional to N_{ph}^2) and the length of the teeth has reduced from 20mm to 14mm (inductance proportional to l). Based on previous measurements (see SMC Mk2, Table 3.2, page 42) this gives an expected inductance for the SMC Mk3 machine of:

Without rotor: $$379\mu H \cdot \left(\frac{34^2}{49^2}\right) \cdot \left(\frac{14}{20}\right) = 128\mu H$$

With rotor: $$425\mu H \cdot \left(\frac{34^2}{49^2}\right) \cdot \left(\frac{14}{20}\right) = 143\mu H$$

Table 4.2 gives an overview of the measured and predicted inductance values for the SMC Mk3 motor. The inductance of the Mk3 stator with rotor is now very similar to the existing motor, with 139μH versus 133μH. This meant there were no issues with running out of volts.

Using FE to predict inductance still underestimates the inductance by 20% to 34%. This is the same error as previously seen, indicating that there is a systematic error in the 2D model compared with measured results. It is believed that this is due to the neglected 3D effects of the endwindings. As the error is fairly consistent in the modelling of the 3-tooth motors so far, it can be used as a 'correction' factor to predict inductance in future, similar motors.

	SMC Mk3 (34 turns per phase, 5 strands of dia. 0.5mm, Delta) Stator S007	**Existing Motor** (14 turns per phase, 9 strands of dia. 0.5mm, Star) Stator S004	Stator S005
DC Line-Line Resistance			
Predicted	**32 mΩ**	**55 mΩ**	
Measured (@25°C)	40 mΩ	54.2 mΩ	54.7 mΩ
Average	**40 mΩ** 27 % less than existing motor	**54.5 mΩ**	
Copper Loss			
with rated current of $5A_{rms}$, $T_{winding}$=60°C	**1.71 W** 27 % less than existing motor	**2.35 W**	
Copper Volume & Mass			
Slotfill	**35.8%**	**24.4 %**	
Volume	**7.65 cm³**	**14.32 cm³**	
Mass	**68.6 g** 46 % less than existing motor	**128.3 g**	

Table 4.1 DC resistance, copper loss and copper volume for SMC Mk3

Line-Line Inductance			
	SMC Mk3 Stator S007	**Existing Motor** Stator S004	Stator S005
Stator Only			
Predicted (FE)	95 µH	85 µH	
Measured Average	x 1.337 **127 µH**	x 1.282 **109 µH**	
With Rotor			
Predicted (FE)	113 µH	112 µH	
Measured Average	x 1.230 **139 µH**	x 1.188 **133 µH**	

Table 4.2 Line-line inductance for SMC Mk3 motor in comparison with the existing motor

4.3.2 Back EMF of SMC Mk3

The same 2D, non-linear FE model as described in Chapter 3.3 was used to predict the back EMF and the no-load iron losses. The SMC material was represented using the non-linear BH-curve and corresponding permeability as shown previously in Fig. 3.2, including new space-factors to adjust for the shorter teeth. The magnet material properties have been changed to reflect the new rare earth magnet. Table 4.3 states the new magnet material data and SMC space-factors used. Fig. 4.2 shows the open circuit flux density plot.

Magnet Material:	VACODYM 677HR rare earth NdFeB
B_r	1.18 T
H_c	915 kA/m
μ_r	1.026

SMC Space-factor:	
Tooth tip	1
Tooth body	0.893
Back iron	2.571

Table 4.3 Magnet material and space-factors for SMC Mk3 motor

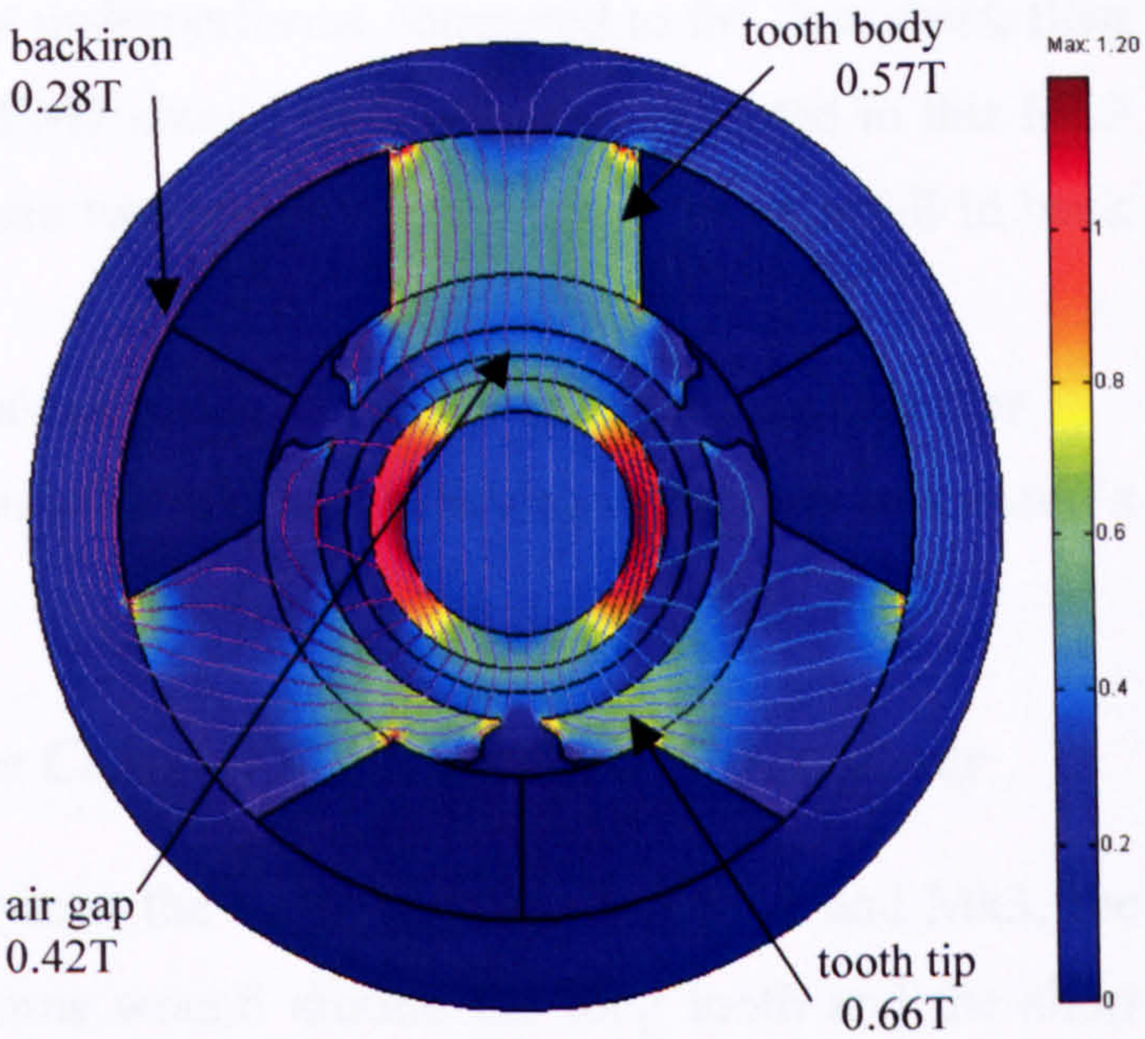

Fig. 4.2 SMC Mk3 Open circuit flux plot (incl. space-factors)

With 34 turns a back EMF of 14.26 V_{rms} was predicted. The measured back EMF of the SMC Mk3 motor came to 14.9Vrms (Fig. 4.3). This is within 5% of the predicted value, which is closer than on any of the previous SMC machines, where plastic bonded magnets were used. The measured value is actually higher than the predicted, which is the other way round compared to Mk1 and Mk2. Similar good agreement between measured and predicted back EMF has been obtained on the existing motor, which uses SmCo rare earth magnets (Table 4.4).

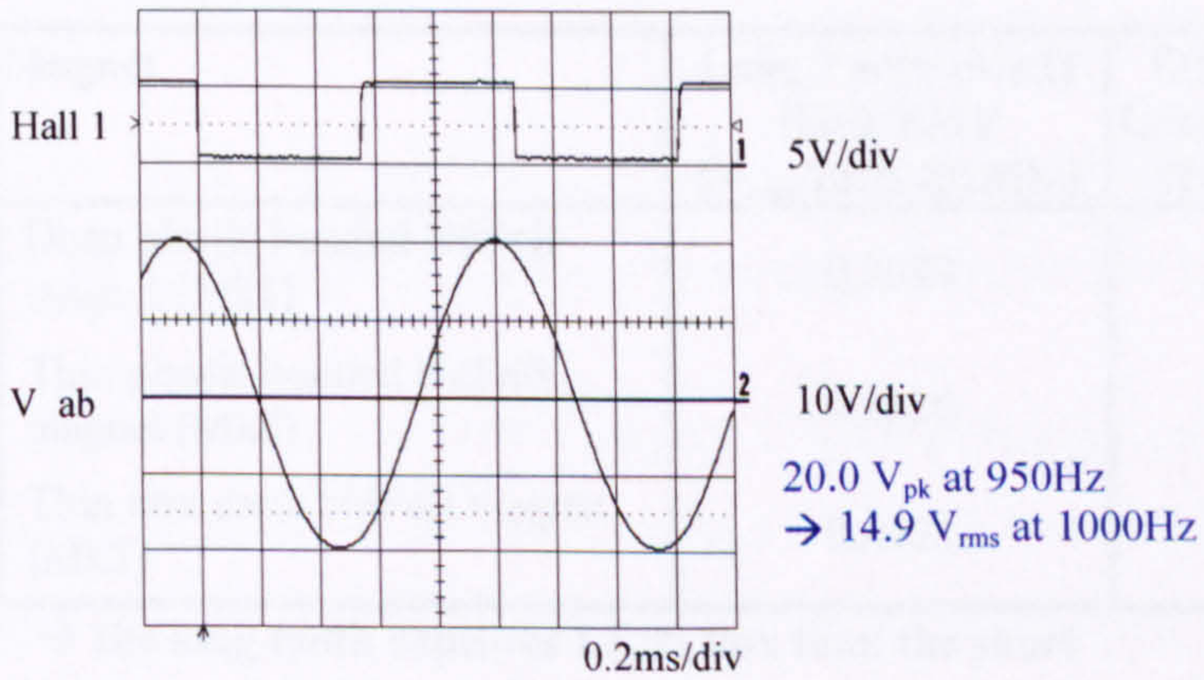

Fig. 4.3 Measured back EMF waveform of SMC Mk3 motor

	SMC Mk3 (34turns per phase, Delta) Stator S007	**Existing Motor** (14turns per phase, Star)
Back EMF Line-Line @ 1000Hz		
Predicted	**14.26 V_{rms}**	**14.21 V_{rms}**
Measured	**14.89 V_{rms}**	**14.14 V_{rms}**

Table 4.4 Predicted and measured back EMF for SMC Mk3

If the machined SMC material generally underperforms compared to the data sheet, then even with rare earth magnets the back EMF should be lower than expected in this Mk3 machine. As this is not the case, there are two possible reasons for the shortfall in back EMF on Mk2 compared to Mk3:

- the plastic bonded magnets are not as strong as suggested in the data sheet, or
- the individual SMC parts used in Mk1/Mk2 are behaving differently to the one's in Mk3.

4.3.3 Further Investigation into the Cause of the Back-EMF Discrepancy

To find out if there is a difference between the SMC parts used in Mk2 and Mk3, the back EMF was measured on 10 test-turns wound around the long tooth and the short tooth. The three different rotor magnets from Mk1 to Mk3 were rotated at low speed, keeping the magnet-SMC axial engagement constant (see Fig. 4.4).

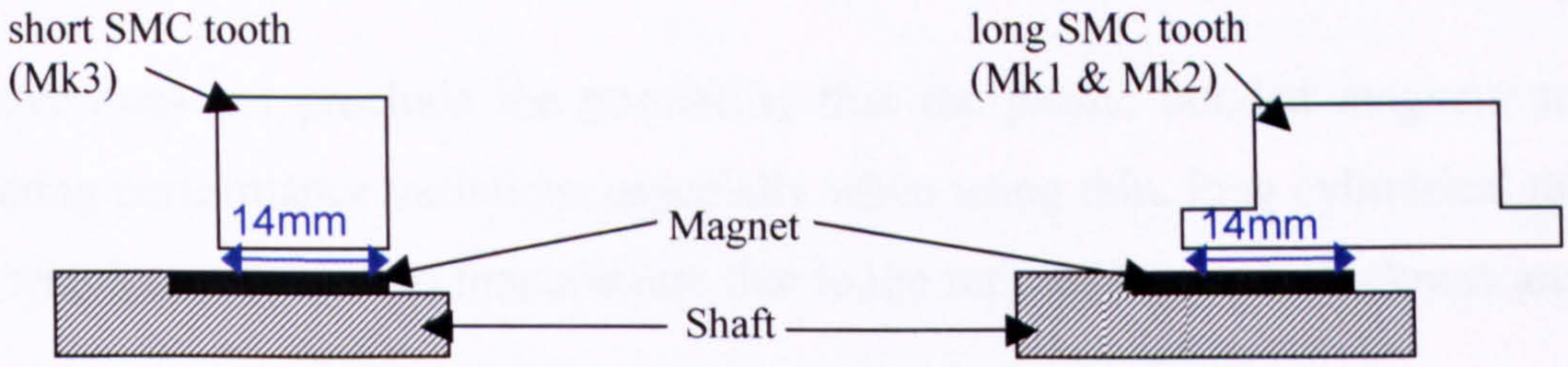

Fig. 4.4 Set-up for back EMF measurement on the short and long tooth

Short Tooth (Mk3) Back EMF [V_{rms}/turn @1kHz]	**Magnet**	**Long Tooth (Mk1) Back EMF [V_{rms}/turn @1kHz]**	**Difference between Long and Short Tooth [V_{rms}/turn @1kHz]**
0.2165	Deep plastic bonded NdFeB magnet (Mk1)	0.2089	0.0076 (3.5%)
0.1381	Thin plastic bonded NdFeB magnet (Mk2)	0.1320	0.0061 (4.4%)
0.4522	Thin rare earth NdFeB magnet (Mk3)	0.4121	0.0040 (0.9%)
→ the long tooth captures LESS flux than the short tooth			

Table 4.5 Comparison of measured back EMF per turn with the same rotor magnet on the short and long SMC tooth

The measured back EMF values show that the long tooth collects less flux from the same magnet as the short tooth does. This is an indication that the thin tooth tips on the long tooth are not contributing as much to collecting the flux as the middle part of the tooth, which is used for the short tooth. The material properties must be different in the thin

sections of the tooth tip compared to the tooth body. It is suspected that the wire-erosion process used to manufacture these prototype parts is damaging the bonding between the particles and producing micro-cracks. Thin sections suffer more damage than thicker one's. When predicting the back EMF on the long tooth an axial length of 31mm had been used, which overestimated the flux linkage. Due to the material damage the effective tooth length is shorter, because the thin tooth tips do not contribute in the same way as the rest. From these results it is not possible to say how much or in what way the SMC properties are damaged, and how much shorter the effective length is. More specific test on parts with different thicknesses, and different manufacturing methods would need to be carried out, but this is beyond the scope of this work. For now, the conclusion is that thin SMC parts are damaged by wire-erosion, and account for the low back EMF measured in Mk1 and Mk2. It would be interesting to see if the performance of the long tooth is improved when using press-tooling, but that remains outside the resources of this project (cost and time).

The above does not preclude the possibility that the plastic bonded magnets are also contributing performance variations especially when using thin, long cylindrical magnets (Mk2), which are difficult to manufacture due to the ratio of thin wall thickness and axial length.

4.3.4 Iron Losses of SMC Mk3 Tested in the Back-to-Back Rig

Using the flux densities from Fig. 4.2 the no-load iron losses were estimated as 7W. Applying rated current of 5A the full load losses were calculated as 9W (see Table 4.6).

Table 4.7 and Table 4.8 show the measured power consumption and derived losses for the SMC Mk3 motor, when tested in the back-to-back rig under no-load and rated load. The rig losses, which include the varying bearing losses depending on the level of unbalance, have some uncertainty attached, and could be overestimated by up to 4-5W when using the fitted curve from Fig. 2.12 (page 32). The no-load motor losses were determined as 11.5W (plus potentially up to 4-5W more), which is 64% more than the predicted 7W. Under load the error is even bigger, reaching nearly 90% (17W instead of 9W). This discrepancy is attributed to bulk eddy currents and a much higher conductivity of the material than initially assumed (see Chapter 5). Prototype machining like wire erosion or mechanical machining is destroying the grain insulation, leading to an increase

in the conductivity. Also, this simple method does not take into account the component size, which will be shown later to have significant influence (Chapter 5).

Modelled Stator Iron Losses: SMC Mk3		
	No-load	**Rated Load** ($5A_{rms}$ line current)
Peak flux density – back iron	0.28 T	0.33 T
Peak flux density – tooth body	0.57 T	0.62 T
Peak flux density – tooth tip	0.66 T	0.77 T
Core loss – back iron	3.333 W	4.556 W
Core loss – one tooth body	0.652 W x 3	0.765 W x 3
Core loss – one tooth tip	0.560 W x 3	0.751 W x 3
Total Predicted Stator Iron Loss	**7.0 W**	**9.1 W**

Table 4.6 Estimated stator iron loss for SMC Mk3 (based on fitted loss curve in W/kg from Fig. 2.9)

Measured Performance SMC Mk3 – Motor Loss @ No-load
(rig losses based on fitted curve – see Fig. 2.12)

N°	Stator	Rotors	$P_{M,in}$ [W]	$P_{G,out}$	P_{Rig} [W]	$P_{M,loss}$ [W]	Unbalance [mg]	Comment
23	SMC Mk3	SMC Mk3 *double*	37.2 W	-	14.3 W	11.5 W	202 208	
Average Measured No-load SMC Mk3 Motor Losses:						**11.5 W**		

Table 4.7 Measured no-load performance of SMC Mk3

Measured Performance SMC Mk3 – Motor Loss @ Load:
(rig losses based on fitted curve – see Fig. 2.12)

N°	Stators & Rotors	$P_{M,in}$ [W]	$P_{G,out}$ [W]	P_{shaft} [W]	ΔP [W]	P_{Rig} [W]	$P_{M,loss}$ [W]	η	Un-balance [mg]	Comment
24	SMC Mk3 *double*	116	66	91	50	15.2	**17.2**	85.1%	269 196	
25	SMC Mk3 *double*	130	79	104	51	15.1	**18.1**	86.1%	257 199	

Table 4.8 Measured performance under load of SMC Mk3

Overall the losses of the SMC Mk3 motor are lower than the losses of Mk1, but higher than Mk2. Reducing the axial length has reduced the losses without increasing the inductance for a similar back EMF. The losses under no-load are about 4.5W higher than in the existing machine, i.e. 11.5W instead of 7W.

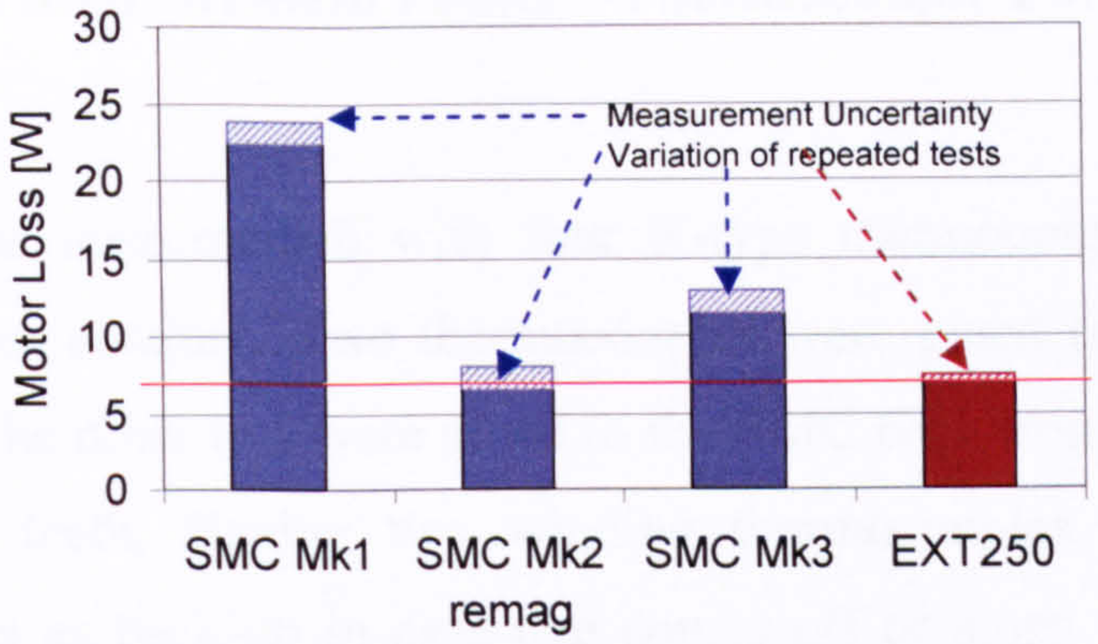

Fig. 4.5 Comparison of measured no-load motor loss (SMC measured in back-to-back rig, EXT250 measured in magnetic levitated turbopump)

The question is: Are the increased losses really a problem? i.e. Do the increased losses really cause the pump to reach its thermal limit? Can the controller deliver the additional power without overheating? To test the effect of the increased losses on the thermal characteristic of the pump, a series of tests were conducted. The thermal results are summarised below.

4.4 Thermal Performance of SMC Mk3 Motor

4.4.1 Test Set-Up and Instrumentation

The SMC Mk3 motor was built into a standard EXT255 turbomolecular pump with one oil-lubricated ball bearing at the bottom and one permanent magnet bearing at the top (Fig. 1.3a) and tested in the laboratory at Edwards. The pump was driven, via a breakout box, by an EXDC controller and forced air-cooled. The motor input power, line voltage, line current and power factor were measured using a power analyzer (Voltech PM3000A). The system input power (power into the controller) was indirectly measured by measuring the DC supply voltage and the DC current as a voltage drop across a 0.1Ω shunt resistor. All these electrical parameters plus the temperature measurements were fed into a data logger.

The pump has been run under two conditions: a) under 'no-load', i.e. no inlet flow and minimum backing pressure of about $5 \cdot 10^{-3}$mbar, and b) under 'full load' i.e. 10mbar backing pressure. The duration of each test was 4 hours or longer to make sure thermal equilibrium had been reached.

4.4.2 Temperature Measurement Points – Thermocouple Locations

Motor

The motor itself was instrumented with four K-type thermocouples to measure the winding and stator temperature. Two thermocouples were glued onto the windings on two different coils. The other two were glued to the SMC back iron ring in two different places between the teeth. Having two winding thermocouples and two back iron thermocouples serves as back-up in case one comes off or stops working, and avoids having to strip down the pump and break up the vacuum system. The second winding temperature reading will either confirm the first or highlight uncertainties in the measuring process or show real thermal gradients in the motor. The same is true of the pair of back iron temperature readings. Fig. 4.6 shows a photo of the thermocouple positions of the SMC motor in a pump body.

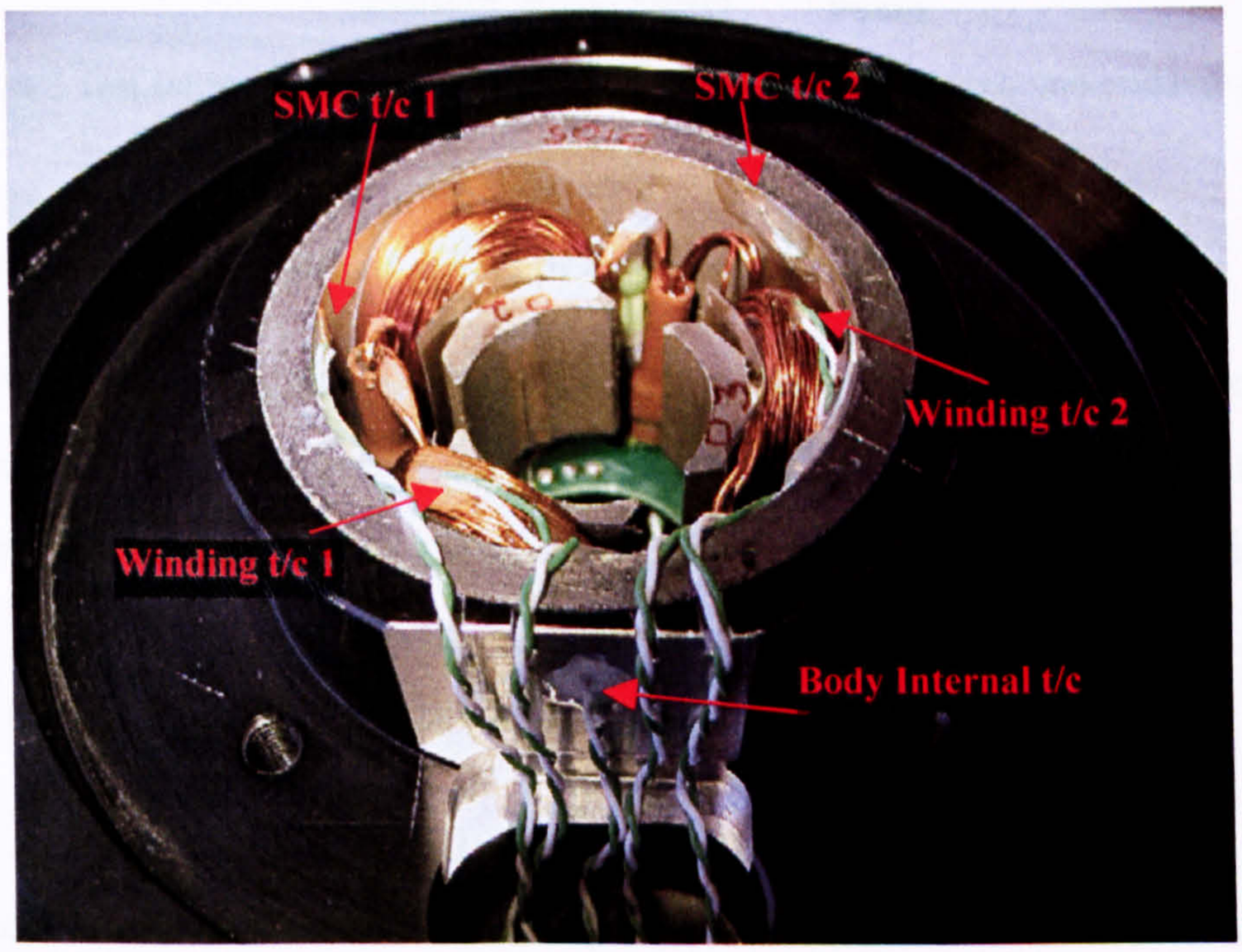

Fig. 4.6 Thermocouple positions on the motor for thermal testing in the turbopump (motor shown is SMC Mk4)

Pump

For the pump a thermocouple was placed within the aluminium body just behind the motor stator, to measure the 'internal body temperature'. Another thermocouple was placed outside on the pump body measuring the external body temperature, and another just above the pump to measure the ambient temperature. An infra-red thermocouple was used to measure the impeller temperature. Fig. 4.7 shows the set-up of the turbopump with all the measuring instruments.

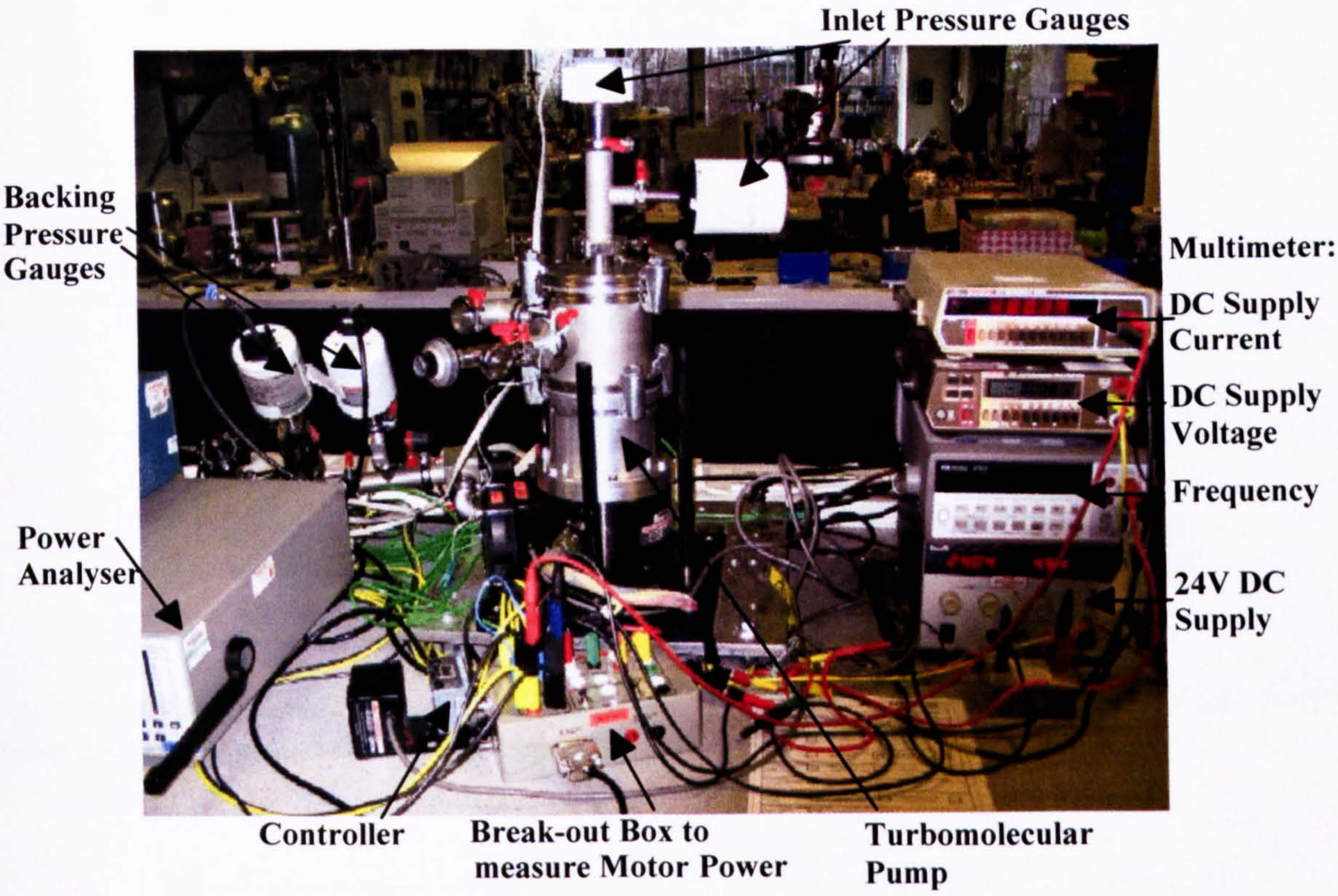

Fig. 4.7 Test set-up for thermal testing the SMC Mk3 motor in a turbomolecular pump

4.4.3 Power Consumption of SMC Mk3 Measured in a Pump

Fig. 4.8 and Fig. 4.9 show the measured power consumption, current, voltage and power factor for the SMC Mk3 motor in comparison to the existing motor under no-load and load. The measured SMC Mk3 motor input power is 40W under no-load and 109W under rated load. This represents an increase of 10W or 35% under no-load, and 14W or 15% under load. These increases in loss are significant.

The power factor of the SMC Mk3 motor is lower (by about 8%) than on the existing motor, which meant that the Hall phasing is not as ideal to make the best use of the current. This direct comparison also relies on the assumption that the bearing losses and windage are identical in both pumps, which might not be the case. The friction loss from the finger felts of the oil bearing and the amount of oil being circulated in the bearing can vary from pump to pump and could add an uncertainty of +/- 3 to 5W (based on typical power fluctuations seen on existing pumps from unit to unit under the same conditions). Nevertheless the important question is how does the increased loss affect the thermal characteristic of the pump.

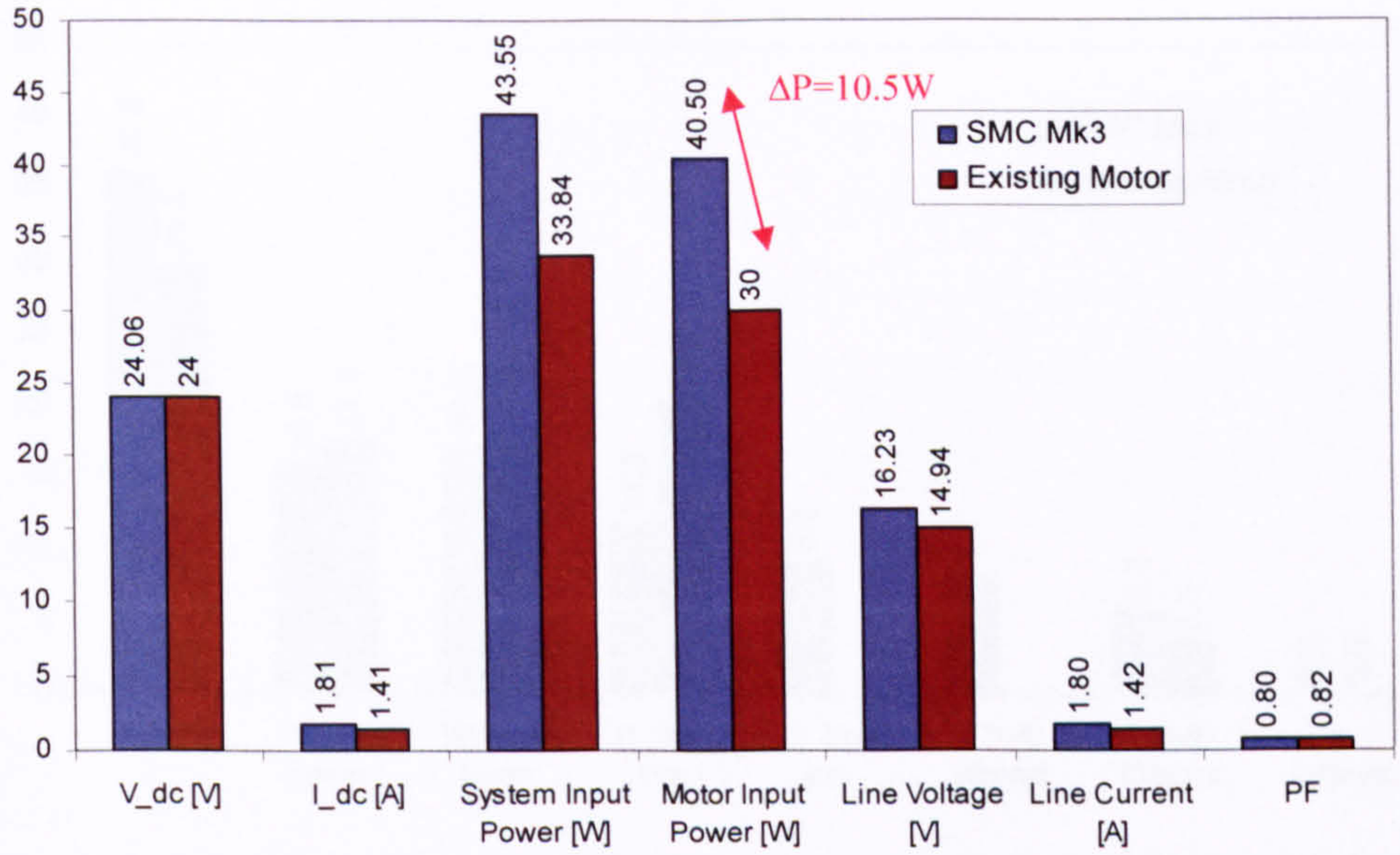

Fig. 4.8 Measured electrical parameters for no-load (backing pressure of $5 \cdot 10^{-3}$mbar) of the SMC Mk3 motor in comparison with the existing motor (EXT250 pump with standard bearings)

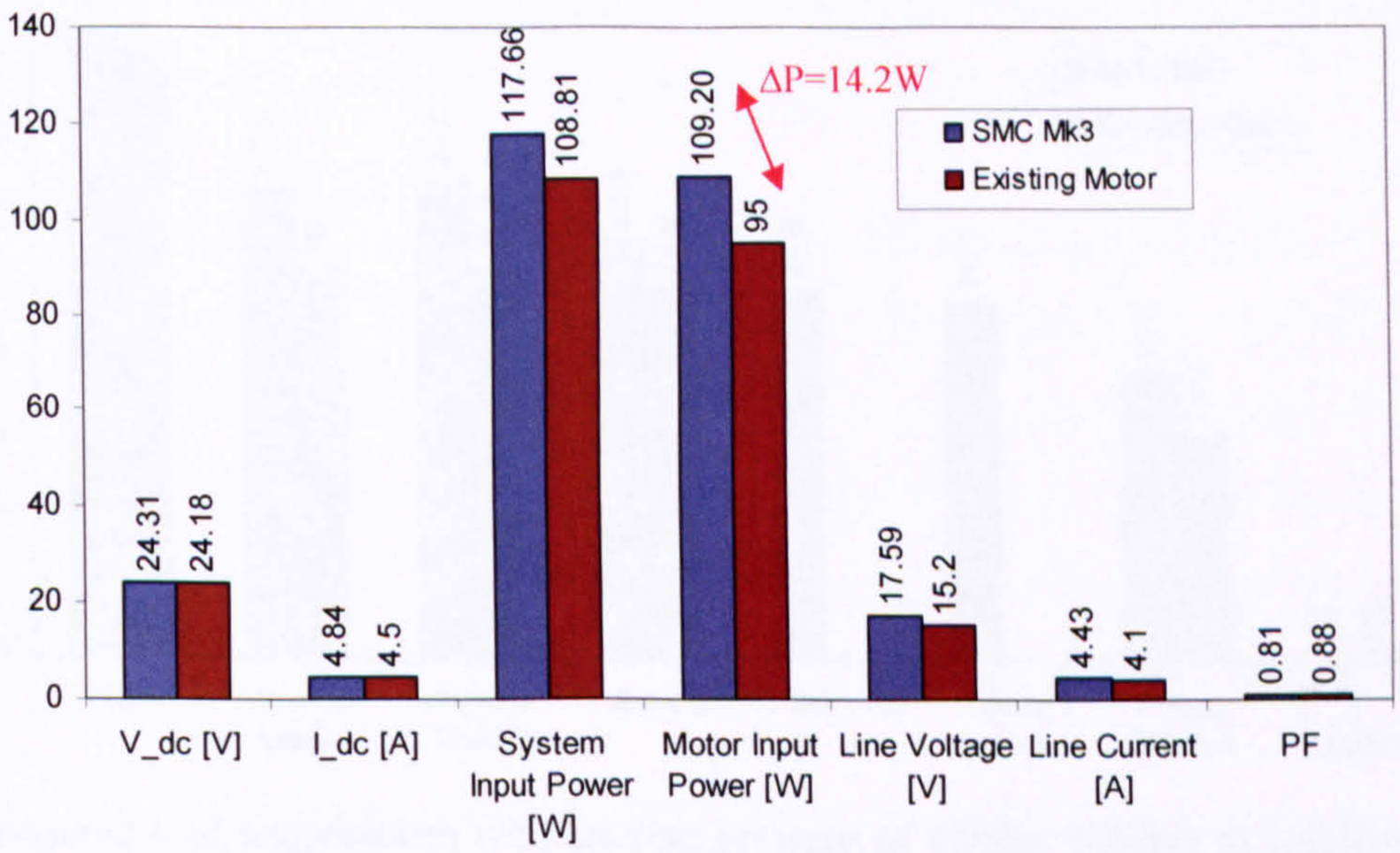

Fig. 4.9 Measured electrical parameters under load (backing pressure of 10mbar) of the SMC Mk3 motor in comparison with the existing motor (EXT250 pump with standard bearings)

4.4.4 Thermal Test Results

Fig. 4.10 and Fig. 4.11 show the various temperatures measured for both load conditions between the SMC Mk3 motor and the existing motor. The temperatures are adjusted for the ambient temperature (i.e. ambient temperature has been subtracted from the measurements) to allow better comparison.

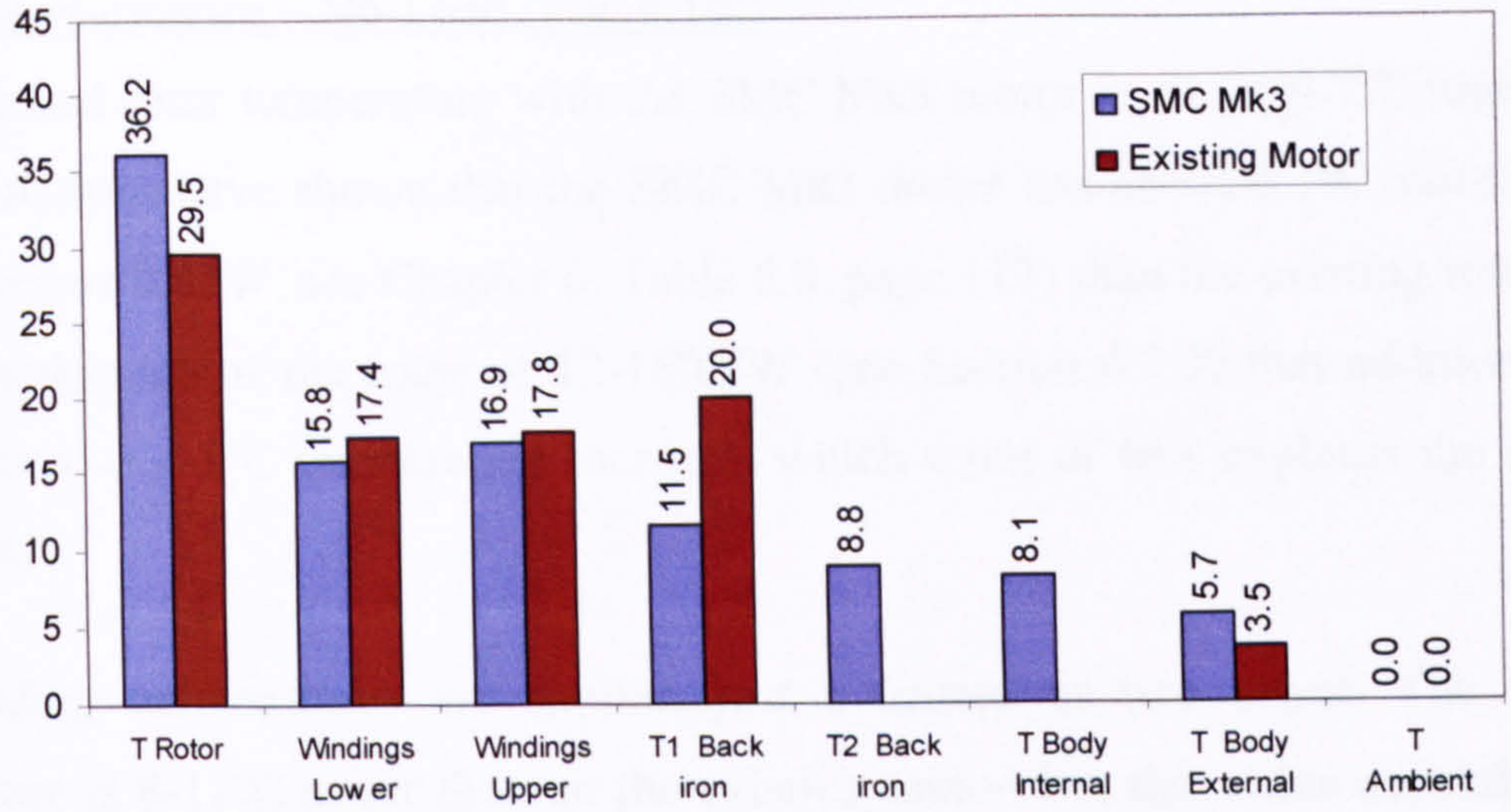

Fig. 4.10 Measured no-load temperatures (backing pressure of $5 \cdot 10^{-3}$mbar) relative to ambient temperature ($T_{ambient}$ = 27-28°C)

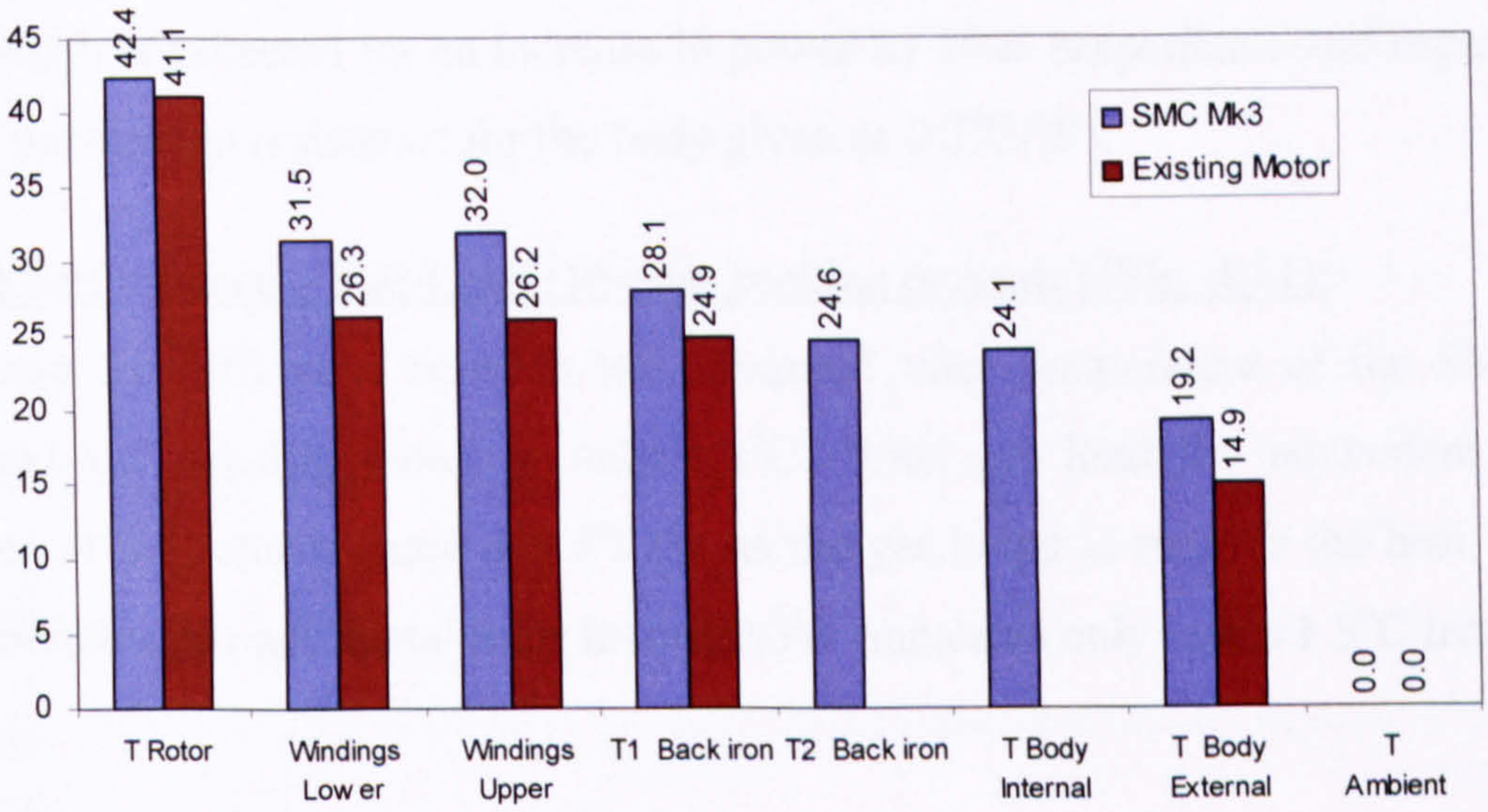

Fig. 4.11 Measured load temperatures with backing pressure of 10mbar relative to ambient temperature ($T_{ambient}$ = 26-29°C)

The interface between the motor stator and the pump body is of great importance for the removal of heat from the motor. In the existing pumps the motor has a ground outer diameter and is held in place with a grub screw. The gap between the motor stator and body can be between 24μm and 68μm (minimum / maximum tolerances). Any gap almost independent of size is bad for the thermal heat transfer, as vacuum is a very good insulator. Unfortunately in the SMC prototypes due to larger tolerances the gap can be even larger (130μm). In the final design that gap can be closed up as the SMC pressed parts have a better surface finish and tighter tolerances than machined SMC. To improve the heat transfer during testing the gap was filled with high vacuum grease (Apiezon-M-Grease). The final solution would be to glue in the stator.

Thermal Performance – No-Load (Fig. 4.10):

The measured rotor temperature with the SMC Mk3 motor is about 6-7°C higher. Rotor loss calculations have shown that the SMC Mk3 motor has about 0.3W more rotor loss (1.11W versus 0.82W, see Chapter 6, Table 6.8, page 117) than the existing rotor. With a thermal resistance of the rotor of 12-16°C/W (see Section 6.7.3) that additional loss is equivalent to a 4-5°C temperature increase, which more or less explains the difference measured.

The winding temperatures are similar, just a degree or two lower. The back iron temperature is 8-11°C lower than on the existing motor, but that value depends strongly on the interface between the stator and the housing. Filling the gap with grease on the SMC motor has certainly improved the heat transfer. This shows that the increased stator iron losses can be removed from the stator. The body temperature has been measured 2°C hotter, which is expected for an increase in power by 10W (experience and experimental value of the thermal resistance for the body given as 0.2°C/W).

Thermal Performance – Full-Load (10mbar backing pressure) (Fig. 4.11):

Under load the difference between the measured rotor temperature of the SMC Mk3 motor and the existing motor is only 1.3°C. With gas load the equivalent thermal resistance of the rotor is more like 5°C/W as the gas helps to remove the heat from the rotor. Therefore the additional rotor loss of 0.3W translates only into a 1.5°C temperature rise.

The winding and back iron temperatures have been measured higher under load. It turned out that the grease used had a very low melting point (47°C) and the back iron under load exceeded this temperature (57°C) causing the grease to melt and leaving a larger air gap around the stator than on the existing motor with the ground OD. Therefore the heat due to the increased stator iron losses could not be removed as effectively as under no load. This should not be a problem when the stator is glued into the body in the final design.

4.4.5 Is the Temperature Rise Acceptable? – Discussion of Results

The most critical temperature in the turbomolecular pump is the impeller, i.e. rotor temperature. This is typically the hottest part and its temperature has to be limited to 90°C ideally, and certainly must not exceed 100°C to avoid adversely affecting product life and reliability due to creep. Despite slightly higher rotor losses in the Mk3 design, the rotor temperature under load was only marginally hotter with 1.5°C. This is only just

beyond the measuring accuracy, but within variation from pump to pump. It is also believed that with a deep, plastic bonded magnet as initially intended and used in Mk1 instead of the thin, rare earth magnet, the rotor losses could be reduced and the temperature would be similar or lower.

The measured winding and back iron temperatures were higher under load than on the existing stator, but far off any real thermal limitation (all materials used are rated class F giving an upper limit of 150°C). The winding temperature is important as it is used as a reference to limit the impeller temperature to 90°C, and determines the set-point of the winding thermistor. Again, it should not be a problem to increase the set-point if the new motor stator runs hotter, as long as the impeller temperature is not adversely affected. Provided the thermal heat transfer from the stator to the aluminium body is improved by gluing the motor into the body, the additional heat can be removed. Long term it should be possible to reduce the stator iron loss by optimising the stator design and using press tooling that does not damage the SMC material properties.

The increase in body temperature compared to the existing design was nearly 5°C under load, which could potentially cause the impeller temperature to rise by 5°C, however no such increase was observed. So far there is no evidence that the increased stator iron losses have affected the rotor temperature adversely. But a hotter body will mean that the outer ring of the bottom ball bearing is exposed to higher temperatures. To find out if this has an effect on the life of the bearing would require many hours of reliability testing.

Despite the small differences in measured temperatures, the biggest difficulty was convincing marketing and technical authorities that the SMC motor could be an alternative motor. The biggest worry was the risk of upsetting and loosing customers due to an inferior product replacement, because the long term impact of higher losses and increased temperature was difficult to quantify.

4.4.6 Other Observations During Testing of the SMC Motor in the Pump

The pump with the SMC Mk3 motor exhibited high transmitted vibrations through its first resonance despite being balanced twice at low speed. This was unusual, but as it was the first and only pump so far with the three-tooth motor, it was not clear if this was a one off phenomenon or an inherent problem in the design. Also the pump used was an old 'customer return' pump with unknown history, so it was hoped that a pump with new parts might be easier to balance. Once passed the resonant speed the pump ran up to full

speed without any problem and testing at full speed and load was fine. For the time being this noisy run-up behaviour was noted and left for future investigations.

4.5 Commercial Aspects

Ideally a replacement motor should have the same or better overall performance. However, the main driver for this project was cost, and in this respect the quote for the SMC motor was very promising.

Absolute prices cannot be stated, as they are commercially sensitive. But to give an idea the cost of the existing motor stator is set to 1, and all other cost are given relative to this. All numbers given are only valid for this individual case study and cannot be generalised.

A unit quote was produced by one of the potential subcontractors based on an annual volume of 10,000 parts. Table 4.9 and Table 4.10 state the expected expenditure and individual cost contributions. The final cost of the motor stator would be 40.9% of the cost of the existing motor stator, a saving of over 50%.

This does not include the savings on the rotor, which are expected to be of similar order. Replacing the 10 individual slab magnets with a single ring magnet, with no flats to machine onto the shaft and less parts to assemble all contribute towards the savings.

The estimated capital expenditure on tooling and test equipment is small compared to the potential cost savings per year. The project would become profitable within a couple of months. One of the reasons that it is so favourable in this case study is the fact that the starting point, i.e. the cost of the existing motor, is high due to a monopoly of a single supplier and the labour intensive nature of the design.

ITEM	RELATIVE COST
Capital Expenditure (equipment cost incl. SMC press tooling, winding machine, resin dispensing system, solder equipment, automatic test etc)	1172
Tooling Cost (winding mandrels, forming and assembly jigs, potting jigs, test jigs, packing tray, insulator forming etc.)	109
ESTIMATED EXPENDITURE	**1281**

Table 4.9 Estimated expenditure for introducing three-tooth SMC stator (in relative units for commercial reasons. 1 unit = cost of existing stator)

ITEM	RELATIVE COST
Procured Parts (incl. SMC parts, slot liner, phase leads, thermistor, Hall pcb board, Hall sensors etc.)	0.2507
Materials (copper wire, glue, potting epoxy)	0.0067
Process Operation Costs (labour, facility & scrap cost) (wind & form, assemble teeth-backiron, insert thermistor, dress leads & sleeve & tin, assembly PCB & hall switches, glue PCB to back iron, Dynamic test, encapsulate assembly, final test & inspection, packing)	0.0735
Other Costs (overheads, depreciation, R&D, sales and admin, handling charges, profit etc.)	0.0761
TOTAL MANUFACTURING COSTS	**0.4070**
Logistics (transport and packaging)	0.0020
TOTAL PRICE EACH @ VOLUME ABOVE	**0.4090**
POTENTIAL COST SAVINGS PER YEAR FOR AN ANNUAL VOLUME OF 10,000	**5910**

Table 4.10 Cost analysis and potential savings of new three-tooth SMC stator (in relative units for commercial reasons. 1 unit = cost of existing stator)

4.6 The End of SMC?

A major review meeting was held at the end of the test phase of the SMC Mk3 motor. The project was threatened with the loss of interest and support from the company, as the performance deficit was seen as too risky.

The aim of the review meeting was to inform and present the results to date, discuss what is acceptable, and to decide whether or not to continue with the SMC technology. Also to negotiate more design freedom (should the project continue), i.e. trying to loosen the design requirements from a direct replacement motor to a more general system approach. But that meant challenging the perception of 'everything has to be the same'.

4.6.1 Results to date

The SMC Mk3 motor offers so far the best all round performance of the three SMC designs. It has very similar line resistance, inductance and back EMF to the existing motor, but it has higher power consumption due to more stator iron losses (bulk eddy currents in the SMC). Measured temperatures were only slightly higher. Commercially the potential cost savings with the segmented 3-tooth arrangement and simple coil assembly are enormous.

The question is now: How much can performance be compromised for such a significant cost saving? What does the customer really look for? Does the customer really care if the motor uses 7W or 11W or 15W? The answer is 'probably not', as efficiency has never been a requirement for turbopump motors. What is much more important and critical is that the pump does not overheat and thermally fold back under the conditions the customer is using it, and for some customers that the pump has very low transmitted vibration.

It is also believed that the losses can be reduced as shown in Mk2 if an increase in inductance with some phase advance were acceptable. A further reduction in loss can be expected when changing from prototype machining to press tooling according to Höganäs, the SMC supplier.

During the development of the prototypes Mk1 to Mk3 much experience in designing with SMC has been gained and the method of predicting the SMC iron losses has been improved (see Chapter 5). It is therefore believed that the predictions and measurements of the next SMC motor would be closer than before, allowing better optimisation at an early design stage.

4.6.2 Outcome of the Review Meeting

From the discussions it was clear that the SMC Mk3 motor would not be acceptable, as there was a fear that the additional losses of 10W or more would push the pump and/or controller into thermal foldback for certain customer applications. Customer satisfaction was seen as more important than a quick introduction of the potential cost savings. However, the cost savings were large enough to justify the development time and cost of a further optimised prototype.

It was agreed to build one more SMC motor (Mk4). This would make the most of the learning and development achieved so far. It was accepted, that the design requirements need to be better understood (i.e. what does the customer really look for), and that a system view should be adopted rather than to develop the motor in isolation from the drive. Hence, it was accepted that an increase in inductance might be required with additional phase advance in the controller to bring the iron losses down. The drive would not run with minimum current, but as long as it does not thermally fold back, it would be a way of benefiting from the potential cost savings quoted with the three-tooth design. It

was accepted that such a change would require full type testing before it could be introduced into production.

It was also agreed that plastic bonded magnets should be reconsidered, to keep the rotor losses and so the impeller temperature to a minimum.

It was decided that the investment into press tooling for the SMC parts should not be made at this stage, despite the uncertainty of damaged material properties with prototype machining methods. The view was that the performance of the prototype should be close to the required performance in spite of the damage from SMC machining. Any improvement gained by changing the manufacturing method would be an additional benefit, but should not be relied on.

It was further proposed that the motors be tested in a fully magnetic levitated pump as to avoid all mechanical bearing friction. This should give a more direct comparison of the actual motor losses, without the uncertainty of varying amounts of bearing losses from test to test and pump to pump. This will be implemented in the testing of the next SMC motor Mk4.

4.7 The Next Step

The SMC project continued. One final prototype was to be built. This time however, more time was spent in designing and optimising the motor in advance. The next two chapters look in more detail at some of the theoretical design methods used. Chapter 5 deals with the iron loss calculation of the SMC stator, and experiences gained during the first three prototypes and the contributions made to improve the iron loss predictions. Chapter 6 summarises the rotor loss calculation. The methods described in both chapters build the theoretical basis for the design of the Mk4 stator, which is described in Chapter 7.

Chapter 5

Working with SMC – Material Issues and Iron Loss Calculations

5.1 Introduction

Iron loss is very important in high-speed electrical machines yet its accurate prediction and its measurement in real machines is well known to be fraught with difficulties. In addition there is as yet little experience with the use of SMC and practical methods to measure and calculate its properties are still the subject of much uncertainty. To add to this it became clear during the project that the method of production of the SMC component is also important, with electric and magnetic properties being adversely affected when the component is not produced by a proper compaction and heat treatment cycle. In particular post-machining of compacted, heat treated components tends to reduce the permeability, increase the coercivity and (particularly if wire erosion has been used) increase conductivity

The initial iron loss calculations of the SMC stators were based on the loss per kg curves given in the data sheets. This turned out not to be very accurate: the no-load power measurements were around 75-80% higher than expected from specific core loss data (Fig. 5.1). Similar discrepancies between measured and predicted iron loss in machined SMC parts have been observed by Reinap et al. [34]. They reported an underestimation of the losses by up to 60% at only 100Hz.

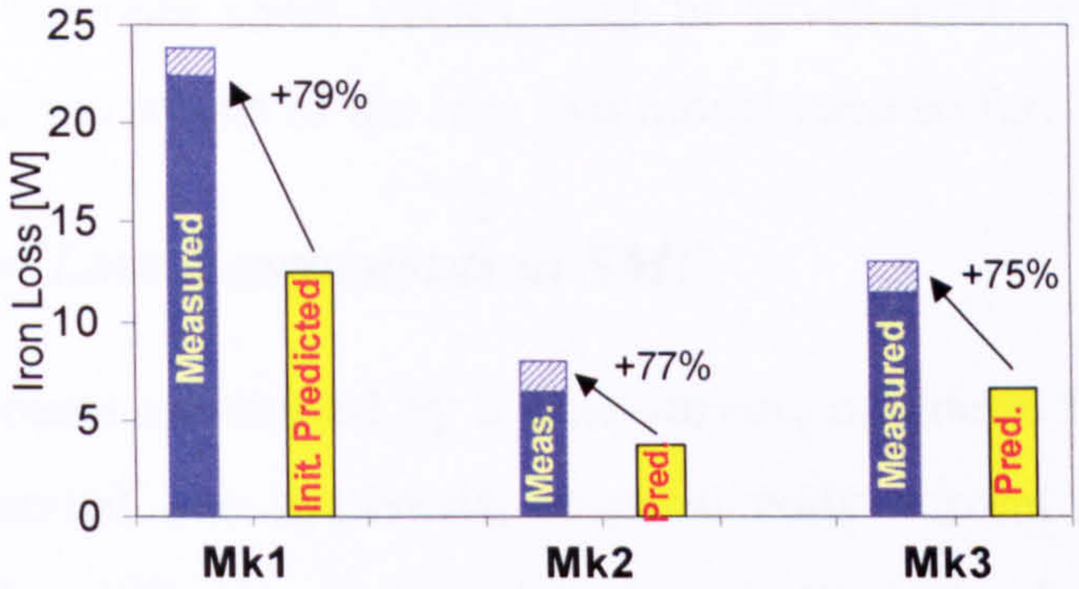

Fig. 5.1 Comparison between measured and initial predicted iron loss using total specific loss data for Somaloy500+0.5%Kenolube at 1000Hz

Using the published data as if it applied to any component effectively implies that eddy currents flowing between grains (so called bulk eddy currents) are ignored or at the very least treated very inaccurately. Taking a closer look at the loss mechanism in the SMC material, and how the core loss data is measured, the importance of bulk eddy currents and their dependency on the actual component dimensions becomes obvious. Lange [35] reported similar experience, where the size of the components had a remarkable influence on the measured iron losses at 750Hz, albeit in his case the component cross-sections were relatively large. It thus became obvious that the bulk eddy currents present in the ring sample test made by the manufacturers needed to be removed to provide material based iron loss data and that a separate calculation for the bulk eddy currents on the basis of the measured conductivity is required. The main challenge in this approach is the uncertainties in the measured conductivities.

This chapter looks at the material properties, and how they are influenced. It describes a method of calculating the iron losses in SMC components by separating material based hysteresis and eddy current losses from the bulk eddy currents taking into account the actual component dimensions. The iron losses of all three SMC motors are calculated and compared with measurement.

5.2 SMC Material Background

Before presenting the method of calculating the iron losses in SMC components, it is useful to have a good understanding of the complex situation with regards to the properties of the SMC material. Therefore, a brief definition of the loss mechanism, plus a short description of the production process and typical measurement techniques, which

are used to obtain the data sheet values, will be given first. This will also help to understand better the limitations of the iron loss model used so far.

5.2.1 Definition of Loss Components in SMC

Iron losses or core losses are caused by a time-varying magnetic field. Traditionally the core losses are separated into hysteresis, classical eddy current losses, and excess or anomalous losses. Sometimes a rotational loss component is also included. For SMC components a further subdivision of the eddy current losses is necessary into: in-grain and bulk eddy currents as shown in Fig. 5.2. A brief definition of the main loss components follows below.

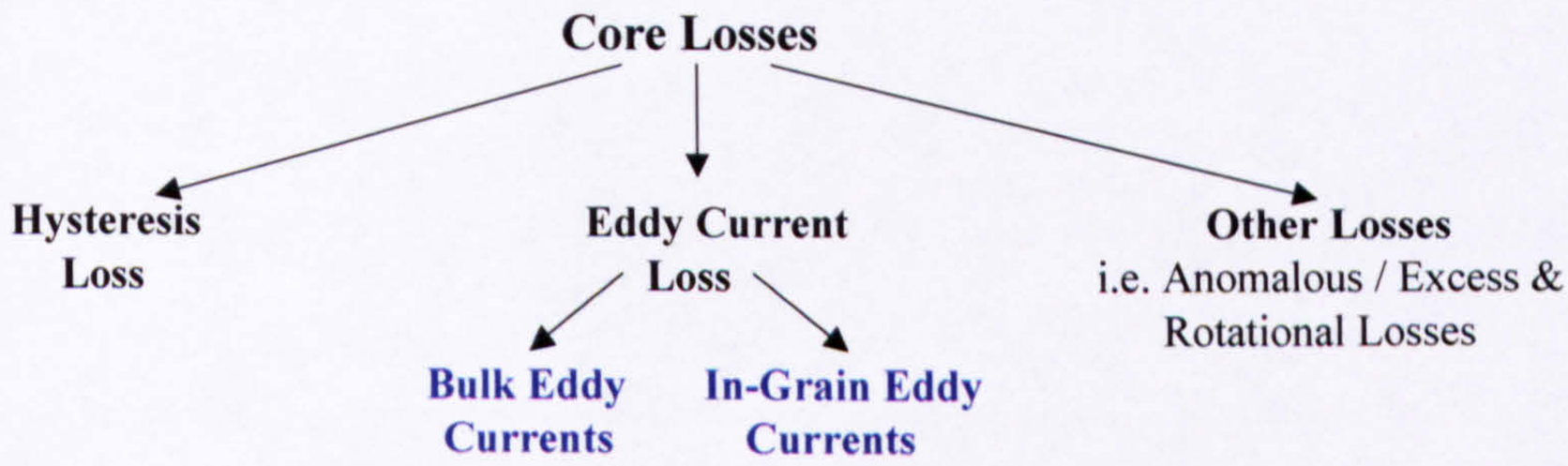

Fig. 5.2 Loss components in SMC

5.2.1.1 Hysteresis Loss

Hysteresis loss is caused by the 'resistance' of the iron to change its magnetic state in the presence of a time-varying magnetic field. It is a material property, largely influenced by metallurgical effects, and therefore independent of the size of the component. Hysteresis loss is mainly determined by the powder particle size, its metallurgical composition, physical stress and the heat treatment process. It accounts for a large portion of the losses in the SMC material due to the rather small particle size limiting domain growth, the large strains that result from compaction and the limited stress relief that is possible without damaging the particle insulation (see section 5.2.2: Effect of Process Parameters).

5.2.1.2 In-Grain Eddy Current Loss

In an ideal world the only place for the eddy currents to flow in the SMC material would be in the grain itself due to the individually insulated iron particles. These in-grain eddy current losses are a material specific property, and are not component size or shape related. Their magnitude depends on the size of the particles, and the larger the grain, the larger the in-grain eddy current loss. Due to the small size of the iron particles (typically

around 0.1mm for Somaloy500), the in-grain eddy current loss is small compared to the bulk eddy current loss as will be seen later.

5.2.1.3 Bulk Eddy Current Loss

Unfortunately, the insulation of the iron particles is not good enough to ignore currents between grains, as was initially assumed, and therefore bulk conductivity exists in most SMC parts. This bulk conductivity allows eddy currents to flow in the whole component (Fig. 5.3). The larger the bulk conductivity, the larger the bulk eddy currents. The magnitude of the bulk eddy currents also varies with the size and shape of the component. It is these bulk eddy currents that are the focus of the investigation into the cause of the large measured iron losses.

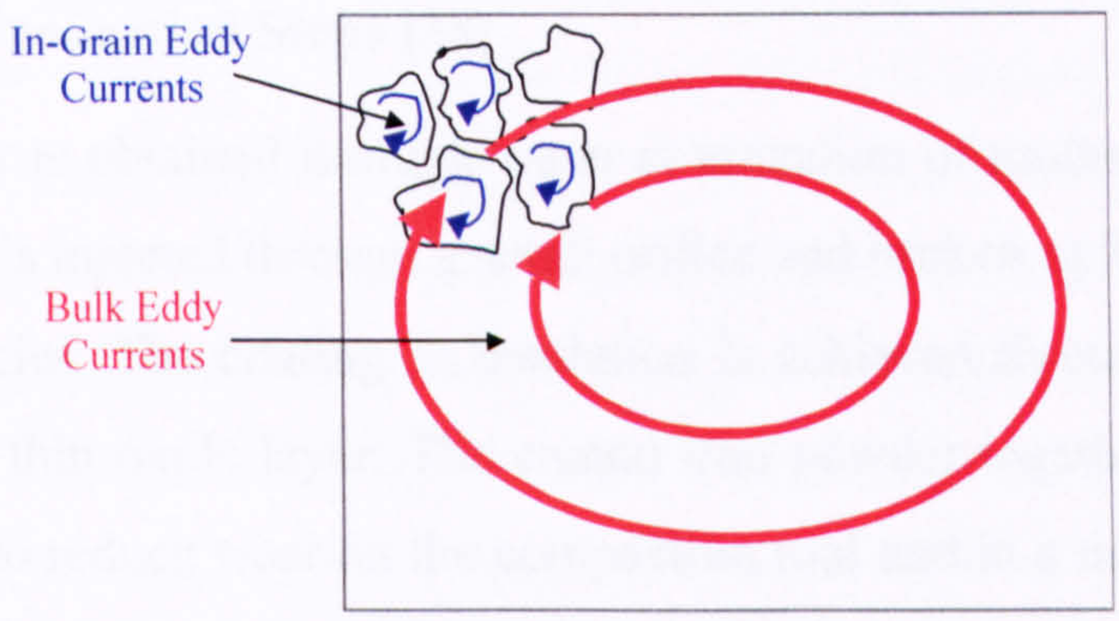

Fig. 5.3 Schematic of in-grain and bulk eddy currents in SMC

5.2.1.4 Other Losses: Anomalous and Rotational Losses

Anomalous losses are extra losses that arise from the domain and grain structure of the iron. They are very difficult to predict. Some curve fits of measured data try to separate them out from the eddy current and hysteresis losses. Typically anomalous loss is associated with frequency to the power of 1.5. In SMC in the working flux density range considered here a good fit is obtained using powers of frequency of 1 (i.e. hysteresis) and 2 (resistance limited eddy currents) and hence anomalous loss will not be considered further in this loss calculation work.

Rotational losses are the additional losses due to a rotational component of the magnetic field vector, which means the magnetic field not only changes in amplitude but also in angular direction. This is the case in the tooth tips and at the joint between the tooth body and the back iron in the motor considered here. As the flux densities in the SMC motors are low and the areas for possible rotational losses small, rotational losses will be ignored for the loss calculation in this work.

5.2.2 Effect of Process Parameters on the Material Properties of SMC

Due to continuous research and development SMC materials are improving all the time, and properties can be tuned [36, 37], by varying a combination of material and process parameters to suit different applications. The final properties of the SMC material are sensitive to several factors:

- the choice of the base powder, i.e. grain size,
- the coating material and thickness,
- the quantity and quality of the lubricant/binder, and
- the processing parameters, like compaction pressure and temperature,
- and subsequent heat treatment (temperature and duration).

5.2.2.1 Basic Production Steps [38]

The iron powder is obtained through water atomization of molten iron, a process where the liquid metal is injected through a small orifice and broken up by jets of water forming small iron particles. The coating or insulation is achieved through a chemical reaction, which creates a thin oxide layer. The coated iron powder together with some additives, e.g. a lubricant to reduce wear on the compaction tool and in a minority of applications a resin in order to increase the mechanical strength of the finished material, is then delivered into a die where the mix is compacted at high pressure and sometimes also at elevated temperatures. This 'green' or uncured material is then heat treated to complete the production process. The heat treatment has two reasons: a) to increase the final mechanical strength, and b) to provide stress relief within the material (and hence reduce hysteresis loss).

5.2.2.2 Choice of Base Powder

The smaller the grain size of the powder the lower the in-grain eddy current losses. The larger the grain size, the lower the hysteresis losses. The thicker the insulation layer the lower the bulk conductivity and hence bulk eddy current losses, but also the lower the permeability. Because of these conflicting effects it is important to select the right base powder to minimize losses in a given application.

5.2.2.3 Effect of Pressure

The pressure during the compacting process is typically between 600 and 800MPa. The higher the pressure the more dense the final product, and hence the better its space-factor

and permeability. A compaction pressure of 800MPa for Somaloy500+0.5% Kenolube will typically produce a material density of 7.3 g/cm^3 and a peak permeability in the order of 450 (for comparison: lamination steel has a density of 7.8 g/cm^3, with a space-factor normal to the flux direction of 0.96, and a peak permeability in the thousands).

5.2.2.4 Effect of Temperature

Core losses are significantly influenced by mechanical stress and strain experienced within the material. Stress relief allows the domains and grains greater freedom to align themselves to an alternating magnetic field, which minimizes the hysteresis losses. However, to fully stress relief iron temperatures in the order of 800°C or higher would be required. The maximum temperature used in curing SMC is 550°C. Anything in excess of this value will be detrimental to the insulation coating of the iron particles. Therefore SMC will always have higher hysteresis losses than conventional laminations. Also the time the temperature is applied will affect the balance between hysteresis and eddy current loss. The lower the temperature and the shorter the cycle the higher the hysteresis losses. The higher the temperature and the longer the cycle, the greater is the danger of damaging the insulation layer and therefore increasing the eddy current losses (i.e. increasing bulk conductivity).

5.2.2.5 Effect of Prototype Machining

As discussed above the material properties depend a great deal on the correct compaction and heat treatment cycle. However, dies and press tooling to compact the parts into their final shape are very expensive, and in the initial stages of a project these costs are not justified to evaluate a new SMC design. Therefore it is common practice to machine the SMC components out of pre-pressed and heat-treated blanks using mechanical machining (milling, turning) or wire erosion (EDM – electrical discharge machining).

Machining can introduce micro-cracks in the material, which reduces the permeability and increases the coercivity. As a consequence less flux enters the machine and the current in the windings needs to be increased to compensate for this, which will increase the losses. On the other hand, these micro-cracks could break the eddy current path depending on geometry and orientation.

Using EDM with high currents can cause a local heating effect damaging the particle insulation, which leads to an increase in conductivity. The more machining there is on a part the greater the material damage. Hence, thin sections are generally more affected.

This may explain why extending the tooth tips on the SMC Mk1 and Mk2 motors had little contribution in collecting flux.

To quantify the amount of damage done using prototype machining methods is difficult as it is difficult to determine the material properties of the real parts once cut due to their complex shapes. According to Höganäs [39] the permeability could be reduced by 50% in extreme cases, but 20-30% might be more likely. Measurements on conductivity have given a spread of 14,000 to 27,000 S/m for notionally the same material and manufacturing process but different component dimensions [40]. Basically every single component has its own story and consistency of final properties can only be expected on parts compacted directly into shape.

5.2.3 Typical Measurement Methods of Published Data

To allow comparison between different base powders and process parameters all measurements are carried out on a 'standard' pressed ring sample with a mean diameter of 50mm and a square cross section of 5x5mm^2. The main properties of interest are the conductivity, BH curve, permeability, and iron losses. Their measurement methods will be briefly described here as these were used later to determine the actual properties of the prototype components (see Appendix B).

5.2.3.1 Conductivity Measurement

The conductivity is typically measured using the four-point method, i.e. injecting a current into a test piece via two probes and measuring the voltage drop using two further probes attached to the test piece at points between the injection points. The difficulties with this method are the very low signal levels, as the current has to be small enough not to damage the particle insulation. It also measures only the surface conductivity, which might be different from the bulk conductivity if the material is not homogenous.

A better method is the so-called 'transformer method', where the SMC ring forms the secondary side of a transformer. The changing flux from the primary side induces a voltage, which causes a current to flow in the ring. The current can be measured with a clamp-on current probe and the voltage can be picked up with turns wound around the outside of the ring. The conductivity of the SMC ring can then be calculated taking into account the cross section area of the ring and the mean circumference. This method has better signal levels and measures the true bulk conductivity, but it requires a ring sample.

5.2.3.2 Measurement of BH curve, permeability and iron loss data

BH curve, permeability and iron loss data are usually obtained using a 'hysteresis-graph'. For this, two toroidal coils are wound around the SMC ring: one coil is the energising coil, the other coil is the sensing coil. The current in the energising coil is setting up a magneto-motive force (MMF) in the SMC ring, which is proportional to the H-field. The current is measured and shaped via an iterative system to give a sinusoidal flux. The sinusoidal flux links the sensing coil and creates a voltage, which can be measured with the sensing coil. Integrating the voltage and taking into account the cross section area of the ring, the flux density B can be calculated.

The hysteresis loops are obtained by plotting $B(t)$ as a function of $H(t)$. The 'tip' of the BH loops defines the BH curve. The enclosed area of the hysteresis loop is a measure of the total iron losses. Permeability is calculated from the maximum B and H values. The 'hysteresis-graph' allows the frequency and flux density to be varied automatically.

5.3 Proposed Approach for SMC Core Loss Calculation

5.3.1 Aim

Considering that the published iron loss data is measured on a standard ring sample, and the fact that the material has reasonably large bulk conductivity, it is clear that the published loss data is not suitable for components with different shape and size to that of the ring sample. Bulk eddy currents vary with shape and dimensions, and will need to be taken into account separately. This requires a separation of the total loss data into material based hysteresis, in-grain eddy current and bulk eddy current loss.

The aim of the work here is not to explain and accurately describe all the fundamental principles behind the losses. This has been the subject of research over several decades. Plenty of papers (e.g. [41-45]) and textbooks (e.g. [30, 46]) have been published. Accurate iron loss calculation is extremely difficult.

Instead, the aim of the work here is to find a better engineering approximation to predict the iron losses in SMC components, so that the discrepancy between predicted and measured losses is reduced.

5.3.2 Overview of the SMC Core Loss Calculation Process

The process of estimating the iron losses in real SMC components consists basically of two parts (Fig. 5.4).

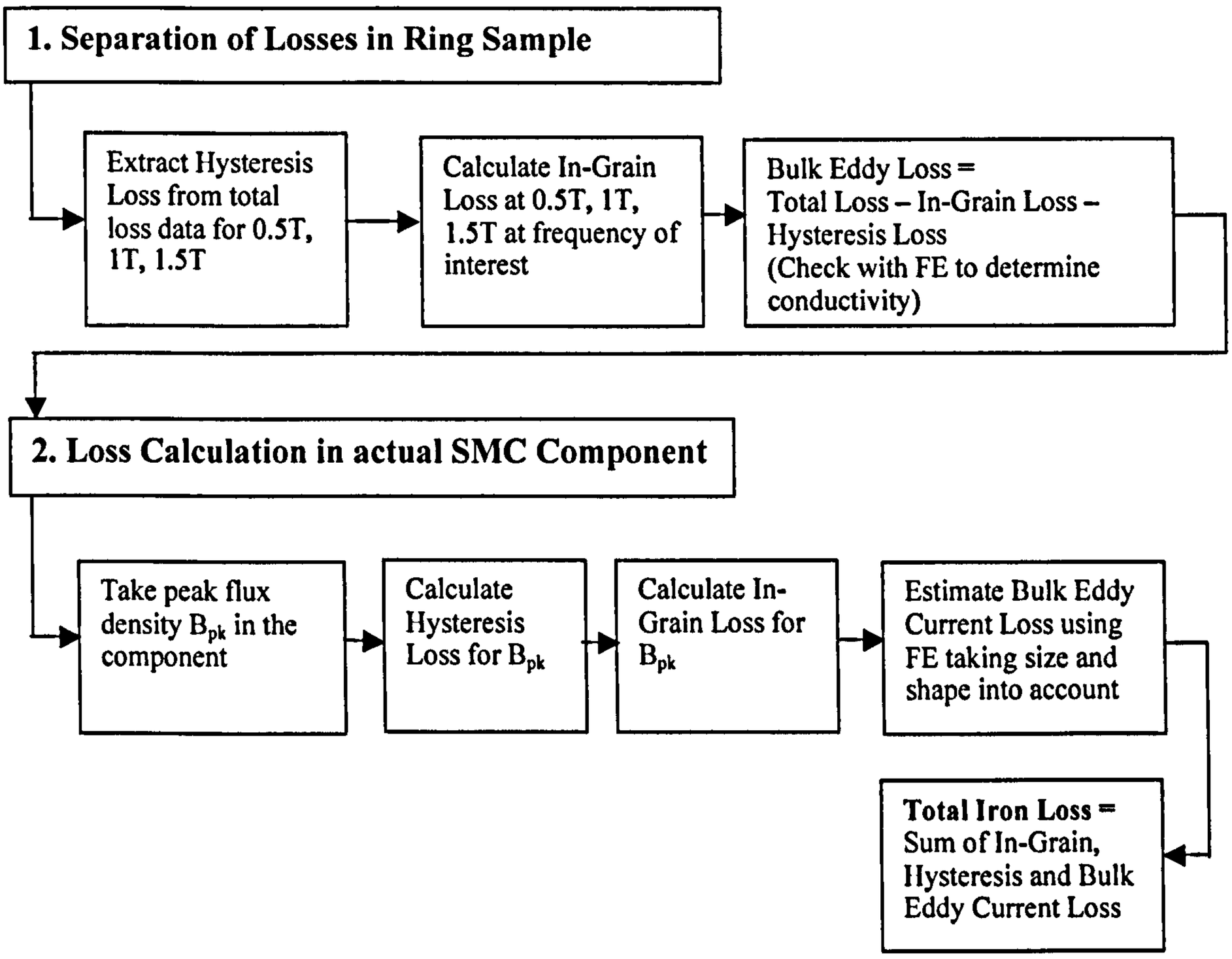

Fig. 5.4 Flow diagram of the SMC core loss calculation process

The first part deals with the separation of the measured iron losses in the ring sample into hysteresis losses, in-grain and bulk eddy current losses. The size-independent, material specific hysteresis losses, for which an equation can be obtained by fitting a curve through the data, are extracted first. The in-grain eddy currents are calculated analytically by approximating the powder particles as spherical parts. The bulk eddy current loss is what is left over, and can be simulated using finite element calculations. Matching the loss data from FE to that derived from measurement data allows an estimation of the conductivity of the SMC material.

The second part calculates the loss for the SMC component of interest as follows. First the size-independent hysteresis and in-grain eddy current losses are calculated based on the equation obtained by curve fitting and the analytical formula. The bulk eddy current loss in the actual SMC component is estimated using a time-harmonic eddy current finite element model, taking account of the size and shape of the component itself. Due to the

complex shapes of the parts (i.e. tooth body, tooth tip) analytical formulas are of limited accuracy. Using FE analysis was found to give the most realistic estimate compared with the measured losses. The total core loss of the motor is then the sum of the hysteresis, in-grain and bulk eddy current losses.

5.4 Separation of Losses in the Ring Sample

5.4.1 Hysteresis Loss

The hysteresis losses can be extracted from the total loss data supplied in the manufacturer's data sheet [23]. Fig. 5.5a shows the total losses plotted as a function of frequency for three different flux densities and Fig. 5.5b shows the same data plotted as total loss per cycle versus frequency.

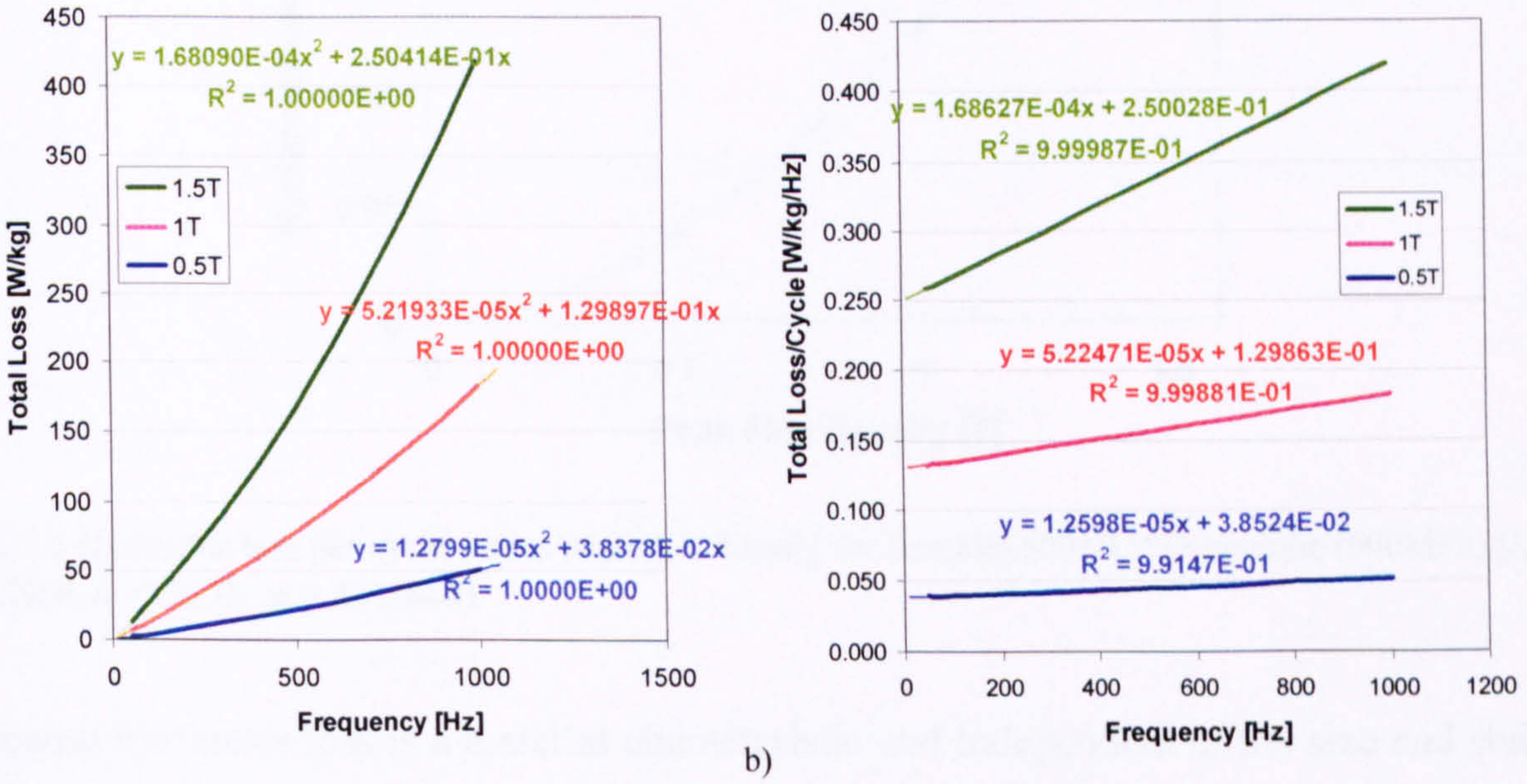

Fig. 5.5 Manufacturer's total loss data [23] for Somaloy500+0.5%Kenolube (600MPa) inclusive curve fit equations: a) total loss versus frequency, b) loss/cycle versus frequency.

It is common to approximate the total loss per kg P with the following equation, where the subscript h stands for hysteresis and e for eddy current part.

$$P = k_h \cdot B_{pk}^{(n+mB_{pk})} \cdot f + k_e \cdot B_{pk}^{2} \cdot f^2 = C_1 \cdot f + C_2 \cdot f^2 \quad \text{or} \quad P/f = C_1 + C_2 \cdot f \tag{5.1}$$

The constants C_1 and C_2 can be determined by curve fitting (see Fig. 5.5). Plotting the hysteresis loss per cycle versus the peak flux density (Fig. 5.6) and fitting a curve of the form of (5.2) [30]

$$P_h / f = k_h \cdot B_{pk}^{(n+mB_{pk})} \tag{5.2}$$

through the data, the constants k_h, n, and m can be determined (Table 5.1). It was found that a non-constant power $(n+m \cdot B_{pk})$ on the flux density gave better agreement with the hysteresis values obtained from measurement and for the eddy current loss calculation compared with FE.

k_h	n	m
0.12988	1.8255	-0.13884

Table 5.1 Hysteresis loss constants for equation (5.2) for Somaloy500+0.5%Kenolube (600MPa)

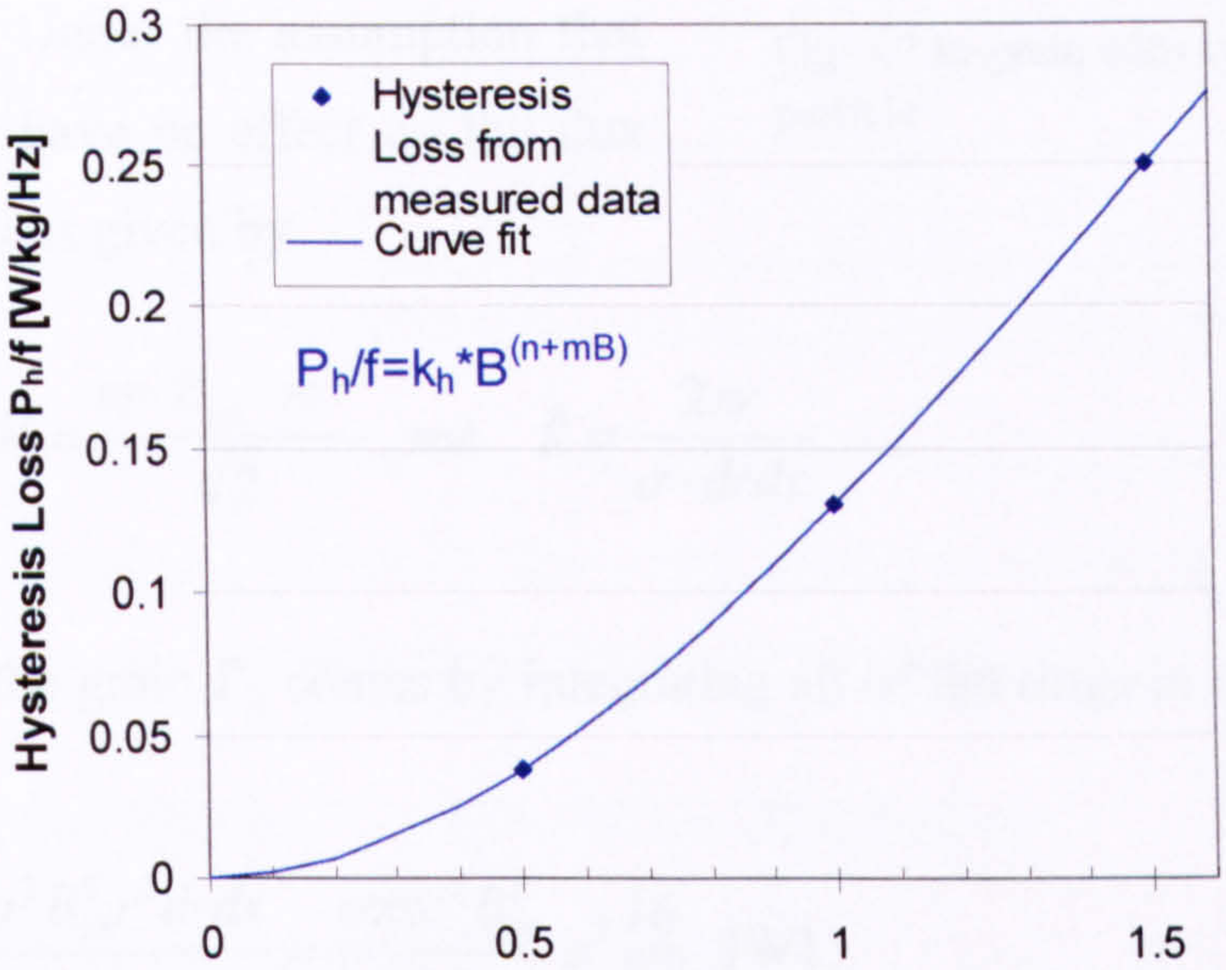

Fig. 5.6 Hysteresis loss per cycle versus peak flux density for Somaloy500+0.5%Kenolobe (600MPa) (k_h = 0.12988, n =1.8255, m = -0.13884)

Because hysteresis loss is a material characteristic and independent of the size and shape of the component, equation (5.2) with the above obtained constants can be used to calculate the hysteresis loss in the ring sample as well as in the actual SMC motor components. The hysteresis loss at a frequency of 1000Hz for three different peak flux densities is given in Table 5.2.

Peak Flux Density [T]	Hysteresis Loss @1000Hz [W/kg]
0.5	38.45
1.0	129.88
1.5	250.22

Table 5.2 Hysteresis loss for Somaloy500+0.5%Kenolube (600MPa), f=1000Hz

5.4.2 *In-grain Eddy Current Loss*

The in-grain eddy current loss can be calculated by approximating the powder iron grains as spherical parts with radius *a* (Fig. 5.7).

These particles are subjected to an alternating magnetic field of peak value B_{pk}. Eddy currents will be induced in slices transverse to the magnetic field in the shape of concentric circles of radius *r* and cross section *dr* by *dx*. Under the assumption that the eddy currents have no effect on the flux the loss in the slice is given by

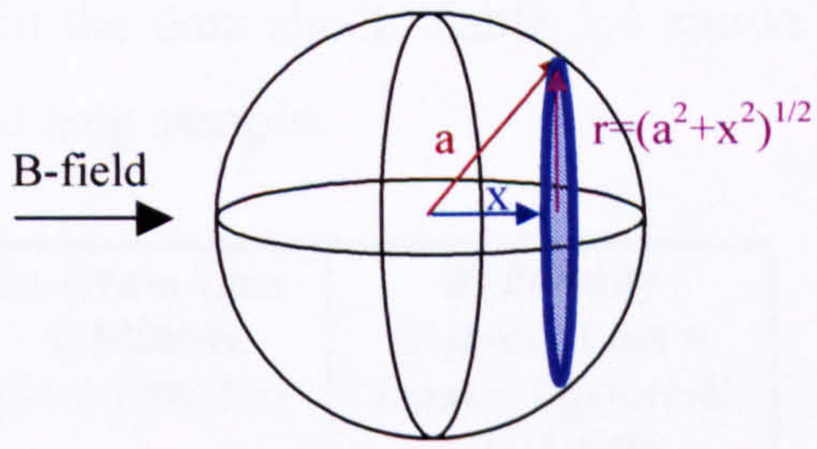

Fig. 5.7 In-grain eddy currents in spherical particle

$$\Delta loss = \frac{V^2}{R} \text{ with } V = \frac{\varpi \cdot B_{pk} \cdot \pi r^2}{\sqrt{2}} \text{ and } R = \frac{2\pi r}{\sigma \cdot dr dx} \tag{5.3}$$

The total loss in the grain P_g comes by integrating all of the rings in one slice and all of the slices:

$$P_g = \int_{-a}^{a} \int_{0}^{\sqrt{(a^2-x^2)}} \frac{\sigma \pi \varpi^2 B_{pk}^2 r^3 dr dx}{4} = \frac{\sigma \pi \varpi^2 B_{pk}^2}{16} a^5 \frac{16}{15} \text{ [W]} \tag{5.4}$$

With a volume of the sphere of $4/3\pi a^3$, the loss/m^3 and the loss/kg are then given by

$$P_g / m^3 = \frac{\sigma \varpi^2 B_{pk}^2}{20} a^2 \text{ [W/m}^3\text{]} \tag{5.5}$$

$$P_g / kg = \frac{\sigma \varpi^2 B_{pk}^2}{20\rho} a^2 \text{ [W/kg]} \tag{5.6}$$

with σ =conductivity, $\omega = 2\pi f$ =frequency of magnetic field, B_{pk}=peak flux density, *a*=radius of grain, ρ=density. For Somaloy500 the grain size is typically around 0.1mm in diameter. The in-grain loss per kg at the motor frequency of 1000Hz is, with a conductivity of the iron grain of $1.04 \cdot 10^7$ S/m and a density of 7200 kg/m^{3}as follows (Table 5.3):

Peak Flux Density [T]	In-Grain Loss @1000Hz [W/kg]
0.5	1.78
1.0	7.13
1.5	16.04

Table 5.3 In-grain eddy current loss for Somaloy500+0.5%Kenolube (600MPa), f=1000Hz

5.4.3 Bulk Eddy Current Loss

5.4.3.1 Using Total Loss Data for the Ring Sample

The bulk eddy current loss in the ring sample is obtained by subtracting the hysteresis and in-grain losses from the total loss data given in the data sheet. Table 5.4 shows the split of the total loss into its loss components for the ring sample.

Peak Flux Density [T]	**Total Loss from Data Sheet** [W/kg]	**Hysteresis Loss @1000Hz** (from Table 5.2) [W/kg]	**In-Grain Loss @1000Hz** (from Table 5.3) [W/kg]	**Bulk Eddy Current Loss = Total – Hysteresis – In-Grain** [W/kg]
0.5	51.2	38.45	1.78	10.97
1.0	182.1	129.88	7.13	45.09
1.5	418.5	250.22	16.04	152.24

Table 5.4 Separation of Losses for Ring Sample of Somaloy500+0.5%Kenolube (600MPa), f=1000Hz

These numbers are only correct for the ring sample. The bulk eddy current loss for the actual motor components needs to be calculated separately (section 5.5.4), because the bulk eddy currents vary with the size and shape of the component.

5.4.3.2 Using Finite Element Analysis for the Ring Sample

The bulk eddy current loss in the ring sample can also be calculated using FE analysis. A 2D axis-symmetric model (Fig. 5.8) has been set up for the ring sample using Comsol/Femlab [47]. The model application mode chosen is a quasi-static, magnetic, time-harmonic model with in-plane induced currents, solving equation (5.7) [47] for the vector potential $\overline{A}$,

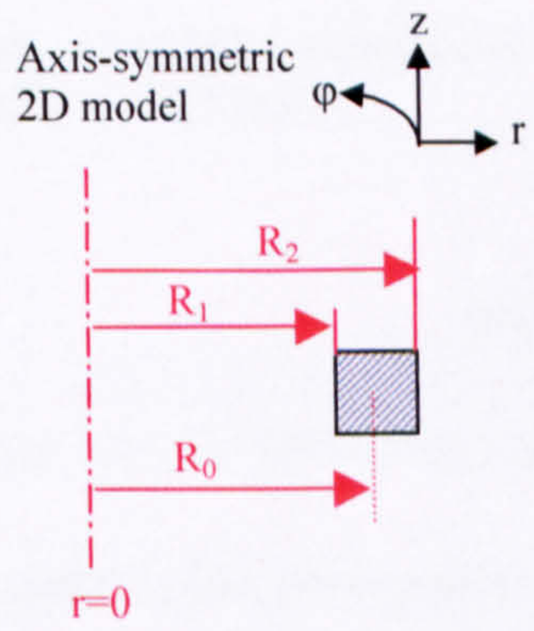

Fig. 5.8 FE model set-up for 'ring sample'

$$\left(j\varpi\sigma - \varpi^2\varepsilon_0\varepsilon_r\right)\overline{A} + \nabla\times\left(\frac{1}{\mu_0\mu_r}\cdot\nabla\times\overline{A}\right) = \overline{J}_e, \tag{5.7}$$

where J_e = external applied current density (in our case J_e=0). The applied flux is in the direction of the φ-axis and the induced currents appear in the r-z plane. This model takes the effect of the eddy currents on the applied field into account. The relative permeability μ_r varies with B, but the model uses an approximation where the value of μ_r corresponding to the average value of B in the ring is used throughout.

During the measurement of the iron losses in the ring (see section 5.2.3.2), the driving force is a sinusoidal flux (controlled by the hysteresis-graph). This can be approximated in the FE model by fixing the H-field around the edges. Due to the circular shape the magnetic field strength is larger at the ID than at the OD, and varies linear with the radius. The boundary condition is therefore

$$H_{\varphi 0} = \frac{B_{pk}}{\mu_0 \cdot \mu_r} \cdot \frac{R_0}{r} \text{ with } R_0 = mean\ \ radius = \frac{R_1 + R_2}{2} \tag{5.8}$$

As long as the losses are resistance limited, the applied magnetic field strength $H_{\varphi 0}$ is enough. If the eddy currents have any effect on the applied field, then more magnetic field strength is applied until the average flux density of the solution is as intended. Fig. 5.9a shows the flux density plot for 1T average at 1000Hz and Fig. 5.9b the corresponding real and imaginary parts of the B-field. Without the effect of the eddy current, the lines would be completely straight. The curvature indicates that some (rather small) skin effect is happening.

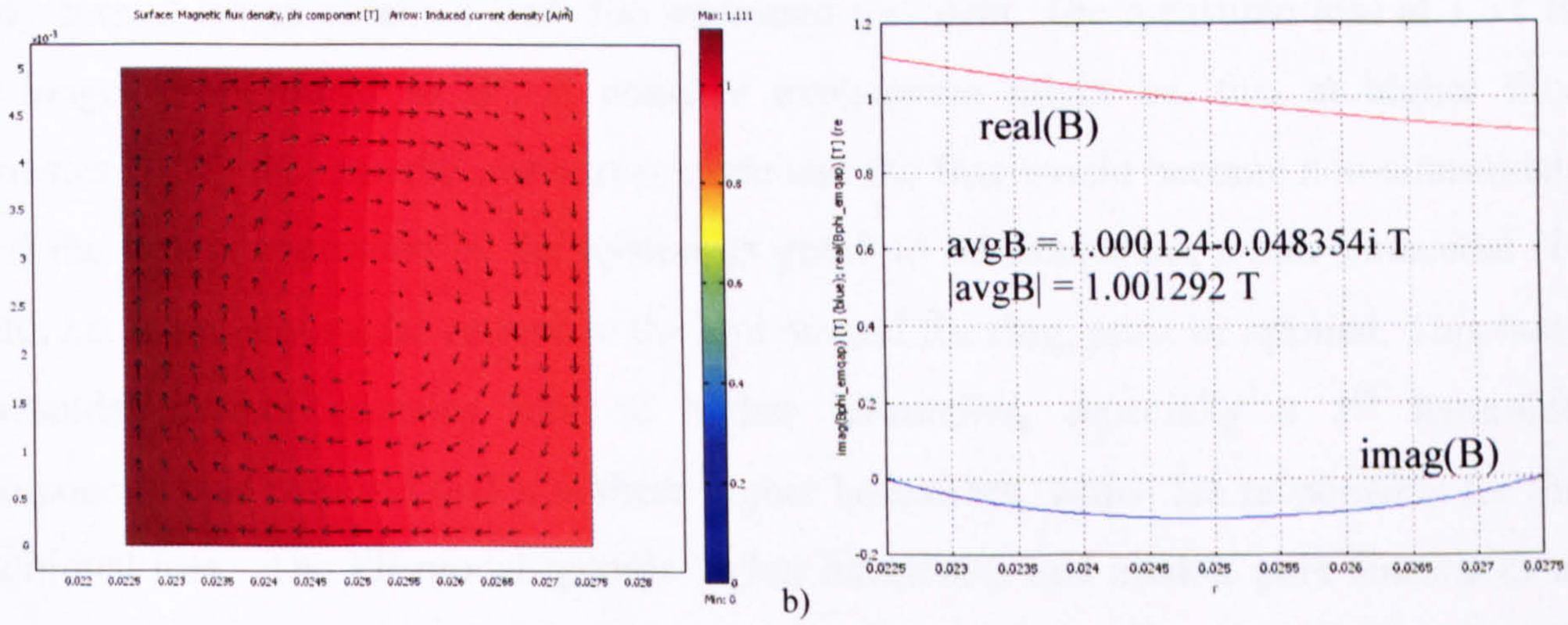

Fig. 5.9 Standard 5x5 mm test ring with 1T average field density applied: a) flux density plot; b) real and imaginary component of B-field in across middle of ring.

The bulk eddy current loss P_e per unit length is calculated from the induced current density J_i by integrating over the domain area and dividing by the conductivity (5.9).

$$\frac{P_e}{l_a} = \frac{1}{2 \cdot \sigma} \cdot \iint_A |J_i|^2 \cdot da \quad \left[\frac{W}{m}\right] \tag{5.9}$$

Due to the axis-symmetric nature of the model a volume integral can be carried out to obtain the loss in Watts of the ring itself. To be able to compare these bulk eddy current losses with the losses obtained from the manufactures data in W/kg, this loss value (in W) needs to be divided by the mass of the ring.

With a known conductivity the losses can be calculated, or vice versa the conductivity can be estimated by adjusting it until the modelled losses equal the measured losses. To match the losses at 1T for Somaloy500+0.5%Kenolube (600MPa) (Table 5.5) a conductivity of 18,800 S/m is required. This is a credible value compared with the conductivity data in [40] ranging from 14451 to 27370 S/m.

Peak Flux Density [T]	**Bulk Eddy Current Loss (from measurement) = Total – Hysteresis – In-Grain [W/kg]**	**Bulk Eddy Current Loss from FE with σ =18,800 S/m δ=7200 kg/m^3 [W/kg]**	**Ratio of FE to 'measured' losses**
0.5	10.97	11.25	1.03
1.0	**45.09**	**45.09**	**1.00**
1.5	152.24	101.36	0.67

Table 5.5 Comparison of bulk eddy current loss obtained from total loss data and FE analysis, for Somaloy500+0.5%Kenolube, f=1000Hz.

The FE calculated values for the eddy current loss agree very well for 0.5T and 1T, but not for 1.5T. The losses at 1.5T are underestimated by more than 30% compared to the eddy current losses obtained from the measured loss data. The measured loss at 1.5T is no longer proportional to B^2. A possible explanation might be, that at higher flux densities (1.5T) the material starts to saturate and the flux would become non-sinusoidal, or if the flux is controlled by the hysteresis graph to be sinusoidal, a non-sinusoidal H-field, i.e. a non-sinusoidal current in the coil around the ring, must be applied. This non-sinusoidal current contains lots of higher harmonics, especially a 3rd harmonic component. It is believed that it is these higher harmonics, which are responsible for the additional loss. The FE model ignores higher harmonics and models pure sinewaves at the fundamental frequency of 1000Hz, and therefore underestimates the losses. This is not ideal, but as the SMC motors in this thesis are typically operating at flux densities below 1T, the bulk eddy currents will be calculated accurately using time-harmonic FE analysis.

5.4.4 Split of Total Loss in the Ring Sample

Fig. 5.10 shows the breakdown of the losses for the ring sample at 1T (values in Table 5.4). Hysteresis loss is the largest component at 71%. Bulk eddy current loss accounts for 25% and in-grain eddy current loss for 4%. This ratio will change significantly in the real SMC motor stator where bulk eddy currents play a significant role.

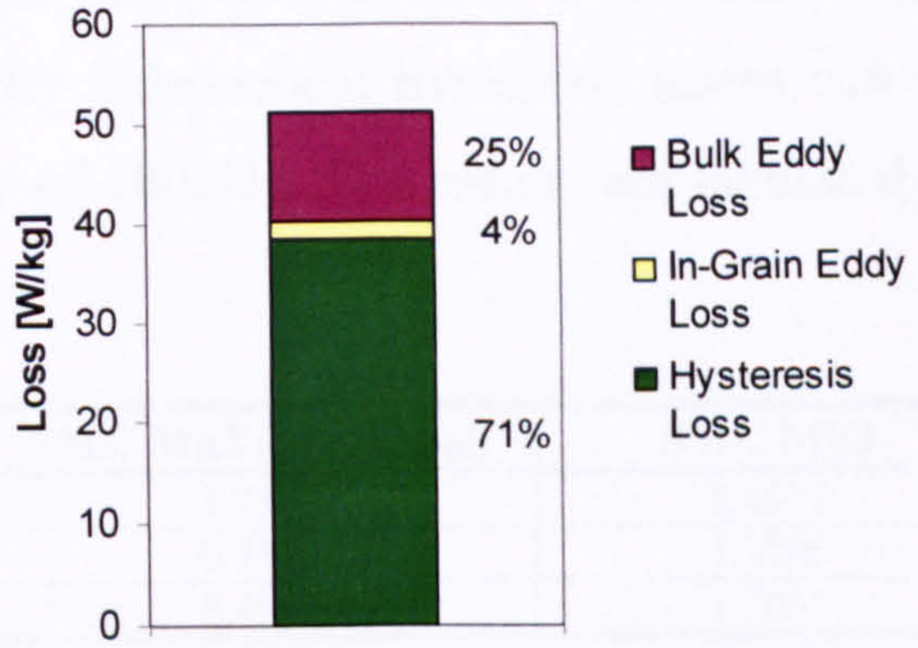

Fig. 5.10 Breakdown of core losses in the standard 'ring sample'

5.5 No-load Core Loss Calculation for Actual SMC Stators

5.5.1 Preparation: Peak flux Density in Different Regions of the Stator

As before the motor stator is divided into three distinct regions – the back iron, the tooth body and the tooth tip. For each region a peak flux density will be chosen from static, radial, 2D-FE flux density plots for distinct rotor positions. For no-load the motor is modelled in open circuit, i.e. without current in the windings. Selecting one peak flux density to be representative of one particular area is only an approximation. However, an element-by-element analysis for one full rotation is time consuming and due to the uncertainties in the material properties of the magnet and the SMC not really justifiable. Table 5.6 shows the peak flux densities for each region for all three SMC motors as used in the following loss calculations. It also summarises the volume and mass of each part, which is used to calculate the loss in Watts from the W/kg values.

	SMC Mk1.1	**SMC Mk2** (remagnetised)	**SMC Mk3**
B_{pk} – back iron [T]	0.38	0.22	0.27
B_{pk} – tooth body [T]	0.68	0.33	0.55
B_{pk} – tooth tip [T]	0.51	0.26	0.66
volume – back iron [m3]	3.26E-05	2.77E-05	2.77E-05
volume – one tooth body [m^3]	1.67E-06	1.90E-06	1.40E-06
volume – one tooth tip [m^3]	1.96E-06	1.96E-06	8.84E-07
mass – back iron [kg]	0.2345	0.1995	0.1995
mass – one tooth body [kg]	0.0120	0.0137	0.0101
mass – one tooth tip [kg]	0.0141	0.0141	0.0064

Table 5.6 Summary of peak flux density, volume and mass of each region for all three SMC motors (mass based on density of Somaloy500 @600MPa = 7200 kg/m^3)

5.5.2 *Hysteresis Loss in the Actual SMC Stators*

Using the peak flux densities from Table 5.6 and equation (5.2) with the constants k_h, n and m for Somaloy500 (Table 5.1) the geometry independent hysteresis losses can be calculated for the motor fundamental frequency of 1000Hz. The results are tabulated in Table 5.7.

	SMC Mk1.1	**SMC Mk2** (remagnetised)	**SMC Mk3**
P_h – back iron [W]	5.4801	1.7107	2.4932
P_h – 3 x tooth body [W]	2.3967	0.7424	1.3796
P_h – 3 x tooth tip [W]	1.6841	0.4928	1.2061
Total Hysteresis Loss [W]	**9.56**	**2.95**	**5.08**

Table 5.7 Hysteresis loss in the three SMC stators

5.5.3 *In-Grain Eddy Current Loss in the Actual SMC Stators*

The in-grain eddy current losses are also size and shape independent. Using the peak flux densities from Table 5.6, and the typical grain radius and conductivity for Somaloy500 the in-grain eddy current losses can be calculated using equation (5.6). The results are summarised in Table 5.8. As expected the in-grain eddy current losses are very small, contributing less than 0.5W.

	SMC Mk1.1	**SMC Mk2** (remagnetised)	**SMC Mk3**
$P_{In\text{-}Grain}$ – back iron [W]	0.2414	0.0688	0.1037
$P_{In\text{-}Grain}$ – 3 x tooth body [W]	0.1186	0.0319	0.0652
$P_{In\text{-}Grain}$ – 3 x tooth tip [W]	0.0784	0.0204	0.0593
Total In-Grain Eddy Current Loss [W]	**0.44**	**0.12**	**0.23**

Table 5.8 In-Grain Eddy Current Loss in the three SMC stators

5.5.4 *Bulk Eddy Current Loss in the Actual SMC Stators*

The bulk eddy current loss is the size and shape dependent loss component. A full 3D time-stepping model would be required to correctly represent the bulk eddy currents and the changing flux paths in the tooth tips, the tooth body, and at the joint between the back iron and the tooth body. However, as a first approximation and for reasons of simplification (engineering approximation), all three parts – back iron, tooth body, and tooth tip – will be modelled separately in 2D with a time-harmonic FE analysis, and a fixed, idealised flux path. The back iron is modelled like the ring sample. It is represented in a 2D axis-symmetric FE model with the field in φ-direction and the currents in the r-z plane. For the tooth body and tooth tip the field is in the z-plane, with

the currents developing in the x-y plane. In each case, the applied magnetic field strength at the boundaries will be chosen so that the average flux density of the solution is equal to the flux densities in Table 5.6.

Fig. 5.11 shows the geometries and dimensions used in the eddy current FE models. The flux paths in the tooth tip are approximated by modelling the tooth tip in three parts: one middle part where the flux goes straight into the tooth body, and two side parts where the flux is turning and flowing along the length towards the middle portion.

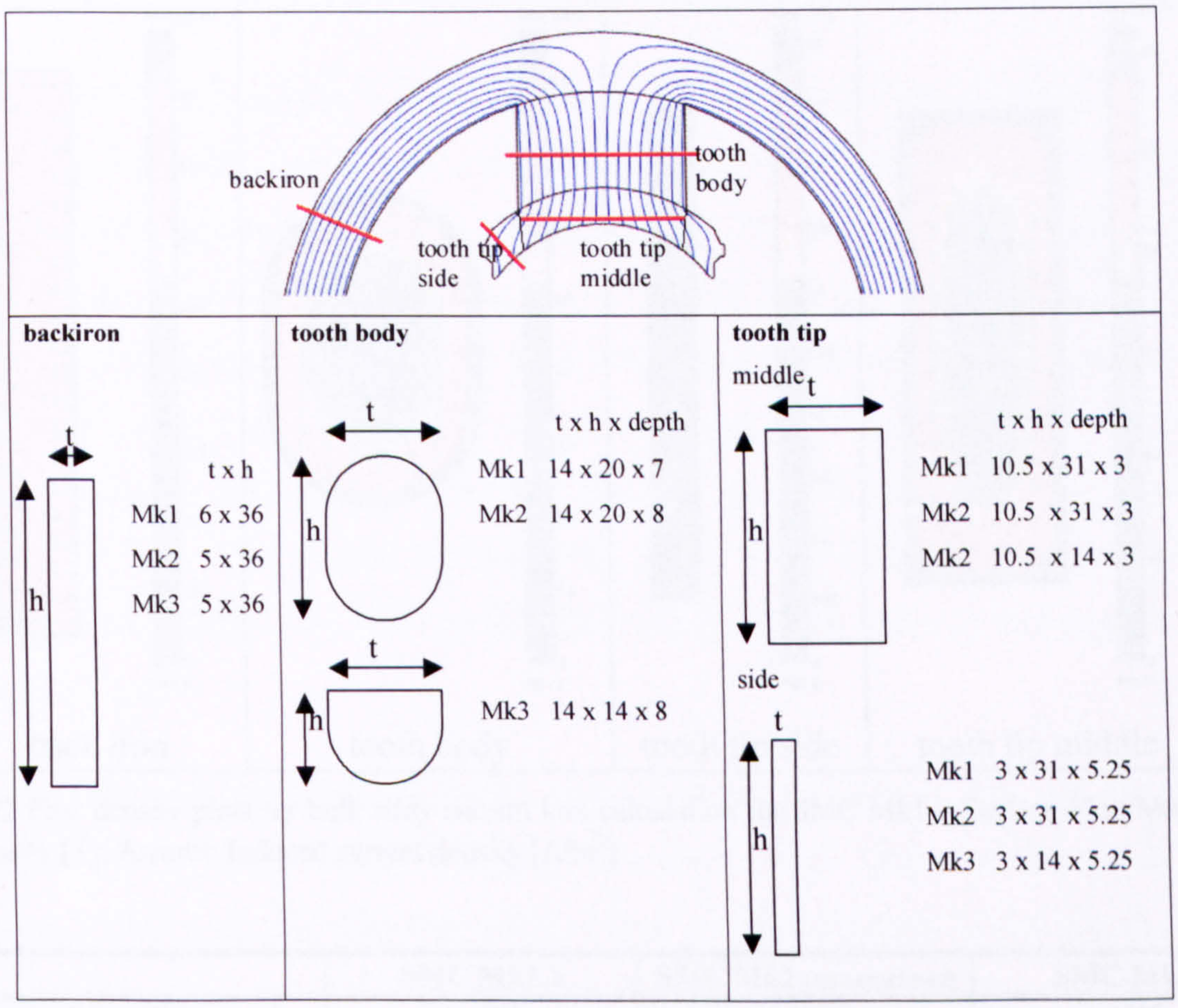

Fig. 5.11 Geometries and dimension used for bulk eddy current loss calculation of the SMC stators

The greatest uncertainty in calculating the bulk eddy currents comes from the conductivity, as it is very difficult to determine what the conductivity of the actual part is. Experience with the material has shown that the conductivity can vary enormously from one part to another [40]. As the back iron is ring shaped like the test sample rings it is possible to measure the conductivity directly using the transformer method (see Appendix B). The resulting average conductivity was 22,115 S/m. This is slightly higher than the 18,800S/m derived from the ring sample by matching the losses, but still within the spread reported in [40] (14,451-27,370 S/m). The measured conductivity of 22,115 S/m will be used for the bulk eddy current loss calculation of the actual SMC

components. The relative permeability was also measured (Appendix B) and a peak value of 450 confirmed. With these values the skin depth at 1000Hz is about 5mm, which is the thickness of the back iron, but significantly smaller than the smallest tooth body dimension (14mm) or tooth tip middle part (10mm). Hence, the flux will be skin limited in the tooth body and tooth tip middle part as can be seen for example in the flux plots for the SMC Mk1 motor (Fig. 5.12). The calculated bulk eddy current losses are summarised in Table 5.9.

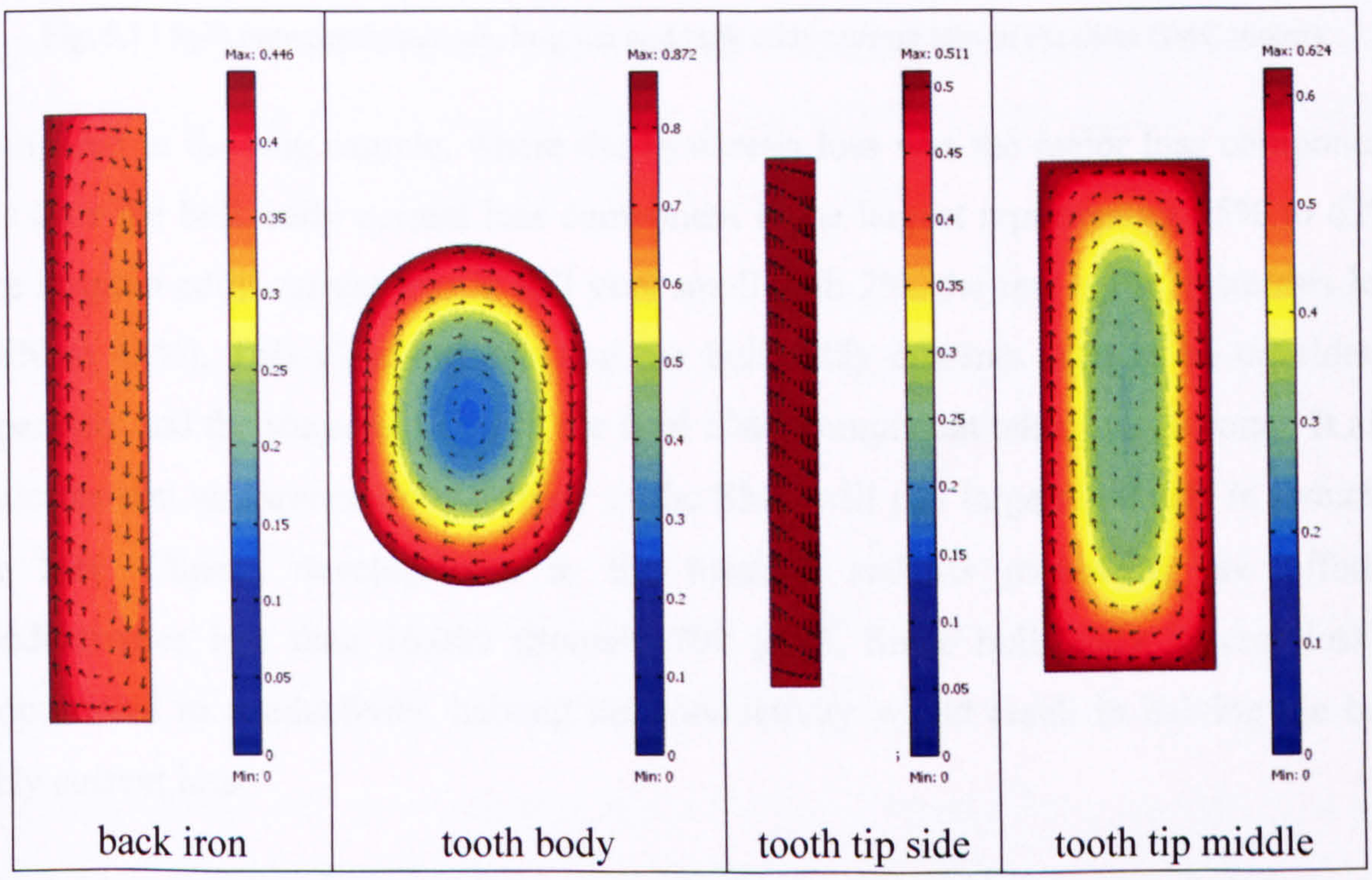

Fig. 5.12 Flux density plots for bulk eddy current loss calculation for SMC Mk1 – Surface Plot: Magnetic flux density [T]; Arrows: Induced current density [A/m^2]

	SMC Mk1.1	**SMC Mk2** (remagnetised)	**SMC Mk3**
$P_{Bulk\ Eddy}$ – back iron [W]	5.4051	1.1026	1.6556
$P_{Bulk\ Eddy}$ – 3 x tooth body [W]	8.4115	2.2431	3.4415
$P_{Bulk\ Eddy}$ – 3 x tooth tip middle [W]	2.3019	0.5991	1.2181
$P_{Bulk\ Eddy}$ – 6 x tooth tip side [W]	0.2345	0.0610	0.1633
Total Bulk Eddy Current Loss [W]	**16.35**	**4.01**	**6.48**

Table 5.9 Bulk eddy current loss in the three SMC stators

5.5.5 Total Loss in the Actual SMC Stators

Fig. 5.13 shows the split between hysteresis, in-grain and bulk eddy current loss in the three SMC prototype stators.

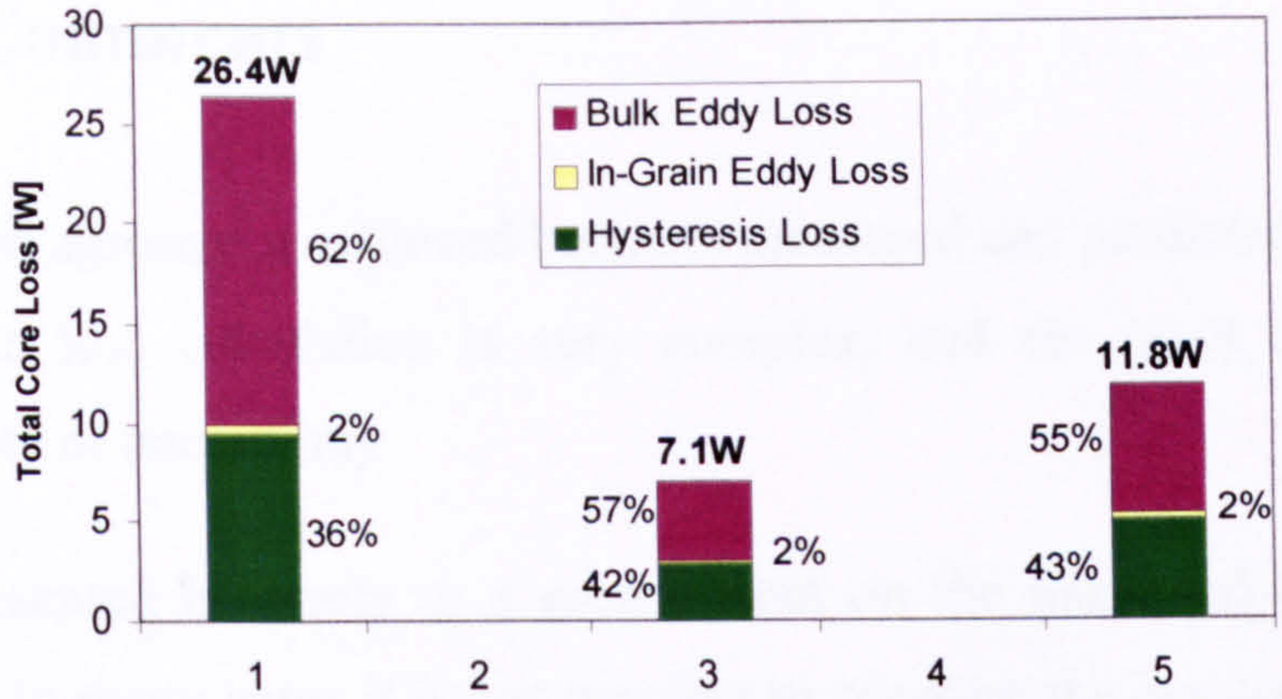

Fig. 5.13 Split between hysteresis, in-grain and bulk eddy current loss in the three SMC motors

Compared to the ring sample, where the hysteresis loss was the major loss component, this time the bulk eddy current loss component is the largest representing 55% to 62%. The in-grain eddy current loss is still very small with 2%, the rest is the hysteresis loss (36% to 43%). This clearly shows that the bulk eddy currents need to be considered separately and the shape and size of the final SMC component taken into account. It also indicates that an increase in resistivity of the SMC will pay large dividends in reducing the loss. Current developments in the material and its processing are offering conductivities less than 10,000 (Somaloy700 [23]). Since bulk eddy current loss is proportional to conductivity, halving the conductivity would result in halving the bulk eddy current loss.

Fig. 5.14 shows that the predicted losses, which take the component size and shape into account, compare much better with the measured losses than did the initial loss prediction, which used total loss data sheet values. The re-calculated losses are all within 20% of the measured results for all three machines, which is as good as can hoped for given the uncertainties in the material properties due to the prototype machining.

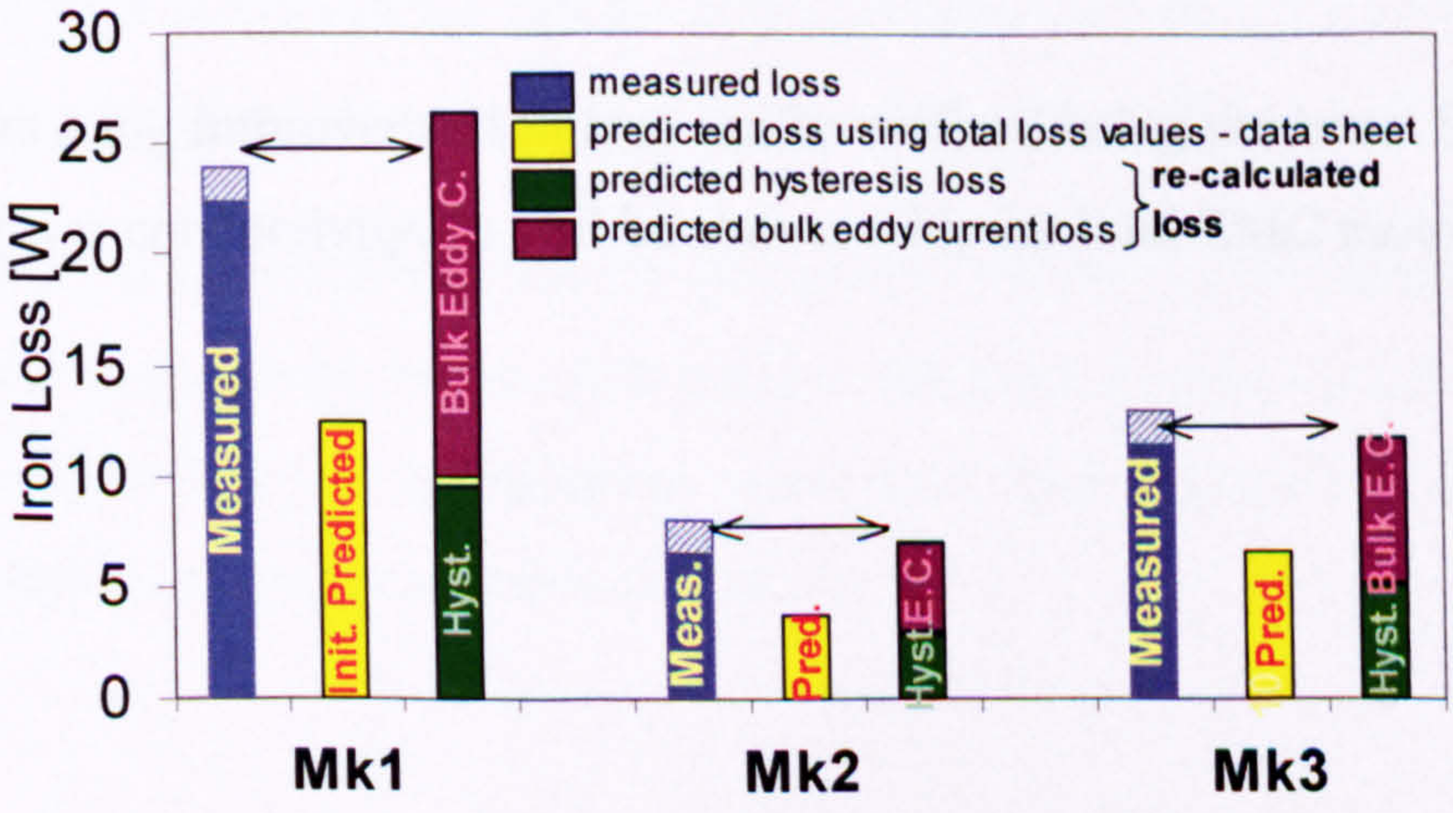

Fig. 5.14 Comparison between measured, initial prediction, and re-calculated iron loss of all three SMC stators

5.6 Final Comments

Despite the good agreement achieved between measured and predicted iron losses in Fig. 5.14, exact iron loss calculation is very complex, and the input data in most cases includes a degree of uncertainty.

The results presented here rely to a great extent on the measured conductivity of the back-iron ring. In many cases it is not possible to measure the conductivity of the actual component, and one has to use a 'typical' value, which could be anything between 14451 and 27370 S/m. As losses are proportional to 1/conductivity, any error in conductivity will translate directly into the same uncertainty in the losses.

The second factor in the loss calculation here is the peak flux density. As the eddy current losses are proportional to B^2, any error in the flux density will be doubled in the loss error.

A further uncertainty arises from the assumption that the material is isotropic. Höganäs indicate [39] that the material could show some directionality caused by the compaction pressure and direction, but so far this is not quantifiable.

The most reliable way in determining the losses is to measure them, but this costs time and money. Therefore, a simple or at least manageable method of loss calculation has been presented, which enables the motor losses to be predicted at the design stage. The method, considering bulk eddy currents separately, yields results which are within 20% of measured values for the motors tested here. This represents a significant improvement on the methods used previously in this project and is probably as accurate as could be hoped for given the uncertainties discussed above.

In these motors a big improvement in loss can be realised using the latest SMC material, which has a lower conductivity, as will be shown with the final SMC motor described in Chapter 7.

Chapter 6

Rotor Losses

6.1 Introduction

Permanent magnet brushless machines equipped with surface mounted magnets are usually considered to have negligible rotor loss, since the rotor rotates in synchronism with the fundamental stator MMF. However, due to time and space harmonics of the stator MMF and stator salient magnetic structure (e.g. teeth), especially in motors with concentrated, short-pitched windings, significant eddy current loss may be introduced in the rotor [48-51].

In general, the rotor eddy current loss is relatively small compared with the stator iron losses and copper losses. Nevertheless, it may cause significant heating of the rotor, especially in a vacuum, where the heat dissipation from the rotor is very poor. To avoid demagnetisation of the magnets or weakening of the impeller material for reasons of material stress and fatigue, the impeller temperature is limited to 100°C. Avoiding exceeding this limit is critical for the life and reliability of turbomolecular pumps, and therefore it is important to keep any losses in the rotating assembly to a minimum.

A common belief at Edwards was that the motor rotor losses were the dominant factor in raising impeller temperature, but no calculations had been carried out to estimate these losses. This chapter looks at the different motor rotor loss mechanisms and uses finite element calculations to quantify their contribution.

6.2 Sources of Motor Rotor Loss

Any non-synchronous variation in the magnetic field, which the rotor is subjected to, can introduce eddy currents in the rotor. These eddy currents create losses in any electrically conducting part of the rotor like the shaft, magnets, or a conductive sleeve.

The magnetic field variations can be the result of

a) the stator winding distribution, i.e. the way the windings are placed in the stator slots, which cause space-harmonics [52-55],

b) the non-sinusoidal time varying phase currents, which result from six-step commutation and PWM, causing time-harmonics [52, 55-58],

c) variations in the air gap flux density driven by the magnet due to slotting, causing so called tooth ripple [59-62],

d) saturation of the magnetic circuit, i.e. tooth tips, tooth body or back iron under load, causing variations in the flux path, creating non-sinousoidal flux components [61, 62].

To model all these effects together would require a non-linear, time-stepping finite element model, which is both time consuming and complex. A simpler approach is to model each mechanism separately and then add the results together afterwards. This superposition is reasonably valid as long as the rotor does not reach flux density levels, which push the material into saturation.

The loss mechanism a) to c) will be analysed in more detail in the next sections, whereas d) is not considered here, because the saturation of the stator iron parts is not an issue in these motors. The flux density in the stator iron parts is low, typically not exceeding 1T under load, therefore not causing any variations in the flux path between rotor and stator.

6.3 Rotor Loss due to Space Harmonics

6.3.1 Harmonic Components and Winding Factors of Magnetic Field H_t

The winding of a phase is usually distributed over a finite number of slots in the stator. As a result, when current (assuming sinusoidal current for the moment – for non-sinusoidal current see the next section 6.4 on Time Harmonics) is flowing through the windings the magneto-motive force (MMF) produced is non-sinusoidally distributed in the air gap. The MMF and hence the magnetic field strength therefore consist of fundamental and harmonic components. These harmonic components are known as the space harmonics.

The magnitude of the space harmonics for a three-phase winding can be obtained by Fourier decomposition of the individual coil MMFs and subsequent superposition considering their 120° space and time distribution. Fig. 6.1 shows the magnetic field strength H_t in the air gap (near the stator bore) for a single coil with coil pitch angle β and slot opening w_{slot} (in metres), corresponding to a slot opening angle γ (in radians or degrees).

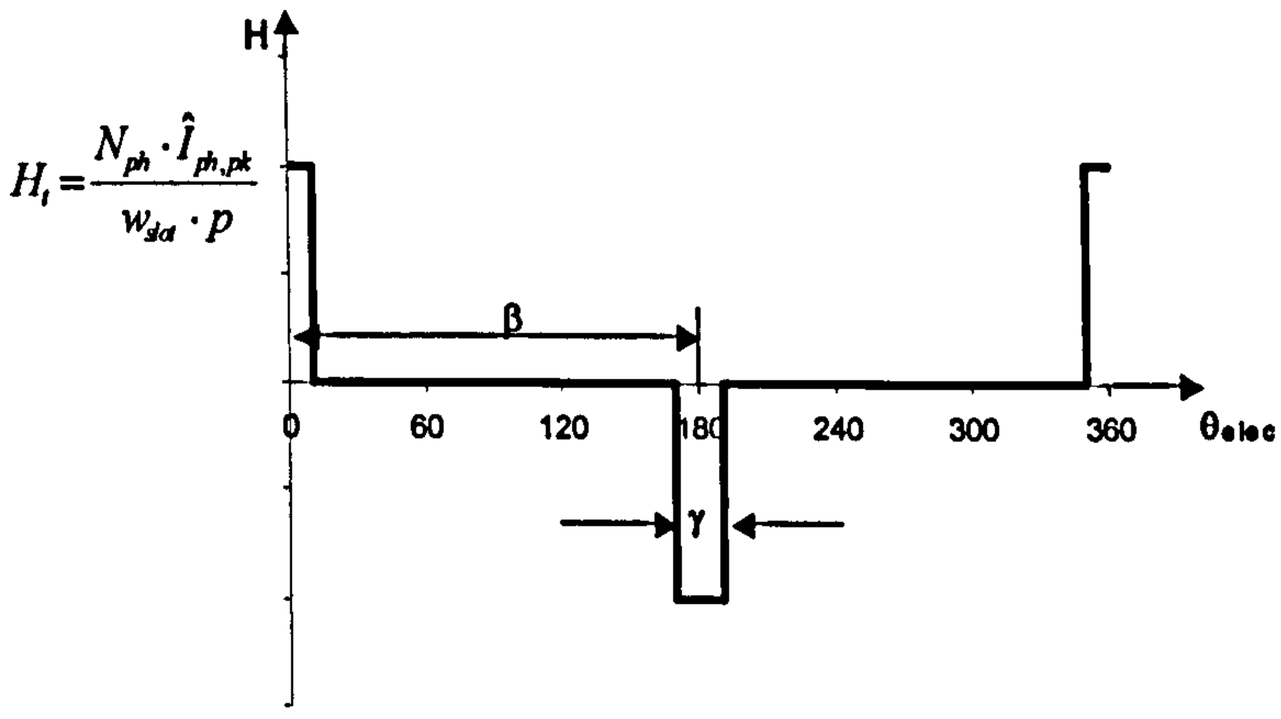

Fig. 6.1 H_t in the air gap near the stator bore for a coil with coil pitch angle β and slot angle γ

$$H_{t,n} = \frac{4}{\pi \cdot n} \cdot \frac{N_{ph} \cdot I_{ph,pk}}{w_{slot} \cdot p} \cdot \sin\left(n\frac{\gamma}{2}\right) \cdot \sin\left(n\frac{\beta}{2}\right) \tag{6.1}$$

Equation (6.1) describes the magnitude $H_{t,n}$ for the nth space harmonic. The factor $4/\pi/n \cdot sin(n \cdot \gamma/2)$ is due to the Fourier decomposition, $N_{ph} \cdot I_{ph,pk}$ are the peak ampere-turns per phase (MMF), w_{slot} is the slot opening, p is the number of pole pairs and the last factor is the so called coil pitch factor k_p:

$$k_{p,n} = \sin\left(n \cdot \beta/2\right) \tag{6.2}$$

where β is the angle of the coil span, and n is the nth harmonic. Depending on β some of the space harmonics can be completely eliminated, i.e. for β=180° (fully pitched winding) as in the existing motor no even harmonics exist, and for β=120° (short pitched winding) as in the three-tooth SMC motor no 3rd harmonic and its multiples exist, but all other odd and even harmonics are present. In comparison to the previous fully pitched motors the question is how much rotor loss is contributed by these additional even space harmonics.

When calculating space harmonics a distribution factor, k_d, is generally required, defined as

$$k_{d,n} = \frac{\sin\left(n \cdot g \cdot \alpha/2\right)}{g \cdot \sin\left(n \cdot \alpha/2\right)} \tag{6.3}$$

where α is the angle between slots, g is the number of slots per pole per phase, and n is the nth harmonic. All the motors under investigation have concentrated windings, and hence the distribution factor is 1 for all harmonics.

Starting from

$$\sin(\varpi t)\cdot\sin(n\theta)+\sin(\varpi t+120^o)\cdot\sin(n(\theta+120^o))+\sin(\varpi t+240^o)\cdot\sin(n(\theta+240^o)) \tag{6.4}$$

it can be shown for a motor with three phases, each 120° apart in space and time, that the space harmonics have no 3rd harmonics and have forward and backward rotating components.

Forward: $\cos(\varpi t - n\theta)$ for $n = 1, 4, 7, \ldots,$

Backward: $\cos(\varpi t + n\theta)$ for $n = 2, 5, 8, \ldots$

Each n^{th} space harmonic travels with a speed of $1/n$ slower than synchronous, as it has a $1/n$ shorter distance to travel in the same time. Table 6.1 lists the space harmonic components for the fundamental current wave, their directions and speeds for both types of motors. The magnitude of the magnetic field strength due to the superposition of the three phases is now

$$H_{t\max,n} = \frac{3}{2} \cdot H_{t,n} \tag{6.5}$$

Space Harmonic n_{space}	Direction	Normalised Speed of Space Harmonic =1/n·(-1)·(-1)^mod(n,3)	Normalised Relative Speed as seen by Rotor =(Speed of space harmonic) - 1	Present in Existing Motor	Present in 3-tooth SMC Motor
1	Forward	+1	0	√	√
2	Backward	-1/2	-3/2	-	√
4	Forward	+1/4	-3/4	-	√
5	Backward	-1/5	-6/5	√	√
7	Forward	+1/7	-6/7	√	√
8	Backward	-1/8	-9/8	-	√
10	Forward	+1/10	-9/10	-	√
11	Backward	-1/11	-12/11	√	√
…..					

Existing Motor: no 3rd harmonics due to 120° space distribution between all 3 windings
no even harmonics due to 180° coil pitch factor
SMC-Motor: no 3rd harmonic due to 120° space distribution between all 3 windings
no 3rd harmonics due to 120° coil pitch factor

Table 6.1 Space harmonic components and their speeds and directions

6.3.2 Modelling of Space Harmonics and Calculation of Eddy Current Loss in the Rotor due to Space Harmonics

There are papers [52-54] using an analytical model to predict eddy current losses in the rotor, but in the majority of publications and in this thesis a finite-element approach is chosen.

The magnetic field strength H_t along the circumference of the stator/air gap boundary can be calculated according to equations (6.1) and (6.5). A steady-state time-harmonic 2D-FE model of the rotor including the air gap can then be created using H_t as a moving current sheet at the boundary. It is assumed that the sleeve, magnets and shaft have constant permeability μ_r and conductivity σ. The model takes full account of the redistribution of the field caused by the eddy currents within limits of the 2D nature of the model (i.e. ignoring end-effects) and assumes sinusoidal-with-time fields. In this flux forced situation ignoring end effects implies that the calculated losses will be an overestimate, which at least errs on the safe side.

Fig. 6.2 shows a typical geometry of such a 2D rotor model. It typically consists of four or five layers depending on whether the magnets are glued directly onto the shaft or there is a magnet carrier as an additional layer. Schematic cross sections of the two existing rotors and the three new SMC rotors Mk1 to Mk3 are shown in Fig. 6.4. These pictures give an overview over the different proportions of sleeve thickness, magnet thickness and shaft diameter. Different colours indicate different materials.

To get good and repeatable results attention needs to be given to the coarseness of the mesh in the subdomains. Where the flux is penetrating into the surface of the shaft, the mesh needs to be very fine to allow good resolution, in case the losses are skin limited. A fine mesh becomes especially important when the flux near the shaft surface is closer to tangential than normal to the surface. Fig. 6.3a shows a mesh after having used the adaptive mesh refiner during the solver process. The very dense area on the shaft surface is clearly visible. The mesh consists of 32776 elements. Fig. 6.3b shows the flux lines and the induced current density plot for the Mk1 rotor for $n_{space} = 2$, clearly showing the four-pole field which is due to the 2nd space harmonic of the fundamental two-pole field.

The FE program gives the induced current densities J_z per unit length. The eddy current loss P_e for each subdomain (material) can be calculated as the time average of the resistive loss:

$$\frac{P_e}{l_a} = \frac{1}{2 \cdot \sigma} \cdot \iint_{area} |J_z|^2 \, da \tag{6.6}$$

where σ is the conductivity of the respective material, and l_a is the axial length of the motor. This is repeated for each different space harmonic n and all the results are added together afterwards. To obtain the total loss for the motor in question the value P_e/l_a given by (6.6) needs to be multiplied by the actual length of the motor.

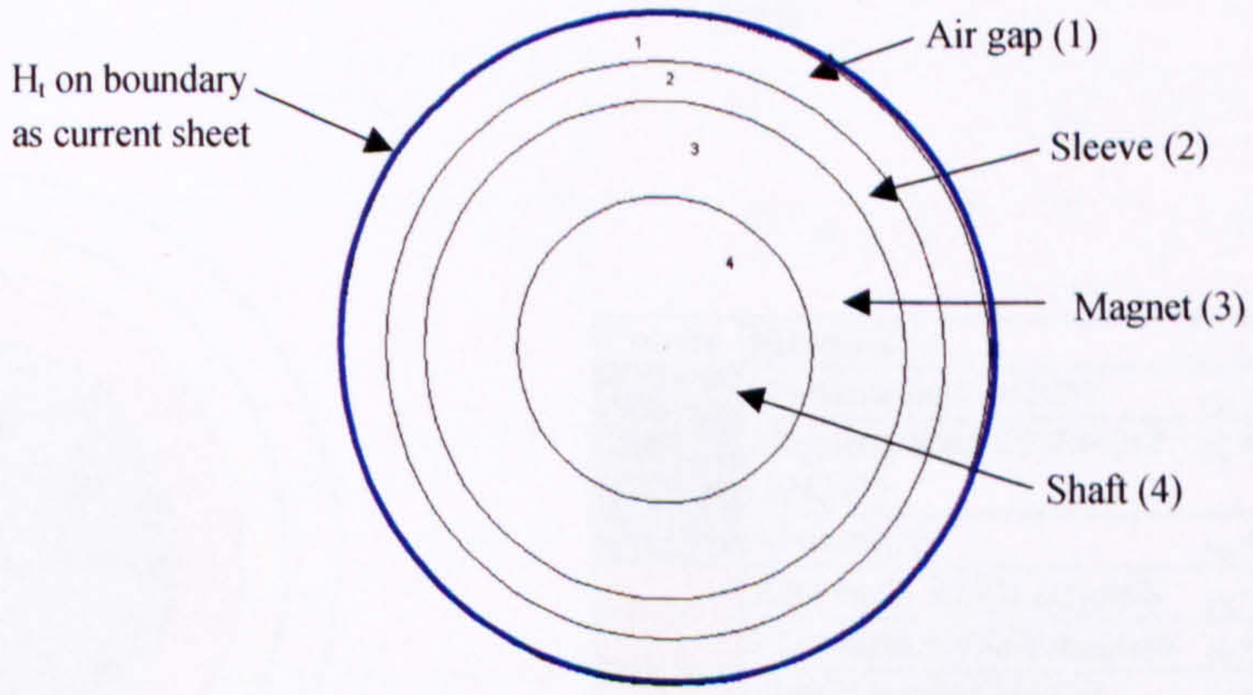

Fig. 6.2 Typical rotor cross section for 2D-FE rotor loss model

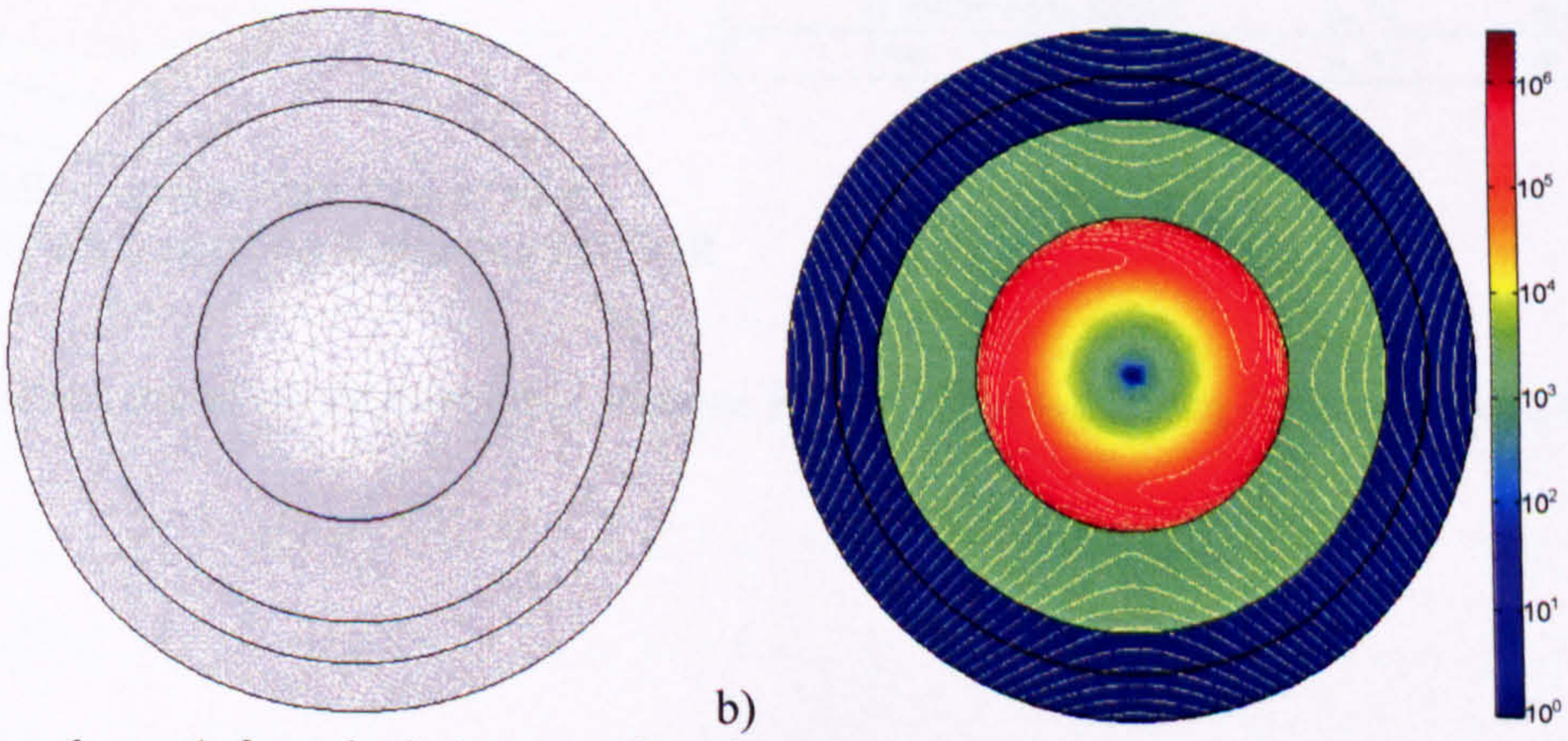

a) b)

Fig. 6.3 a) Example mesh for calculating rotor loss, b) Magnitude of induced current density $|J_z|$ for $n_{space}=2$ (for Mk1 rotor)

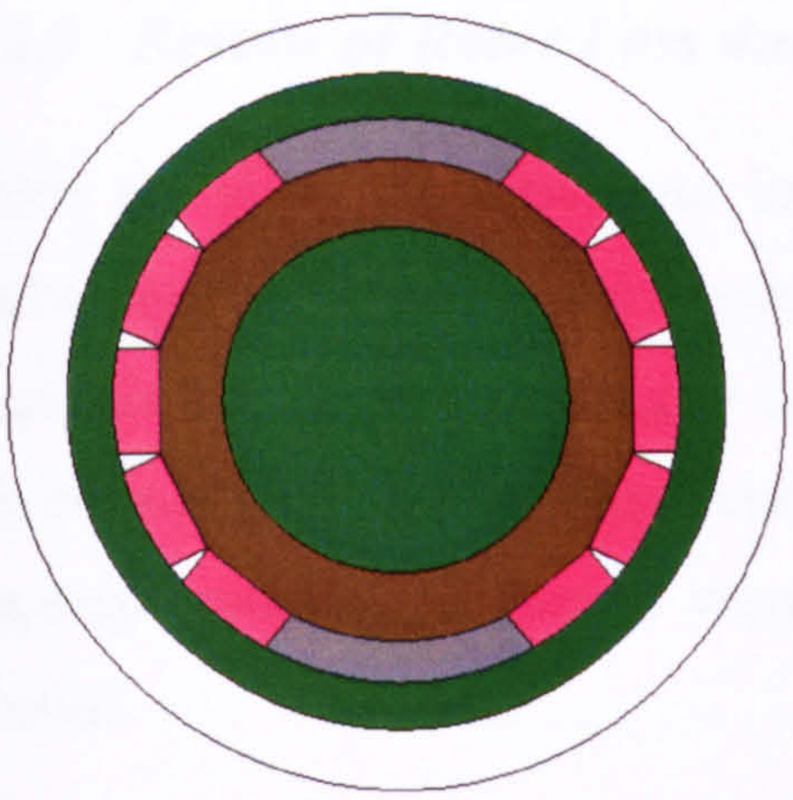

a) Existing rotor with stainless-steel sleeve, rare earth SmCo magnets, magnetic steel carrier

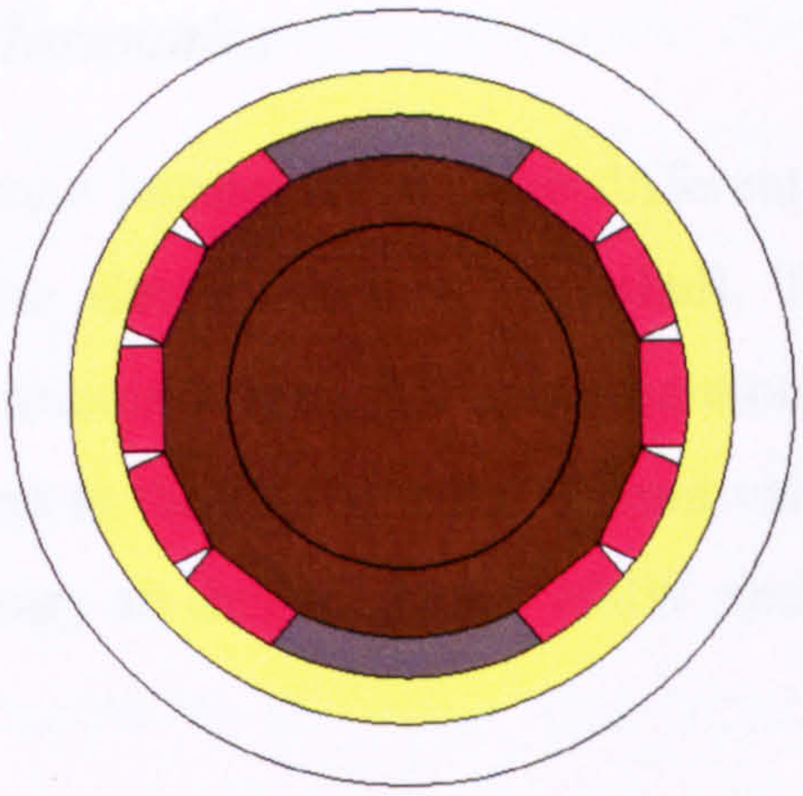

b) Existing rotor with carbon fibre sleeve, rare earth SmCo magnets, magnetic steel shaft

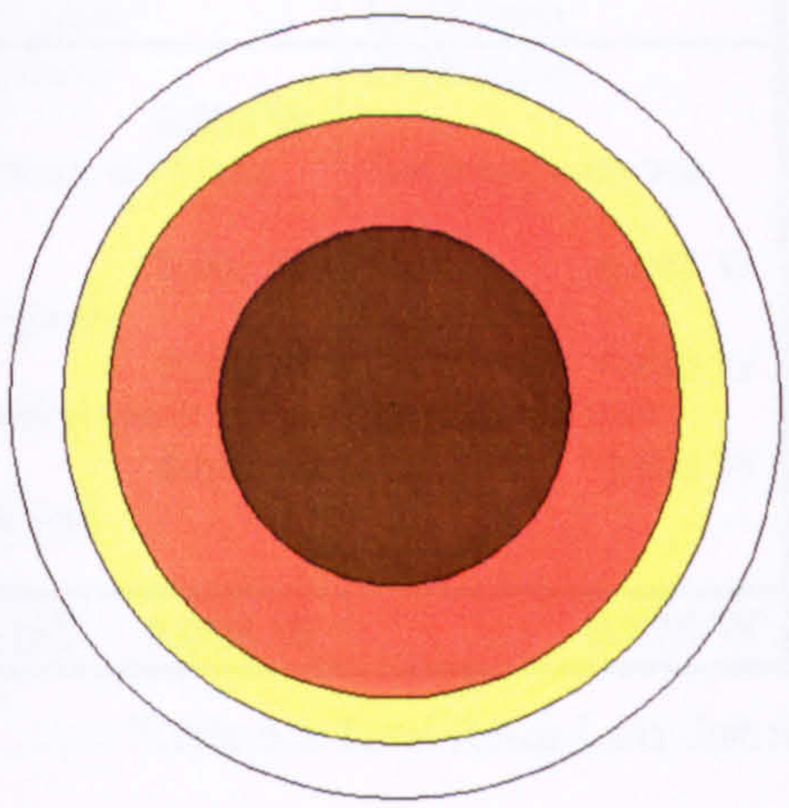

c) SMC rotor Mk1: carbon fibre sleeve, 'deep' plastic bonded NdFeB magnet on magnetic steel shaft

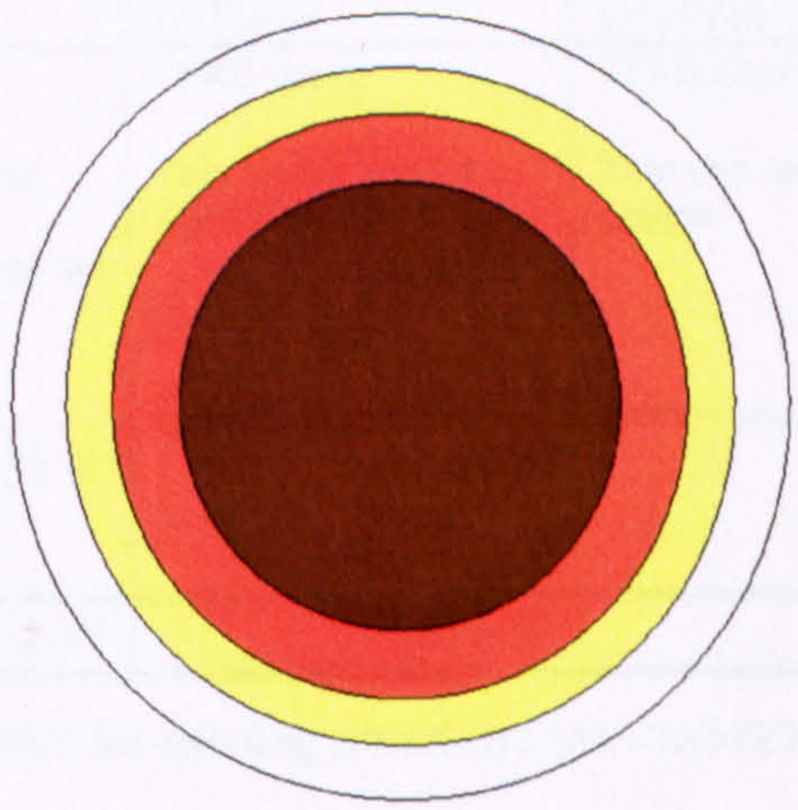

d) SMC rotor Mk2: carbon fibre sleeve, 'thin' plastic bonded NdFeB magnet on magnetic steel shaft

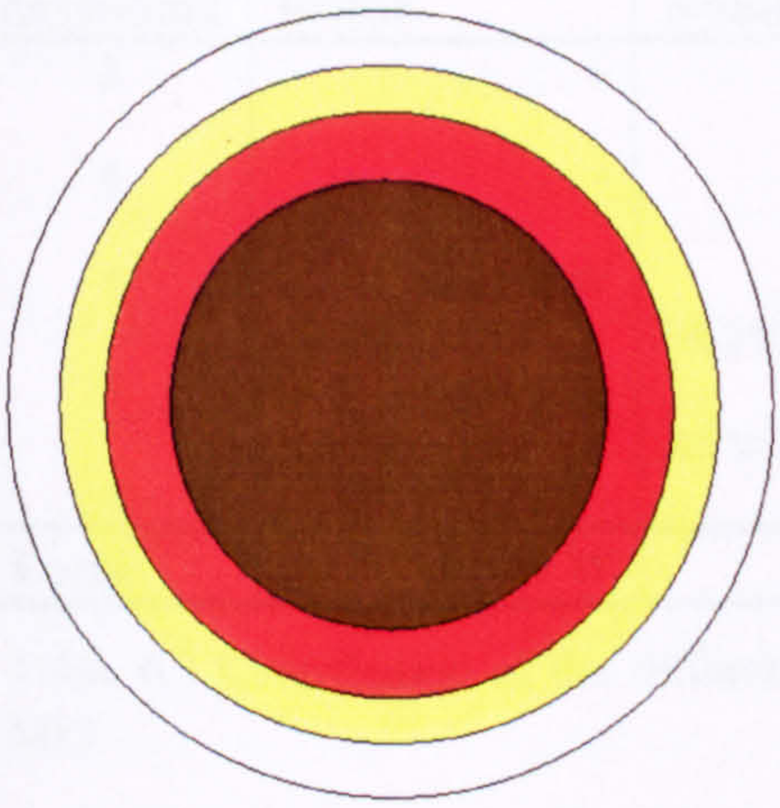

e) SMC rotor Mk3: carbon fibre sleeve, 'thin' rare earth NdFeB magnet on magnetic steel shaft

Colour	Material		
	Stainless steel 303S31	$\mu_r=1$	$\sigma=1.4\cdot10^6$ S/m
	Magnetic Steel 871M40-T (EN24T)	$\mu_r=100$	$\sigma=5\cdot10^6$ S/m
	Aluminium	$\mu_r=1$	$\sigma=2\cdot10^7$ S/m
	Rare earth SmCo magnets	$\mu_r=1.0645$	$\sigma=1.8\cdot10^6$ S/m
	Rare earth NdFeB magnets	$\mu_r=1.04$	$\sigma=7\cdot10^5$ S/m
	Plastic bonded NdFeB magnets	$\mu_r=1.375$	$\sigma=5\cdot10^3$ S/m
	Carbon fibre sleeve	$\mu_r=1$	$\sigma=0$ S/m
	Air	$\mu_r=1$	$\sigma=0$ S/m

Fig. 6.4 a)-e) Schematic of motor rotor cross sections for rotor loss modelling (time and space harmonics)

6.3.3 Results of Rotor Loss due to Space Harmonics

Table 6.2 gives the total rotor loss due to space harmonics for the different motors, including values where the losses occur: in the sleeve, magnet, and shaft. Table 6.3 analyses the losses according to their space harmonic origin. All space harmonic losses are calculated for a peak phase current equivalent to the fundamental current value of the six-step commutated current waveform necessary to deliver about 100W shaft output power.

Space Harmonic Rotor Loss				
Standard Rotor l_a=27.1mm	**Splitflow Rotor** l_a=27.1mm	**SMC Mk1.1** l_a=31mm	**SMC Mk2** l_a=31mm	**SMC Mk3** l_a=14mm
St-St sleeve **0.003 W** SmCo rare earth mag **0.001 W** Alu spacer **0.003 W** Mild steel carrier **0.001 W** St-St shaft -	CFRE sleeve - SmCo rare earth mag **0.001 W** Alu spacer **0.003 W** Carbon steel shaft **0.001 W**	CFRE sleeve - Deep plastic bonded NdFeB magnet **0.001 W** Carbon steel shaft **0.030 W**	CFRE sleeve - Thin plastic bonded NdFeB magnet **0.003 W** Carbon steel shaft **0.361 W**	CFRE sleeve - Thin rare earth NdFeB magnet **0.062 W** Carbon steel shaft **0.050 W**
Total 0.008 W	**0.005 W**	**0.031 W**	**0.364 W**	**0.112 W**

Table 6.2 Total Rotor Loss due to Space Harmonics for existing rotors and Mk1 to Mk3

Space Harmonic Rotor Loss					
n^{th} harmonic	**Standard Rotor**	**Splitflow Rotor**	**SMC Mk1.1**	**SMC Mk2**	**SMC Mk3**
2	-	-	**0.0311 W** **99.6%**	**0.3599 W** **98.9%**	**0.1104 W** **98.8%**
4	-	-	**0.0001 W** **0.3%**	**0.0027 W** **0.8%**	**0.0009 W** **0.76%**
5	**0.0074 W** **93.7%**	**0.0044 W** **95.2%**	**0.0000 W** **0.1%**	**0.0011 W** **0.3%**	**0.0005 W** **0.4%**
7	**0.0005 W** **6.3 %**	**0.0002 W** **4.7%**	.	.	.
8	-	-	.	.	.
Total	**0.008 W**	**0.005 W**	**0.031 W**	**0.364 W**	**0.112 W**

Table 6.3 Contribution of the different space harmonics to the rotor loss for existing rotors and Mk1 to Mk3

6.3.3.1 Space Harmonic Losses in the Existing Rotors

The existing motors have the lowest rotor losses caused by space harmonics compared with any of the three-tooth designs Mk1 to Mk3. This is due to the fact that the fully pitched winding has no even space harmonics, and no multiples of three due to the three-phase system. Therefore the first existing space harmonics are the 5^{th} and 7^{th}. The

penetration depth of the 5th harmonic is much lower (shorter pole pitch) than that of a 2nd for example, and therefore the losses caused by the 5th or any higher harmonics are small. The 5th together with the 7th account for more than 99% of the space harmonic losses in these rotors. Any loss due to higher harmonics is insignificant (less than 1mW).

The rotor with the stainless steel sleeve has slightly higher losses than the one with the non-conductive carbon fibre sleeve, although the difference here is small. A conductive sleeve near the stator surface is more susceptible to the stator flux variations and therefore a prime location for the eddy currents to develop. On the other hand a conductive sleeve can act as a shield for the materials below, reducing the overall rotor losses [55, 58], but this is only effective if the skin depth is less than the thickness of the sleeve. The losses are then said to be skin limited (or inductance limited), but this is not the case here (stainless steel sleeve thickness = 1.3mm, skin depth at 5th space harmonic (relative speed 1.2ω) = 12.3mm). The losses in the rare earth magnets are low, despite SmCo having a 360 times higher conductivity than plastic bonded NdFeB magnets (see Mk1 rotor). This is mainly because the first space harmonic is the 5th, but also due to the fact that the magnets are segmented (5 slabs per pole rather than one arc segment). Fig. 6.5 shows the flux plot of the 5th space harmonic for the two existing rotors.

Overall the space harmonic losses in the existing rotors are with less than 10mW so small, that it is not worth worrying about.

6.3.3.2 Space Harmonic Losses in the Three-Tooth Motor Rotors

All three-tooth motors have more rotor losses due to space harmonics than the existing motors. As shown in Section 6.3.1 all even harmonics are present in the three-tooth motors, so that the first space harmonic is the 2nd, which is the main source of the rotor loss, being responsible for nearly 99% of the total space harmonic loss (see Table 6.3). The effect of the 2nd space harmonic is so much larger than the 5th in the existing motors, because its relative speed as seen by the rotor is largest (1.5ω), the pole pitch of the 4-pole field is greater and therefore the penetration depth of the flux deeper, than in any of the higher space harmonics. Fig. 6.6a and b show the flux lines for the 2nd and 4th space harmonics (4-pole field and 8-pole field respectively) for the Mk1 motor. It can clearly be seen that less flux lines from the 4th space harmonic are reaching the shaft.

Comparing the three different SMC motor rotors with each other, the Mk1 rotor with the 'deep' plastic bonded magnets has the smallest rotor losses with about 31mW, whereas

the Mk2 rotor with the 'thin' plastic bonded magnets has the largest losses with about 364mW. The main difference in construction between these two rotors is the position of the magnet-shaft boundary. The nearer a highly conductive material is to the stator surface the stronger the field that reaches it, and therefore more eddy currents can be induced. However, the situation is even more complex, when comparing these numbers, as the lack in magnetic loading due to the thinner magnet in Mk2 has been compensated with a higher electric loading to keep the output power constant. Hence, not only has the shaft surface moved closer to the stator surface, but also the magnetic flux strength from the stator has increased. Both conditions combined cause the losses to increase by nearly 12 times compared to Mk1.

Mk3 has the same radial dimensions as Mk2, but the thin plastic bonded NdFeB magnets have been replaced with thin rare earth NdFeB magnets, which are more highly conductive ($\sigma=7\cdot10^5$ compared with $5\cdot10^3$ for plastic bonded magnets, i.e. 140 time more conductive). Despite the highly conductive magnets the overall loss in the motor is less than that of the Mk2. Again, that's because the balance between electric loading and magnetic loading has changed. The larger field from strong rare earth magnets has been compensated with a shorter axial length and less turns per phase. The result is that the overall space harmonic rotor losses are between the Mk1 and Mk2 losses. However, the split between the losses in the magnet and the shaft is totally different in Mk3. The losses in the magnet have gone up, even after taking the shorter length into account, but at the same time the loss in the shaft has significantly reduced. Basically, the losses in the conductive magnets weaken the field that reaches the shaft, and are so shielding the shaft from developing more eddy current losses. Fig. 6.6a and Fig. 6.7a and b show the flux plots for the 2^{nd} space harmonic for the three SMC rotors. The colours indicate the induced current density. The larger current density in the conductive rare earth magnets of the SMC Mk3 rotor are clearly visible compared to the other two rotors using plastic bonded magnets.

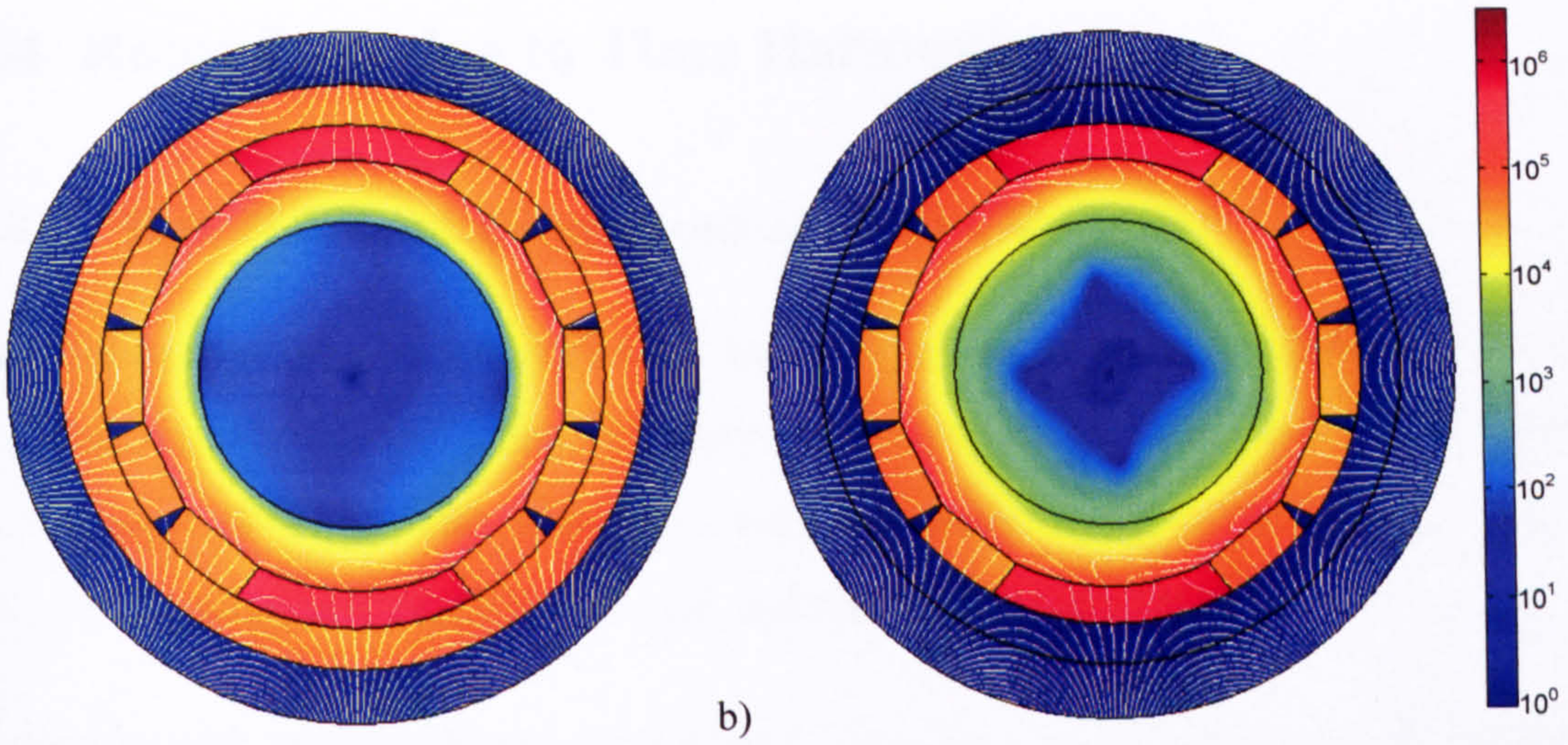

a) b)

Fig. 6.5 Magnitude of induced current density and flux line plots of the 5th space harmonic for the two existing rotors: a) with stainless steel sleeve, b) with carbon fibre sleeve

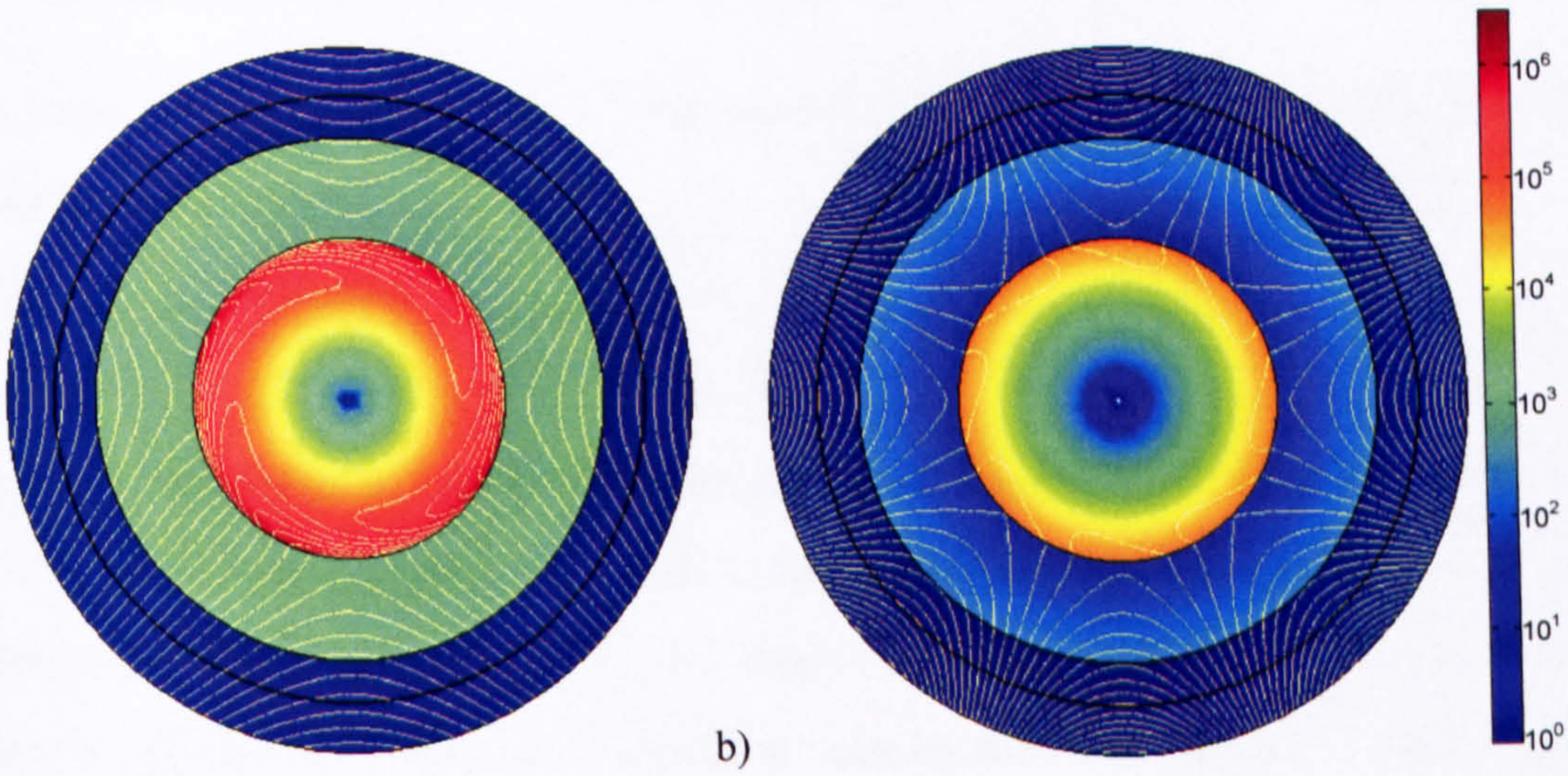

a) b)

Fig. 6.6 Magnitude of induced current density and flux line plots of the 2nd (a) and 4th (b) space harmonics for the SMC Mk1 rotor

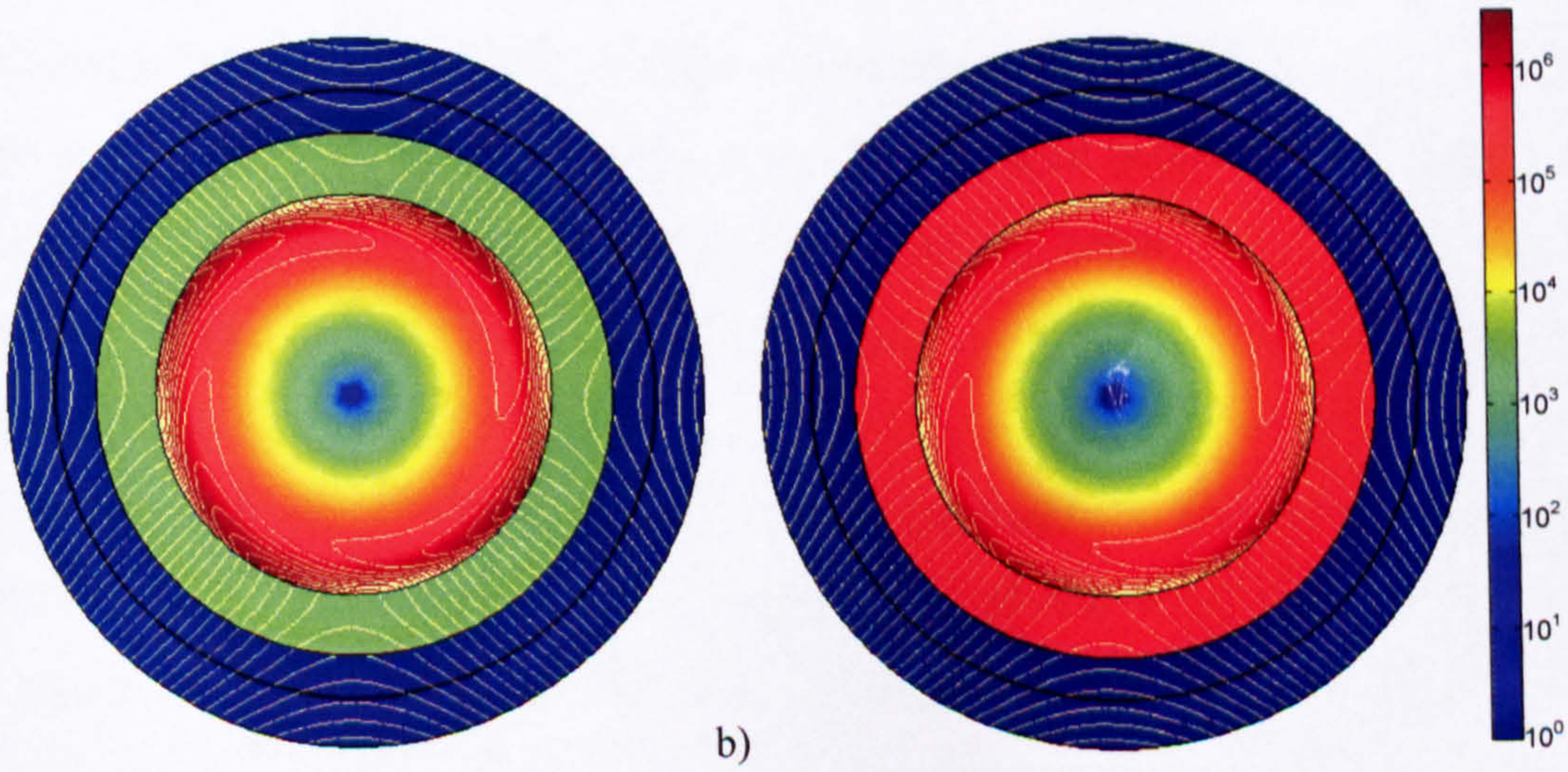

a) b)

Fig. 6.7 Magnitude of induced current density and flux line plots of the 2nd space harmonic for the SMC Mk2 rotor (a) and the SMC Mk3 rotor (b)

Note: all plots in Fig. 6.5 to Fig. 6.7 are shown on the same scales: colours indicating magnitude of induced current density $|J_z|$.

6.4 Rotor Loss due to Time Harmonics

6.4.1 Time Harmonic Components of Phase Currents

The permanent magnet brushless DC motor is driven by a 6-step inverter, switching the DC-link voltage to the phase windings and controlling the current with pulse-width-modulation (PWM). The phase currents are therefore non-sinusoidal. They can be Fourier decomposed into fundamental and harmonic components.

Following the same principal for the time harmonics as with the space harmonics, it can be shown that for a motor with three phases, each 120° apart in space and time, i.e.

$$\sin(n\omega t)\cdot\sin(\theta)+\sin(n(\omega t+120^o))\cdot\sin(\theta+120^o)+\sin(n(\omega t+240^o))\cdot\sin(\theta+240^o) \quad (6.7)$$

the time harmonics have no 3rd harmonics and also produce forward and backward rotating components.

Forward: $\cos(n\omega t-\theta)$ for $n = 1, 4, 7, ...,$

Backward: $\cos(n\omega t+\theta)$ for $n = 2, 5, 8, ...$

Each n^{th} time harmonic rotates at n times higher speeds than the rotating field produced by the fundamental current. Each time harmonic has its space harmonics according to section 6.3. Table 6.4 shows the full matrix of space and time harmonics for a three-phase winding and their relative speeds as seen by the rotor (rotor reference frame).

To be able to compare the calculated rotor losses for the different motor designs, modelled current waveforms based on measured resistance, inductance and back EMF have been used, as measured waveforms were not available for the same load levels. The current waveforms are fairly realistic as good agreement between modelled and measured current waveforms has been achieved for various other load levels. The measured currents contain a few more irregularities due to variations in the on/off periods caused by imperfect Hall sensor alignment for instance or other phase imbalances, so that the losses in reality will be higher than the ones predicted here. However, using the modelled current waveforms allows a good comparison of the effects of the different motor structures on the rotor losses. Fig. 6.8 shows the modelled current waveform for 100W output power for the Mk1 motor, and the corresponding harmonic spectrum. The magnitude of the even harmonics is typically so small that the major time harmonics are 5^{th}, 7^{th}, 11^{th}, 13^{th}, 17^{th}, and 19^{th} order, which are seen by the rotor as 6^{th}, 12^{th} and 18^{th} harmonics.

Space Harmonics (no multiple of 3rd due to three-phase system)

Time Harmonics (no multiple of 3rd due to three-phase system) — **relative speed as seen by the rotor**	n_{space}=1 fundamental $+1\omega_e$ forward	n_{space}=2 $-1/2\ \omega_e$ backward	n_{space}=4 $+1/4\ \omega_e$ forward	n_{space}=5 $-1/5\ \omega_e$ backward	n_{space}=7 $+1/7\ \omega_e$ forward	n_{space}=8 $-1/8\ \omega_e$ backward	n_{space}=10 $+1/10\ \omega_e$ forward	.....
n_{time}=1 fundamental $+1\omega_e$ forward	0	-1.5	-0.75	-1.2	-0.86	-1.125	-0.9	
n_{time}=2 $-2\omega_e$ backward	-3	0	-1.5	-0.6	-1.29	-0.75	-1.2	
n_{time}=4 $+4\omega_e$ forward	+3	-3	0	-1.8	-0.43	-1.5	-0.6	
n_{time}=5 $-5\omega_e$ backward	-6	+1.5	-2.25	0	-1.71	-0.375	-1.5	
n_{time}=7 $+7\omega_e$ forward	+6	-4.5	0.75	-2.4	0	-1.875	-0.3	
n_{time}=8 $-8\omega_e$ backward	-9	+3	-3	0.6	-2.14	0	-1.8	
n_{time}=10 $+10\omega_e$ forward	+9	-6	1.5	-3	0.43	-2.25	0	
.....								

causing Space Harmonic Loss

causing Time Harmonic Loss

Table 6.4 Matrix of space and time harmonics and their relative speeds as seen by the rotor
{relative speed (in rotor reference frame) = rel.speed_time harmonic (in stator reference frame) * rel.speed_space harmonic (in stator reference frame) –1}

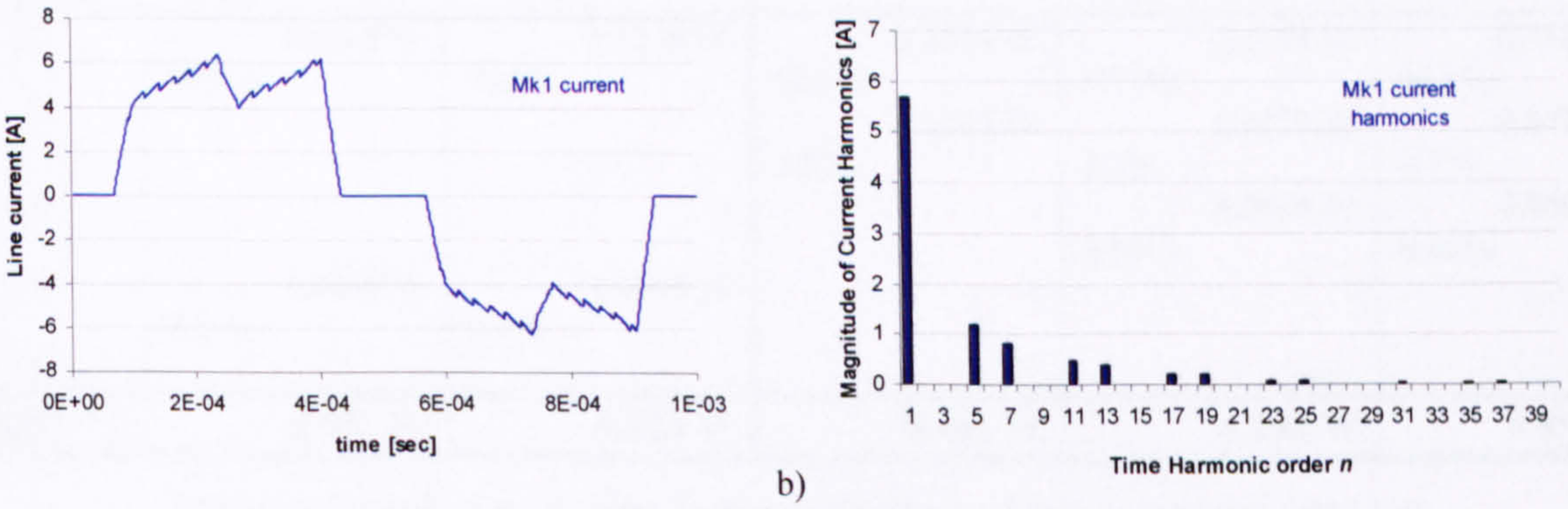

a) b)

Fig. 6.8 Modelled Mk1 current for about 100W output power a) waveform b) harmonic spectrum

6.4.2 Modelling of Time Harmonics and Calculation of Eddy Current Loss in the Rotor due to Time Harmonics

The same two-dimensional FE model of the rotor with a current sheet on the stator surface, as set-up for the space harmonics (section 6.3.2), is used. The only difference in input parameters is a different relative speed and different current magnitude according to the relevant time harmonics. The calculation of the eddy current loss due to time harmonics also uses equation (6.6).

6.4.3 Results of Rotor Loss due to Time Harmonics

Table 6.5 gives an overview over the total rotor loss due to time harmonics for the different motors, including values where the losses occur: in the sleeve, magnet, and shaft. Table 6.6 analyses the losses according to their space harmonic origin, and Fig. 6.9 gives an example for Mk1 of the contribution from the different time harmonics to the total rotor loss.

Time Harmonic Rotor Loss				
Standard Rotor l_a=27.1mm	**Splitflow Rotor** l_a=27.1mm	**SMC Mk1.1** l_a=31mm	**SMC Mk2** l_a=31mm	**SMC Mk3** l_a=14mm
St-St sleeve **0.233 W**	CFRE sleeve -	CFRE sleeve -	CFRE sleeve -	CFRE sleeve -
SmCo rare earth mag **0.166 W**	SmCo rare earth mag **0.356 W**	Deep plastic bonded NdFeB magnet **0.020 W**	Thin plastic bonded NdFeB magnet **0.021 W**	Thin rare earth NdFeB magnet **0.648 W**
Alu spacer **0.106 W**	Alu spacer **0.170 W**			
Mild steel carrier **0.047 W**	Carbon steel shaft **0.097 W**	Carbon steel shaft **0.441 W**	Carbon steel shaft **1.174 W**	Carbon steel shaft **0.247 W**
St-St shaft -				
Total 0.552 W	**0.623 W**	**0.461 W**	**1.195 W**	**0.895 W**

Table 6.5 Total rotor loss due to time harmonics for existing rotors and Mk1 to Mk3

Time Harmonic Rotor Loss					
n^{th} Space harmonic	**Standard Rotor**	**Splitflow Rotor**	**SMC Mk1.1**	**SMC Mk2**	**SMC Mk3**
1	**0.5508 W 99.8%**	**0.6225 W 99.9%**	**0.4524 W 98.2%**	**1.1674 W 97.7%**	**0.8521 W 95.2%**
2	**-**	**-**	**0.0083 W 1.8%**	**0.0275 W 2.3%**	**0.0421 W 4.7%**
4	**-**	**-**	**.**	**0.0005 W 0.04%**	**0.0005 W 0.06%**
5	**0.0010 W 0.2 %**	**0.0005 W 0.1%**	**.**	**.**	**.**
7	**.**	**.**	**.**	**.**	**.**
Total	**0.552 W**	**0.623 W**	**0.461 W**	**1.195 W**	**0.895 W**

Table 6.6 Contribution of space harmonics to the total time harmonics rotor loss

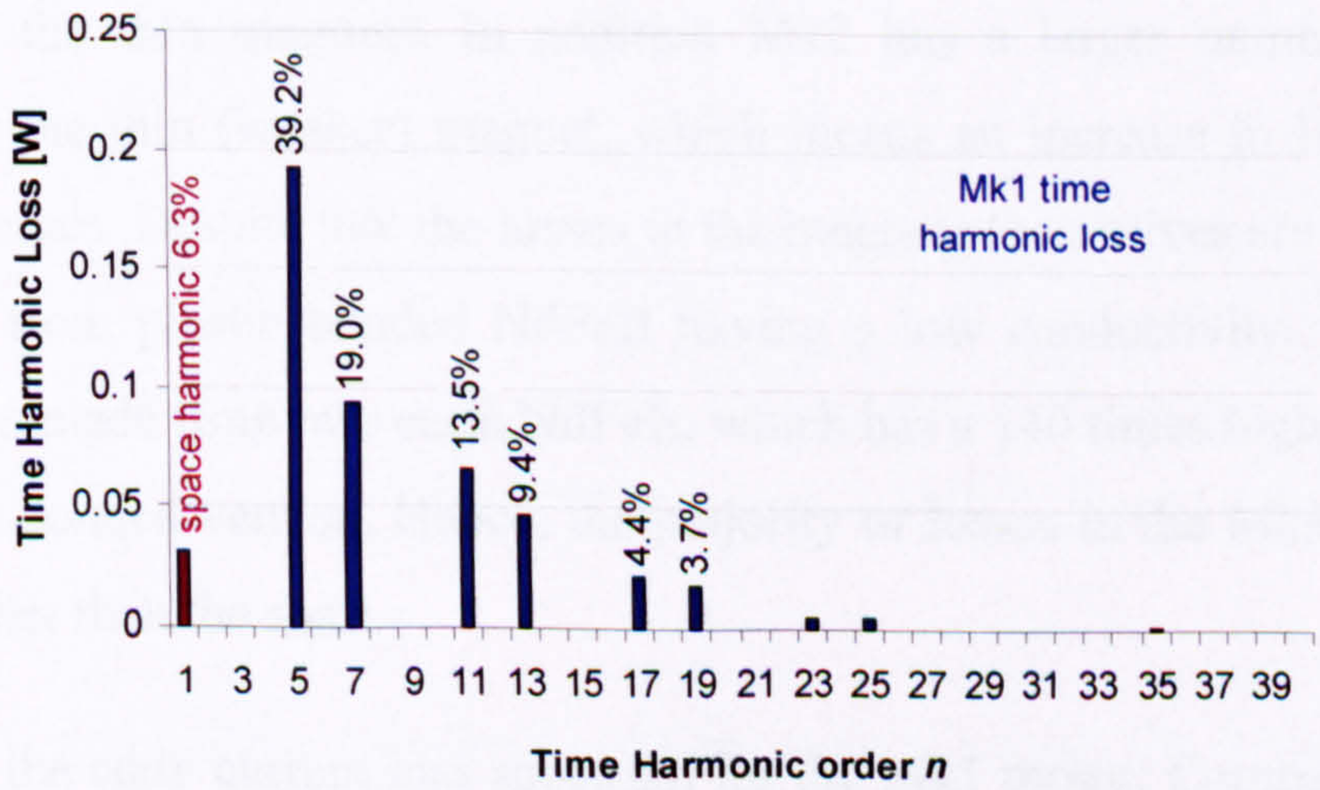

Fig. 6.9 Contribution of time harmonics to the total rotor loss (based on current spectrum Fig. 6.8b)

6.4.3.1 Time Harmonic Losses in the Existing Rotors

From Table 6.6 it is evident that more than 99% of the time harmonic rotor losses in the existing motors are caused by the fundamental space harmonic. Time harmonics of the next existing space harmonic, which is the 5^{th} in the fully pitched winding, are so small, that they can be ignored. Compared to the space harmonics, which contribute less than 10mW of loss, the magnitude of the time harmonics loss is significant with 552mW and 623mW, which cannot be neglected.

The difference between the two rotor constructions, one with stainless-steel sleeve, the other with carbonfibre sleeve, is not enormous, but the rotor with the stainless steel sleeve has slightly lower overall losses. The majority of the loss is in the sleeve, which acts as a shield to the rest of the rotor, and reduces the flux reaching the magnets, spacer and shaft. As a consequence the losses in the magnets, spacer and shaft are reduced.

6.4.3.2 Time Harmonic Losses in the Three-Tooth Motor Rotors

The majority, i.e. more than 95%, of the time harmonic losses in the three-tooth motors is caused by the fundamental space harmonic. The effect of the even space harmonics due to the short-pitched winding is small. Of all the harmonics, only the 2^{nd} space harmonic contributes significantly, accounting for about 5% on the Mk3 and less on the other two motors. Time harmonic loss from any higher space harmonics can be ignored.

The Mk1 motor has the lowest rotor losses from time harmonics – even lower than the existing motors. This shows that the idea of using a 'deep' plastic bonded magnet to reduce rotor losses has been successful. Mk2 and Mk3 both have higher losses than the existing motors, especially Mk2 with nearly twice as much loss as the existing motors. The loss in Mk2 is mainly in the shaft, as the shaft surface is much closer to the stator surface due to the thin magnets. In addition Mk2 has a larger number of turns to compensate for the thin (weaker) magnet, which means an increase in Ht, which leads also to higher losses. Despite that the losses in the magnets themselves are small, because they are made from plastic bonded NdFeB having a low conductivity. Mk3 uses thin magnets too, but made from rare earth NdFeB, which has a 140 times higher conductivity than the plastic bonded version. Hence, the majority of losses in the Mk3 rotor occur in the magnet, rather than the shaft.

Fig. 6.9 shows the eddy current loss spectrum for the Mk1 motor. Comparing that to the harmonic spectrum of the current waveform (Fig. 6.8b), it can be seen that the loss,

which is associated with the fundamental component of the phase current (i.e. the space harmonic loss), is small compared to the losses from the higher time harmonic components of the current. The maximum loss component comes from the 5^{th} time harmonic, followed by the 7^{th}, 11^{th} and 13^{th} time harmonic. This is true for all the other motors as well, both existing and SMC designs alike.

6.5 Rotor Loss due to Slotting / Tooth Ripple

6.5.1 Background of Tooth Ripple Losses

The magnetic field from the magnets sees a variation in air gap reluctance when passing the slots. These variations lead to flux concentrations at the tooth corners and lower flux density levels in the slot areas. These periodic variations of the air gap flux density introduce eddy currents in the rotor as the rotor rotates. Because the air gap field in PM machines is generally larger than the MMF field, the ripple field produced by the slotting tends to be driven in a flux (from the magnets) rather than an MMF source manner [59].

The magnitude of these flux variations (ripples) depends upon the width of the slot opening: the wider the slot opening the larger the losses [51, 59]. The period of these ripples depends on the number of slots in the stator lamination: the more slots the higher the ripple-frequency that causes the eddy currents in the rotor. For N_{slots} slots the frequency is $N_{slots} f_{mech}$ [60], i.e. f_{mech} is 1000Hz in all the motors considered here, but the existing motor has six teeth, hence 6000Hz ripple frequency, whereas the SMC motors have only three teeth, so half the ripple frequency (3000Hz).

6.5.2 Modelling of tooth ripple loss

The eddy currents from these slot harmonics can be modelled by setting up a 2D model of one slot over one tooth pitch and letting the rotor travel passed the slot with the circumferential rotor speed $v = \varpi_{mech} \cdot r_{i,stator}$, where $\varpi_{mech} = 2\pi \cdot f_{mech}$ in rad/s and $r_{i,stator}$ the stator bore radius is. For the SMC motors: $r_{i,stator}$ = 11mm, f_{mech} = 1000Hz, and v=69.1 m/s.

The model uses a rectilinear coordinate system, which ignores the curvature. This is a simplification, which is strictly only appropriate for machines with large number of slots

per magnetic pole. In the case of the three-tooth motors this is not the case, and it must be accepted that such a model might be inaccurate.

The model does not include armature reaction flux, so that all the results are for an unloaded machine (phase current=0). As it is only a 2D model it also neglects any end effects.

The periodic boundary conditions are set, so that a fixed amount of flux passes from the rotor to the stator. Again, this is not quite true for a two pole machine with diametrically magnetised magnets as these produce a sinusoidal flux distribution rather than a constant flux over one pole pitch as with radially magnetised magnets. In areas where eddy currents can develop (where a conductivity is specified) an external current has to be applied to force the net induced velocity current to zero over the tooth pitch, so that only the induced eddy currents due to the slots are present. Fig. 6.10 shows a typical flux plot and induced eddy currents of the tooth model of Mk1.

The total eddy current loss due to tooth ripple is obtained by integrating the current density across the subdomains according to equation (6.6), multiplying by the axial length and the number of teeth on the stator.

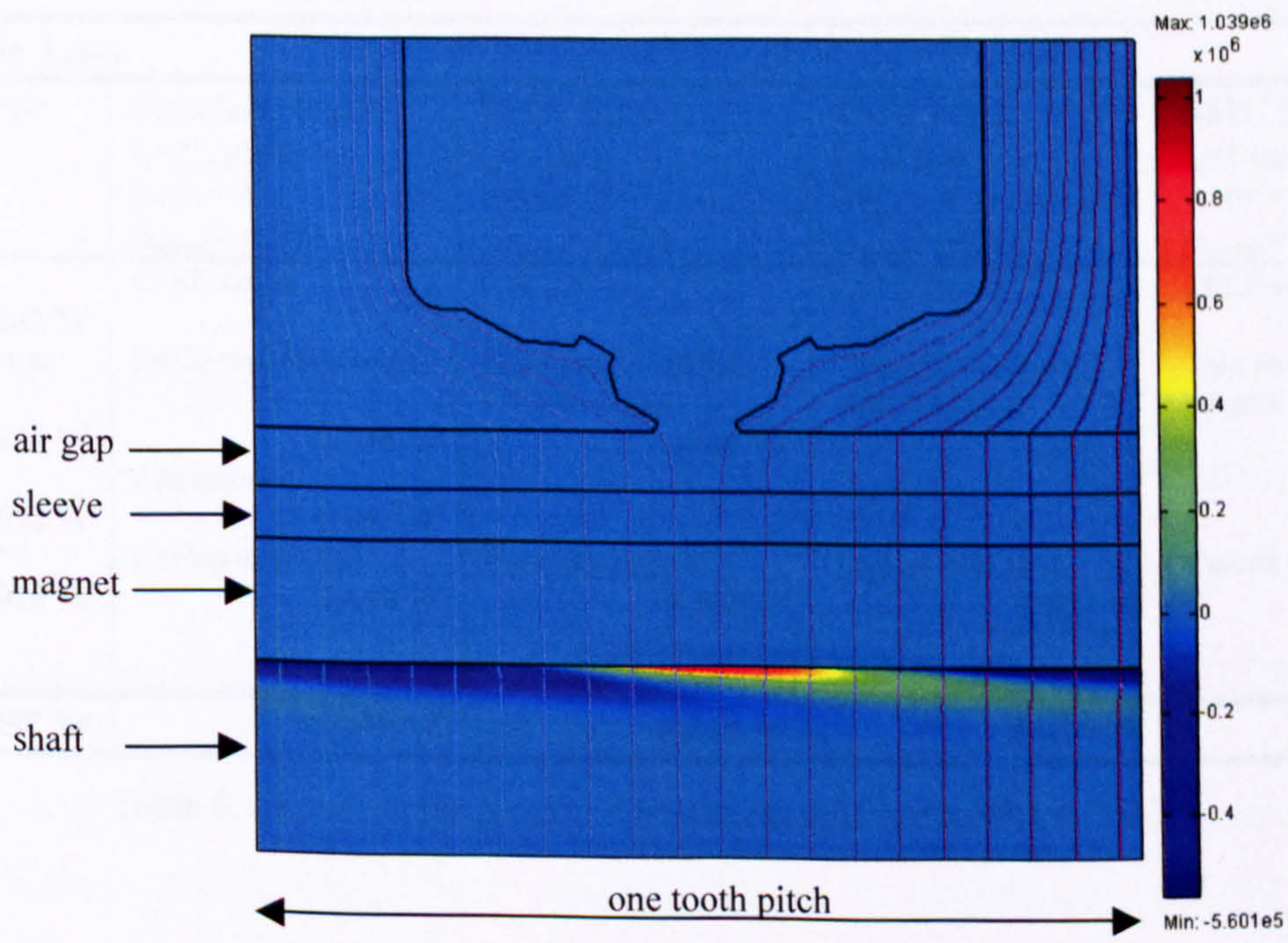

Fig. 6.10 Eddy currents due to slot/tooth ripple on Mk1 (colours show induced current density in A/m^3)

6.5.3 Results of Rotor Loss due to Tooth/Slot Ripple

Table 6.7 summarises the rotor loss due to the stator slotting for the different motors. Mk1 and Mk2 have the lowest losses with around 21-24mW. This is mainly due to the non-conductive sleeve and the plastic bonded magnets with a low conductivity. Nearly all of these losses appear in the shaft. Again it shows that the idea of the 'deep' plastic bonded magnet to reduce the rotor losses performs as expected. All the other rotors, which use sintered rare earth magnets with a conductivity 140 times larger than the plastic bonded magnets, have significant losses in the magnet. The existing rotor with the stainless-steel sleeve performs worst of all due to the losses in that sleeve.

Tooth ripple loss will depend on the ratio of slot opening w_{slot} to air gap length l_{gap}, and also on the ratio of the slot opening w_{slot} to the tooth pitch λ. The tooth pitch is much smaller in the existing motors than in the three-tooth motors due to the six teeth, and therefore the ratio of w_{slot}/λ is larger and so are the losses per unit length of slot. Despite only three-teeth and half the length, Mk3 has similar losses as the existing splitflow rotor. This is due to the significant larger magnetic field in the air gap (losses are proportional to B^2).

Tooth Ripple Loss				
Standard Rotor l_a=27.1mm teeth = 6 B_{airgap}= 0.24T	**Splitflow Rotor** l_a=27.1mm teeth = 6 B_{airgap}= 0.24T	**SMC Mk1.1** l_a=31mm teeth = 3 B_{airgap}= 0.28T	**SMC Mk2** l_a=31mm teeth = 3 B_{airgap}= 0.21T	**SMC Mk3** l_a=14mm teeth = 3 B_{airgap}= 0.44T
St-St sleeve **0.162 W** SmCo rare earth mag **0.034 W** Alu spacer **0.051 W** Mild steel carrier **0.010 W** St-St shaft -	CFRE sleeve - SmCo rare earth mag **0.035 W** Alu spacer **0.054 W** Carbon steel shaft **0.010 W**	CFRE sleeve - Deep plastic bonded NdFeB magnet **0.001 W** Carbon steel shaft **0.020 W**	CFRE sleeve - Thin plastic bonded NdFeB magnet **0.000 W** Carbon steel shaft **0.024 W**	CFRE sleeve - Thin rare earth NdFeB magnet **0.068 W** Carbon steel shaft **0.039 W**
Total 0.257 W	**0.099 W**	**0.021 W**	**0.024 W**	**0.107 W**

Table 6.7 Tooth ripple loss for the existing rotors and Mk1 to Mk3

6.6 General Comments on Eddy Current Losses in the Rotor

6.6.1 Summary of Rotor Loss

Table 6.8 summarises the losses estimated in the previous sections. When comparing the different rotor structures and interpreting the results, the different magnetic loadings, electric loadings, and axial length of each machine needs to be considered.

Total Rotor Loss					
	Standard Rotor	**Splitflow Rotor**	**SMC Mk1.1**	**SMC Mk2**	**SMC Mk3**
Space harmonics	**0.008 W 1.0 %**	**0.005 W 0.7 %**	**0.031 W 6.0%**	**0.364 W 23.0 %**	**0.112 W 10.0 %**
Time harmonics	**0.552 W 67.5 %**	**0.623 W 85.7 %**	**0.461 W 89.9 %**	**1.195 W 75.5 %**	**0.895 W 80.4 %**
Tooth Ripple Loss	**0.257 W 31.5 %**	**0.099 W 13.6 %**	**0.021 W 4.1 %**	**0.024 W 1.5 %**	**0.107 W 9.6 %**
Total	**0.817 W**	**0.727 W**	**0.513 W**	**1.583 W**	**1.114 W**

Table 6.8 Summary of rotor eddy current loss for all motors according to their source: space harmonics, time harmonics, tooth ripple loss

The three-tooth motors have more space harmonic losses as might be expected due to the even harmonics from the short-pitched winding, but their contribution to the total loss is small compared to the time harmonics. Because nearly all the time harmonic loss is caused by the fundamental space harmonic, the presence of the even space harmonics does not affect the overall rotor loss in any significant way. The tooth ripple loss benefits from the smaller number of teeth.

Overall the SMC Mk1 rotor has the lowest calculated rotor losses with about 0.5W. This suggests that the initial idea of using a deep plastic bonded magnet has proven to be a successful concept and should be considered in future designs.

6.6.2 Resistance Versus Inductance Limited

The mechanisms which drive rotor losses are complex and mean that each design needs to be looked at individually. For some designs a conductive sleeve might be advantageous, providing a shielding effect, whereas for others it might be detrimental.

Skin depth and geometric dimensions like sleeve and magnet thickness, and pole pitch versus air gap, are all factors, which play a significant role and determine if the eddy currents are resistance limited or inductance limited.

In the resistance limited case the effect of the eddy currents on the field is small and therefore neglected. However, this is only acceptable when the skin depth associated with the inducing field harmonics is relatively large compared with the radial thickness of the component. In the inductance limited case the eddy currents have a dominant effect on the field, to such an extent that full ampere-turn reflection can be obtained. Ampere-turn reflection happens if the air gap is small compared to the pole pitch, and the skin depth small compared to the radial dimensions.

Table 6.9 shows the skin depth for the various materials used in the rotors at the most significant harmonic frequencies. The skin depth of the plastic bonded magnet is so large, even at very high frequencies that it is satisfactory to assume, that the eddy currents are resistance limited. For the stainless steel sleeve and the rare earth magnets the skin depth is still larger than the component thickness, but only about 2-4 times larger. The aluminium spacing ring and the magnetic steel shaft are definitely skin limited, i.e. have inductance limited eddy currents.

Skin Depth	$\delta = \sqrt{\frac{2}{\varpi \cdot \sigma \cdot \mu_0 \cdot \mu_r}} = \sqrt{\frac{1}{\pi \cdot f \cdot \sigma \cdot \mu_0 \cdot \mu_r}}$				
Frequency	**Plastic bonded NdFeB** μ_r=1.375 σ =5 10^3 S/m	**Rare Earth NdFeB** μ_r=1.04 σ =7 10^5 S/m	**Stainless Steel** μ_r=1 σ =1.4 10^6 S/m	**Magnetic Steel** μ_r=100 σ =5 10^6 S/m	**Aluminium** μ_r=1 σ =2 10^7 S/m
1000 Hz	191.95 mm	18.65 mm	13.45 mm	0.71 mm	3.56 mm
6000 Hz (5^{th} & 7^{th} time harm.)	78.36 mm	7.62 mm	5.49 mm	0.29 mm	1.45 mm
12000 Hz (11^{th} & 13^{th} time harm.)	55.41 mm	5.38 mm	3.88 mm	0.21 mm	1.03 mm
18000 Hz (17^{th} & 19^{th} time harm.)	45.24 mm	4.40 mm	3.17 mm	0.17 mm	0.84 mm

Table 6.9 Skin depth of various materials at the most significant harmonic frequencies

6.6.3 Accuracy of the Rotor Loss Estimations

How accurate these rotor loss estimations are is difficult to say. The FE models are obviously based on assumptions, which have been highlighted (see Section 6.3.2, and Section 6.5.2). Rather than claiming to model all effects accurately, the main purpose is to identify design trends, and to give an indication of the total rotor loss in comparison to the stator iron and copper loss.

Mecrow et al [59] uses the same tooth ripple model as described above and found very good agreement with measurements, generally in the order of 6%, but would consider up to +/- 20% a realistic assessment of the model accuracy.

Zhu et al [52] uses a thermometric method to measure rotor loss and compares it with analytical predictions. In this particular paper good agreement was achieved with the improved model taking into account the eddy current reaction field, whereas the model ignoring the effect of the eddy currents on the forcing field overestimated the losses. This means, should the eddy current reaction field have an effect, but has been neglected, the losses calculated are more likely to be overestimated, i.e. worst case (too pessimistic).

In the three-tooth motors discussed the eddy current reaction field is believed to be neglectable as the component thickness is smaller than the skin depth at the important frequencies, and therefore the predicted rotor loss of between 0.5W to 1.5W in a 100W machine, corresponding to 0.5% to 1.5% of full rated power, seems realistic, give or take 20%.

6.7 Effect of Rotor Loss on Impeller Temperature

If the rotor loss in these turbomolecular pump motors is only of the order of 1W or less, what effect does this have on the impeller temperature?

6.7.1 Complexity of Thermal Equilibrium in a Vacuum Pump

The steady-state impeller temperature depends not only on the motor rotor loss, but also on the gas windage and friction loss, the bearing loss, and on the effective thermal conductivity of the air. It is very difficult to separate the motor rotor loss from the other losses in the pump. The situation is also complicated by the fact that the effective thermal conductivity of air in a vacuum is not constant, but very much pressure dependent. Fig. 6.11 shows the effective thermal conductivity for air as a function of pressure. Under no load, the pressure in the turbopump is very low, which means the effective thermal conductivity is also very low, but so is the gas friction. Under load the windage loss increases, but so does the thermal conductivity, which actually helps cooling the impeller to a certain extent. Thermal modelling becomes very complex, because the pressure changes across the turbopump stages. It is also very difficult to determine how much of the windage or bearing loss heats up the impeller rather than going directly into the pump body.

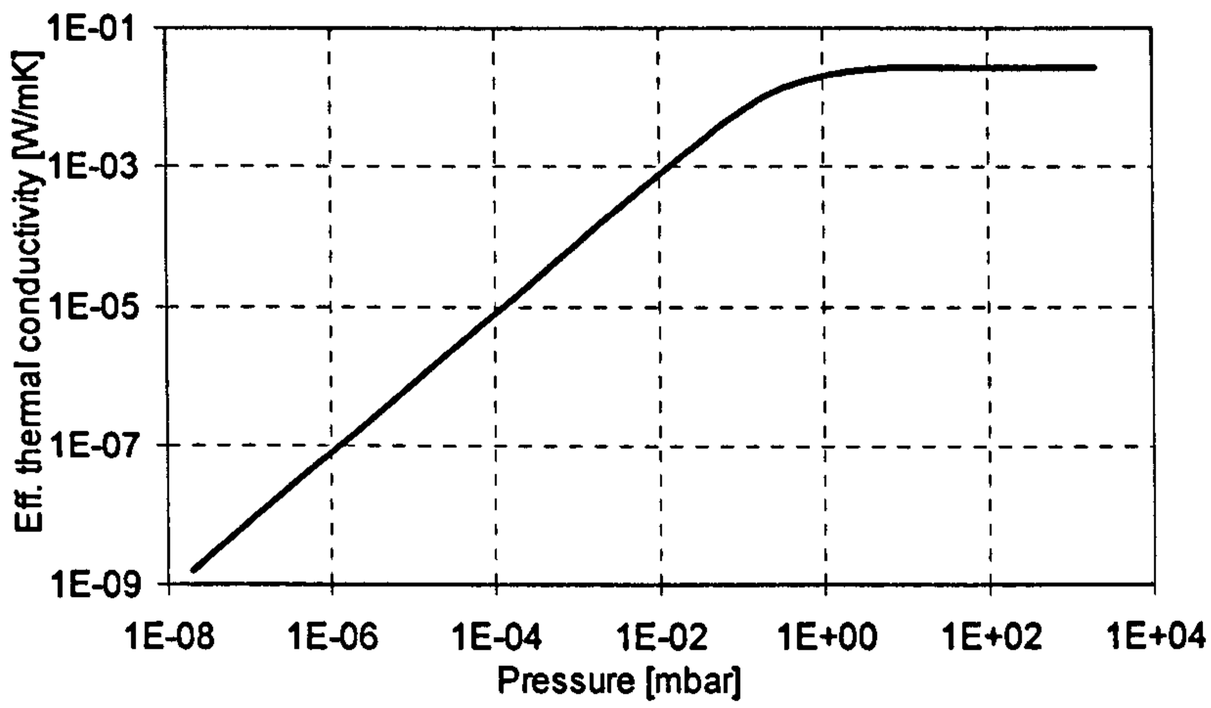

Fig. 6.11 Example of effective thermal heat conductivity of air as a function of pressure (wall separation 1mm, higher wall temperature 90°C, lower wall temperature 30°C) [63]

A common assumption in Edwards so far has been that most of the bearing loss goes directly into the pump body and that the windage loss in a vacuum, especially with backing pressures of $1 \cdot 10^{-2}$mbar or less, can be neglected. Hence the motor rotor loss was thought to be the main cause of impeller heating.

The theoretical estimation of the motor rotor loss presented earlier predicted losses of about 1W. This apparently low level of motor rotor loss lead to doubts about the original assertion, that the motor rotor loss is the dominant factor in raising impeller temperature. To verify or disprove the assertion, the following brief investigation was carried out.

6.7.2 Impeller Temperature as a Function of Backing Pressure

To minimise the bearing losses the SMC Mk3 motor was tested in a fully magnetically levitated turbomolecular pump, in which the impeller has no mechanical contact to the pump body. The impeller temperature was measured with an infra-red thermocouple for two backing pressure conditions: a) backed by a rotary vane pump (RV12) reaching a backing pressure of $1 \cdot 10^{-2}$mbar, and b) backed by a combination of a small turbomolecular pump (EXT70) and an RV pump reaching a backing pressure of $1 \cdot 10^{-4}$ mbar, two decades lower than with the RV pump on its own.

Fig. 6.12 and Fig. 6.13 show the measured impeller temperature and motor input power for the two different backing pressure conditions. The winding, body and ambient temperature are included for reference. The impeller temperature dropped by 18.9°C while the power dropped by 1.6W (equivalent to a thermal resistance of the impeller of 11.8°C/W), when the pressure was lowered. The only difference in these two tests was the backing pressure. It shows clearly that a pressure of $1 \cdot 10^{-2}$mbar is still creating

significant windage, equivalent to 1.6W, compared to a pressure of $1 \cdot 10^{-4}$ mbar. The measured change in power supports the measured change in impeller temperature and shows that the windage loss is both real and increasing the impeller temperature.

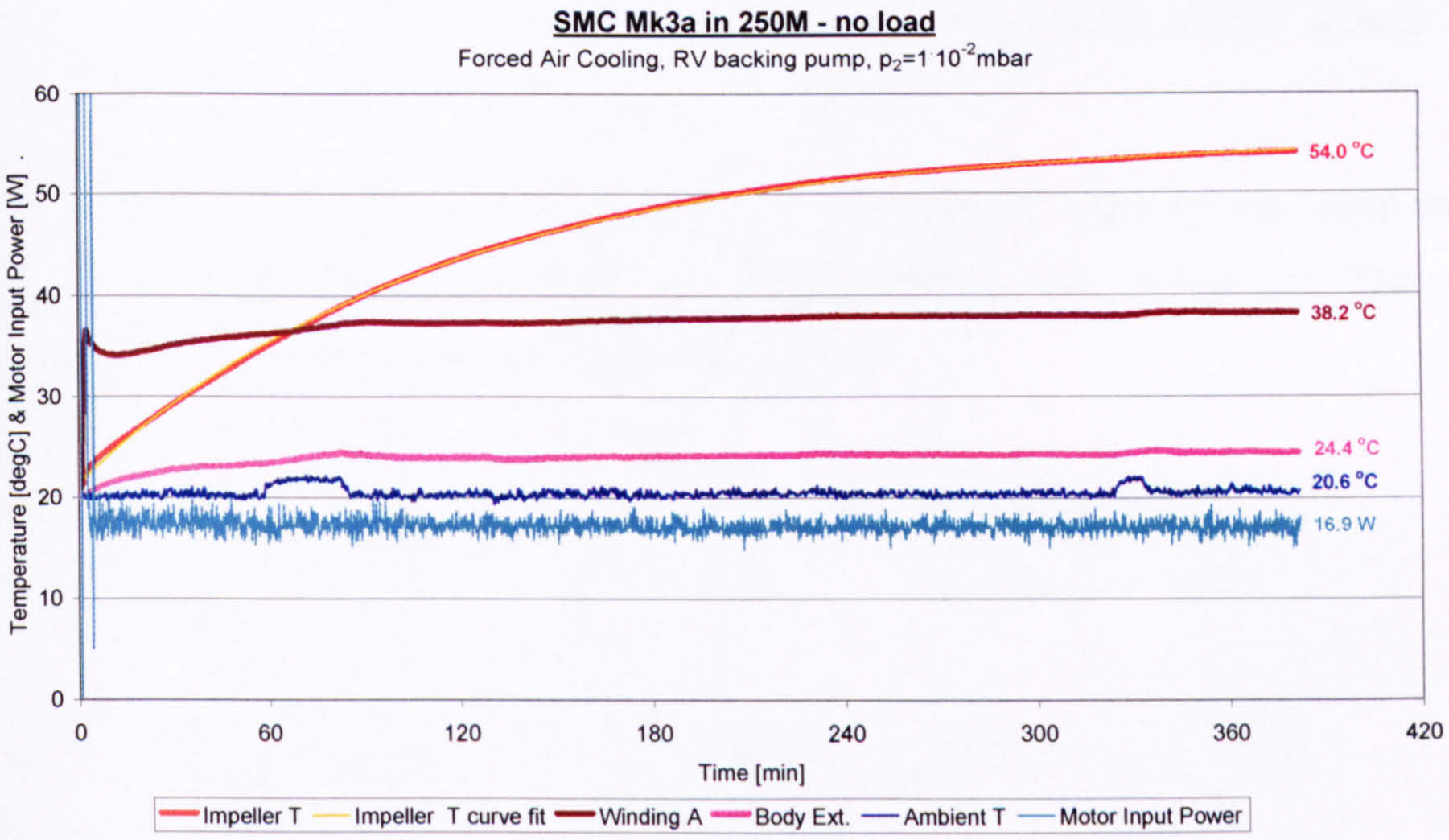

Fig. 6.12 Impeller, winding, body temperature and motor power at $1 \cdot 10^{-2}$mbar backing pressure

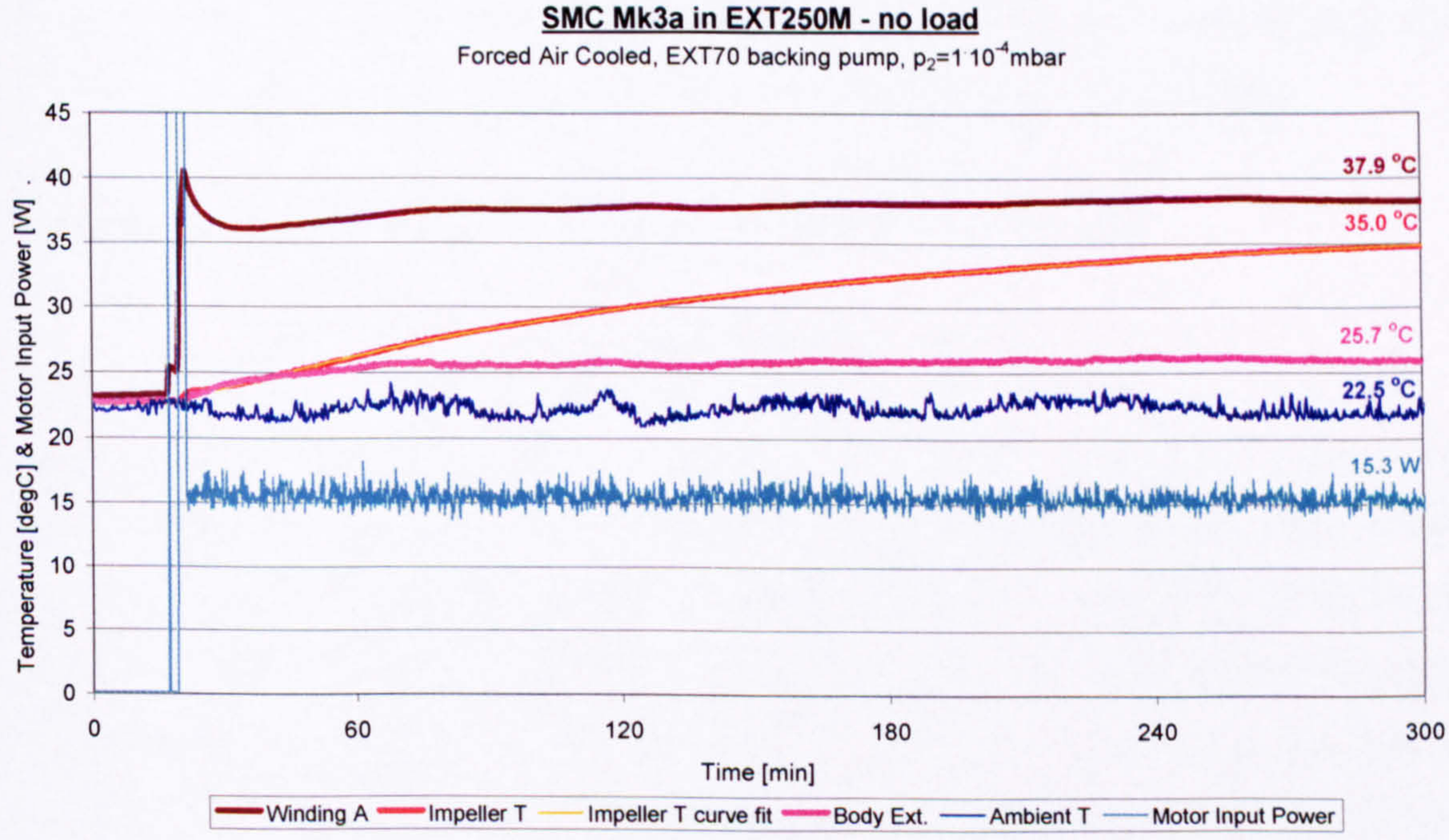

Fig. 6.13 Impeller, winding, body temperature and motor power at $1 \cdot 10^{-4}$mbar backing pressure

In standard turbopumps, which have an oil lubricated ball bearing at the bottom, such a difference in backing pressure is hardly noticeable, as the friction and bearing drag of the mechanical bearing is much larger and dominates the power consumption (hence the

common assumption that windage at these pressures is negligible). But in this magnetically levitated pump small differences in power consumption can be measured and a significant difference in impeller temperature was noticed.

6.7.3 Curve-Fit Using Temperature Rise to Determine Rotor Power and Equivalent Thermal Heat Transfer Coefficient

One method quite often used is the thermometric method, whereby the initial rate of change of rotor temperature is used to determine the specific power loss. The power balance of the impeller can be described as follows:

$$\text{Heat generated} = \begin{matrix}\text{Heat lost}\\ \text{at surface}\end{matrix} + \begin{matrix}\text{Rate of change of}\\ \text{stored thermal energy}\\ \text{in the material}\end{matrix}$$

$$P_{Loss} = \left(T_{impeller} - T_0\right) \cdot h \cdot a_{impeller} + \left(m_{alu} \cdot c_{alu} + m_{steel} \cdot c_{steel}\right) \cdot \frac{dT_{impeller}}{dt} \tag{6.8}$$

with $T_{impeller}$ being the impeller temperature, T_0 the initial impeller temperature at the start of the test, h the thermal heat transfer coefficient, a the surface area of the impeller, m the mass of the aluminium impeller and steel shaft, c the specific heat capacity of aluminium and steel respectively, and dT/dt the rate of change of impeller temperature.

The impeller temperature follows an exponential curve of the form

$$T_{impeller} = \left(T_1 - T_0\right) \cdot \left(1 - e^{-t/\tau}\right) + T_0 \tag{6.9}$$

with T_1 the final equilibrium temperature, T_0 the start temperature, and τ the time constant. A curve fit based on these two equations (6.8) and (6.9) using the solver function in a spreadsheet such as Excel, provides some information about the power in the impeller that causes the temperature rise. Table 6.10 summarises the parameters. Using this method the heat power in the impeller for a backing pressure of $1 \cdot 10^{-2}$mbar is estimated at about 2.7W, where as it is only about 0.9W, when the backing pressure drops to $1 \cdot 10^{-4}$mbar, giving a total power difference of 1.8W, which compares very close to the measured 1.6W difference in total motor input power. This proves that even at these low pressures the windage losses are bigger at 1.6 to 1.8W than the predicted motor

rotor loss at 1W. The impeller temperature rise per Watt is estimated between 11.9°C/W and 15.1°C/W, which is in line with the experimentally obtained value of 11.8°C/W.

No systematic testing of impeller temperature under load was carried out, as the main focus was always on the stator iron losses in SMC. However, based on impeller temperatures under load using the same curve fit procedure an equivalent heat transfer coefficient for high backing pressures (e.g. 1mbar) is estimated at a value of around 3°C/W. The higher pressure causes more windage loss, but at the same time provides more molecules to bounce between impeller and the surrounding parts to help transferring the heat from the impeller into the rest of the pump (i.e. better cooling of the impeller).

Thermal curve fit			**Backing Pressure of $1{\cdot}10^{-2}$mbar**	**Backing Pressure of $1{\cdot}10^{-4}$mbar**
Parameter		**Units**		
mass alu impeller	m_{alu}	kg	0.40	0.40
specific heat capacity	c_{alu}	J/(kg·K)	960	960
mass steel shaft	m_{steel}	kg	0.37	0.37
specific heat capacity	c_{steel}	J/(kg·K)	500	500
initial temperature	T_0	°C	23.4	23.5
equilibrium temperature	T_1	°C	55.3	36.8
time constant	τ	sec	6755	8584
thermal heat transfer	h'	W/°C	0.084	0.066
coefficient	1/h'	°C/W	**11.9**	**15.1**
Estimated Rotor Loss	P_{loss}	**W**	**2.7**	**0.9**

Table 6.10 Parameters for thermal curve fit for the two test cases (area of impeller is included in *h'*)

6.7.4 Conclusion: Effect of Rotor Loss on Impeller Temperature

With regards to the predicted motor rotor loss, a loss of about 1W causes only an 11-15°C temperature rise on the impeller under low pressure, and only a 3°C temperature rise under high pressures. From these results it is clear that the estimated rotor losses on their own do not account for the measured impeller temperature changes. Other sources of loss like friction, windage and bearing drag in ball bearings have much greater effect than previously assumed. The work in this chapter has helped to challenge the long standing assumption that impeller temperature is mainly the 'motor's fault' as windage, friction and bearing drag was assumed to be neglectable in a vacuum, which is clearly not the case. There is plenty of room for future work in the area of thermal modelling of the turbomolecular pump, but that is beyond the scope of this thesis.

Chapter 7

The Fourth SMC Machine (Mk4): Improved Machine Design

7.1 Introduction

Three SMC prototype motors have been built and tested so far. None of the motors was found acceptable as a direct replacement of the existing laminated design. The reasons were either: a) high iron losses (Mk1, Mk3), or b) large inductance, i.e. running out of volts under load (Mk2). However, during the development of these motors a lot of experience in designing with SMC has been gained, and the methods of predicting iron and rotor losses have been improved. It was strongly felt that a better SMC motor design was possible with a further reduction in total loss by adjusting some of the stator dimensions, going back to a deep, plastic bonded magnet as per the initial design concept and using a new, improved SMC material. More design freedom was negotiated by convincing the project stakeholders to adopt a system view rather than looking at the motor in isolation of the drive. In a review meeting it was agreed that an increase in inductance would be acceptable and that some phase advance could be built into the design.

This chapter summarises the changes and design decisions behind the SMC Mk4 motor and compares the predicted performance with measurements made in a magnetically levitated turbomolecular pump.

7.2 Choice of Materials

7.2.1 New SMC Material for the Stator

In Chapter 5 the material issues with SMC have been discussed. To reduce the hysteresis losses a larger grain size is required to encourage better domain growth. Also, better particle insulation and a heat treatment process that allows better stress relief without damaging the particle insulation is necessary to minimise hysteresis loss. To reduce the bulk eddy current loss a material with a high resistivity (i.e. low conductivity) is needed. An increase in permeability would also help to improve the motor performance.

Höganäs has greatly supported this project and kindly given access to a material that at the time was still in its development stage, but promised to fulfil the above requirements. The new material X-SMC-11 (now developed into Somaloy700) has a typical grain diameter of 0.2mm, twice the size of Somaloy500, a promised permeability of up to 600 and a conductivity of less than 10,000. Fig. 7.1 shows the comparison of the total losses measured on the standard ring sample. At a frequency of 1000Hz the losses are reduced by about 22% in the ring sample. Using this new material a noticeable reduction in the iron losses was expected for Mk4.

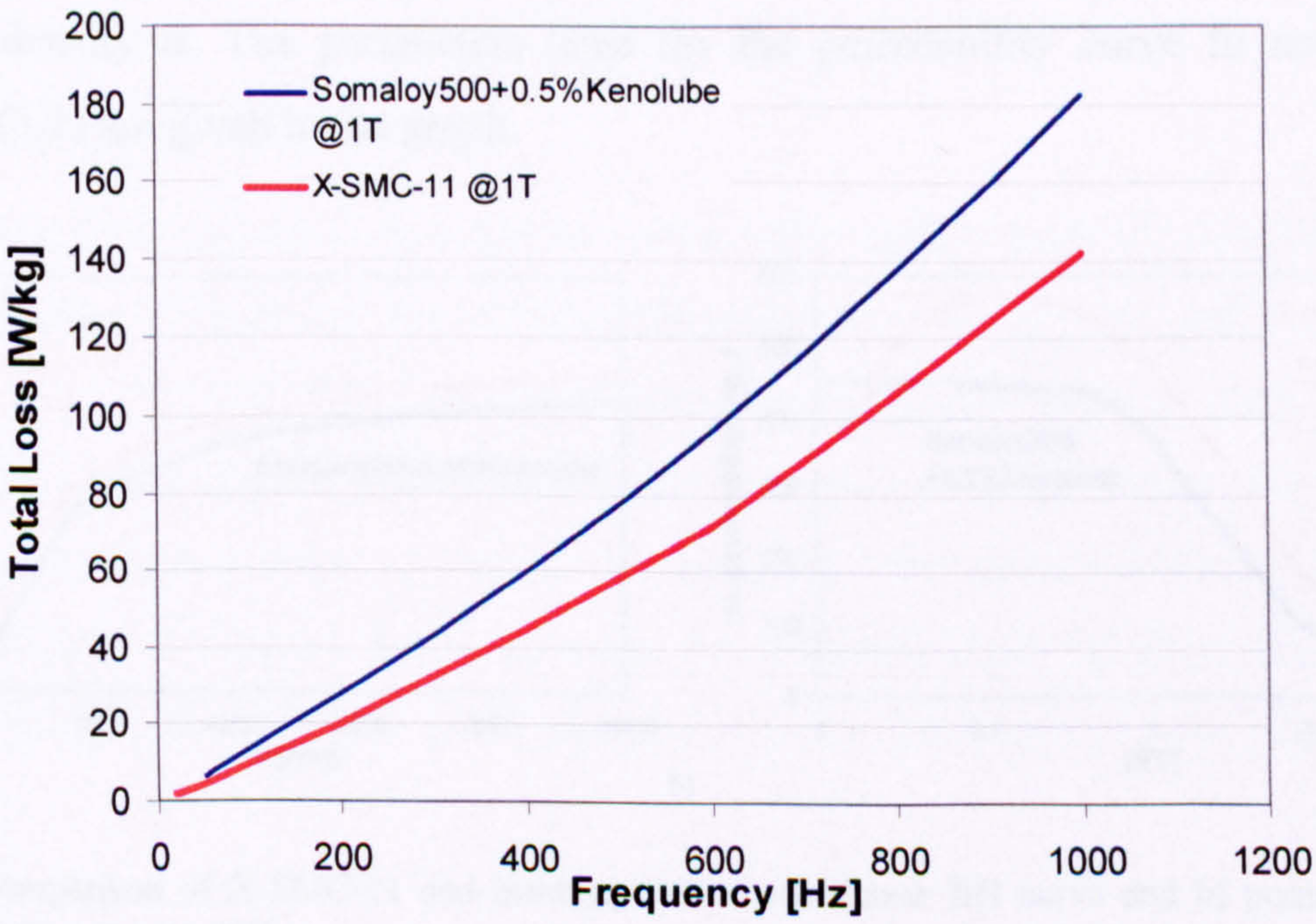

Fig. 7.1 Comparison of total losses of X-SMC-11 and Somaloy500+0.5%Kenolube at 1T measured on the standard ring sample [64]

Fig. 7.2 shows the hysteresis loss per cycle as a function of the peak flux density for the X-SMC-11 material in comparison to Somaloy500, including the constants used for calculating the hysteresis loss according to equation (5.2). The hysteresis loss constants are obtained from the total loss data per cycle by using a best curve fit. Comparing the loss/cycle at 1T the new material promises a reduction in hysteresis loss of 37%.

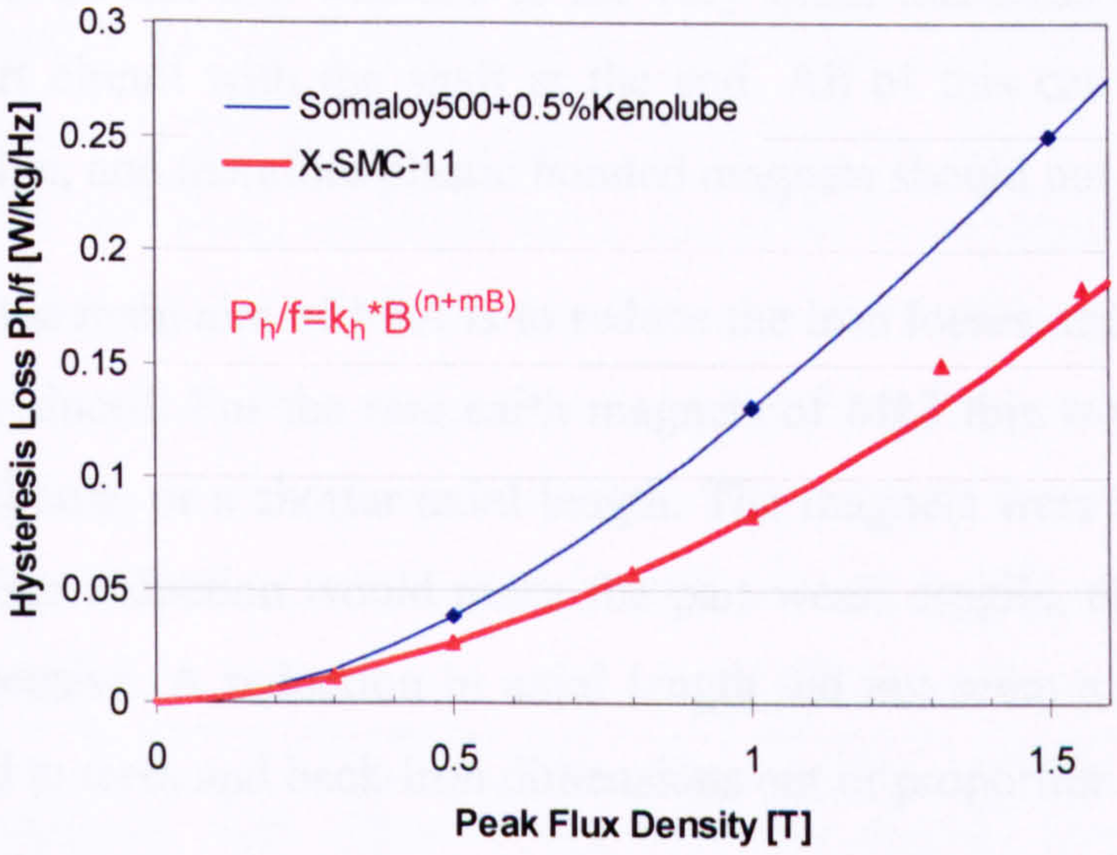

with the following parameters for X-SMC-11:

k_h	0.08216
n	1.56377
m	0.11360

Fig. 7.2 Comparison of hysteresis loss per cycle versus peak flux density for X-SMC-11 and Somaloy500

Fig. 7.3a shows the BH-curve of the two materials. The steeper slope represents the increase in permeability. In Fig. 7.3b the relative permeability is plotted as a function of the flux density *B*. The parameters used for the permeability curve fit according to equation (3.1) are given in the graph.

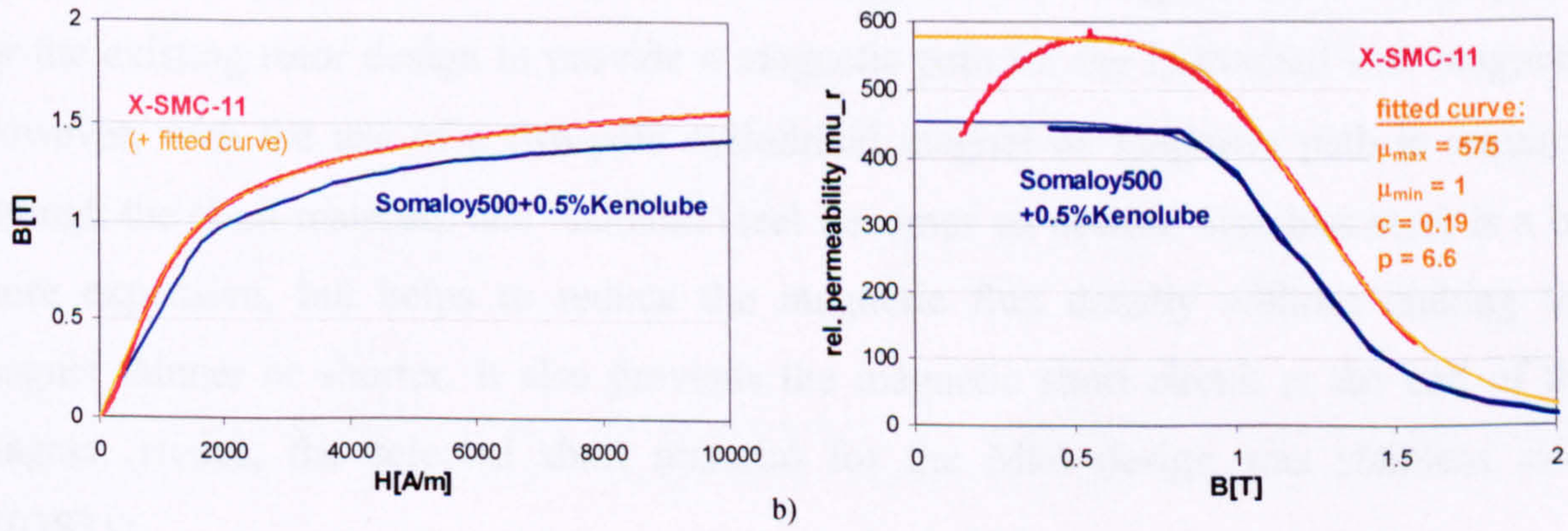

Fig. 7.3 Comparison of X-SMC-11 and Somaloy500: a) non-linear BH curve and b) permeability as a function of flux density [64]

7.2.2 Magnet Material

Sintered and plastic bonded neodymium-iron-boron magnets have both been used in the previous prototypes. The initial concept was for deep plastic bonded magnets to keep the rotor losses to a minimum. Unfortunately the plastic bonded magnets gained a bad reputation due to the much lower fields than predicted especially in Mk2. However, it is believed that this was due to the very small thickness of the magnet, and the magnetic short circuit with the shaft at the end. All of this can be taken into account in a new design, and therefore plastic bonded magnets should not be ruled out.

As the main aim of Mk4 is to reduce the iron losses, the flux density in the iron needs to be reduced. For the rare earth magnets of Mk3 this would mean either an even smaller thickness, or a shorter axial length. The magnets were already thin at 1.86mm, and any further reduction would make the part weak, fragile, difficult to manufacture and more expensive. A reduction in axial length did not seem a viable option either, as it would lead to teeth and back-iron dimensions out of proportion with each other.

Therefore the Mk4 motor returns to the original concept using again a deep plastic bonded magnet for the SMC Mk4 motor. The material chosen is EPN71/63 from SG Magnets, a different supplier to the first prototypes. The magnet is protected by the existing non-conductive, carbon-fibre sleeve, as with previous designs.

7.2.3 Shaft Material

So far all prototypes have had magnetic, carbon steel shafts. Magnetic steel was required for the existing rotor design to provide a magnetic path for the individual slab magnets. However, with the use of a two-pole cylindrical magnet no magnetic path is required through the shaft material, and stainless steel becomes an option. Stainless steel is a bit more expensive, but helps to reduce the magnetic flux density without making the magnet thinner or shorter. It also prevents the magnetic short circuit at the end of the magnet. Hence, the selected shaft material for the Mk4 design was stainless steel (303S31).

7.3 Physical Dimensions

The maximum space envelope was still the same as defined by the existing laminated motor. The dimensions, which were open to choose, were the magnet / shaft interface for

the rotor design, and the axial length, width and 3D shape of the stator teeth, and back iron for the stator. These will be discussed next.

7.3.1 Magnet ID and Shaft Diameter

One of the reasons why the deep plastic bonded magnet was abandoned after Mk1 was the risk of rotor dynamic problems resulting from the thin shaft (shaft was 10mm compared with 13.6mm of the existing shaft). It was feared (based on one bad experience in the past) that the shaft might not be stiff enough to withstand the forces during run-up and at full speed, especially for some of the larger pump variants with longer and heavier impellers. However, further modelling carried out by a colleague working in the field of rotor dynamics has shown that the cylindrical magnet itself provides additional stiffness, and that a shaft diameter of 10mm would be acceptable even for the pump with the longest and heaviest impeller (EXT70-70-200 splitflow pump).

Fig. 7.4a shows the model and Fig. 7.4b shows the first natural bending frequency as a function of shaft diameter and different magnet length. A higher natural frequency indicates a stiffer shaft, which is the case for the new cylindrical magnet compared to the existing design, even at a shaft diameter as low as 10mm.

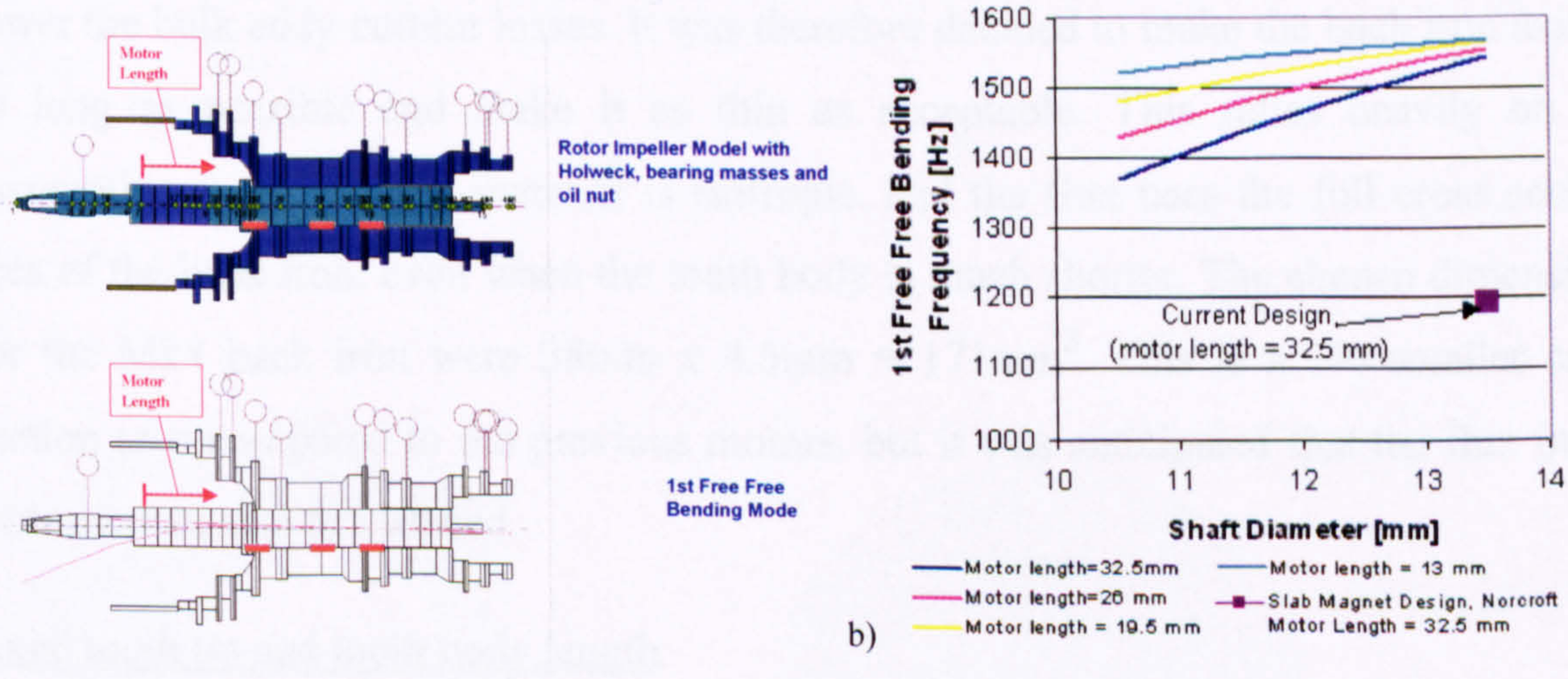

Fig. 7.4 EXT70/70/200 Splitflow Rotor: a) rotor dynamic model with plastic bonded NdFeB cylindrical rotor magnet, b) free-free frequency as a function of shaft diameter and motor axial length [65]

Ideally the shaft would be made as big as possible to reduce the risk of bending, but that becomes a compromise of how much magnet thickness is required to give the desired back EMF. Several scenarios have been modelled with FE and a magnet ID of 10.5mm (shaft diameter of 10.4mm) was selected for Mk4. This gives a magnet thickness of 2.91mm.

7.3.2 Back Iron, Tooth and Tooth Tip Dimensions

To find the best shape, ideally a 3D optimisation program would be required. In the absence of such a tool individual dimensions were selected by a manual optimisation process, i.e. running several 2D-FE models with varying dimensions and determining the trend to minimise iron loss.

During the work on the SMC iron losses of the first three prototypes (see Chapter 5) it became obvious that the bulk eddy currents are a significant part of the losses, and that they depend a great deal on the component dimensions. If the smallest dimension of the cross section normal to the flux is greater than the skin depth of the material then the eddy currents are no longer purely resistance limited and the losses go up. This is the case in the tooth body and tooth tips as their smallest dimensions are typically larger than the skin depth (skin depth of X-SMC-11 at 1000Hz is about 6mm to 9mm depending on permeability, i.e. larger than with Somaloy500).

Back iron

The back iron was 36mm x 5mm = 180mm^2 in the previous motors (Mk2 & Mk3). For the same cross section area, the losses are a function of the smallest component dimension, which in this case is the width of the back iron – the smaller the width, the lower the bulk eddy current losses. It was therefore decided to make the back iron axially as long as possible and make it as thin as acceptable. This relies heavily on the assumption that the SMC material is isotropic, and the flux uses the full cross section area of the back iron, even when the tooth body is much shorter. The chosen dimensions for the Mk4 back iron were 38mm x 4.5mm = 171mm^2. This is a 5% smaller cross section area compared to the previous motors, but it was anticipated that the flux in the motor would also be reduced.

Axial tooth tip and tooth body length

One of the main advantages of SMC is its ability to carry three-dimensional flux. The initial idea was to have extended tooth tips to collect the magnetic flux, and a shorter tooth body to reduce the amount of endwindings. However, analysis of the bulk eddy current loss has shown that for the same tooth cross section area a long, thin tooth would have less eddy currents than a round one. This leads to a tooth body of similar height as the tooth tips.

The prototype motors Mk1 & Mk2 had a tooth tip length of 31mm and Mk3 of 14mm. For Mk4 a length somewhere between these values was chosen. An axial length of 19mm for the tooth tips was selected as a result of the magnet strength and back EMF requirement. The tooth body was chosen to be slightly shorter, i.e. 16mm, to give a better hold for the windings and not to loose all of the benefit of shorter endwindings.

The tooth tips were made much simpler in shape by removing the small features on the sides, plus adding some more material to reduce the flux density. In addition the step at the tooth-backiron interface was removed on the tooth (Fig. 7.5b). All this should help to reduce the damage done by machining very thin sections of the SMC material.

Slot opening

To avoid running out of volts the inductance needed to be limited. An increase in inductance compared to the existing motor with some phase advance was allowable for Mk4. To reduce the inductance, the slot openings were increased. This reduced the slot leakage flux significantly, and hence reduced the inductance with hardly any effect on the back EMF. However, larger slot openings will have a negative effect on the rotor tooth ripple losses. However, the total rotor iron losses will not be more than in the existing rotors due to using deep plastic bonded magnets and a stainless-steel shaft (see section 7.6.2 about rotor loss in Mk4). Consequently, the slots were opened up from 2.0mm to 4.6mm.

Fig. 7.5 shows a photo of the SMC components: the back iron ring, one tooth and all the parts without coils.

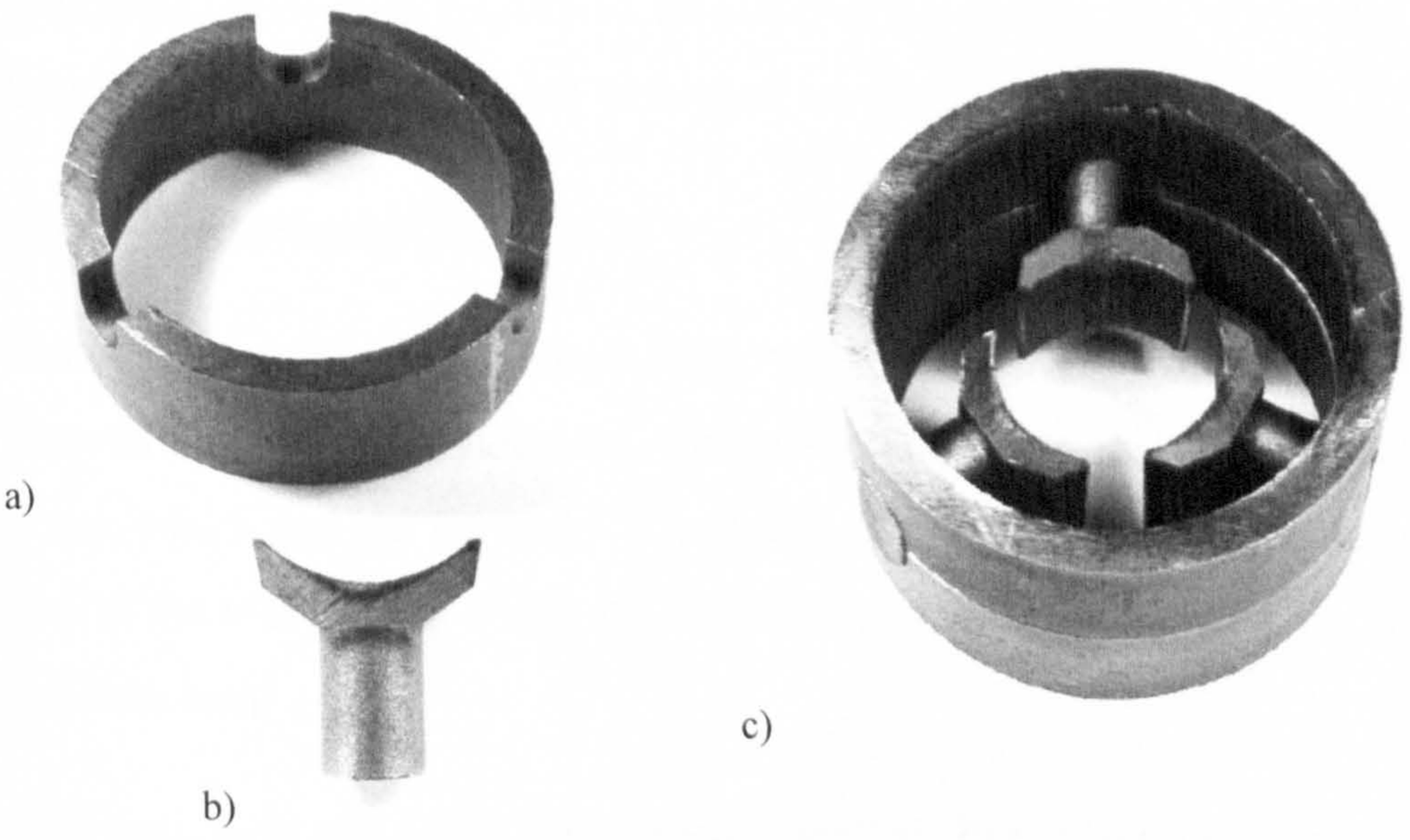

Fig. 7.5 SMC components for the Mk4 motor: a) one of the two back iron rings, b) one of three teeth, c) all the parts for the SMC stator

7.4 The Complete Mk4 Stator

7.4.1 Prototyping

The only shortcoming of the new SMC material is the difficulty of prototyping. Trials had shown an even greater sensitivity of material properties to machining and wire erosion than with Somaloy500. To avoid this the initial plan was to machine the SMC parts in their 'green' state, i.e. after compaction but before heat treatment. This should give more consistent material properties, and any stresses introduced in the part during machining could at least be partially be relieved by heat treating it afterwards. Machining in the green state is not easy, as the strength of the material is lower, but on the other hand it is also much softer to cut. Nevertheless thin sections are tricky and must be handled extremely careful. In the end, 'green-cutting' of these motor parts was not feasible and the parts for Mk4 were spark-eroded out of prefabricated (compacted and heat treated) blanks.

To determine how the EDM process had affected the material properties, especially the conductivity and permeability of the material, measurements on the back iron rings were carried out (see Appendix B). The conductivity of the two back iron rings was 9,790 S/m and 13,380 S/m. This is not far off a promised conductivity of less than 10,000, but it also shows a significant variation between supposedly identical parts. The permeability of the back iron ring was measured with a peak value of 300 to 350, significantly lower than the promised 600. The properties of the tooth component were not measured, but are expected due to the thinner sections to be more seriously affected. Hence, testing a prototype motor with respect to its material properties is a worst-case scenario, and an improvement can be expected with parts compacted into shape.

7.4.2 Assembly of SMC Mk4

Due to the simpler tooth shape there was no longer any feature on the teeth to locate them in the back iron. However, with some simple tooling the teeth were located against a rod, which defined the stator ID, during the gluing process. Not having the step at the end of the tooth also avoided having additional air gaps / glue gaps in the interface with the back iron.

The back iron and teeth were glued together. The tolerances were chosen, so that the back iron rings would touch before the teeth are clamped. This gave better accuracy on

squareness of the two back iron rings, which was critical for the assembly into the body's bore. Clamping the teeth was the other option, which would give better contact between the parts if it could be guaranteed that they would all touch. However, if one tooth was smaller than the others it might not get clamped, and the back iron could become tilted. There was also a danger of cracking either the back iron or tooth corners. Both were undesired effects. As the glue gaps are small (nominal of 0.15mm = 5.2% of the 2.84 mm air gap), the effect on the electromagnetics was believed to be small.

As there were only enough parts to make one motor of the new design, it was decided not to pot the motor. This would allow the winding to be removed and replaced and permit small modifications to the SMC parts should it be required. As the motor was built directly into a turbo pump, there was also less risk damaging the unpotted tooth tips, than there would be in the back-to-back rig due to the way the shaft is inserted into the motor stator. Fig. 7.6 shows the complete Mk4 stator with coils and hall sensor board.

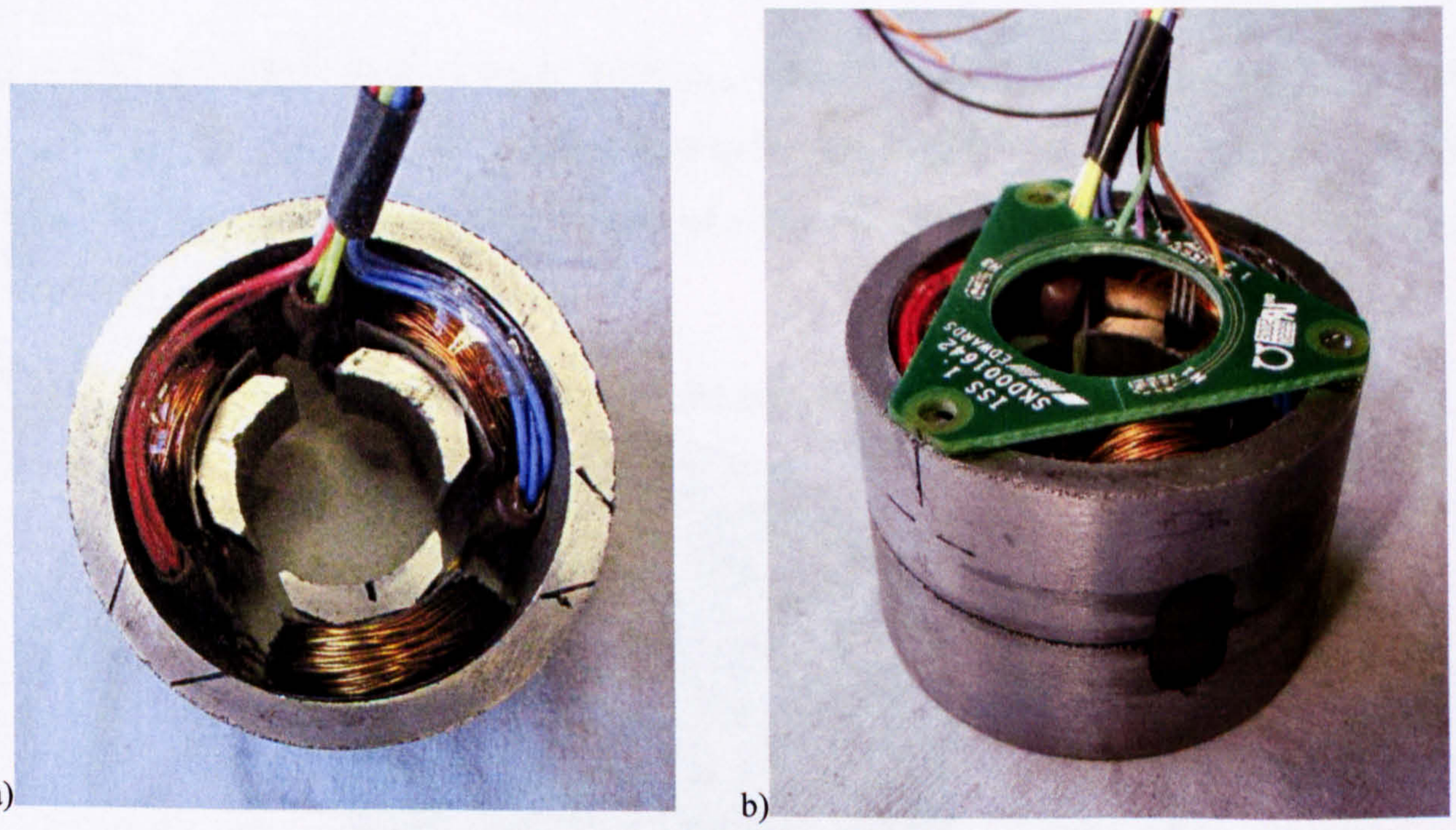

Fig. 7.6 The complete SMC Mk4 stator: a) top view, b) complete with Hall sensor board

7.5 Machine Parameters – Design Versus Measurement

7.5.1 Back EMF and Open-Circuit Peak Flux Densities

To minimise the impact on the drive, the aim was to keep the line back EMF very similar to the existing value of $14.5V_{rms}$, maybe a bit lower to allow for more voltage headroom for the increased inductance in this new design. The measured back EMF values in the past had been about 10-15% lower than the predicted values with plastic bonded magnets. This was partly due to the magnet being magnetically short-circuited by the magnetic shaft and partly due to optimistic data sheets. The rotor design for Mk4 uses a non-magnetic shaft material, avoiding so the magnetic short-circuit. To allow for optimistic magnet data a 10% reduction was included in the prediction. The back EMF is predicted as before from a 2D finite-element model of the motor in open circuit. Fig. 7.7 shows the flux density plot, and Fig. 7.8 shows the back EMF versus axial length (i.e. tooth tip length) and number of turns per phase. As a result a tooth tip length of 19mm and 50 turns per phase were chosen for Mk4, giving an expected back EMF of $14.1V_{rms}$.

The measured back EMF came to $14.9V_{rms}$. This is 5.5% higher than predicted, which means the assumption of 10% reduction was too pessimistic, but it is the closest results of all the motors built so far. The number of turns can easily be reduced to make sure that the motor does not run out of volts.

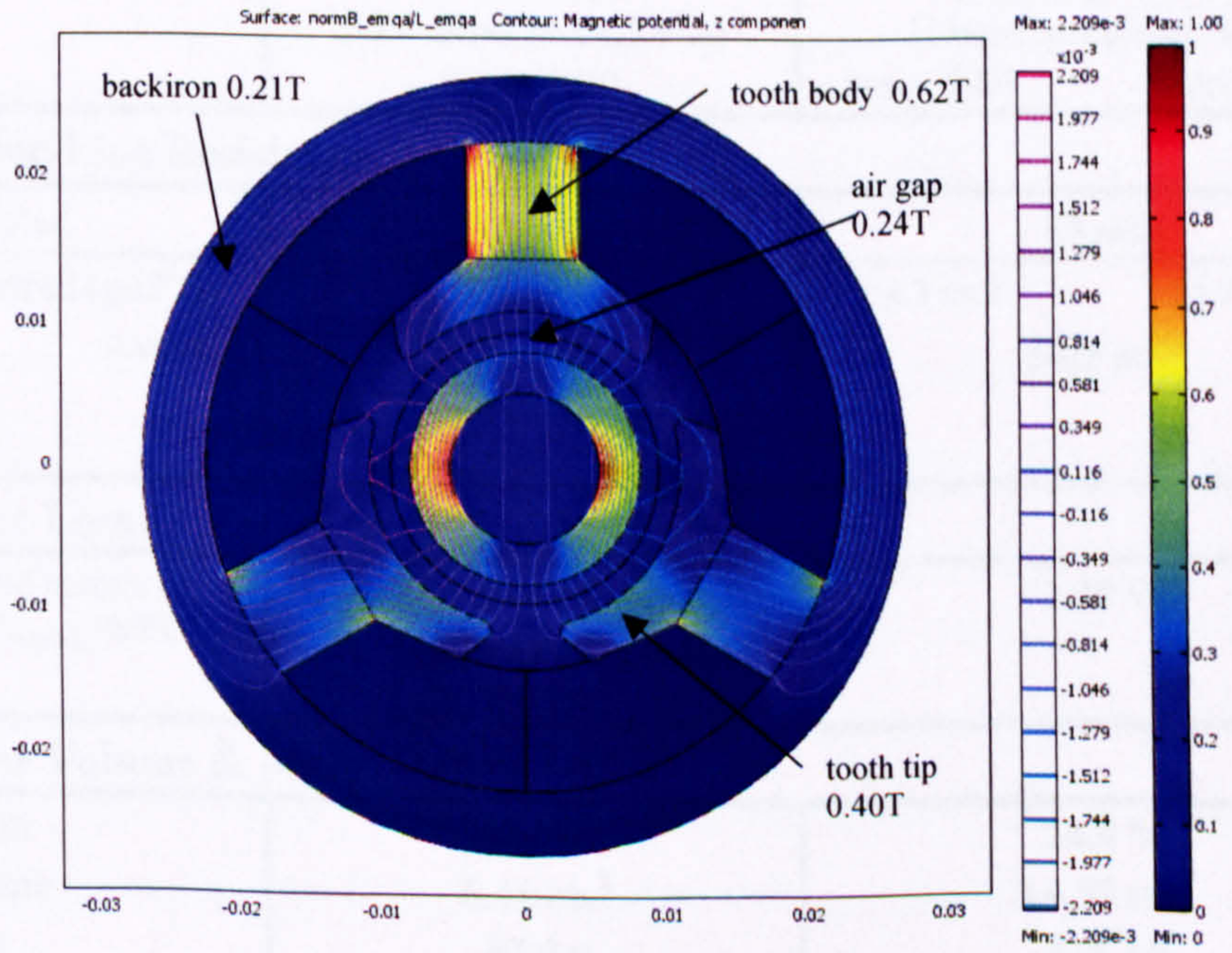

Fig. 7.7 Open-circuit flux density plot for SMC Mk4 motor (flux densities include the space-factor for the back iron (sf=2) and tooth body (sf=0.75); magnet data: B_r=0.7T, H_c=430kA/m; μ_{r_SMC}=575 non-linear). Flux linkage for one turn per meter: 0.00372 Wb/m)

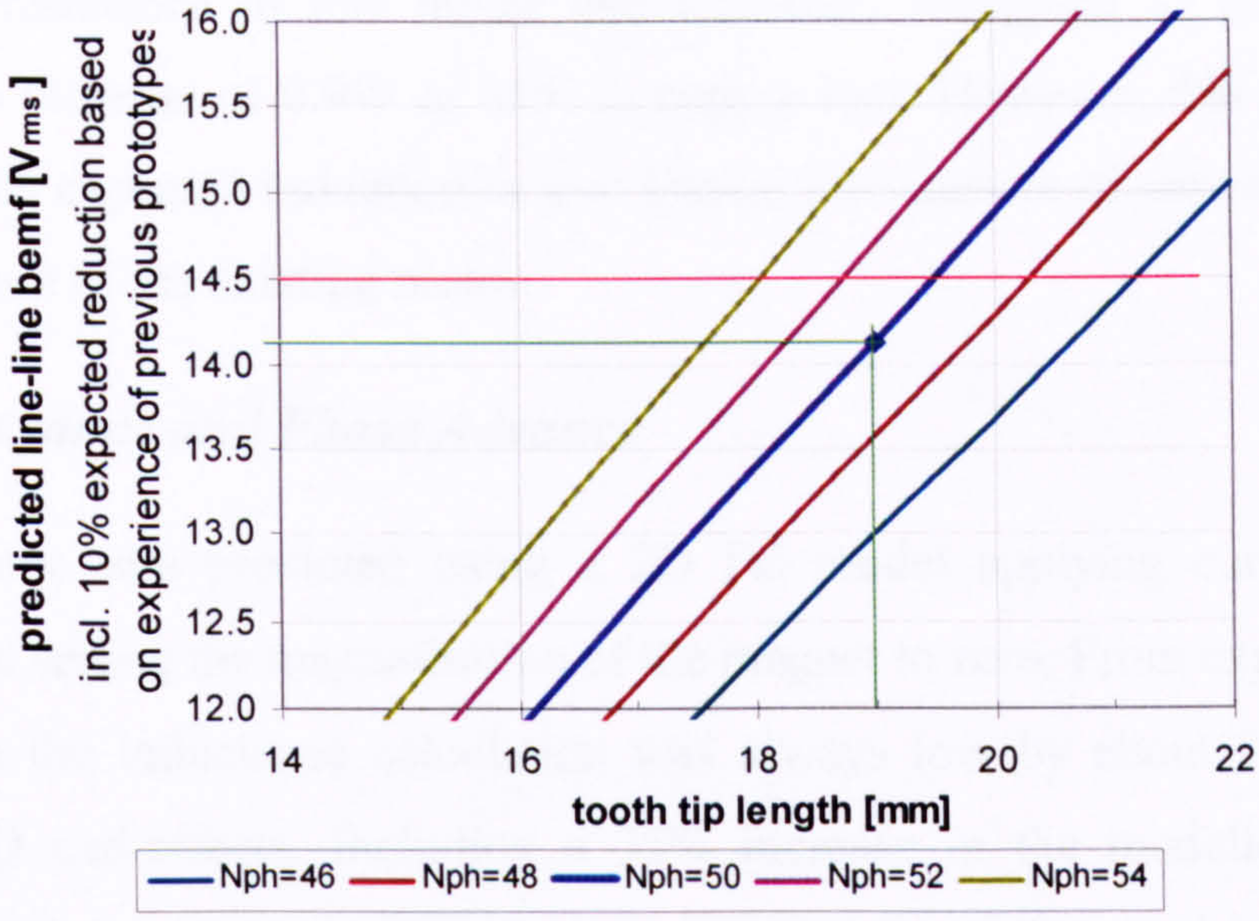

Fig. 7.8 Predicted back EMF as a function of tooth tip length and number of turns per phase (based on above FE model)

7.5.2 Resistance and Copper Loss

The motor was wound with 50 turns of 3 parallel strands of 0.5mm wire diameter. The slot fill factor was only 23%, which is low as can be seen from the space between the coils in Fig. 7.6a, and could probably be increased. However, the axial height of the coils (i.e. the size of the endwindings) just allowed the hall board to be fitted flat on the back iron ring, which was necessary in order to avoid exceeding the overall stator length.

	SMC Mk4 (50turns per phase, Delta) Stator S010	**Existing Motor** (14turns per phase, Star) Stator S004	Stator S005
DC Line-Line Resistance			
Predicted	**73 mΩ**	**55 mΩ**	
Measured (@25°C)	76 mΩ	54.2 mΩ	54.7 mΩ
Average	**76 mΩ** **39 % more** than existing motor	**54.5 mΩ**	
Copper Loss			
with rated current of $5A_{rms}$, $T_{winding}$=60°C	**3.26 W** **39 % more** than existing motor	**2.35 W**	
Copper Volume & Mass			
Slotfill	**23.3%**	**24.4 %**	
Volume	**6.41 cm^3**	**14.32 cm^3**	
Mass	**57.4 g** **55 % less** than existing motor	**128.3 g**	

Table 7.1 DC resistance, copper loss, and copper volume for SMC Mk4

Overall the resistance in this motor had increased compared to the existing motor, leading to an increase of 0.9W or 39% in copper loss. However, this will be more than covered by the expected reduction in iron losses. The amount of copper used is less than half the amount of the existing motor.

7.5.3 Inductance and Phase Advance

The inductance was predicted using a 2D FE model applying current to the phase windings, but setting the magnetisation of the magnet to zero. From experience of the last three motors the inductance calculation was always low by about 30-35% due to the neglected 3D end-effects. Including a 35% increase in the modelled inductance the expected line-line inductance for 50 turns and 16mm tooth body length is 245μH (see Fig. 7.9).

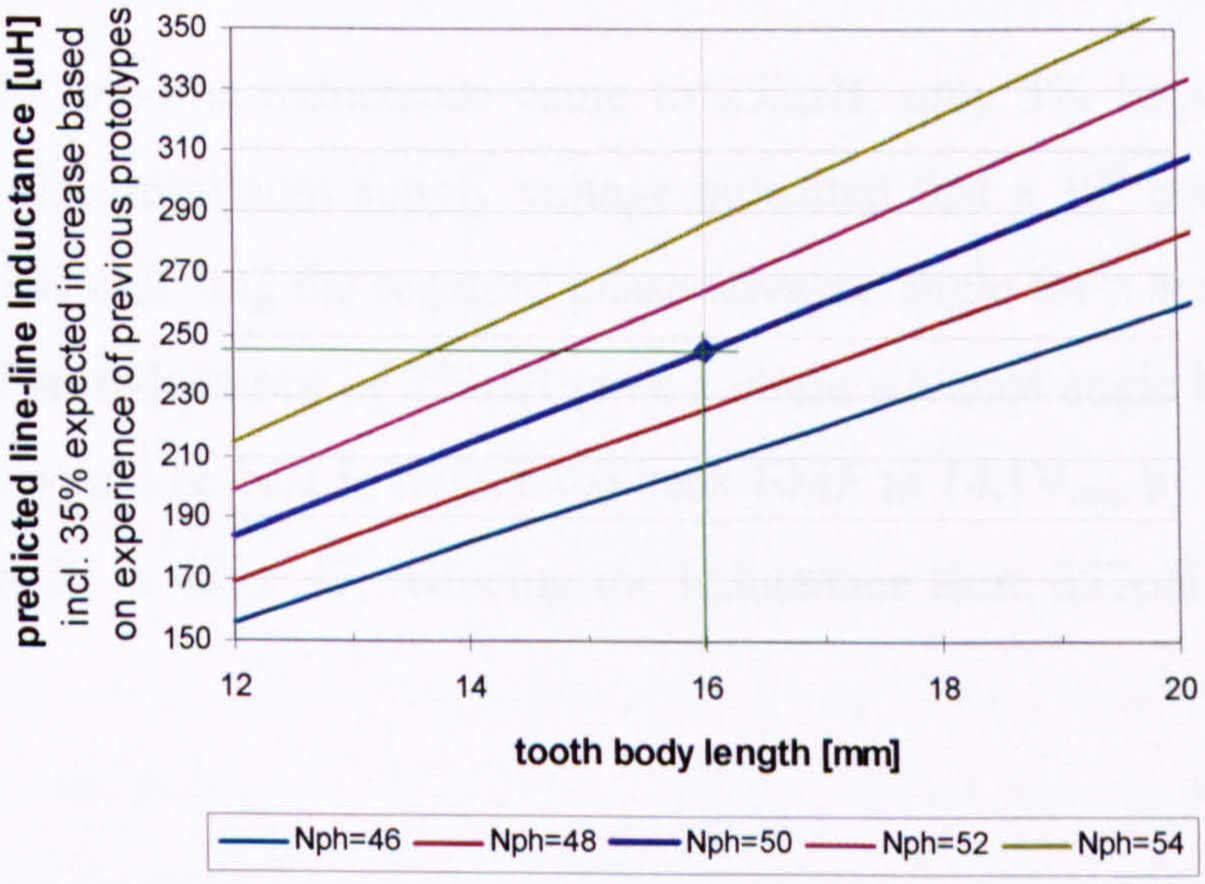

Fig. 7.9 Predicted Line-line Inductance for SMC Mk4 motor as a function of tooth body length and number of turns per phase

This is 2.2 times the line-line inductance of the existing motor. To cope with the larger inductance and the associated voltage drop, the drive needs to apply the current earlier. A maximum phase advance angle of 30° was selected for reasons presented in Chapter 3. Simulating the drive characteristic (see 3.6), the output power can be calculated as a function of the applied phase advance for a given supply voltage, back EMF, resistance and inductance. Fig. 7.10 shows the resultant output power. The requirement was for a minimum of 110W output power at –5% supply voltage, allowing the power then to drop to around 75-80W for –10% supply voltage. A phase advance angle of 30° just fulfils the requirements.

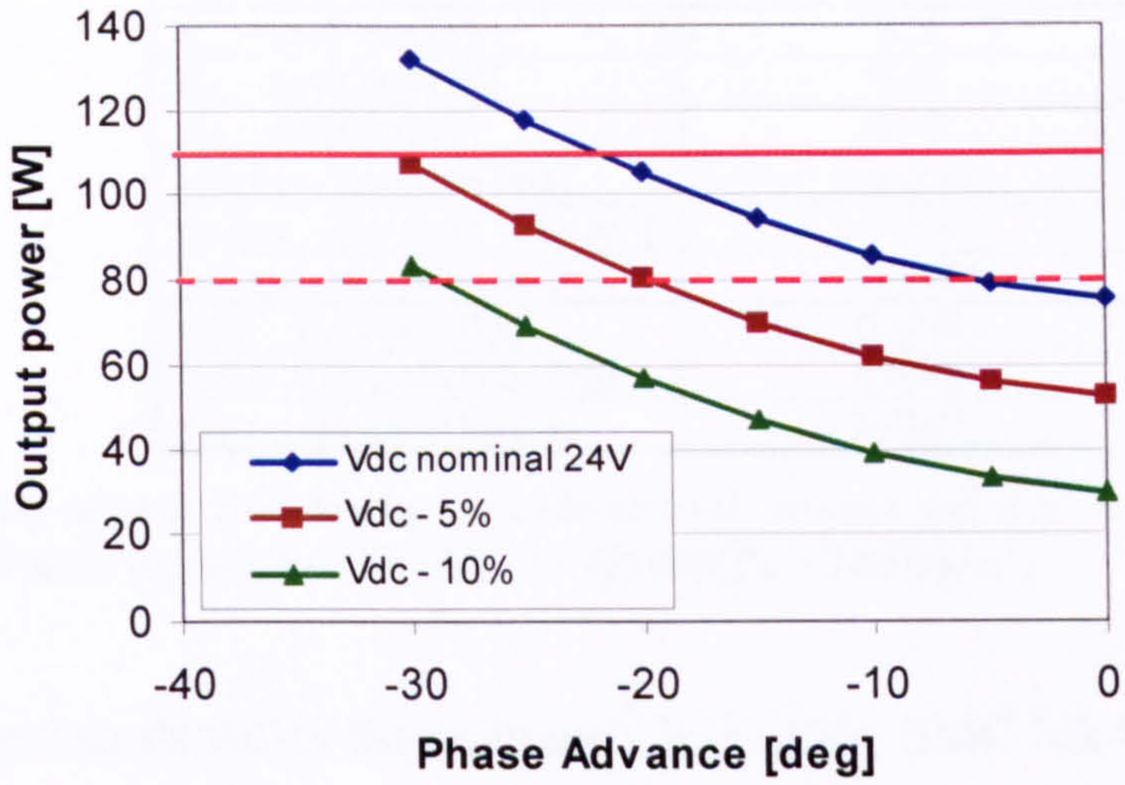

Input parameter: e_ll=14.1V_{rms}, L_ll=245μH, R_ll=0.09Ω, allowing for 0.5V drop in controller, pwm-index=0.99 (nearly in full voltage control), frequency=1000Hz.

Fig. 7.10 Simulated output power as a function of phase advance angle.

The measured line-line inductance came to 252μH, only 3% larger than the expected value. Tests with minimum supply voltage indicated that a 30° phase advance angle is not enough. Remodelling the required phase advance angle for a measured back EMF of 14.9V_{rms} and an inductance of 252μH gave a phase advance angle between 35° and 40°. Long term it would be best to reduce the back EMF to 14.1V_{rms} by reducing the number of turns from 50 to 48 or 47, reducing the inductance from 252μH to 232μH or 222μH respectively.

7.6 Predicted Iron Losses

7.6.1 No-load SMC Core Losses

Following the method presented in Chapter 5 the hysteresis, in-grain and bulk eddy current loss were calculated separately. The stator was divided as before into three regions: the back iron, the tooth body, and the tooth tip. The peak flux densities in each region were determined by FE (Fig. 7.7, page 133), and Table 7.2 summarises the values used for the SMC Mk4 motor stator.

	SMC Mk4
B_{pk} – back iron [T]	0.21
B_{pk} – tooth body [T]	0.62
B_{pk} – tooth tip [T]	0.40
volume – back iron [m3]	2.66E-05
volume – one tooth body [m^3]	8.91E-07
volume – one tooth tip [m^3]	1.31E-06
mass – back iron [kg]	0.1968
mass – one tooth body [kg]	0.0066
mass – one tooth tip [kg]	0.0097

Table 7.2 Summary of peak flux density (in open-circuit), volume and mass of each region for the SMC Mk4 motor (mass based on density of X-SMC-11 @800MPa = 7400kg/m^3)

With the above flux densities the hysteresis loss of the SMC Mk4 motor was calculated according to equation (5.2), using the material constants for the new X-SMC-11 material (see Fig. 7.2, page 126). Table 7.3 (at the end of the section) shows the calculated hysteresis loss for SMC Mk4 in comparison to the previous motors. The hysteresis loss of Mk4 is with 2.65W the lowest so far thanks to the improved material properties.

The in-grain iron losses were calculated according to equation (5.6), with a mean grain diameter of 0.2mm for X-SMC-11. This is double the grain diameter of Somaloy500, potentially leading to a factor of four increase in the in-grain iron losses. However, as flux density levels and stator volume was less than before, the in-grain losses were not much more than in previous motors (see Table 7.4).

The bulk eddy current losses were modelled using FE as described in Chapter 5. The conductivity used in the FE models is 13,550 S/m, which was the result of matching the bulk eddy current losses modelled in FE of the standard test ring to the bulk eddy current losses obtained from the total losses measured by the manufacturer minus hysteresis minus in-grain loss for the standard ring. Table 7.5 summarises the losses in comparison to the previous motors. Here a significant loss reduction has been realised, mainly due to the lower conductivity of the new SMC material.

The total predicted stator iron loss of the SMC Mk4 motor comes to 5.4W, which is a significant reduction compared to the previous motors, and theoretically even better than the existing laminated motor with 6.5-7W. The losses of the SMC Mk4 motor are made up of 49% hysteresis loss, 11% in-grain eddy current loss and 41% bulk eddy current loss (see Table 7.6).

	SMC Mk1.1	SMC Mk2 (remagnetised)	SMC Mk3	SMC Mk4
P_h – back iron [W]	5.4801	1.7107	2.4932	1.3570
P_h – 3 x tooth body [W]	2.3967	0.7424	1.3796	0.7443
P_h – 3 x tooth tip [W]	1.6841	0.4928	1.2061	0.5462
Total Hysteresis Loss [W]	**9.56**	**2.95**	**5.08**	**2.65**

Table 7.3 Hysteresis loss for SMC Mk4 in comparison to the previous motors

	SMC Mk1.1	SMC Mk2 (remagnetised)	SMC Mk3	SMC Mk4
$P_{In\text{-}Grain}$ – back iron [W]	0.2414	0.0688	0.1037	0.2407
$P_{In\text{-}Grain}$ – 3 x tooth body [W]	0.1186	0.0319	0.0652	0.2110
$P_{In\text{-}Grain}$ – 3 x tooth tip [W]	0.0784	0.0204	0.0593	0.1289
Total In-Grain Eddy Current Loss [W]	**0.44**	**0.12**	**0.23**	**0.58**

Table 7.4 In-grain eddy current loss for SMC Mk4 in comparison to the previous motors

	SMC Mk1.1	SMC Mk2 (remagnetised)	SMC Mk3	SMC Mk4
$P_{Bulk\ Eddy}$ – back iron [W]	5.4051	1.1026	1.6556	0.4870
$P_{Bulk\ Eddy}$ – 3 x tooth body [W]	8.4115	2.2431	3.4415	0.9884
$P_{Bulk\ Eddy}$ – 3 x tooth tip middle [W]	2.3019	0.5991	1.2181	0.6389
$P_{Bulk\ Eddy}$ – 6 x tooth tip side [W]	0.2345	0.0610	0.1633	0.0993
Total Bulk Eddy Current Loss [W]	**16.35**	**4.01**	**6.48**	**2.21**

Table 7.5 Bulk eddy current loss for SMC Mk4 in comparison to the previous motors

	SMC Mk1.1		SMC Mk2 (remagnetised)		SMC Mk3		SMC Mk4	
Hysteresis Loss [W]	9.56	36%	2.95	42%	5.08	43%	2.65	49%
In-Grain Loss [W]	0.44	2%	0.12	2%	0.23	2%	0.58	11%
Bulk Eddy Current Loss [W]	16.35	62%	4.01	57%	6.48	55%	2.21	41%
Total Stator Iron Loss [W]	**26.35**		**7.08**		**11.79**		**5.44**	

Table 7.6 Total no-load loss of SMC Mk4 in comparison to the previous motors

7.6.2 Rotor Losses

Three sources of rotor loss are identified in Chapter 6: space harmonics, time harmonics and tooth ripple loss. All three will be predicted for the Mk4 rotor, and compared with the previous rotor losses. The calculation methods and FE models used are described in detail in Chapter 6.

Fig. 7.11 shows a schematic of the rotor construction of Mk4. It is very similar to the first SMC rotor as it employs a deep plastic bonded magnet, protected with a non-conductive carbon fibre sleeve. However, the shaft material has been changed from magnetic carbon steel to stainless steel. Stainless steel is non-magnetic, i.e. $\mu_r = 1$, and has a 3.5 times lower conductivity than carbon steel ($1.4 \cdot 10^6$ S/m compared to $5 \cdot 10^6$ S/m). As a

consequence the skin depth of stainless steel is much larger than of magnetic carbon steel (see Table 6.9, 13.5mm versus 0.7mm for 1000Hz). Hence, the eddy current losses in the shaft are not skin limited. This can clearly be seen from the flux and current density plots for the space harmonics and tooth ripple loss calculation (Fig. 7.12 and Fig. 7.13).

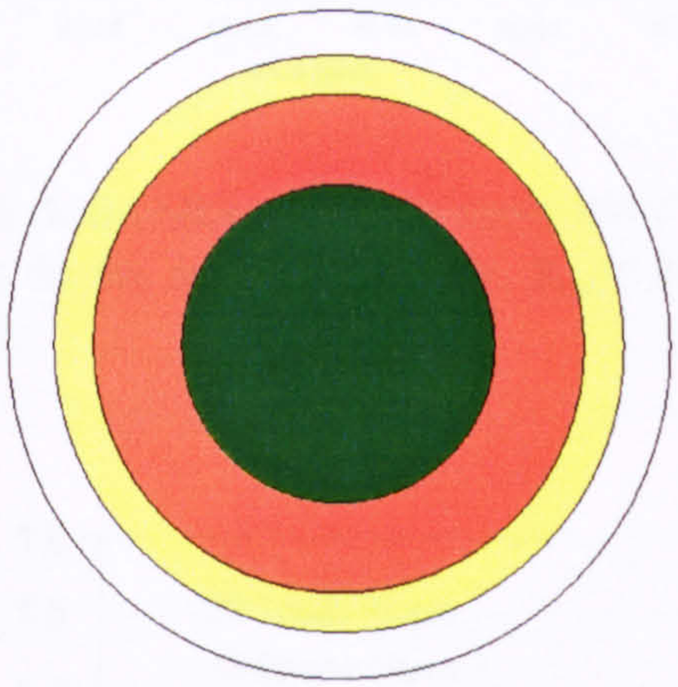

Colour	Material
	Stainless steel 303S31 μ_r=1, σ =1.4·10^6 S/m
	Plastic bonded NdFeB magnets μ_r=1.375, σ =5·10^3 S/m
	Carbon fibre sleeve: μ_r=1, σ =0 S/m
	Air: μ_r=1, σ =0 S/m

Fig. 7.11 Schematic of SMC Mk4 rotor cross section

To be able to compare the calculated rotor losses with the previous rotor constructions, the losses are based on a modelled current waveform that delivers about 100W shaft output power. Fig. 7.14 shows the waveform for Mk4 and its harmonic spectrum.

The space and time harmonic losses, as well as the tooth ripple losses are summarised in Table 7.7 to Table 7.9 for the Mk4 rotor in comparison to the previous rotors. Fig. 7.15 compares the total rotor losses graphically

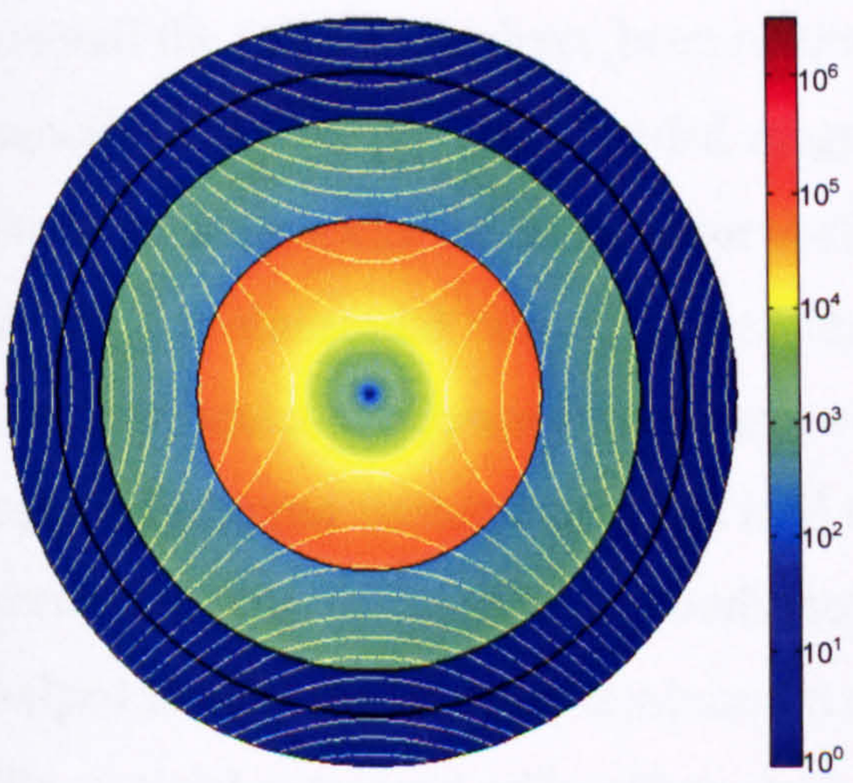

Fig. 7.12 SMC Mk4 – Flux plot and magnitude of induced eddy current density (A/m^2) due to the 2nd space harmonic (same scale as Fig. 6.7, for comparison)

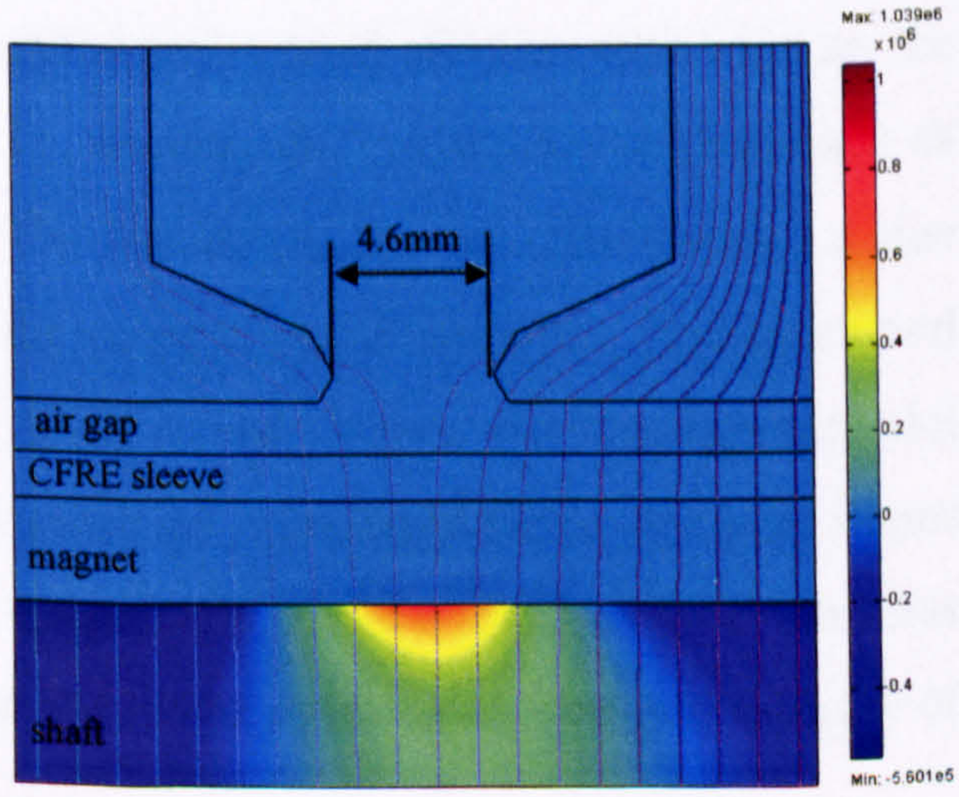

Fig. 7.13 SMC Mk4 – Flux plot and induced current density (A/m^2) due to slot/tooth ripple loss (same scale as Fig. 6.10, for comparison)

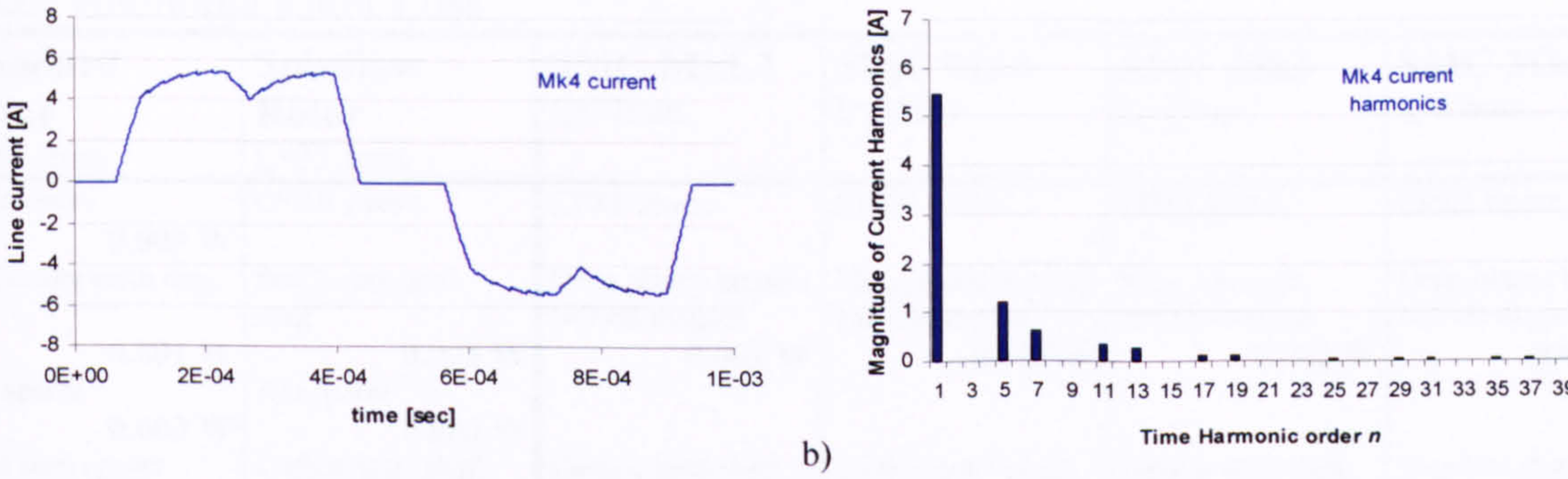

a) b)

Fig. 7.14 Modelled Mk4 current for about 100W shaft output power: a) waveform, b) harmonic spectrum. (Parameters for the model: V_{dc}=23.2V, R_{LL}=0.075Ω, L_{LL}=252uH, E_{LL}=14.9V, phase_adv=-30deg, pwm-index=0.97)

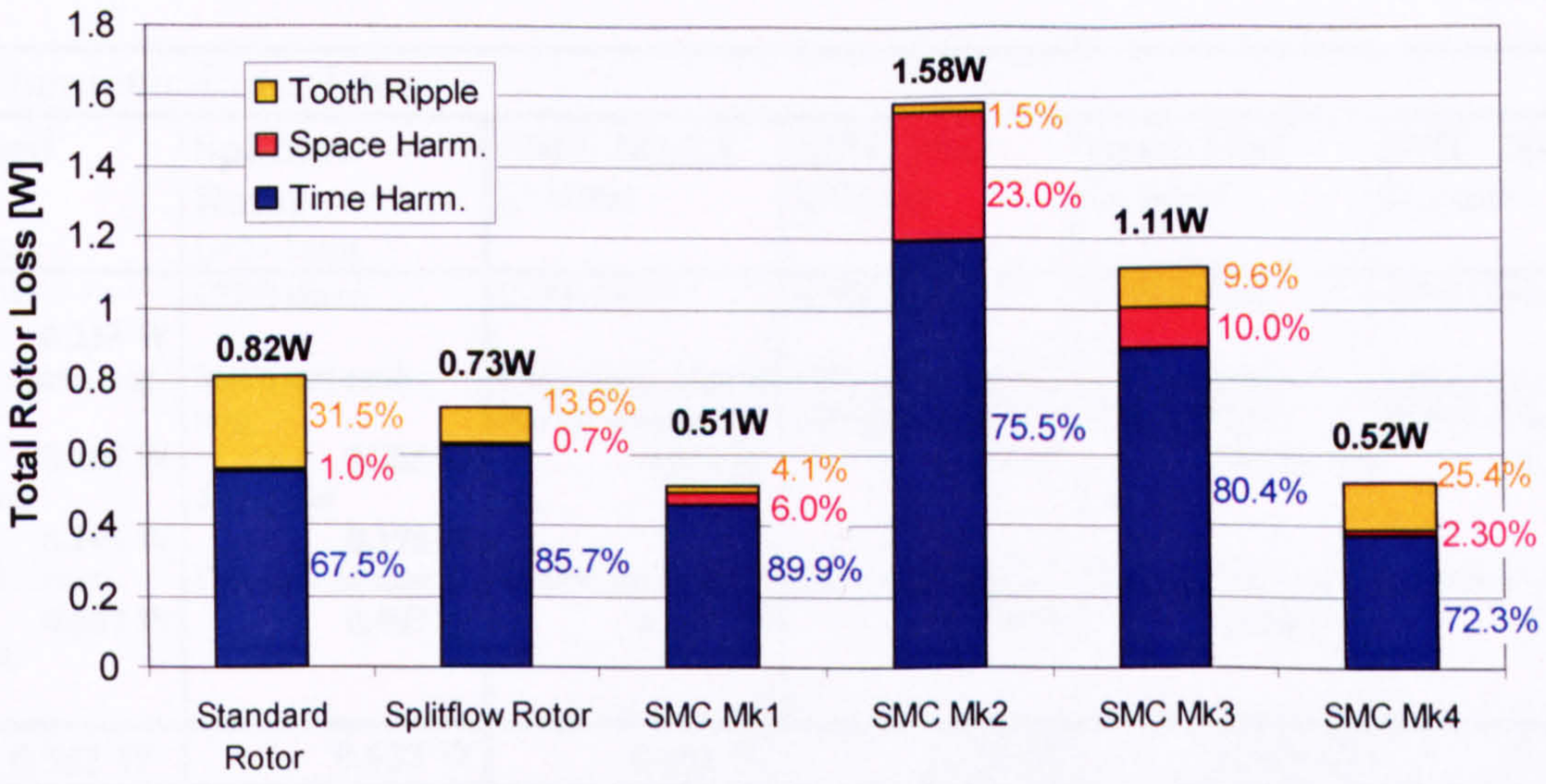

Fig. 7.15 Total rotor losses of all the motors in comparison

Overall the rotor losses have been reduced in Mk4 to the level of Mk1, which shows the benefit of the deep plastic bonded magnets, i.e. moving the conductive shaft surface as far as possible away from the stator surface. The loss due to the time harmonics, i.e. due to the non-sinusoidal current waveform, is the largest loss component. The space and time harmonics are lower than in any of the SMC motors before, but the increased slot opening (4.6mm versus 2mm) has lead to a significant increase in the tooth ripple losses compared with the other three-tooth motors. Conversely, using a stainless steel shaft has helped to keep the losses to a minimum due to the lower conductivity and permeability of the material compared with carbon steel.

Space Harmonic Rotor Loss					
Standard Rotor l_a=27.1mm	**Splitflow Rotor** l_a=27.1mm	**SMC Mk1.1** l_a=31mm	**SMC Mk2** l_a=31mm	**SMC Mk3** l_a=14mm	**SMC Mk4** l_a=19mm
St-St sleeve **0.003 W**	CFRE sleeve -	CFRE sleeve -	CFRE sleeve -	CFRE sleeve -	CFRE sleeve -
SmCo rare earth mag **0.001 W**	SmCo rare earth mag **0.001 W**	Deep plastic bonded NdFeB magnet **0.001 W**	Thin plastic bonded NdFeB magnet **0.003 W**	Thin rare earth NdFeB magnet **0.062 W**	Deep plastic bonded NdFeB magnet **0.001 W**
Alu spacer **0.003 W**	Alu spacer **0.003 W**				
Mild steel carrier **0.001 W**	Carbon steel shaft **0.001 W**	Carbon steel shaft **0.030 W**	Carbon steel shaft **0.361 W**	Carbon steel shaft **0.050 W**	Stainless steel shaft **0.011 W**
St-St shaft -					
Total 0.008 W	**0.005 W**	**0.031 W**	**0.364 W**	**0.112 W**	**0.012 W**

Table 7.7 Space harmonic rotor loss for the SMC Mk4 motor in comparison to the previous motors

Time Harmonic Rotor Loss					
Standard Rotor l_a=27.1mm	**Splitflow Rotor** l_a=27.1mm	**SMC Mk1.1** l_a=31mm	**SMC Mk2** l_a=31mm	**SMC Mk3** l_a=14mm	**SMC Mk4** l_a=19mm
St-St sleeve **0.233 W**	CFRE sleeve -	CFRE sleeve -	CFRE sleeve -	CFRE sleeve -	CFRE sleeve -
SmCo rare earth mag **0.166 W**	SmCo rare earth mag **0.356 W**	Deep plastic bonded NdFeB magnet **0.020 W**	Thin plastic bonded NdFeB magnet **0.021 W**	Thin rare earth NdFeB magnet **0.648 W**	Deep plastic bonded NdFeB magnet **0.008 W**
Alu spacer **0.106 W**	Alu spacer **0.170 W**				
Mild steel carrier **0.047 W**	Carbon steel shaft **0.097 W**	Carbon steel shaft **0.441 W**	Carbon steel shaft **1.174 W**	Carbon steel shaft **0.247 W**	Stainless steel shaft **0.367 W**
St-St shaft -					
Total 0.552 W	**0.623 W**	**0.461 W**	**1.195 W**	**0.895 W**	**0.375 W**

Table 7.8 Time harmonic loss of the SMC Mk4 motor in comparison to the previous motors.

Tooth Ripple Loss					
Standard Rotor l_a=27.1mm teeth = 6 B_{airgap}= 0.24T	**Splitflow Rotor** l_a=27.1mm teeth = 6 B_{airgap}= 0.24T	**SMC Mk1.1** l_a=31mm teeth = 3 B_{airgap}= 0.28T	**SMC Mk2** l_a=31mm teeth = 3 B_{airgap}= 0.21T	**SMC Mk3** l_a=14mm teeth = 3 B_{airgap}= 0.44T	**SMC Mk4** l_a=19mm teeth = 3 B_{airgap}= 0.24T
St-St sleeve **0.162 W**	CFRE sleeve -	CFRE sleeve -	CFRE sleeve -	CFRE sleeve -	CFRE sleeve -
SmCo rare earth mag **0.034 W**	SmCo rare earth mag **0.035 W**	Deep plastic bonded NdFeB magnet **0.001 W**	Thin plastic bonded NdFeB magnet **0.000 W**	Thin rare earth NdFeB magnet **0.068 W**	Deep plastic bonded NdFeB magnet **0.002 W**
Alu spacer **0.051 W**	Alu spacer **0.054 W**				
Mild steel carrier **0.010 W**	Carbon steel shaft **0.010 W**	Carbon steel shaft **0.020 W**	Carbon steel shaft **0.024 W**	Carbon steel shaft **0.039 W**	Stainless steel shaft **0.129 W**
St-St shaft -					
Total 0.257 W	**0.099 W**	**0.021 W**	**0.024 W**	**0.107 W**	**0.132 W**

Table 7.9 Tooth ripple loss of the SMC Mk4 motor in comparison to the previous motors.

7.7 Testing of Mk4 in a Magnetic Levitated Turbo Pump

7.7.1 Test Set-Up and Instrumentation

The SMC Mk4 motor was built directly into a turbo pump, to quickly get an idea how the new motor performed in its intended application. To minimise the bearing losses, the motor was built into a fully magnetically levitated turbomolecular pump (EXT250M), which has a radial permanent magnet bearing at the top and bottom and an active axial magnetic bearing at the bottom (Fig. 1.3b). Testing the motor directly in a pump meant that direct loss data as obtained from the testing in the back-to-back rig was not available for this motor. This made determining the losses for the SMC Mk4 motor more difficult and uncertain, especially in comparison to the prediction and to the previous SMC motors.

The set-up was identical to the one described in Section 4.4 when testing the SMC Mk3 motor in a pump. The motor input power, line voltage, line current and power factor were measured using a PM3000A power analyzer. The system input power, i.e. power into the controller, was measured by measuring the DC supply voltage and the DC current as a voltage drop across a 0.1Ω resistor. The pump was instrumented with seven thermocouples: two on the windings, two on the SMC core back, one on the body internally (next to the SMC core back), one externally, and one infra-red thermocouple to measure the impeller temperature. The ambient temperature was also monitored. All the measurements (electrical and thermal) were fed into a data logger.

The pump was forced air cooled and run under two conditions: a) under 'no-load', i.e. no inlet flow and minimum backing pressure of about $5 \cdot 10^{-4}$mbar, and b) under 'full load', i.e. with an inlet flow giving $5 \cdot 10^{-2}$mbar at the inlet of the pump. The duration of each test was 4hours or longer to ensure that thermal equilibrium had been reached.

7.7.2 Power Consumption of SMC Mk4 in a Magnetic Levitated Pump

Fig. 7.16a and b show the measured power consumption, current, voltage and power factor for the SMC Mk4 motor in comparison to the existing motor under no-load and full load. The no-load motor input power for the SMC Mk4 motor is only 2.4W higher than that of the existing motor, and under load the difference is even less with 1.6W. Of all the SMC motors built, these power levels are the closest so far to those of the existing motor, and thought to be acceptable.

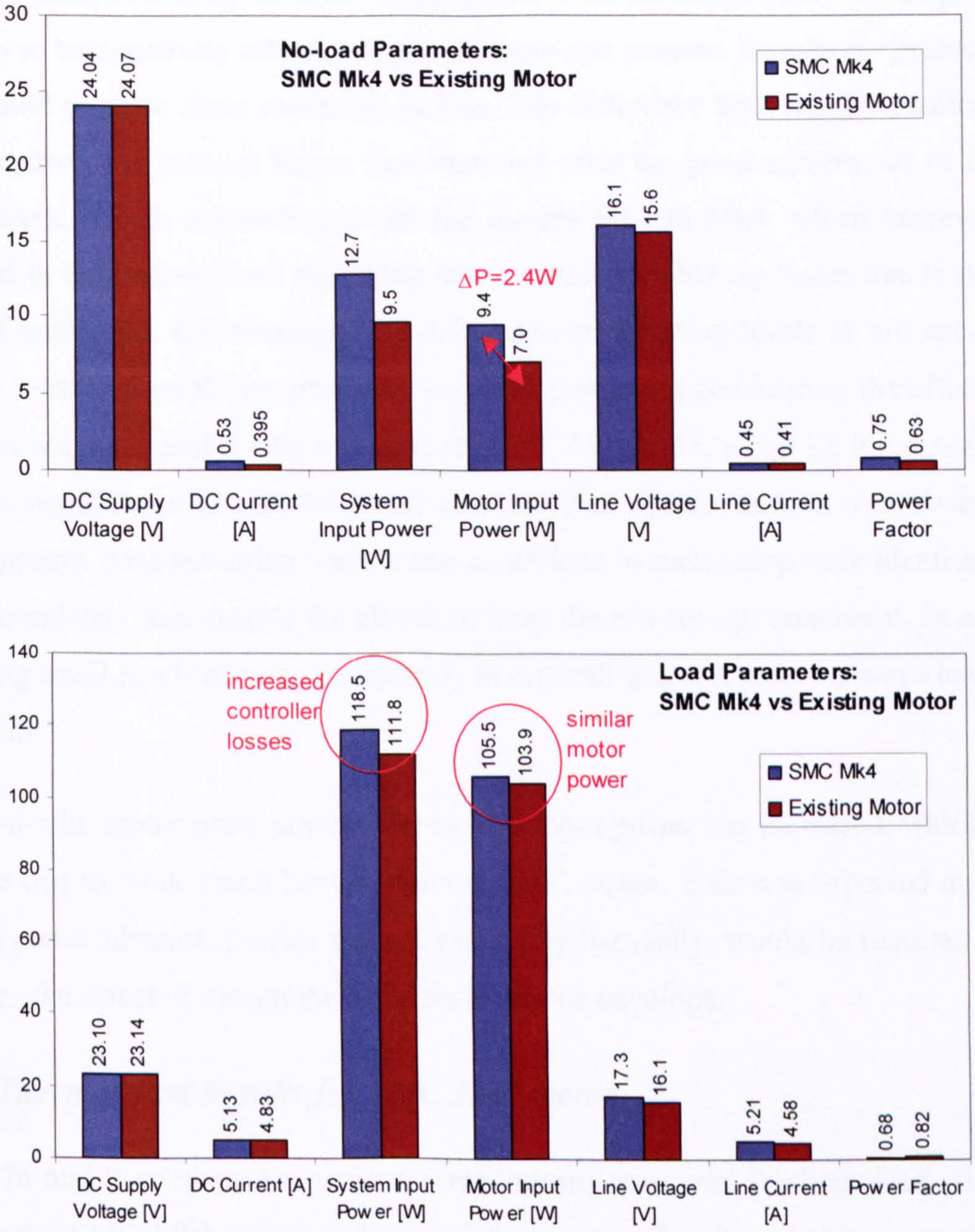

Fig. 7.16 Measured parameters in a magnetic levitated turbo pump for the SMC Mk4 motor in comparison with the existing motor: a) no-load, b) full load (inlet pressure = $5 \cdot 10^{-2}$mbar) (SMC Mk4 motor required about 42° phase advance to keep the pump at full speed)

In a magnetically levitated pump under no-load, the total motor input power is typically assumed to be equivalent to the stator iron losses, as the copper losses are negligible (<0.03W), and the magnetic bearing and gas friction is also assumed to be negligible. It is also assumed in comparing the results of the two pumps, that the test conditions and neglected losses are identical. For the SMC Mk4 motor, this indicates stator iron losses of about 9.4W compared to a predicted value of 5.4W.

The 2.4W increase on the no-load power is disappointing as the predicted iron losses were just 5.4W, even lower than those of the existing motor. Furthermore, the results

here were measured using an SMC motor made from prototype parts whose properties are likely to be negatively affected by the wire-erosion process. Results for pressed SMC parts should produce some reduction in loss. The difference between the predicted and measured iron loss is much larger than expected after the good agreements of the iron loss predictions with measurements for the motors Mk1 to Mk3, which however were measured in the back-to-back rig taking into account variable rig losses due to different levels of unbalance. Unfortunately the unbalance or vibration levels at full speed have not been measured on the magnetically levitated pump, but considering the effect of the unbalance magnetic pull during run-up (see below 7.7.4 and Chapter 8), it is possible that there is a significant effect on the power consumption, and the error in iron losses is less than it appears. Also assuming that the test conditions in each pump were identical might not be completely true despite the efforts to keep the test set-ups consistent. In addition, measuring small levels of power accurately is difficult and will nearly always have more uncertainty.

Despite similar motor input powers, the system input power has increased, which means the drive had to work much harder with the SMC motor. This was expected due to the required phase advance. Further testing, especially thermally, would be required to fully determine the effect of this on the drive performance envelope.

7.7.3 Thermal Test Results for SMC Mk4 motor

Fig. 7.17a and b compare the various temperatures measured for both load conditions between the SMC Mk4 motor and the existing motor. To allow better comparison the temperatures are plotted as temperature rise above ambient.

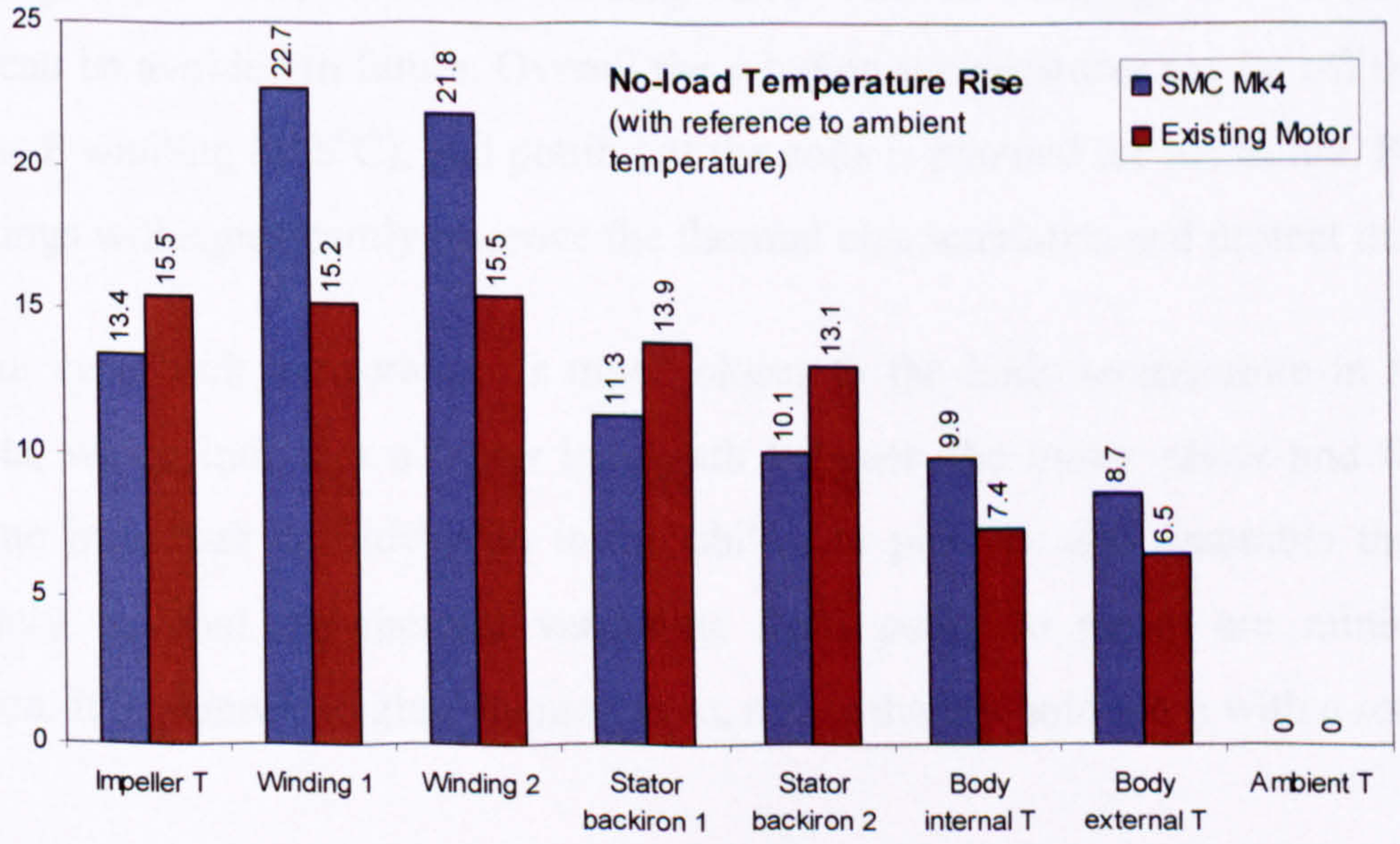

a)

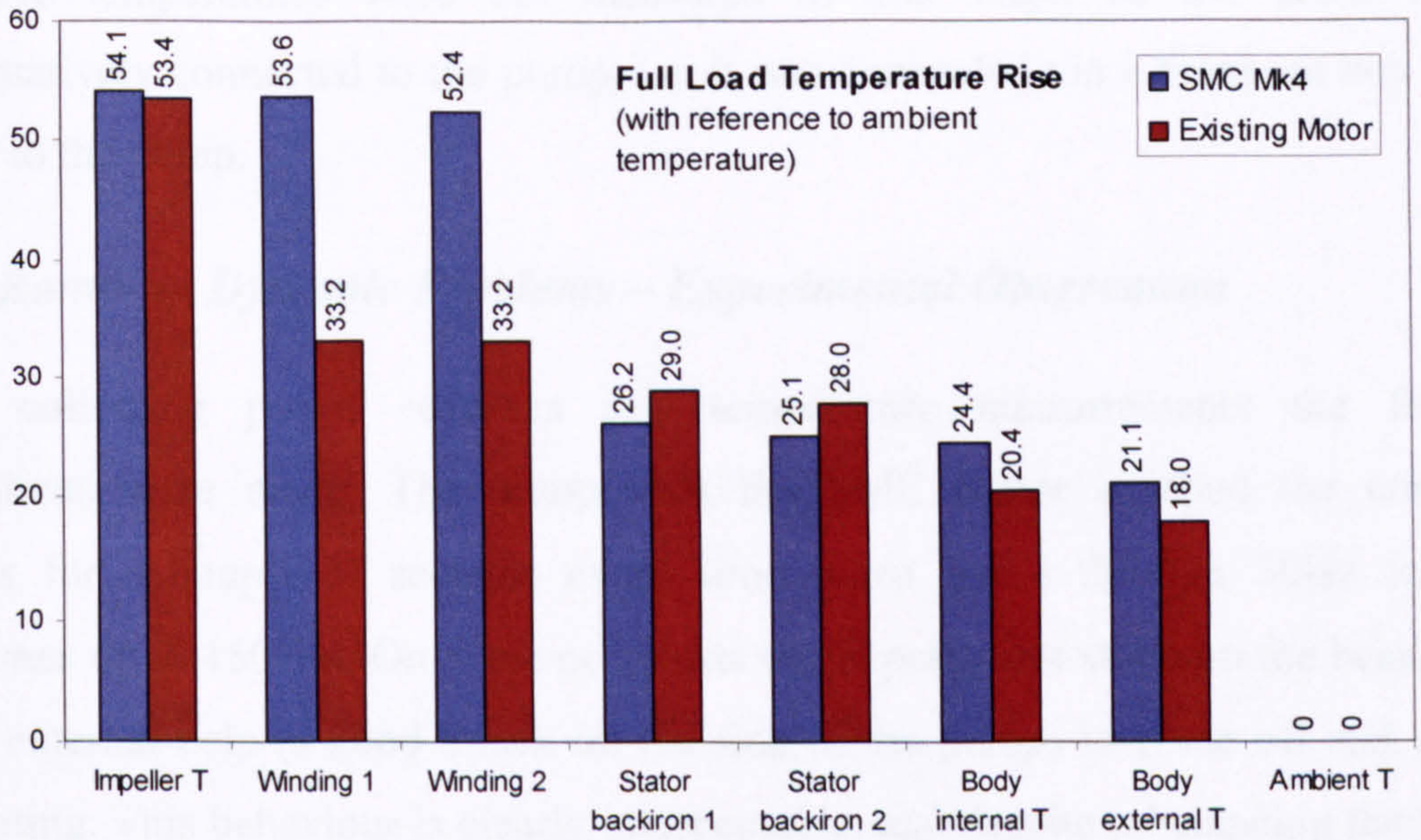

b)

Fig. 7.17 Comparison of measured temperatures relative to ambient temperature between SMC Mk4 and the existing motor: a) no-load ($T_{ambient}$=21-22°C), b) full load ($T_{ambient}$=21-22°C).

The most critical temperature in a turbomolecular pump is the impeller temperature. The measured impeller temperature with the SMC Mk4 motor is almost identical, measured 2°C lower under no-load, and 1°C higher under load, i.e. within measuring accuracy and repeatability of the infra-red thermocouple.

The biggest difference is in the winding temperature. The winding temperature is determined by the amount of copper loss, and the thermal heat transfer coefficient between the winding and the stator core back. Due to the low fill factor in the SMC Mk4 motor the copper losses are higher and the coils have poorer contact to the core back in this prototype compared to previous potted ones (see Mk3 results). This is due to the way the windings were wound (random winding versus formed winding). However, all these features can be avoided in future. Overall the winding temperatures are far off their limit for a class F winding (155°C), and potting of the coils is planned for the future. Potting of the windings will significantly improve the thermal characteristics and protect the SMC.

The stator core back temperature is much closer to the body temperature in the SMC Mk4 tests, which indicates a better heat path between the motor stator and the pump body. One important consideration is the ability to produce and assemble the motors consistently, so that the thermal variations from pump to pump are minimised in production. It is planned to glue the motors in, rather than to hold them with a screw.

The drive temperatures were not measured at this stage, as the drive was not representatively connected to the pump, i.e. it was connected via a breakout box and not directly to the pump.

7.7.4 Ramp-up Dynamic Problems – Experimental Observation

Whilst collecting power readings and temperature measurements the following observations were made: The pump with the SMC motor touched the emergency bearings for a couple of seconds every time when going through 30Hz to 120Hz (sometimes up to 150Hz). On some occasions the impeller got stuck on the bearings and needed external help (a good knock on the side of the pump) to come off and continue accelerating. This behaviour is clearly unacceptable, and despite rebalancing the impeller assembly this contact could not be avoided or significantly improved.

Previously during the testing of Mk3 in a standard, non-magnetic levitated pump it was noted that the pump exhibited unusually high levels of transmitted vibration through its first resonance (see Section 4.4.6). As it was an old, refurbished pump it was not considered further. However, having witnessed two pumps repeatedly behaving in the same way, this became a serious issue, and the focus of investigation into unbalanced magnetic pull from the three-tooth design (see Chapter 8).

7.8 The Next Step

The SMC Mk4 motor had been the best alternative motor so far in respect to the stator and rotor losses. It delivered acceptably low power levels and achieved suitable thermal performance. However, solving the noisy ramp-up behaviour became the highest priority. Hence, the next chapter focuses on understanding and quantifying unbalanced magnetic pull in the three-tooth motors.

Chapter 8

Unbalanced Magnetic Pull in the 3-Tooth, 2-Pole Design

8.1 Introduction

During the testing of the three-tooth, two-pole motors unusually high levels of acoustic noise and transmitted vibration were observed, especially when tested in the fully magnetically levitated pump. In these pumps the impeller assembly touched the emergency bearings for a couple of seconds every time when ramping up. Despite rebalancing of the impeller assembly, this contact could not be avoided or significantly reduced. As the only difference between these pumps and the existing product is the motor, this indicated that the new motor must introduce some additional forces.

It is well known from the theory of induction motors [66, 67] that such a three-tooth design leads to an inherent asymmetry in the magnetic path, which creates unbalanced magnetic pull (UMP). However, UMP in permanent magnet machines is generally thought to be far smaller than in induction machines, because the air gap is usually larger and the low permeability of the magnets dominates the magnetic circuit. In most permanent magnet machines UMP is usually treated as small enough to be neglected. Our initial assumption based on [68], that the UMP in these permanent magnet motor designs is so small as not to cause a problem, has proved to be wrong.

This chapter looks at the UMP in the asymmetric 3-tooth, 2-pole motor, comparing the level of UMP caused by the magnetic field from the magnets alone with the level of

UMP caused by the interaction of the magnetic field from the magnet with the magnetic field from the current in the windings. It is a practical and theoretical study to quantify the effects of UMP with emphasis on this particular application and hence to provide a more general understanding of UMP effects in permanent magnet machines. Finite Element analysis based on the Maxwell stress tensor method is used to calculate the force. The contribution of the normal and tangential component of the magnetic field density from the magnets and the windings will be analysed to determine which one contributes most to the UMP force. Finally the effect of some design parameters will be investigated to identify possibilities to reduce or eliminate UMP altogether.

8.2 Unbalanced Magnetic Pull

8.2.1 Brief History of Unbalanced Magnetic Pull

Unbalanced Magnetic Pull is not a new phenomenon. The calculation of UMP in induction machines with an eccentrically mounted rotor with respect to the stator bore has been the subject of many papers for nearly 100 years, which are referenced in [69, 70]. The work at the beginning of the last century was summarised by Gray and Pertsch in 1918 [69] in a critical review of the published papers on UMP in dynamo-electrical machines. The question of UMP was typically discussed in combination with noise and vibration issues of rotating machines, and all the papers until 1918 seemed to report only on UMP due to eccentricity. Rosenberg's paper [70] followed on from there, and expanded the work looking into the effects on UMP in multipolar and bipolar machines with salient poles and with cylindrical fields with distributed windings, but he did not describe the real cause of UMP. UMP due to harmonic fields in the air gap had still not been discussed at that time.

It was Stiel [71] in 1919 who first recognised the relationship between slot numbers and magnetic noise. He systematically tested the effects of higher harmonic fluxes on the torque-speed characteristics of polyphase induction motors and suspected that magnetic radial forces were the cause of noise. But he did not give a theoretical explanation.

Fritze [72] analysed Stiel's results theoretically in 1921, and discovered, that considerable vibration and magnetic noise occur in radial machines whose air gap field contains two harmonic flux waves with pole pairs differing by one. His work has built the foundation of induction motor noise analysis and theoretical understanding of UMP.

The two harmonic fields could be two stator fields, two rotor fields or one stator with one rotor field. Such a situation can arise from the choice of stator and/or rotor slotting or asymmetries in the magnetic circuit.

Chapman [73] dealt simultaneously and independently with the same subject, but his work was not published until 1923. He came to the same conclusion as Fritze about the harmonic fields in the air gap. Furthermore he came up with a rule for rotor-slot combinations to be avoided, and highlighted the danger of resonance caused by disturbing forces occurring at the motor's critical speed.

Since then many research investigations have been done on UMP, noise, and vibration. Von Kaehne [74] carried out a survey of published work on UMP in rotating electrical machines in 1963, and summarised the present state of knowledge of UMP, its origins, effects and influencing factors (see section 8.2.2 for cause and effects of UMP). In principal, UMP can occur in any type of machine, but the majority of work has been done on induction motors with the main focus on UMP caused by eccentricity. Induction machines are widely used, and due to their very small air gap are very sensitive to magnetic imbalances. Some of the studies are referenced in [74-78].

Generally UMP is far smaller in permanent magnet machines because the air gap is usually larger and the low permeability of the magnet dominates the magnetic circuit and lessens the effect of asymmetries in the iron or winding elements. In most permanent magnet machines UMP has been treated as small enough to be neglected [68, 74].

One of the applications today for permanent magnet motors where UMP is important is the spindle motor for hard disk drives (HDD). It's been this application which in the last ten to twenty years [79] initiated most of the studies on UMP and its effects on the performance of permanent magnet machines, especially brushless permanent magnet motors [80-88].

Most of the work done on UMP has investigated the effect of eccentricity [80, 82, 84, 89-91], but more recently the increasing popularity of fractional slot per pole machines because of their low winding losses has resulted in renewed attention to UMP in permanent magnet machines with asymmetrical teeth arrangements. Investigations into the effect of intrinsic unbalance in the electromagnetic structure are reported in [81, 83, 85-88]. In [92-94] specific attention is given to the effects of stator excitation. The authors of [94] have calculated the UMP force for brushless permanent magnet motors

with diametrically asymmetric phase windings and shown that the contribution from the stator slots under open circuit is relatively small compared to the contribution due to the stator MMF. It will be shown that this is also the key source for the UMP force in the motor under investigation here.

8.2.2 Cause and Effects of Unbalanced Magnetic Pull

Unbalanced Magnetic Pull can be defined as the net radial magnetic force acting on the rotor of an electrical machine. UMP is caused by the existence of a non-uniform magnetic flux density distribution in the air gap. In principal, there are several factors [74, 83, 87], which can lead to an unbalanced magnetic field distribution in the air gap, and cause UMP.

The causes of UMP can broadly be classified into two categories: extrinsic and intrinsic UMP [87]. Fig. 8.1 gives an overview of the main causes and their classifications.

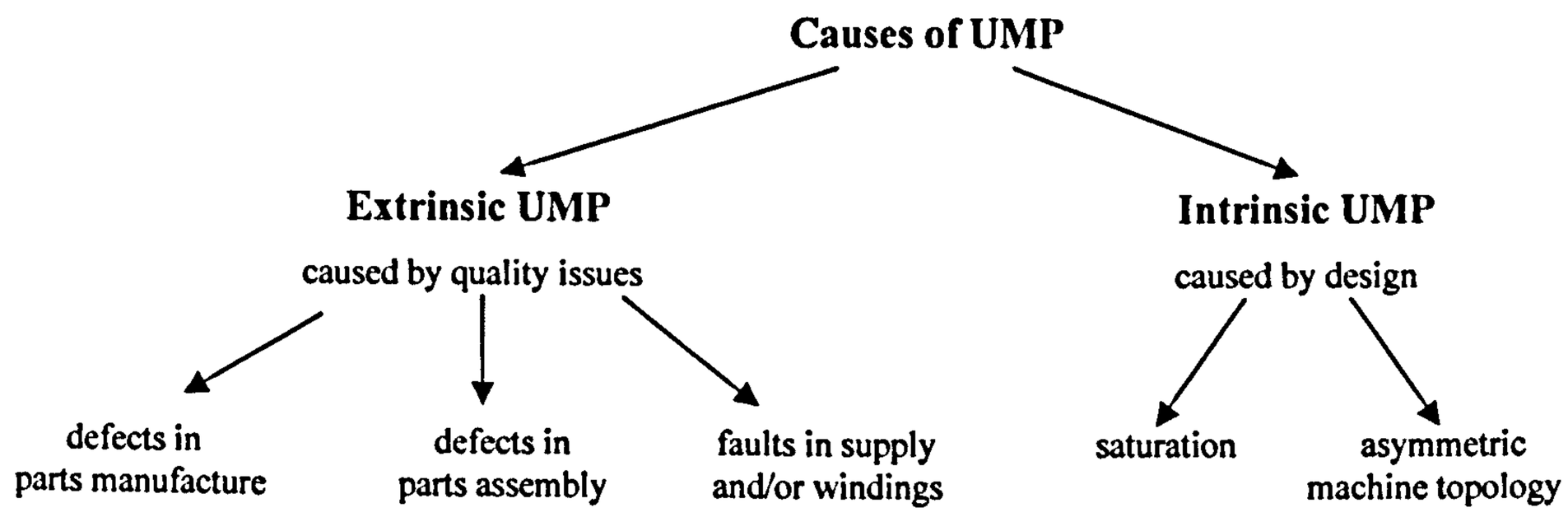

Fig. 8.1 Classification of main causes of Unbalanced Magnetic Pull

Extrinsic UMP covers all the causes, which in an ideal world would not exist, i.e. any unbalanced magnetic field distribution caused by component quality issues. Examples are:

<u>Defects in parts manufacture:</u>

Mechanical: bent shaft, unbalanced mass, stator bore and core and rotor roundness errors
Magnetic: imperfect (asymmetric) magnetisation of the permanent magnets e.g. different magnetisation levels, different magnetisation patterns, variations in thickness or pole arc length of the poles.

<u>Defects in parts assembly:</u>

Mechanical: inaccurate positioning of the rotor with respect to the stator (non-concentric stator / rotor), bearing tolerances, assembly tolerances.

Supply or Winding Faults:

Unbalanced voltage supply, faults in the supply system (short circuits, loss of phases, surges, etc), or faults in the windings of the machine (interturn short circuits, shortcircuited coils) can also lead to a distorted flux distribution in the air gap.

As there is no perfect manufacturing process, most motors have inherent abnormalities due to manufacturing and assembly imperfections. Common examples are the cases covered in various papers investigating UMP due to eccentricity. With good quality control of the components and the processes in production and assembly extrinsic UMP can be reduced to acceptably low levels.

Intrinsic UMP on the other hand is inherent in the design of the motor. Even with perfect components, production and assembly processes this kind of UMP still exists:

Saturation:

Under heavy load or during start up, high currents can saturate the iron in the teeth or back iron. This can lead to an asymmetric flux distribution in the machine's air gap causing UMP. Saturation can potentially happen in any machine independent of the slot-pole combination

Asymmetric topology of the machine:

Some machine designs have an inherent asymmetry in their electromagnetic structure. This is mainly due to a non-symmetric slot-pole combination. Machines with fractional slot windings are especially susceptible to UMP [94], because their MMF wave contains even and odd harmonics. If there are harmonic fields in the air gap, which differ by one pole-pair from each other or from the fundamental, then a resultant radial force is set up. However, if rotational symmetry exists, the forces set up by the fractional pitch windings cancel each other [85].

For 3-phase PM brushless machines the condition for UMP can be expressed as [94]

$$2p = N_{slot} \pm 1 \tag{8.1}$$

where N_{slot} is the slot number and $2p$ the pole number, i.e. if the slot number and the pole number differ by one, UMP exists. Typical slot/pole combinations with inherent UMP are 3-slot/2-pole, 3-slot/4-pole, 9-slot/8-pole, 9-slot/10-pole, 15-slot/14-pole, 15-slot/16-pole, etc.

The focus of this chapter is on the intrinsic UMP due to an asymmetric topology. Saturation is not an issue in the turbopump motor as the flux levels are kept low to avoid excessive iron losses at high speed. A brief calculation of the effect of eccentricity will be carried out to have a comparative idea about the magnitude of the UMP forces due to the inherent asymmetry and due to eccentricity.

In general, the main effects of UMP are excessive vibrations and noise emission. These vibrations can speed up bearing wear in contact bearings and reduce bearing life. There is a serious danger of setting up resonance, when the forcing frequency of the UMP coincides with the natural frequencies of the stator core, teeth, frame or system. In extreme cases this can even lead to a contact between the rotor and stator with consequential possible damage of the motor or other parts of the machine.

8.3 Experimental Observations

8.3.1 Observations During Run-Up

During the testing of the three-tooth, two-pole motors it was observed that the pump touched the emergency bearings for a couple of seconds every time when ramping up to speed, especially through the speed range from 30Hz to 120Hz and sometimes up to 150Hz. The pass-off specification in production only tolerates a maximum contact time of 2sec (ideally no contact), but not 10-20 sec as experienced on these pumps. Sometimes the shaft got 'stuck' on the emergency bearings and needed some external help to come off the bearings. This was not observed with the existing motor. Once the pump passed 250Hz the three-tooth motor ran smoothly up to full speed.

8.3.2 Observations During Full-Speed Running and Coast-Down

At full speed (1000Hz) no problems were noticed, not even when run under full load, drawing about $5A_{rms}$, i.e. 110W motor input power. When the pump was coasting down with no current in the windings, no contact with the emergency bearings was observed either, and the pump was quiet down to 0Hz.

8.3.3 Initial Conclusion of Experimental Observations

The balance of the impeller and rotating assembly was very good and was definitely not the cause of the run up failures. These observations point towards the three-tooth motor

introducing some additional forces. The only difference between the new and the existing motor design is the tooth and winding layout. The existing motor is a symmetric, six-tooth motor with fully-pitched overlapping windings, whereas the new motor has three teeth, with concentrated, short-pitched non-overlapping coils.

The other conclusion that is drawn from the above observations is, that the force is dependent on current. With zero current in the winding i.e. during coast-down, no effect of the UMP force was noticed. This means that UMP caused by the magnetic field from the magnets interacting with the three-tooth asymmetry is not enough to upset the dynamics of the pump. The UMP force only becomes a problem when the current is large enough. Only during run-up, when the motor takes its highest current (two to three times as high as under full load operation) and produces its largest torque, are problems observed.

It is clear from these observations that in this application UMP forms limits on the design and operation of the motor.

8.4 Experimental Investigations

8.4.1 3-Dimensional Frequency Spectrum

To find out and better understand what was causing the mechanical contact with the emergency bearings in the three-tooth motor, the transmitted vibration of the pump body was measured during run-up up to half speed, i.e. 30,000rpm, and down. A frequency spectrum was taken every 100rpm. Fig. 8.2a and b show the resultant waterfall plots, which are a 3-dimensional frequency spectrum. The frequency spectrum is plotted along the x-axis and the magnitude of each frequency is indicated by colour. The lighter the colour the larger the peak. The y-axis represents the different rotational speeds during ramp up or down.

During run-up the pump shows the largest magnitude of transmitted vibration at the 2^{nd} harmonic, in the range of 80-140Hz. This corresponds to a rotational speed of the pump of 40 to 70Hz. In section 8.5.4 it will be shown that the dominant UMP frequency is the 2^{nd} harmonic.

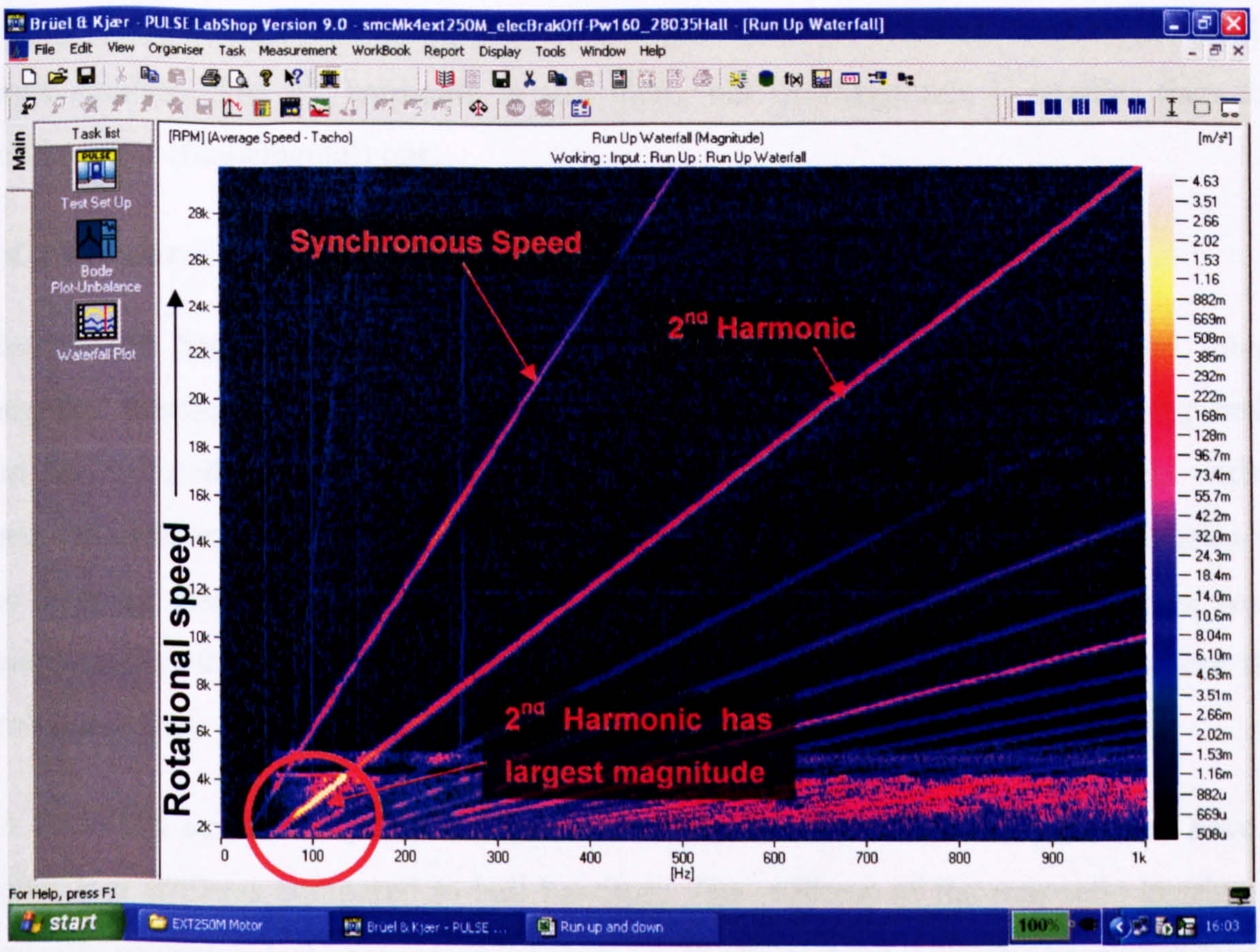

a)

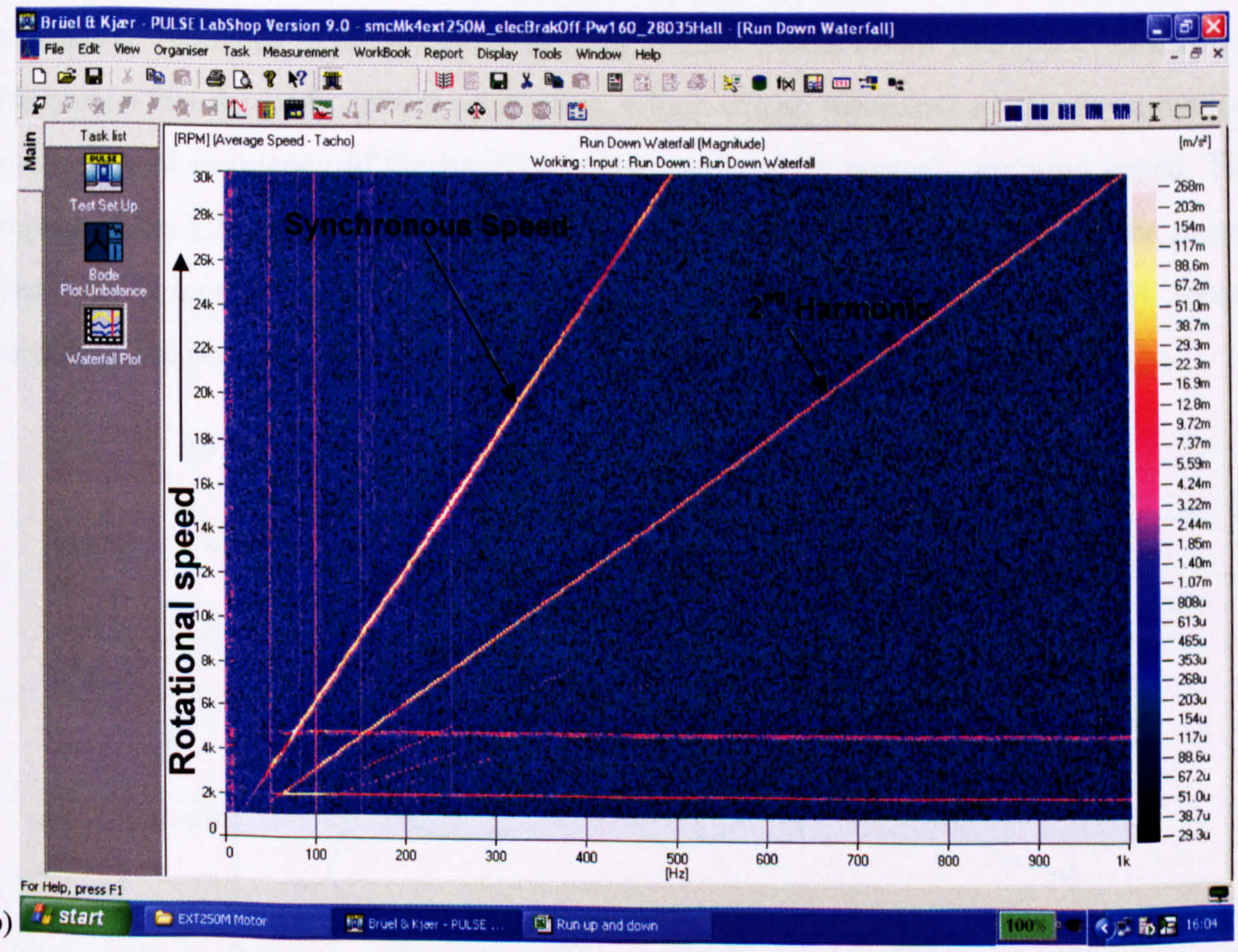

b)

Fig. 8.2 Waterfall plot of SMC-Mk4 motor in EXT250M a) during run-up, b) during coast-down

During coast-down of the pump the transmitted vibration is much smaller (about 10 times smaller). The 2nd harmonic is still there, but its magnitude is smaller than the synchronous (fundamental) one.

8.4.2 Natural Frequency of Magnetic Bearing System

The natural frequency of the rotating assembly suspended by the upper and lower magnetic bearing has been measured. An accelerometer was connected to the pump body and the levitated impeller was gently hit on the blade rows in different positions with a force-hammer to excite the upper and lower bearing system. The natural frequencies of the impeller assembly, which are influenced by the stiffness of the two bearings, were determined as 45Hz and 74.5Hz respectively (Fig. 8.3), exactly in the range where the problem occurs.

As described earlier the pump is supported purely on magnetic bearings, which have a rather low stiffness compared to ball bearings. The stiffness of the magnetic bearing is typically several orders of magnitude lower, i.e. the theoretical magnetic bearing stiffness in this pump is around $9 \cdot 10^4$N/m compared to a ball bearing stiffness of $>10^8$N/m. Hence the natural frequency of the magnetic bearing system is well below full-speed. In practice this means that the UMP creates a vibration, which causes resonance at speeds equivalent to the natural frequency of the bearing system well below normal operating speed. The impact of the UMP force is therefore most severe during the run up phase of the pump. Once the resonant frequency is excited, the passive bearing system basically looses control of the positioning of the shaft causing contact with the emergency bearings.

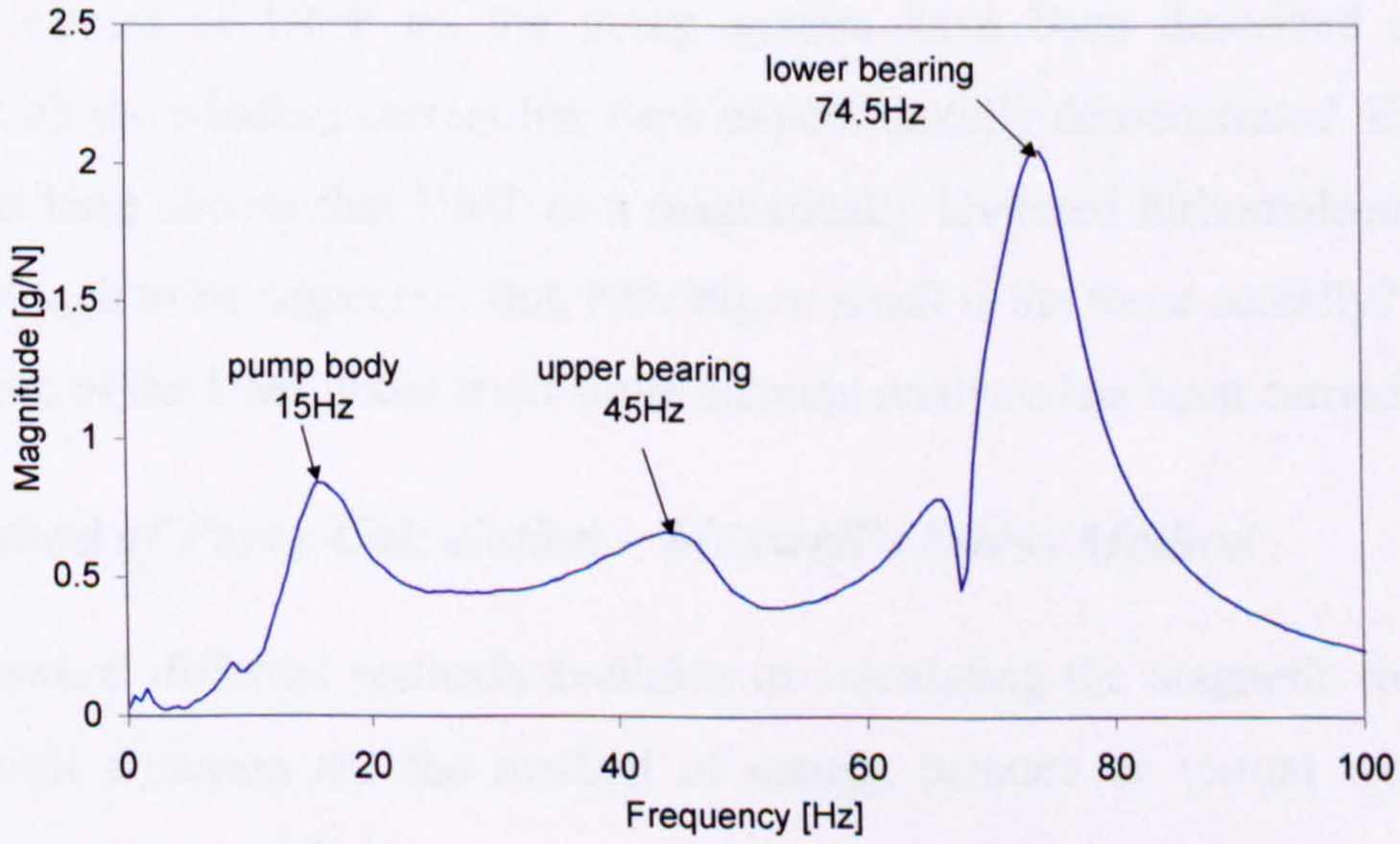

Fig. 8.3 Measured natural frequency of the rotating assembly with magnetic bearings on EXT250M

8.4.3 Effect of Magnitude of Current

The initial observations clearly showed that the pump only touched the emergency bearings during ramp-up. This happened at a point where the drive allows the maximum current to flow to allow a fast acceleration of the impeller. The current level can reach up to $15A_{rms}$ at that point.

To prove that it is the interaction of the magnetic field of the stator windings with the magnetic field from the magnet that causes the problem, and that the magnitude of the UMP force depends on the current, several ramp up trials were carried out with the current limit reduced each time. It was only at a level of less than $2A_{rms}$ during the critical frequency range that no contact of the pump with the emergency bearings occurred. This means that to avoid resonant excitation taking up the clearance of 191μm radially between the shaft and the emergency bearing the current has to be reduced by at least a factor of 7.5 (ratio of 15A to 2A).

From the experimental evidence it is clear that the unbalanced magnetic force is dominated by the second harmonic of the motor frequency and that this excites the natural resonance frequency of the magnetic bearings. The magnetic bearing control may become unstable and loose control or it may be that the resonance simply exceeds the stiffness of the bearing. The effect is largest when the current is large.

8.5 UMP Force Calculation Using Finite Element Analysis

So far the effects of UMP on the pump system have been described and a clear dependence on the winding current has been experimentally demonstrated. Experimental observations have shown that UMP in a magnetically levitated turbomolecular pump is not small enough to be neglected. But, how big or small is the force actually? To find out the actual size of the UMP force itself finite element analysis has been carried out.

8.5.1 Method of Force Calculation – Maxwell's Stress Method

There are several different methods available of calculating the magnetic force [95-98]. The two most common are the method of energy balance or virtual work, and the Maxwell stress tensor method.

The virtual work or energy method calculates the force based on the variation of the magnetic energy/coenergy of the system when its moving part is physically displaced. The Maxwell stress method calculates the force on a body by integrating the magnetic stresses over a surface enclosing the body. It can be used for any structure on which the force is needed (ferromagnetic or current carrying, or both).

The accuracy of both methods relies on the resolution of the elements along the circumference of the air gap. The Maxwell stress method is easy to implement in 2D FE as the surface integral reduces to a line integral, and because of its simplicity it has been chosen as the method to calculate UMP in this thesis.

Applying Maxwell stress method to the three-tooth, two-pole motor, the integration surface is typically placed in the middle of the air gap. There the local normal (radial) and tangential stress component can be described at angle θ and time t as follows [99, 100]:

$$\sigma_n(\theta,t)=\frac{1}{2}\cdot(H_nB_n-H_tB_t)=\frac{1}{2\mu_0}\cdot\left(B_n^2-B_t^2\right) \tag{8.2}$$

$$\sigma_t(\theta,t)=B_n\cdot H_t=\frac{1}{\mu_0}B_n\cdot B_t \tag{8.3}$$

where B is the magnetic flux density, H the magnetic field strength, and σ the magnetic stress. The index n represents the normal component and the index t the tangential component of the respective parameter. μ_0 is the permeability of free space (in the air gap).

In PM machines with a large air gap saturation is not a problem, hence the normal and tangential component of B can be expressed as the superposition of the field from the magnet and from the stator windings.

$$B_n=B_{n,mag}+B_{n,coil} \tag{8.4}$$

$$B_t=B_{t,mag}+B_{t,coil} \tag{8.5}$$

Inserting (8.4)-(8.5) into (8.2)-(8.3), and multiplying it out the normal and tangential stress can be expressed as:

$$\sigma_n = \frac{1}{2\mu_0} \cdot \left[\left(B_{n,mag} + B_{n,coil} \right)^2 - \left(B_{t,mag} + B_{t,coil} \right)^2 \right] = \tag{8.6}$$

$$= \frac{1}{2\mu_0} \cdot \left[\left(B_{n,mag}^2 - B_{t,mag}^2 \right) + \left(B_{n,coil}^2 - B_{t,coil}^2 \right) + 2\left(B_{n,mag} B_{n,coil} - B_{t,mag} B_{t,coil} \right) \right]$$

$$= \begin{array}{c}\text{normal stress} \\ \text{from magnets}\end{array} + \begin{array}{c}\text{normal stress} \\ \text{from windings}\end{array} + \begin{array}{c}\text{normal stress from} \\ \text{interaction of both fields}\end{array}$$

$$\sigma_t = \frac{1}{\mu_0} \cdot \left(B_{n,mag} + B_{n,coil} \right) \cdot \left(B_{t,mag} + B_{t,coil} \right) = \tag{8.7}$$

$$= \frac{1}{\mu_0} \cdot \left[\left(B_{n,mag} B_{t,mag} \right) + \left(B_{n,coil} B_{t,coil} \right) + \left(B_{n,mag} B_{t,coil} + B_{n,coil} B_{t,mag} \right) \right]$$

$$= \begin{array}{c}\text{tangential stress} \\ \text{from magnets}\end{array} + \begin{array}{c}\text{tangential stress} \\ \text{from windings}\end{array} + \begin{array}{c}\text{tangential stress from} \\ \text{interaction of both fields}\end{array}$$

It can be seen that the normal and tangential stress or force density consists of three parts: the stress from the magnet field plus the stress from the field from the windings plus the stress from the interaction of both. Therefore the total force is more than the superposition of the force from the magnets only and the force from the windings only. The third term, which represents the effect the two fields have on each other, is dominant in the total force calculation.

To get the net radial force/length, which would determine if there is a UMP force acting on the rotor or not, one cannot integrate σ_n along the air gap directly as this would even in a fully balanced system lead to a non-zero value, whereas the net tangential force which is proportional to torque, can be found by integrating (8.7) over the circumference (0-2π) in the middle of the air gap.

To determine the net radial force/length at any given time t_0 (i.e. at any given rotor position) the x- and y-component of the stress ((8.8)-(8.9)) need to be calculated first, and then integrated over the full circumference ((8.10)-(8.11)).

$$\sigma_x(\theta, t_0) = \sigma_n \cdot \cos(\theta) - \sigma_t \cdot \sin(\theta) \tag{8.8}$$

$$\sigma_y(\theta, t_0) = \sigma_n \cdot \sin(\theta) + \sigma_t \cdot \cos(\theta) \tag{8.9}$$

$$\frac{F_x(t_0)}{l} = \int_0^{2\pi} \sigma_x(\theta, t_0) \cdot r \cdot d\theta = \int_0^{2\pi} \sigma_n \cdot \cos(\theta) \cdot r \cdot d\theta - \int_0^{2\pi} \sigma_t \cdot \sin(\theta) \cdot r \cdot d\theta \tag{8.10}$$

$$\frac{F_y(t_0)}{l} = \int_0^{2\pi} \sigma_y(\theta, t_0) \cdot r \cdot d\theta = \int_0^{2\pi} \sigma_n \cdot \sin(\theta) \cdot r \cdot d\theta + \int_0^{2\pi} \sigma_t \cdot \cos(\theta) \cdot r \cdot d\theta \tag{8.11}$$

A resultant F_x and F_y indicate the size and direction of the resultant UMP force.

8.5.2 Finite-Element Model

A two-dimensional finite-element model has been constructed using Femlab [47] to calculate the UMP force with and without excited stator windings. The model used the 'Perpendicular Currents' application mode, which models situations where the currents (i.e. the currents in the windings) are perpendicular to the modelling plane. This implies that the magnetic field is present only in the modelling plane (x-, y-plane). The two-dimensional model assumes no variation in the z-direction and ignores effects from the end windings or magnet overhang for the hall sensors. To include end effects a full 3D model would be required. But for a first approximation a 2D model was found to be justifiable. At the model boundary (stator outside diameter) the magnetic potential A_z is set to zero, which forces the field to be tangential to the boundary.

Femlab has a built-in function calculating the resultant force on a subdomain using Maxwell Stress Tensors. Results are in the form of an x- and y-component of the net force per meter axial length. The magnitude of the UMP force |F| is calculated by $|F| = \sqrt{F_x^2 + F_y^2}$.

Fig. 8.4 shows the subdomains and the mesh used in the 2D FE model. It contains 26172 elements, with very fine resolution in the air gap along the contour of integration. A refined mesh with 101464 elements was used to check convergence of the force calculation. The results of the UMP force were within <1%.

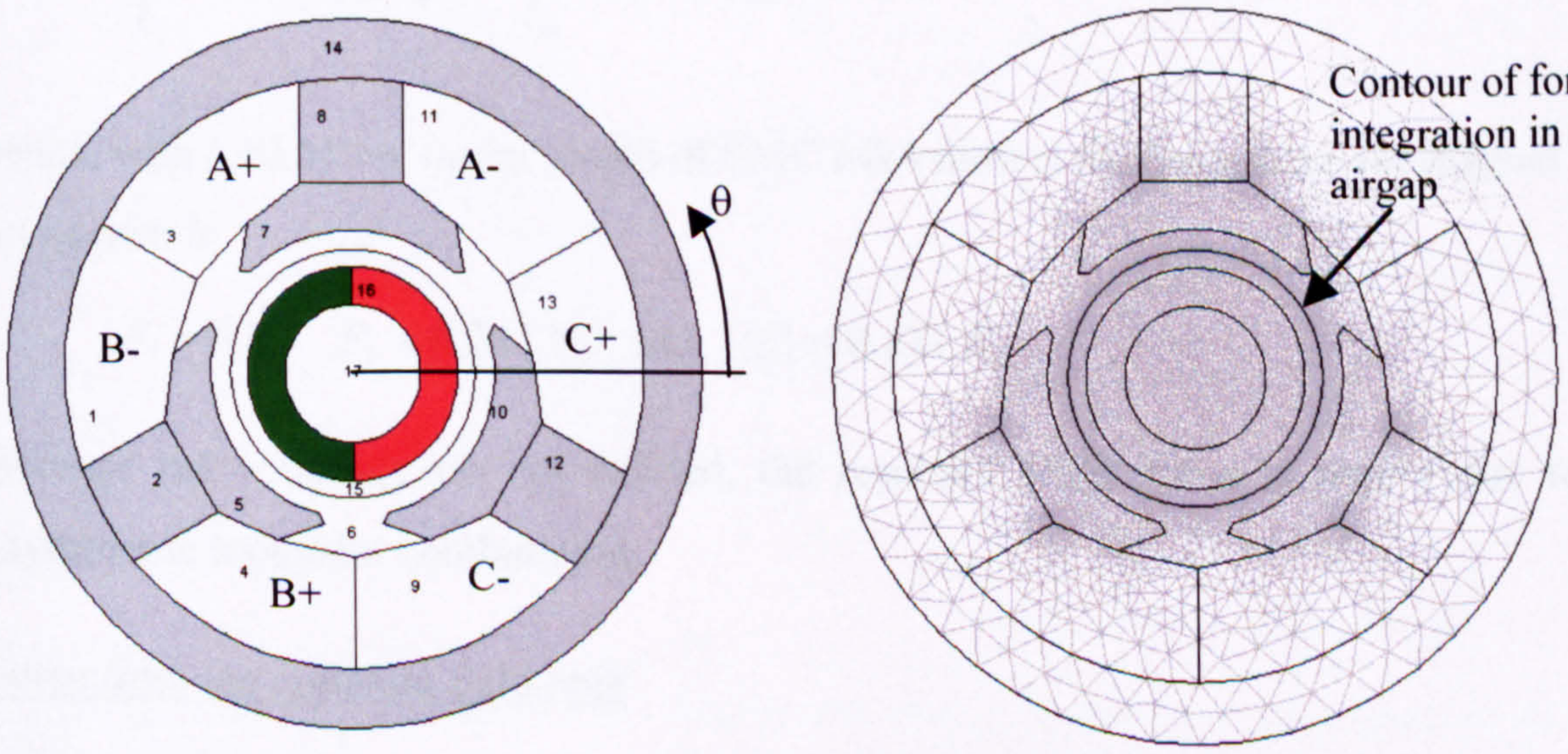

Fig. 8.4 Two-dimensional FE model of 3-tooth motor and mesh

8.5.3 FE Results: Worst Case – Maximum UMP Force

Let's consider first the worst case, i.e. maximum UMP force. This happens when both fields, that is the field from the magnet and the field from the armature, are aligned and both are pointing towards a tooth.

To demonstrate that there is a significant contribution to the force from the interaction of the magnet field with the armature field, three distinct models are considered:

- Force from the magnet field only
- Force from the armature field only as a function of armature current
- Total force when both fields are present as a function of armature current.

Force from the magnet field only

Fig. 8.5a shows the field from the magnet under open circuit (no current in the windings) with the magnet pole towards the top tooth (rotor position at $\theta=90^{o}$, y-direction), and Fig. 8.5b shows the corresponding normal and tangential flux density component in the middle of the air gap. The normal field is nearly sinusoidal, except for some distortion around the slot openings. Due to the uneven number of slots the distortion is asymmetric. This asymmetry is enough to create an unbalanced force.

The resultant UMP force components from the FE programme are

$$\frac{F_x}{l_a} = -0.00051 \frac{N}{m}; \quad \frac{F_y}{l_a} = 14.793 \frac{N}{m};$$

hence, with l_a=0.019m (axial length of SMC Mk4 motor) the force from the magnet field on its own is

$$F_x = 0 \text{ N}, \quad F_y = 0.281 \text{ N}, \quad \text{and} \quad |F| = 0.281 \text{ N}.$$

Because the windings are not excited, the resultant UMP force is purely due to the asymmetric tooth/slot combination.

Force from the armature field only

The motor is delta wound and operated in brushless DC mode. The winding is excited so that $i_b=i_c=-\frac{1}{2}i_a$, giving a resultant field that is in the same direction as the magnet field.

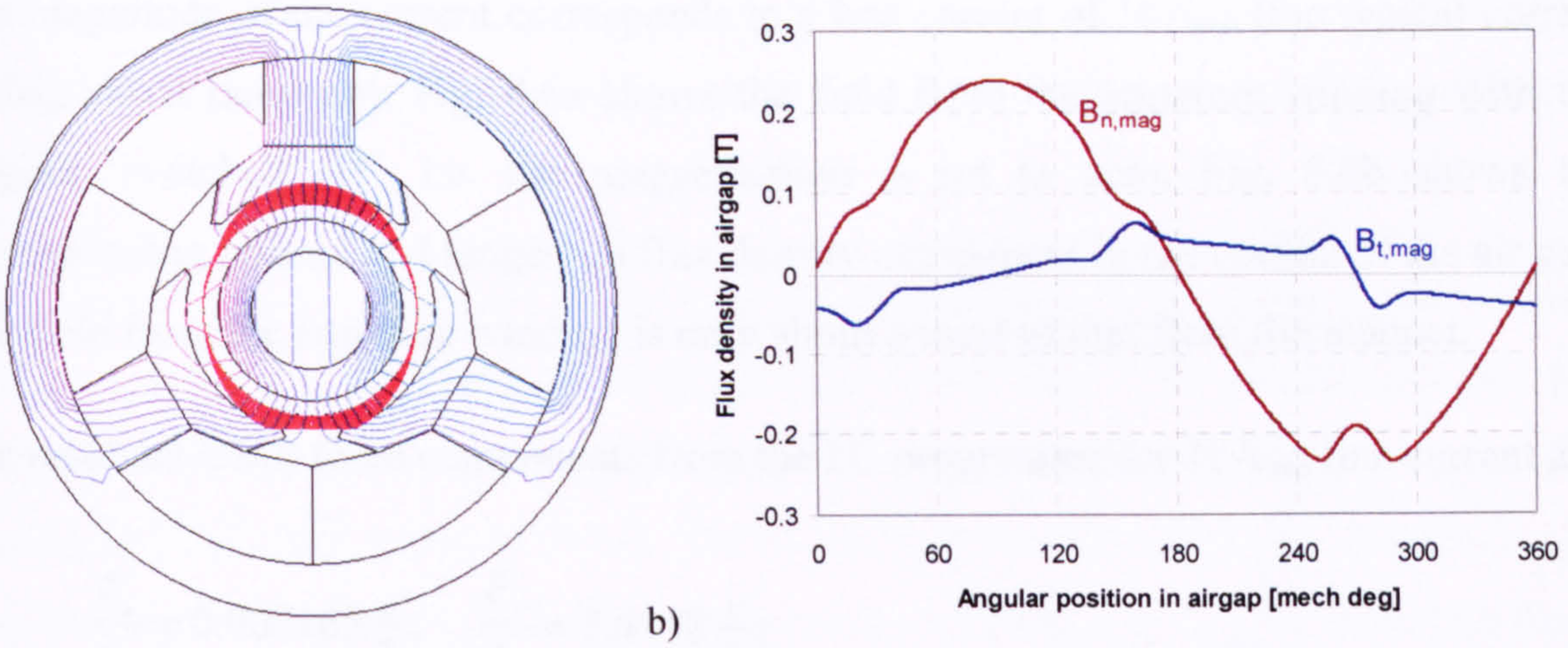

Fig. 8.5 Magnet field only (open circuit): a) field lines and magnetic stress vectors on rotor, b) air gap field distribution

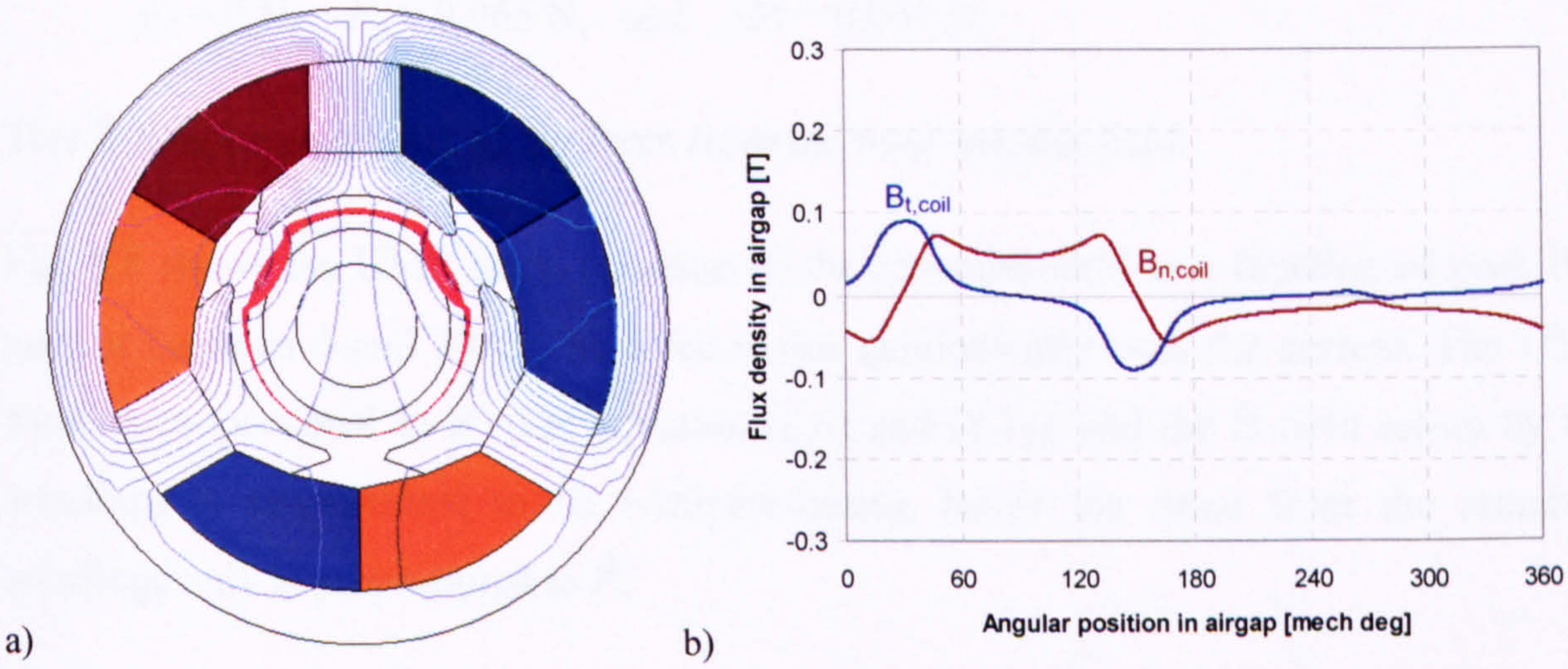

Fig. 8.6 Armature winding field only with $10A_{rms}$ line current: a) field lines and magnetic stress vectors on rotor, b) air gap field distribution

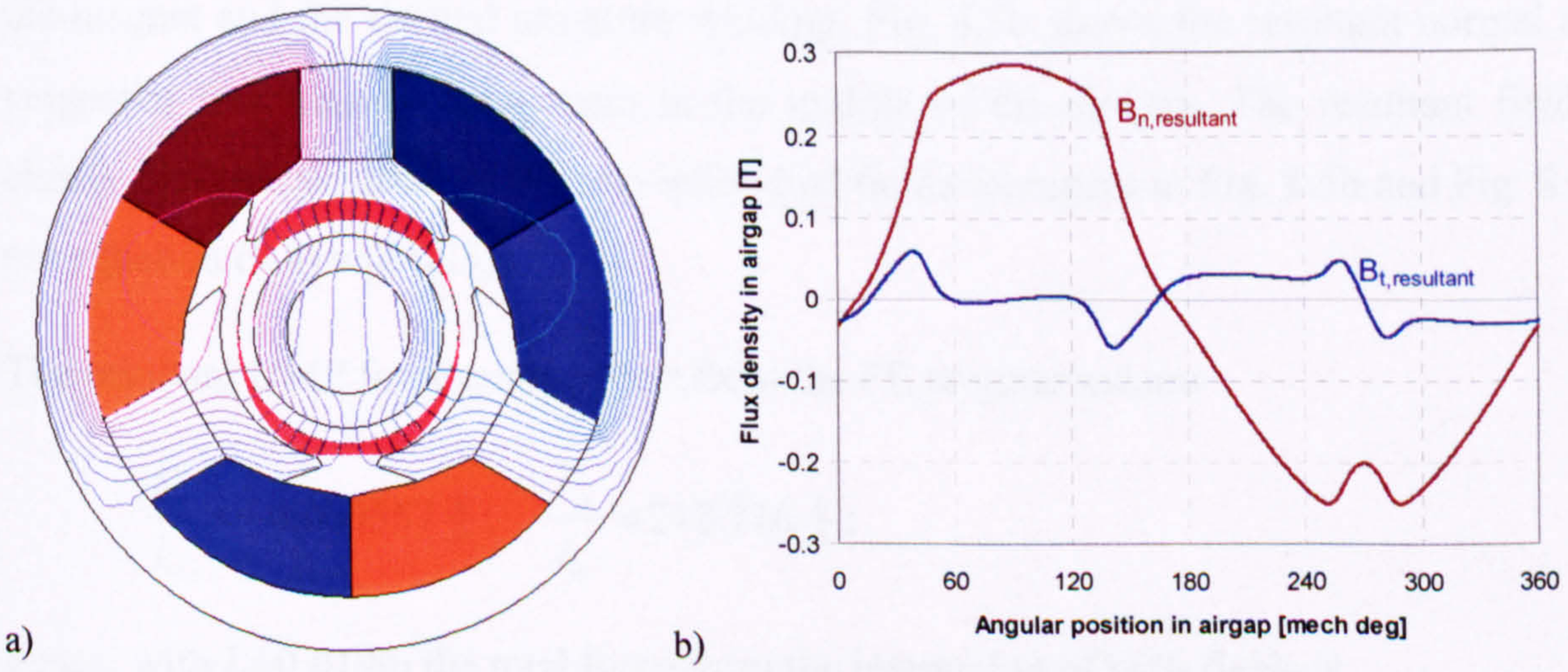

Fig. 8.7 Resultant field from magnet and winding with $10A_{rms}$ line current – both aligned for maximum UMP: a) field lines and magnetic stress vectors on rotor, b) air gap field distribution

The magnitude of the current corresponds to a line current of $10A_{rms}$ (the typical current during initial ramp up). Fig. 8.6a shows the field from the armature winding with the magnet 'switched off', i.e. the magnetisation is set to zero. Fig. 8.6b shows the corresponding normal and tangential flux density component in the middle of the air gap. The field from the armature winding is only about a third of that from the magnet.

The resultant UMP force components from the FE programme for $10A_{rms}$ line current are

$$\frac{F_x}{l_a} = 0.000165\,\frac{N}{m}; \quad \frac{F_y}{l_a} = 3.4118\,\frac{N}{m};$$

hence, with l_a=0.019m the force from the armature field on its own is only

$$F_x = 0\ \text{N}, \quad F_y = 0.065\ \text{N}, \quad \text{and} \quad |F| = 0.065\ \text{N}.$$

This is less than a quarter of the force from the rotor magnet field.

Fig. 8.8 shows the UMP force variation of the armature field as a function of peak line current between 0 and 20A. The force varies quadratically with the current. The UMP force is proportional to B^2 (see equation (8.6) and (8.7)), and the B-field set-up by the windings is proportional to NI (Ampere-turns), hence the force from the armature windings only is proportional to I^2.

Force from both fields together: magnet field and armature field aligned

This is the combination of the two cases above. Fig. 8.7a shows the resultant field from the magnet and the excited armature winding. Fig. 8.7b shows the resultant normal and tangential flux density component in the middle of the air gap. The resultant field is clearly the superposition of the two individual fields (compare to Fig. 8.5b and Fig. 8.6b, see equation (8.4) and (8.5)).

The resultant UMP force components from the FE programme are

$$\frac{F_x}{l_a} = -0.000557\,\frac{N}{m}; \quad \frac{F_y}{l_a} = 218.716\,\frac{N}{m};$$

hence, with l_a=0.019m the total force from the interaction of both fields is

$$F_x = 0\ \text{N}, \quad F_y = 4.156\ \text{N}, \quad \text{and} \quad |F| = 4.156\ \text{N}.$$

The total UMP force with 4.16N is clearly more than the sum of the individual forces from the magnet field and from the armature field (both together only 0.346N). The

difference of 3.814 N, due to the interaction of both fields, accounts for about 92% of the total force. This shows clearly that the interaction of both fields is by far the dominant force.

Fig. 8.9 shows the total UMP force variation with current. The offset at zero current corresponds to the force from the magnet field on its own. The relationship between force and current appears almost linear, despite the total UMP force being proportional to $(B_{mag}B_{coil}+B_{coil}^2)$ (see equation (8.6)). This is because the field from the magnet B_{mag} is significantly larger than the field from the armature winding B_{coil} and therefore the linear relationship dominates in this motor.

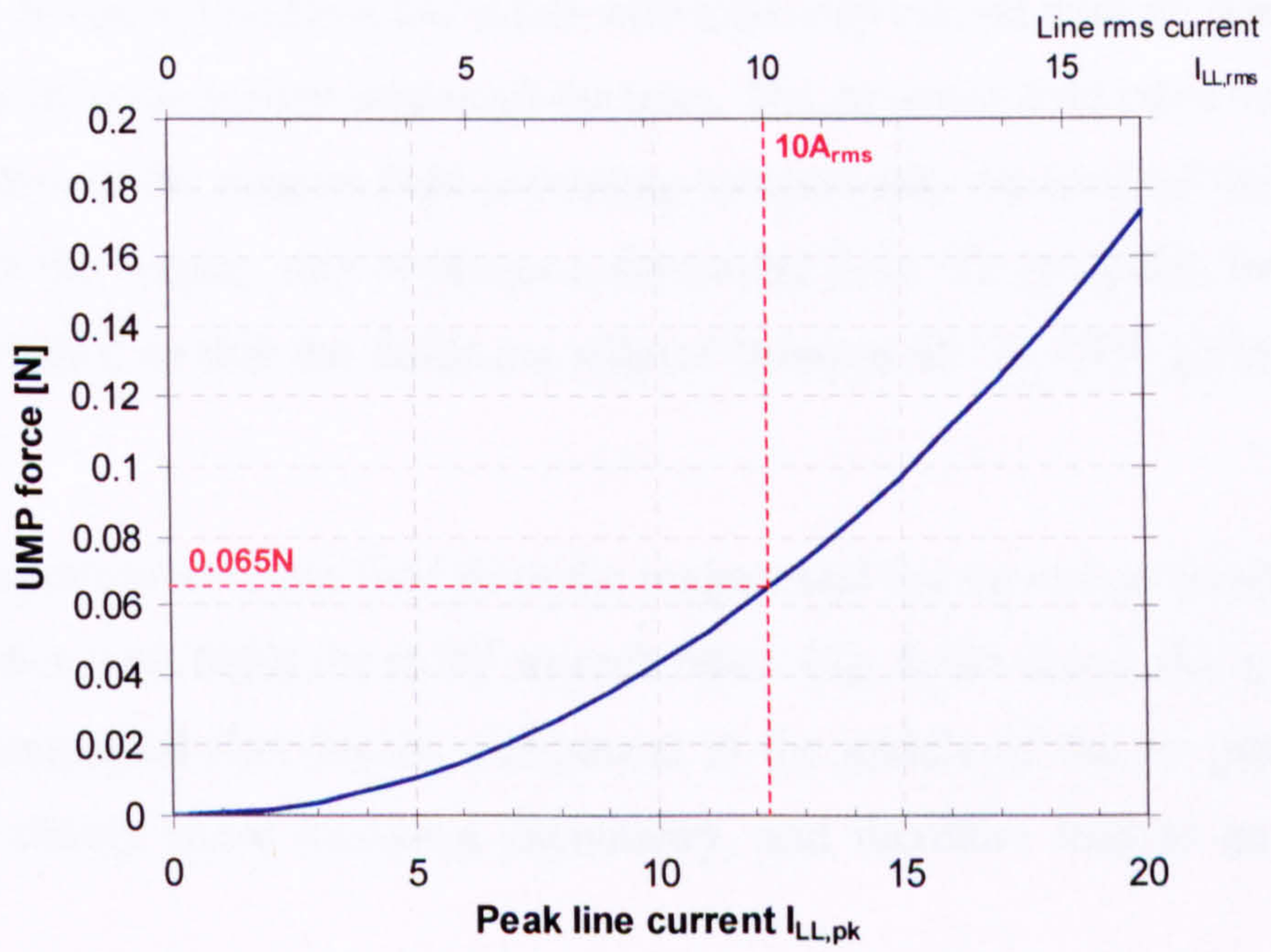

Fig. 8.8 UMP force due to armature field only as a function of peak line current (or rms line current)

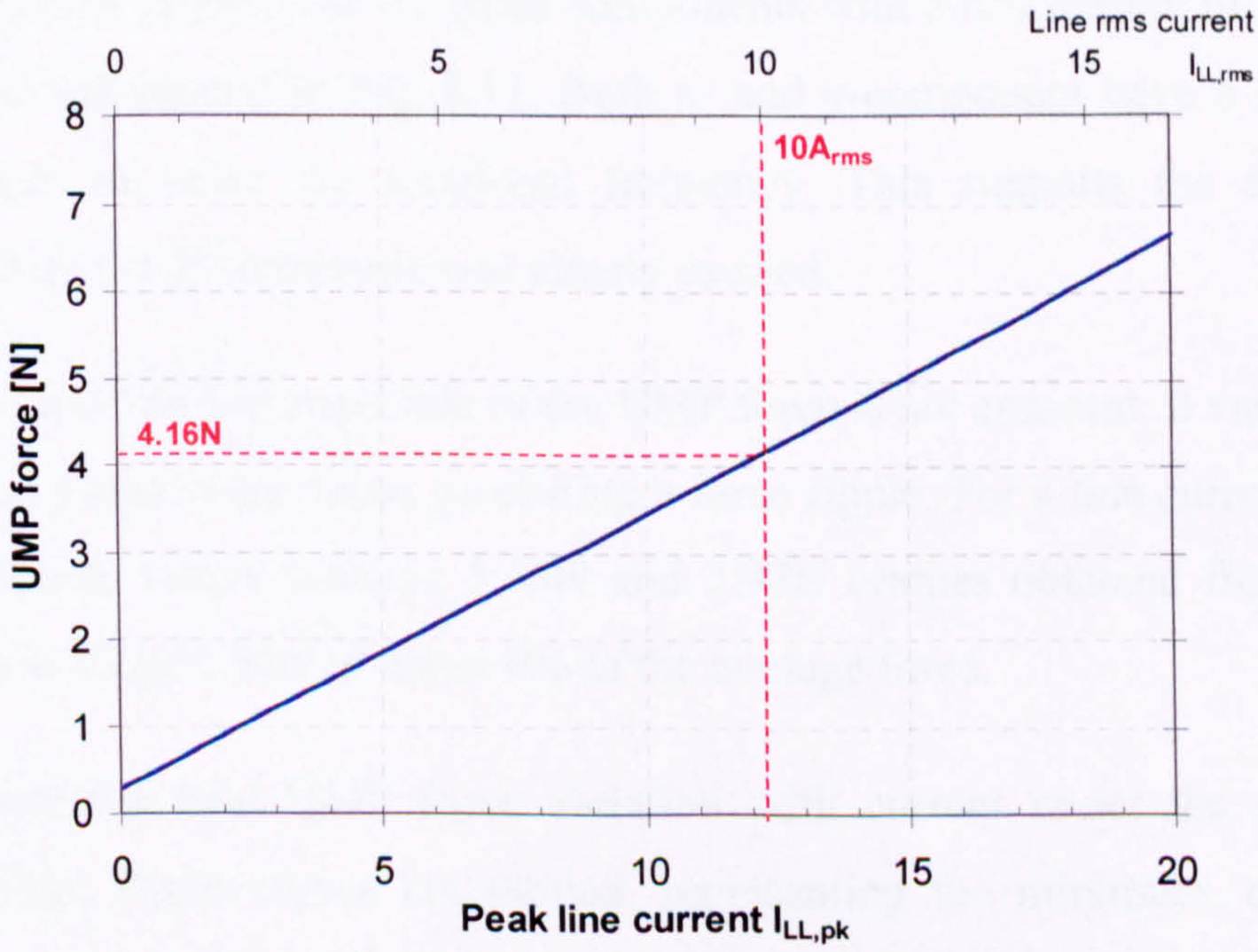

Fig. 8.9 Maximum UMP force due to interaction of magnet and armature field (both aligned) as function of peak line current (or rms line current)

8.5.4 FE Results – UMP Force During One Full Rotation With Fields at a Right Angle to One Another to Produce Maximum Torque

In the previous section the case of both fields aligned has been considered to determine the maximum possible UMP force as a worst-case scenario. However, during normal operation as a motor the magnet field and the armature field are positioned as close as possible at right angles to produce maximum torque. This more realistic case will be modelled in this section.

Force from both fields together: magnet field and armature field at right angles

The motor is driven in brushless DC mode with a six step current control, which does not allow both fields to be at right angles all the time. The armature field takes on six distinct directions, whereas the magnet field is rotating continuously. Because of the diametrical magnetisation the magnet ring produces a sinusoidal field. To maximise the torque the current is switched so that the fields are aligned between 60^{o} to 120^{o}, giving maximum torque at 90^{o}.

Fig. 8.10a shows the resultant field from the magnet and the excited armature winding at the instant when both fields are at 90^{o} to each other. Fig. 8.10b shows the corresponding normal and tangential flux density component in the middle of the air gap. Both field components clearly show rotational asymmetry, and therefore lead to an unbalanced force.

For one full rotation of the rotor the force components with a line current of $10A_{rms}$ have been calculated and plotted in Fig. 8.11. Both x- and y-component have a fundamental force component of twice the rotational frequency. This supports the experimental observation where the 2^{nd} harmonic was clearly excited.

During one full rotation the amplitude of the UMP force is not constant. It varies between a minimum and a maximum value, producing a force ripple. For a line current of $10A_{rms}$ the force amplitude varies between 3.63N and 3.97N (values obtained from FE). The force variation is about 0.34N or about 9% of the average force.

Fig. 8.12 shows the total UMP force variation with current under the condition of maximum torque. Three curves are plotted, representing the minimum, average, and maximum UMP force. The difference between maximum and minimum represents the magnitude of the force ripple. The relationship between force and current appears almost

linear again, because the field from the magnet B_{mag} is significantly larger than the field from the armature winding B_{coil} and therefore the linear relationship dominates in this motor.

When comparing the maximum UMP force magnitude, calculated for operation with magnet and stator fields at right angles, with the worst-case UMP magnitude, calculated earlier for magnet and winding fields aligned, the difference is not large. Comparing the value at $10A_{rms}$ line current, the force difference is less than 5% (3.97N versus 4.16N). Hence, the worst-case situation does not overestimate the force in the real motor by very much.

8.5.5 Summary of FE Results

The FE results confirm the experimental observation, that there is a significant difference between the UMP force in the unexcited motor (during coast down) and that in the motor being driven. With zero current in the winding the UMP force is quite modest with only 0.28N. This force is purely due to the asymmetry caused by the uneven number of slots.

When the motor is driven, the force increases nearly linearly with the current. The highest currents, and hence forces, are seen during ramp-up. Typically currents of about $10A_{rms}$ are measured, causing a UMP force of around 4N. This is more than 13 times the no-load force, a large difference to the unexcited case.

Modelling the force variation during one full revolution, the x- and y-component clearly show a fundamental component varying with twice the rotational frequency of the motor. This agrees with the experimental evidence where the 2nd harmonic was clearly excited.

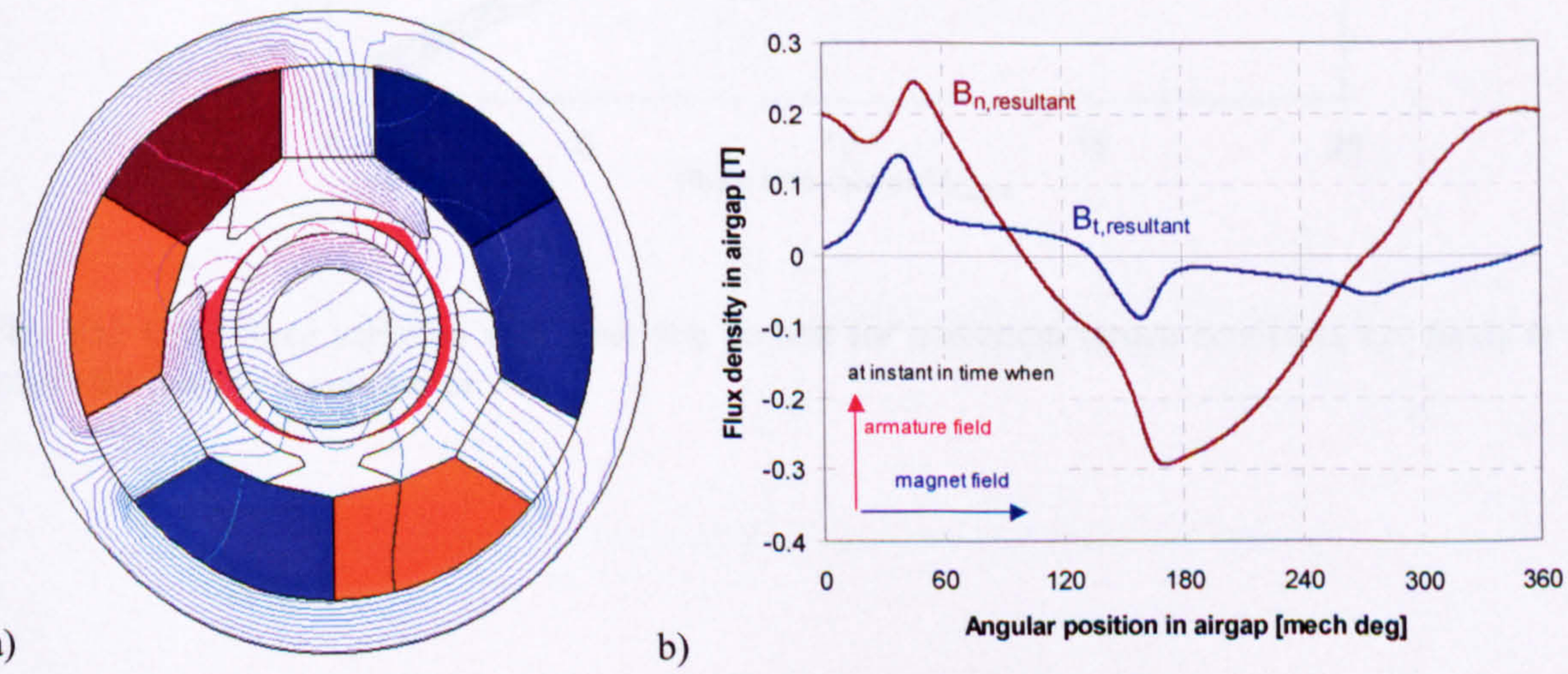

a) b)

Fig. 8.10 Resultant field from magnet and winding with 10Arms line current – both fields at right angles for maximum torque: a) field lines and magnetic stress vectors on rotor, b) air gap field distribution

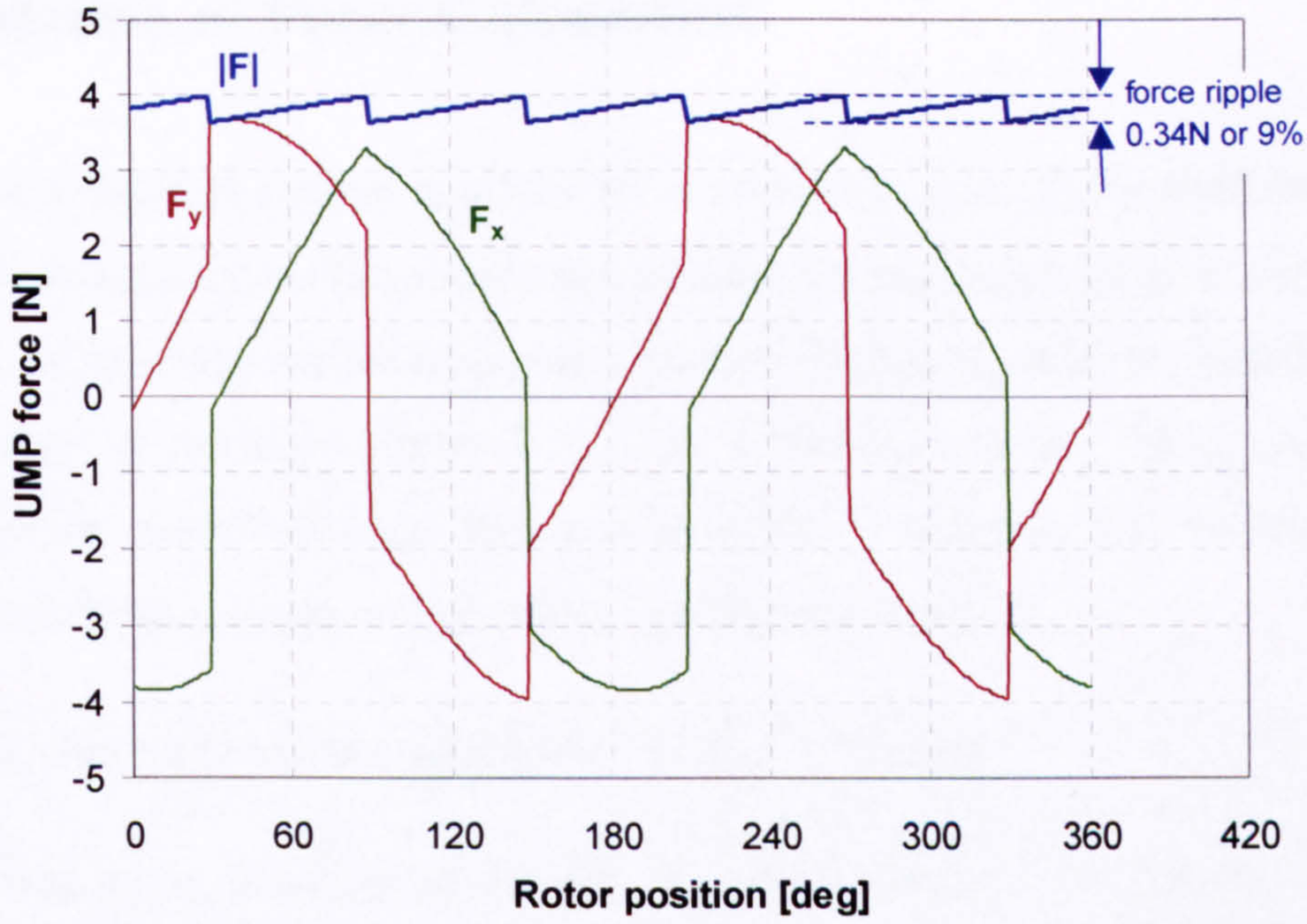

Fig. 8.11 UMP force components with $10A_{rms}$ line current for one full rotation in the 3-tooth, 2-pole motor – magnet field and armature field oriented as to produce maximum torque under brushless DC current control.

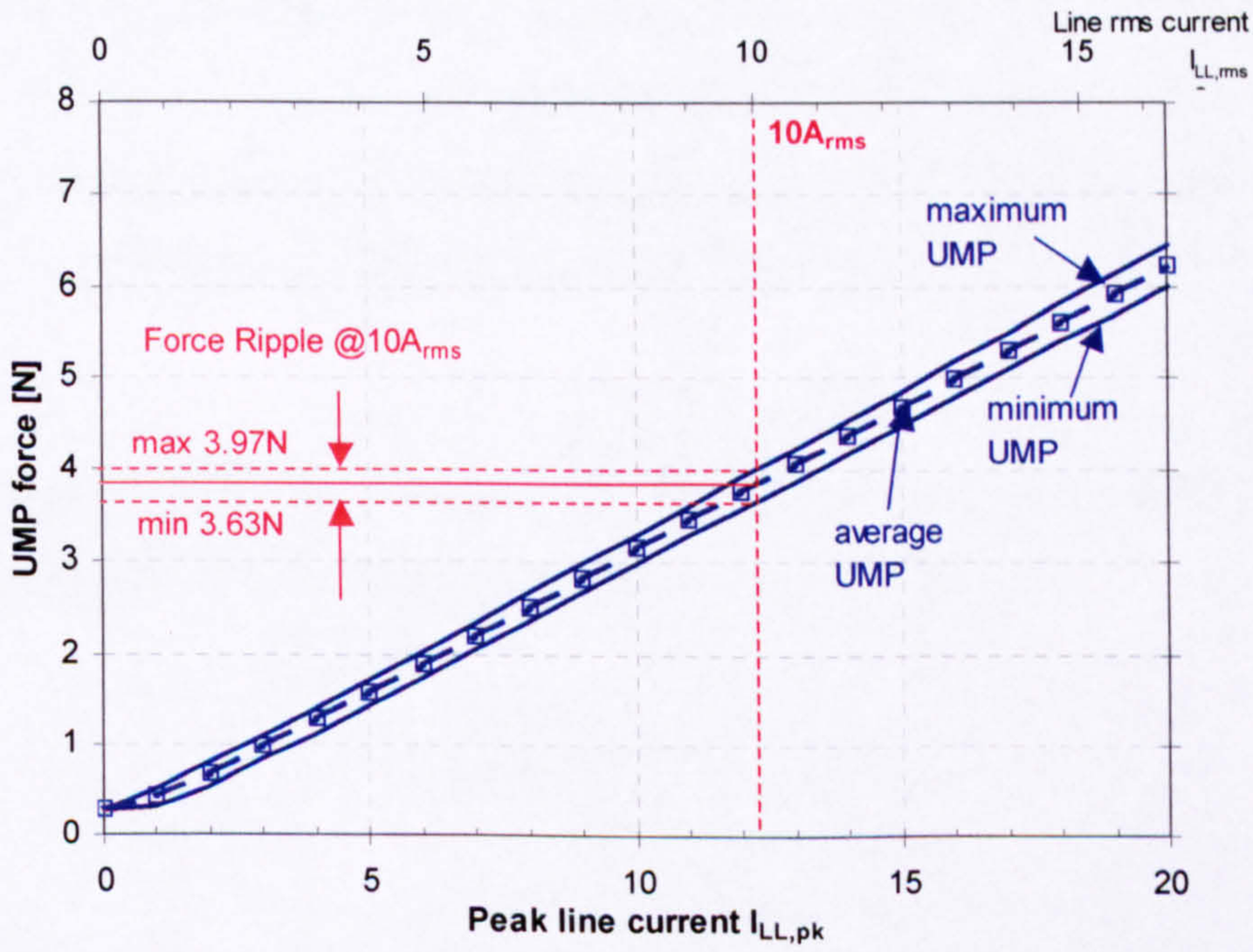

Fig. 8.12 UMP force variation with peak line current for maximum torque condition, i.e. fields at right angles for 3-tooth, 2-pole motor.

8.6 Validation of Force Calculation

The question is whether a force of about 4N is enough to take up the mechanical gap of nominal 191μm radially between shaft and emergency bearings? 4N is a small force for any mechanical bearing, but for a magnetic bearing with a much lower radial stiffness it may be enough to cause problems. It is very difficult to predict the dynamic effects during transients and resonance, but it is possible to estimate and measure a static displacement, and to estimate a steady-state resonance amplitude.

8.6.1 Static Displacement Calculated From FE Results

The UMP force F_{UMP}, calculated from FE, can be translated into a displacement x if the bearing stiffness k is known.

$$F_{UMP} = k \cdot x \rightarrow x = \frac{F_{UMP}}{k} \tag{8.12}$$

The upper magnetic bearing has a maximum theoretical stiffness of about 86000 N/m to 95000 N/m [101]. Experimental test results have shown that the stiffness can be as low as 50000 N/m, but typically between 65000-80000 N/m [102]. The axial centre of the motor is half way between the lower and upper bearing, so that the UMP force produced by the motor is split equally between the bearings (see cross-section of pump Fig. 1.3, and Fig. 8.13).

Given a calculated UMP force of 4N for $10A_{rms}$ and an upper bearing stiffness of 65000N/m, the displacement at the top bearing is about 31μm.

$$x = \frac{\frac{1}{2} \cdot 4N}{65000 \frac{N}{m}} = 30.7 \cdot 10^{-6} m$$

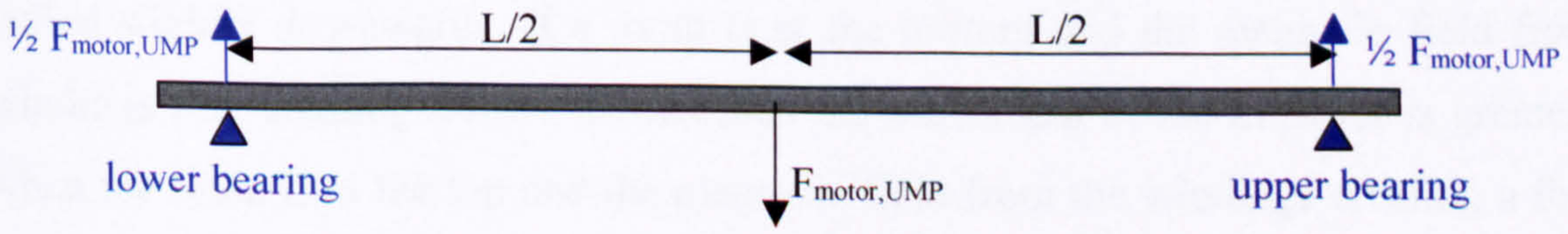

Fig. 8.13 UMP force distribution between upper and lower bearing

8.6.2 Experimental Set-Up to Measure Static Displacement

The pump without its envelope was mounted horizontally and levitated (Fig. 8.14). The orientation of the pump body was chosen so that the motor stator had either a tooth at the top or at the bottom. The motor was supplied with a DC current between two phases. The DC current equals the instantaneous peak current of the square wave current applied during one switching cycle. When the current is applied the UMP force will deflect the shaft out of its zero position. The deflection at the top bearing was measured with a Laser Scan Micrometer, which had a resolution of 0.5μm.

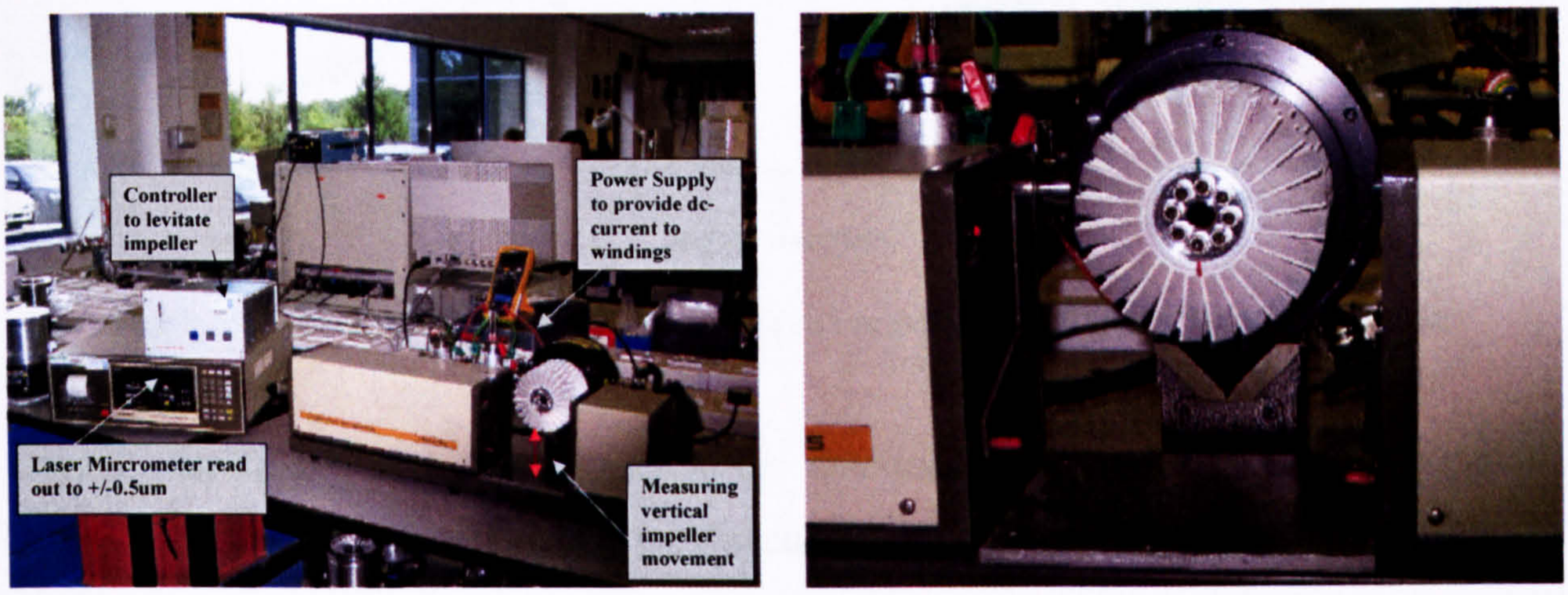

Fig. 8.14: a) Experimental set-up of measuring static displacement as a function of current, b) close-up of impeller

8.6.3 Measurement Results

Fig. 8.15 shows the measured displacement as a function of DC current. The DC current is equivalent to the instantaneous peak line current in the motor. The theoretical displacements based on the FE calculations are also shown for two different bearing stiffness, 65000N/m and 80000N/m.

The variation in the measured results is due to the fact that even with no current in the winding the impeller cannot be assumed to be perfectly concentric. Due to gravity it is pulled slightly downwards. If a tooth is at the bottom and the magnetic field from the windings also creating a force downwards the movement of the impeller is greater than when the tooth is at the top and the magnetic field from the windings creating a force to the top, too. In the later case the movement of the impeller is less, because it first has to overcome the downward gravity and eccentricity.

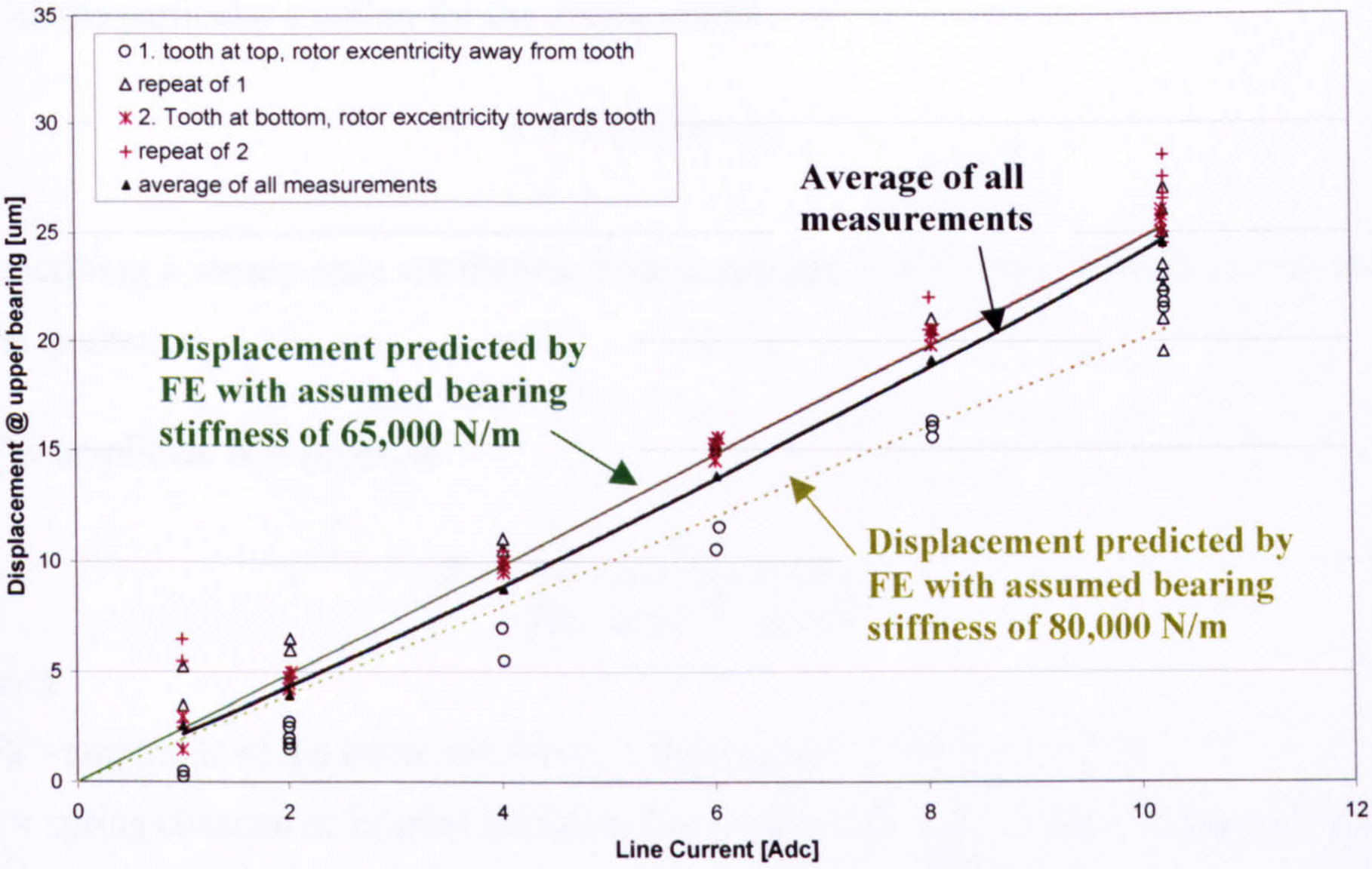

Fig. 8.15 Comparison between measured and predicted displacement as a function of current

Overall, the measured results lie within the theoretical results, which confirms the FE force calculation. During ramp-up with a current of $10A_{rms}$ or $12.25A_{pk}$ (equivalent to $12.25A_{dc}$ in the static test) the expected displacement according to Fig. 8.15 is just over 30μm (extrapolated – DC supply was only capable of delivering maximum $10A_{dc}$). This agrees very well with the calculated displacement according to (8.12). This is still significantly smaller than the available nominal radial air gap of about 191μm. It is important to remember that the above measurement is only a static measurement, and in reality the motor is spinning, experiencing all sorts of rotor dynamic effects especially during transients.

8.6.4 Resonance Amplitude for Harmonically Excited Vibration

As described earlier, it is very difficult to calculate dynamic effects during transient operation (e.g. start up). But it is possible to estimate the steady-state resonance amplitude for a single-degree of freedom system, which is subjected to a harmonically forced excitation, like a UMP force.

The differential equation of motion for this case, which can be found in any textbook on vibration [103, 104], is

$$m\ddot{x} + c\dot{x} + kx = F_0 \cdot \sin(\varpi t) \tag{8.13}$$

with the particular solution for the displacement x of

$$x = X\sin(\varpi t - \phi) \tag{8.14}$$

describing a steady-state oscillation with amplitude X and same frequency ω as that of the excitation.

The amplitude X is given as

$$X = \frac{F_0}{\sqrt{\left(k - m\varpi^2\right)^2 + \left(c\varpi\right)^2}} \tag{8.15}$$

with

F_0 = amplitude of the harmonic force, in this case the UMP force of 4N.

k = spring constant or bearing stiffness. In our case this is the lumped bearing stiffness of both bearings, each has about 80,000N/m, hence k=160,000 N/m.

m =mass of the system, i.e. mass of the impeller and rotating assembly, m=0.96 kg.

ω =excitation frequency. For resonance the excitation frequency coincides with the natural frequency of system $\omega_n = \sqrt{\frac{k}{m}} = 2\pi f$, hence ω_n =408 rad/s or f=65 Hz.

This is the right order of magnitude compared with the measured natural frequencies of 45Hz and 75Hz for the rotating assembly (see Fig. 8.3).

c = viscous damping factor. In the absence of any knowledge about the damping factor, a typical starting point is to take 10% (or 5% for very lightly damped systems) of the critical damping, which is defined as $c_c = 2m\omega_n$. In this case c_c=783 kg/s and with 10% the damping factor is c=78 kg/s (or with 5% c=39 kg/s).

Hence, using a damping factor of 10%, the steady-state resonance amplitude for the 1st rigid body mode, is

$$X = \frac{4N}{\sqrt{\left(160{,}000N/m - 0.96kg\cdot\left(408rad/s\right)^2\right)^2 + \left(78kg/s\cdot 408rad/s\right)^2}} = 126\mu m$$

With a damping factor of 5% of the critical damping the resonance amplitude would be 251μm. The gap according to drawings between the shaft and the emergency bearing is 191μm +/- 9μm. This means a minimum gap of 182μm. In addition the shaft can have per drawing a maximum run out of 25μm, which can reduce the gap to 157μm. It can easily been seen that 4N could be enough to use up all the space, especially if there is

additional eccentricity due to manufacturing and assembly tolerances (could be as much as 40μm reducing the gap to 117μm).

On the other hand, this implies that more damping could reduce the resonance amplitude. To avoid contact between the shaft and the emergency bearing a safety factor of 2 will be applied between the minimum mechanical gap and the resonance amplitude. This means that a steady-state resonance amplitude of <60μm is required. This would be achieved with a damping factor of c=172 kg/s, equivalent to 22% of the critical damping. To investigate if increasing the damping in the magnetic levitated turbomolecular pump is a realistic solution is outside the scope of this work.

When passing a natural frequency, resonance can be set up with much larger amplitudes than the static ones. Taking into account that some eccentricity and shaft run-out is unavoidable in real life, it is possible that the calculated force of 4N is enough to take up the clearance.

8.6.5 Effect of Eccentricity on UMP Force

During the measurements described in Section 8.6.3 it was noticed that the impeller could not be assumed to be perfectly concentric, and that the results varied if the horizontally mounted pump was rotated by 180° around a horizontal axis (fields parallel or anti-parallel, tooth or slot at the bottom). Gravity in the horizontal arrangement would already put an offset on the shaft position and introduce some eccentricity. To establish how eccentricity contributes to the UMP force further FE calculations were carried out.

The worst case was modelled, i.e. magnet field and current field are aligned and shaft moved closer to one tooth due to eccentricity. This gives the maximum force. The eccentricity was varied between 0μm and 200μm, which is the maximum clearance between shaft and emergency bearing (clearance between rotor sleeve and stator teeth is about 1.5mm). The results are listed in Table 8.1.

UMP force in N (axial length of motor = 0.019m)			
Eccentricity towards tooth [μm]	Magnet only (current = $0A_{rms}$)	Magnet aligned with current ($5A_{rms}$)	Magnet aligned with current ($10A_{rms}$)
0	0.281	2.202	4.156
50	0.375	2.298	4.252
100	0.469	2.393	4.349
200	0.664	2.584	4.542

Table 8.1 Effect of eccentricity on UMP force

The effect of eccentricity is much smaller compared to the effect of the current in the SMC-Mk4 motor. A 200μm eccentricity introduces an additional 0.38N UMP. This is of similar magnitude to the UMP from the magnetic field of the magnets only (as experienced during coast-down), but only a small proportion of the UMP force when the windings are excited (only 9% of the force when the windings are excited with $10A_{rms}$ during run-up).

It can be concluded that the interaction of the harmonics of the excited windings with the magnetic field is by far the largest cause of the UMP problem. Asymmetry of the magnetic design (uneven number of teeth) or eccentricity create only a small UMP force.

8.7 Analysis of Contributing B-field Components

To find a way of avoiding or at least reducing the UMP force, it would be helpful to have a good understanding of which magnetic field component is contributing most to the resultant UMP force.

8.7.1 General Description of Fields by Fourier Series and Their Contribution to the UMP Force

The normal and tangential field from the magnet and from the phase coils, which can be obtained analytically or by Finite Element analysis, can be described as a Fourier series.

$$B_{n,mag} = \sum_{k=1}^{\infty} \hat{B}_{n,mag\_k} \cdot \sin\left(k\theta + \alpha_{n\_k}\right) \tag{8.16}$$

$$B_{t,mag} = \sum_{l=1}^{\infty} \hat{B}_{t,mag\_l} \cdot \cos\left(l\theta + \alpha_{t\_l}\right) \tag{8.17}$$

$$B_{n,coil} = \sum_{k=1}^{\infty} \hat{B}_{n,coil\_k} \cdot \sin\left(k\theta + \beta_{n\_k}\right) \tag{8.18}$$

$$B_{t,coil} = \sum_{l=1}^{\infty} \hat{B}_{t,coil\_l} \cdot \cos\left(l\theta + \beta_{t\_l}\right) \tag{8.19}$$

Substituting (8.16)-(8.19) into (8.6)-(8.7) and then (8.8)-(8.11) the x- and y-component of the force can be calculated. It consists of several terms, where each is the product of

two Fourier series multiplied by either $sin\theta$ or $cos\theta$. After applying trigonometric identities, each force component can be broken down into a combination of the following integrals:

1. $\int_0^{2\pi} \cos(k+l)\theta \cdot \sin\theta \, d\theta = 0$

2. $\int_0^{2\pi} \cos(k+l)\theta \cdot \cos\theta \, d\theta = 0$

3. $\int_0^{2\pi} \sin(k+l)\theta \cdot \sin\theta \, d\theta = 0$

4. $\int_0^{2\pi} \sin(k+l)\theta \cdot \cos\theta \, d\theta = 0$

5. $\int_0^{2\pi} \cos(k-l)\theta \cdot \sin\theta \, d\theta = 0$

6. $\int_0^{2\pi} \sin(k-l)\theta \cdot \cos\theta \, d\theta = 0$

7. $\int_0^{2\pi} \cos(k-l)\theta \cdot \cos\theta \, d\theta \neq 0$, if $|k-l|=1$

8. $\int_0^{2\pi} \sin(k-l)\theta \cdot \sin\theta \, d\theta \neq 0$, if $|k-l|=1$

From these eight different integrals only the last two lead to non-zero values, if $|k-l|=1$. For all other combinations of harmonic numbers (k and l vary between 1 and infinity), all integrals are zero.

That means, that only harmonics next to each other contribute to a net radial force. This is the same as saying that only harmonic fields whose pole pairs differ by one create UMP. The two harmonic fields that together contribute to a UMP force can be both from the magnet field or both from the stator field, i.e. 1st harmonic from magnet field with 2nd harmonic from magnet field, or 1st harmonic from armature field with 2nd harmonic from armature field, or they can be from a combination of the two, 1st harmonic from the magnet field with 2nd harmonic from the armature field or vice versa. Table 8.2 shows the possible combinations of harmonics next to each other that theoretically contribute to the UMP force, like 1-2, 2-1, 2-3, 3-2, 3-4, 4-3 and so on.

		Harmonic component of winding field										
		1	2	3	4	5	6	7	.....	n-1	n	n+1
Harmonic component of magnet field	1		1-2									
	2	2-1		2-3								
	3		3-2		3-4							
	4			4-3		4-5						
	5				5-4		5-6					
	6					6-5		6-7				
	7						7-6		....			
	.....							....		....		
	n-1								....		(n-1)-n	
	n									n-(n-1)		n-(n+1)
	n+1										(n+1)-n	

Table 8.2 Possible combinations of B-field harmonics, which can contribute to an UMP force in general

8.7.2 Harmonic Content of Magnet and Armature Field in the 3-Tooth, 2-Pole Motor

In the particular case of the 3-tooth motor, the harmonic contents obtained by Fourier analysis of the magnet field (see Fig. 8.5b) and the armature field (see Fig. 8.6b) are shown in Fig. 8.16 and Fig. 8.17.

Harmonic content of magnet field

The magnet field in the air gap is nearly sinusoidal as it would be expected due to the diametrical magnetisation of the ring magnet. It therefore has a large fundamental component and only very small higher harmonics. The higher harmonics are due to the effect of the slot openings, which distort the field. Because the air gap is relatively large (2.84mm) the effect of the slots is small. For *s* number of slots, only harmonics of the order n=ks+/- 1 exist (k integer). As there are three slots, only harmonics on each side of multiples of three exist, i.e. 2 and 4, 5 and 7, and so on, as can be seen in Fig. 8.16.

Harmonic content of armature field

The armature winding of the 3-tooth motor consists of three phases, each made up of a concentrated, short-pitched coil. The three phases are offset 120° in space and time, and therefore all multiples of 3 cancel each other out. The concentrated coils are short-pitched with a pitch angle of β=120°. The pitch winding factor of the n^{th} harmonic is defined as $k_{p,n} = \sin\left(n \cdot \beta/2\right)$, again leading to zero for all multiples of three. This means

for the 3-tooth motor that the armature winding field contains all harmonics except multiples of three, i.e. only 1-2, 4-5, 7-8 etc. exist as can be seen in Fig. 8.17.

Effect on UMP

In the previous section it was shown that only harmonics next to each other can create a UMP force. In the specific case of the 3-tooth, 2-pole motor, where no 3rd harmonics exist in either the magnet field or armature field, only the combinations shown in Table 8.3 can cause UMP. These are all combinations of the fundamental with the 2nd harmonics, the 4th with the 5th, 7th with 8th, and so on. The magnitudes of the 4th and higher harmonics are so small, that the main contributors to the UMP force are the fundamental and the 2nd harmonic. These will be analysed in more detail in the next section.

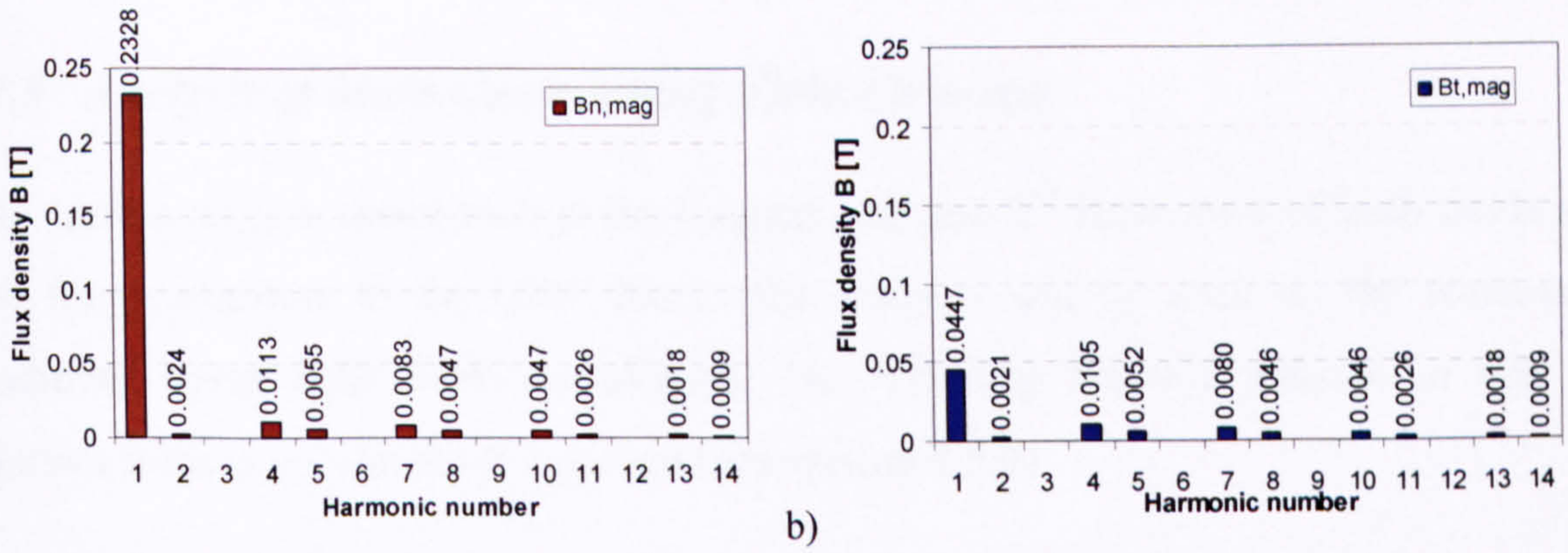

Fig. 8.16 Harmonic content of the magnetic field in the air gap under open circuit (magnet only) a) normal components, b) tangential components

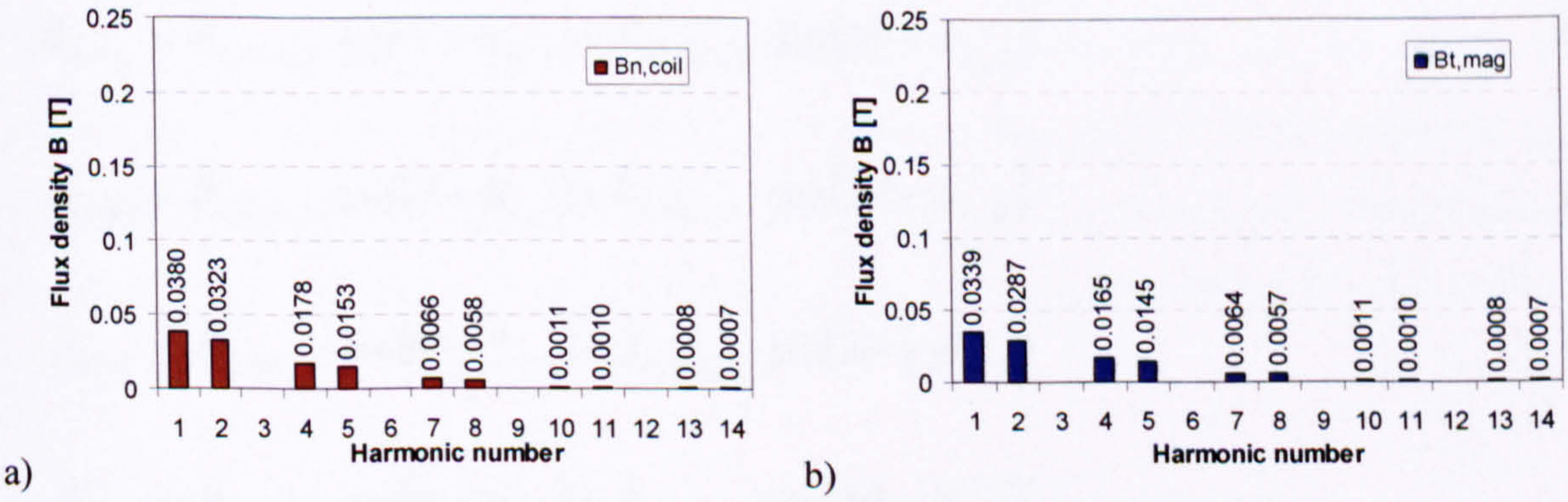

Fig. 8.17 Harmonic content of the magnetic field in the air gap due to the armature field with $10A_{rms}$ line current a) normal components, b) tangential components

		Harmonic number of winding field (no multiple 3rd harmonics, due to 3phase system and short pitched windings)							
		1	**2**	**4**	**5**	**7**	**8**		
Harmonic number of magnet field (no multiple 3rd harmonics due to 3 slots)	**1**		1-2						
	2	2-1							
	4				4-5				
	5			5-4					
	7						7-8		
	8					8-7			
									.....
								.....	

Table 8.3 Possible combination of B-field harmonics, which contribute to the UMP force in the 3-tooth, 2-pole motor.

8.7.3 Analysis of Main Contributing Field Elements

This section takes a closer look at the fundamental and 2nd harmonics of both fields and how they contribute to the UMP force. The analysis will be done on the worst-case condition, where both fields are aligned. The reference frame is chosen so that the resultant force is only in the y-direction (see section 8.5.3).

According to equations (8.16)–(8.19) each field can be described as a Fourier series. Because the amplitudes of the 4th and higher harmonics are small, the fields will be described in a first approximation by only the first two terms, hence

$$B_{n,mag} = \hat{B}_{n,mag\_1} \cdot \sin\left(\theta + \alpha_{n\_1}\right) + \hat{B}_{n,mag\_2} \cdot \sin\left(2\theta + \alpha_{n\_2}\right) \tag{8.20}$$

$$B_{t,mag} = \hat{B}_{t,mag\_1} \cdot \cos\left(\theta + \alpha_{t\_1}\right) + \hat{B}_{t,mag\_2} \cdot \cos\left(2\theta + \alpha_{t\_2}\right) \tag{8.21}$$

$$B_{n,coil} = \hat{B}_{n,coil\_1} \cdot \sin\left(\theta + \beta_{n\_1}\right) + \hat{B}_{n,coil\_2} \cdot \sin\left(2\theta + \beta_{n\_2}\right) \tag{8.22}$$

$$B_{t,coil} = \hat{B}_{t,coil\_1} \cdot \cos\left(\theta + \beta_{t\_1}\right) + \hat{B}_{t,coil\_2} \cdot \cos\left(2\theta + \beta_{t\_2}\right) \tag{8.23}$$

The magnitudes and phase angles obtained from Fourier analysis of the field distribution in the air gap are given in Table 8.4.

$\hat{B}_{n,mag\_1}$	0.2328 T	α_{n_1}	0°	$\hat{B}_{n,mag\_2}$	0.0024 T	α_{n_2}	-90°
$\hat{B}_{t,mag\_1}$	0.0447 T	α_{t_1}	180°	$\hat{B}_{t,mag\_2}$	0.0021 T	α_{t_2}	-90°
$\hat{B}_{n,coil\_1}$	0.0380 T	β_{n_1}	0°	$\hat{B}_{n,coil\_2}$	0.0323 T	β_{n_2}	-90°
$\hat{B}_{t,coil\_1}$	0.0339 T	β_{t_1}	0°	$\hat{B}_{t,coil\_2}$	0.0287 T	β_{t_2}	-90°

Table 8.4 Magnitudes and phase angles from Fourier series for fundamental and 2nd harmonic term of the magnetic field from the magnet and armature winding

The force in the y-direction is defined by equation (8.11). Inserting (8.6) and (8.7) into it, the following expression is obtained:

$$F_y = \frac{l_a \cdot r}{2\mu_0} \cdot \int_0^{2\pi} \left\{ B_{n,mag}^2 - B_{t,mag}^2 + B_{n,coil}^2 - B_{t,coil}^2 + 2 \cdot B_{n,mag} B_{n,coil} - 2 \cdot B_{t,mag} B_{t,coil} \right\} \sin(\theta) \cdot d\theta +$$

$$+ \frac{l_a \cdot r}{\mu_0} \cdot \int_0^{2\pi} \left\{ B_{n,mag} B_{t,mag} + B_{n,coil} B_{t,coil} + B_{n,mag} B_{t,coil} + B_{n,coil} B_{t,mag} \right\} \cos(\theta) \cdot d\theta \qquad (8.24)$$

Each of these terms will be calculated in turn, to identify which one has the largest effect on the UMP force. The result is shown in Table 8.5.

The total force came to 4.151N using only the first two parts of the Fourier series. This is very similar to the FE result of 4.156N, which included all higher frequency components. This agreement is more than 99%, and therefore the contribution of all higher harmonics can safely be neglected.

Out of the 16 different combinations there are two, which together contribute to around 77%. These are the combination of the fundamental magnet normal with either the normal or tangential 2nd harmonic of the armature field. These are by far the largest contributor. The next largest are the two based on the fundamental tangential magnet with either the normal or tangential 2nd harmonic of the armature again. They together are counting for about 15%. Overall, only four combinations are responsible for 92% of the UMP force in this 3-tooth, 2-pole motor.

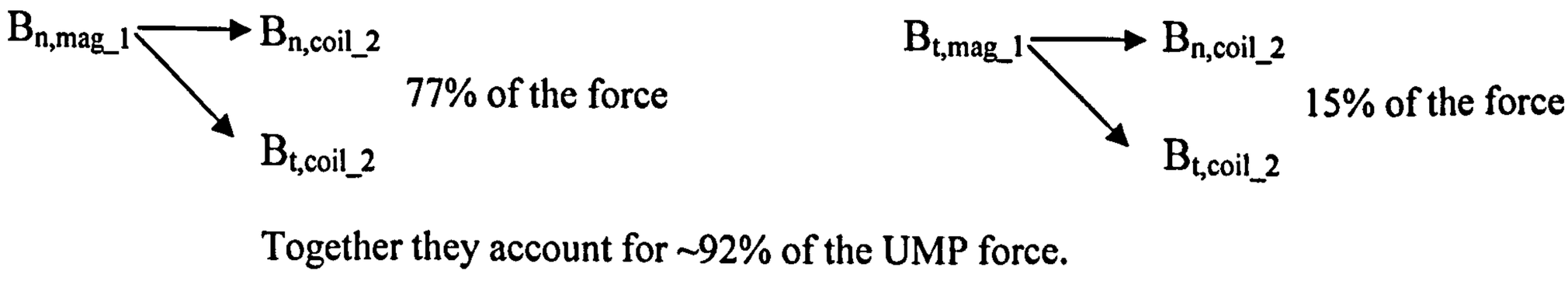

Fig. 8.18 The four combinations mainly responsible for UMP in the 3-tooth, 2-pole motor

Term	Interaction of fields	UMP force value [N]	% of total UMP force	
$B_{n,mag}^2$	1st normal magnet with 2nd normal magnet $F = \frac{l_a \cdot r}{2\mu_0} \cdot \pi \cdot \hat{B}_{n,mag\_1} \cdot \hat{B}_{n,mag\_2} \cdot \sin(\alpha_{n\_1} - \alpha_{n\_2})$	0.125729 N		
$-B_{t,mag}^2$	1st tangential magnet with 2nd tangential magnet $F = -\frac{l_a \cdot r}{2\mu_0} \cdot \pi \cdot \hat{B}_{t,mag\_1} \cdot \hat{B}_{t,mag\_2} \cdot \sin(\alpha_{t\_1} - \alpha_{t\_2})$	0.021124 N		
$B_{n,coil}^2$	1st normal coil with 2nd normal coil $F = \frac{l_a \cdot r}{2\mu_0} \cdot \pi \cdot \hat{B}_{n,coil\_1} \cdot \hat{B}_{n,coil\_2} \cdot \sin(\beta_{n\_1} - \beta_{n\_2})$	0.276203 N		
$-B_{t,coil}^2$	1st tangential coil with 2nd tangential coil $F = -\frac{l_a \cdot r}{2\mu_0} \cdot \pi \cdot B_{t,coil\_1} \cdot B_{t,coil\_2} \cdot \sin(\beta_{t\_1} - \beta_{t\_2})$	-0.218940 N		
$2B_{n,mag}B_{n,coil}$	**1st normal magnet with 2nd normal coil** $F = \frac{l_a \cdot r}{2\mu_0} \cdot \pi \cdot \hat{B}_{n,mag\_1} \cdot \hat{B}_{n,coil\_2} \cdot \sin(\alpha_{n\_1} - \beta_{n\_2})$	**1.692109 N**	**40.8%**	
	2nd normal magnet with 1st normal coil $F = \frac{l_a \cdot r}{2\mu_0} \cdot \pi \cdot \hat{B}_{n,coil\_1} \cdot \hat{B}_{n,mag\_2} \cdot \sin(\beta_{n\_1} - \alpha_{n\_2})$	0.020523 N		
$-2B_{t,mag}B_{t,coil}$	1st tangential magnet with 2nd tangential coil $F = -\frac{l_a \cdot r}{2\mu_0} \cdot \pi \cdot \hat{B}_{t,mag\_1} \cdot \hat{B}_{t,coil\_2} \cdot \sin(\alpha_{t\_1} - \beta_{t\_2})$	0.288690 N	7.0 %	
	2nd tangential magnet with 1st tangential coil $F = -\frac{l_a \cdot r}{2\mu_0} \cdot \pi \cdot \hat{B}_{t,coil\_1} \cdot \hat{B}_{t,mag\_2} \cdot \sin(\beta_{t\_1} - \alpha_{t\_2})$	-0.016020 N		
$B_{n,mag}B_{t,mag}$	1st normal magnet with 2nd tangential magnet $F = \frac{l_a \cdot r}{2\mu_0} \cdot \pi \cdot \hat{B}_{n,mag\_1} \cdot \hat{B}_{t,mag\_2} \cdot \sin(\alpha_{n\_1} - \alpha_{t\_2})$	0.110013 N		
	2nd normal magnet with 1st tangential magnet $F = \frac{l_a \cdot r}{2\mu_0} \cdot \pi \cdot \hat{B}_{n,mag\_2} \cdot \hat{B}_{t,mag\_1} \cdot \sin(\alpha_{n\_2} - \alpha_{t\_1})$	0.024141 N		
$B_{n,coil}B_{t,coil}$	1st normal coil with 2nd tangential coil $F = \frac{l_a \cdot r}{2\mu_0} \cdot \pi \cdot \hat{B}_{n,coil\_1} \cdot \hat{B}_{t,coil\_2} \cdot \sin(\beta_{n\_1} - \beta_{t\_2})$	0.245419 N		
	2nd normal coil with 1st tangential coil $F = \frac{l_a \cdot r}{2\mu_0} \cdot \pi \cdot \hat{B}_{n,coil\_2} \cdot \hat{B}_{t,coil\_1} \cdot \sin(\beta_{n\_2} - \beta_{t\_1})$	-0.246402 N		
$B_{n,mag}B_{t,coil}$	**1st normal magnet with 2nd tangential coil** $F = \frac{l_a \cdot r}{2\mu_0} \cdot \pi \cdot \hat{B}_{n,mag\_1} \cdot \hat{B}_{t,coil\_2} \cdot \sin(\alpha_{n\_1} - \beta_{t\_2})$	**1.503515 N**	**36.2 %**	
	2nd normal magnet with 1st tangential coil $F = \frac{l_a \cdot r}{2\mu_0} \cdot \pi \cdot \hat{B}_{n,mag\_2} \cdot \hat{B}_{t,coil\_1} \cdot \sin(\alpha_{n\_2} - \beta_{t\_1})$	-0.018309 N		
$B_{n,coil}B_{t,mag}$	1st normal coil with 2nd tangential magnet $F = \frac{l_a \cdot r}{2\mu_0} \cdot \pi \cdot \hat{B}_{n,coil\_1} \cdot \hat{B}_{t,mag\_2} \cdot \sin(\beta_{n\_1} - \alpha_{t\_2})$	0.017957 N		
	2nd normal coil with 1st tangential magnet $F = \frac{l_a \cdot r}{2\mu_0} \cdot \pi \cdot \hat{B}_{n,coil\_2} \cdot \hat{B}_{t,mag\_1} \cdot \sin(\beta_{n\_2} - \alpha_{t\_1})$	0.324902 N	7.8 %	
UMP Force F_y =		**4.150656 N**		

Table 8.5 Contributing components to the UMP force according to equation (8.24). red is contribution from magnet field only, green is contribution from armature field only, and yellow is contribution from the interaction of both fields. (l_a=axial length = 0.019m; r=radius of middle of air gap=0.009475m)

The fundamental normal component of the flux from the magnet is essential to the motor design and torque production, but the 2nd harmonic components from the coils are only there due to the choice of the short pitched, concentrated coil arrangement.

The next section investigates whether the UMP force in this three-tooth, two-pole motor can be influenced by design, without changing the fundamental design concept.

8.8 Effect of Design Parameters on UMP

8.8.1 Introduction

In the previous section the main B-field components contributing to the UMP force were identified. The two largest components, responsible for more than 75% of the UMP force, were shown to be the interaction of the magnet's normal fundamental B-field with the second harmonic of the normal and tangential B-field from the coils.

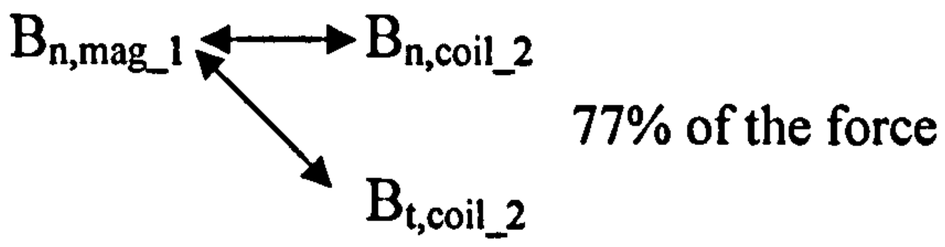

Finite element analysis so far has helped to quantify the magnitude of the UMP force, but has offered little insight into how to improve the design to reduce UMP effectively. Here analytical formulations are useful and can help to study the relationships behind the design parameters involved.

Hence, finding simple analytical expressions for these terms can help to show the underlying dependencies, and whether there are possibilities to reduce the UMP by design. More complex B-field expressions can be found in [94, 105-108], but that goes beyond the scope of the project, and does not add any more clarity.

8.8.2 Simple Analytical Formulas for the Main UMP B-Field Components

Fundamental normal component of the B-field from the magnet: B_{n,mag_1}

The normal B-field component from the diametrically magnetised cylindrical magnet is nearly sinusoidal, especially when ignoring the effects of the stator slots (see Fig. 8.5b open-circuit air gap field distribution). Assuming the stator iron is infinitely permeable and no fringing and leakage is happening between the magnet and stator surface, the peak

B-field in the air gap can be described by equation (8.25), where B_r and μ_r are the remanence and relative permeability of the magnet, $r_{o,mag}$ is the magnet outer radius, l_{mag} and l_{gap} are the magnet and air gap radial length, and r is the point of interest in the air gap.

$$B_{n,mag}(r) = B_{gap} = \frac{B_r \cdot l_{mag}}{\frac{r}{r_{o,mag}} \cdot l_{mag} + \mu_r \cdot l_{gap}} \tag{8.25}$$

With B_r=0.7T, μ_r=1.295, l_{mag}=0.00291m, l_{gap}=0.00284m, $r_{o,mag}$=0.00816m and r=0.009475m (middle of the air gap), the flux density is 0.2887T, compared to 0.2328T (see Table 8.4) from the FE model. Equation (8.25) overestimates the field by 24%, because it is based on the assumption that the iron is infinitely permeable including the shaft, but the SMC Mk4 rotor uses a non-magnetic steel shaft, which has a μ_r of 1. This basically increases the effective air gap, which reduces the flux density; but for a first approximation equation (8.25) will be used.

<u>2nd Normal and tangential component of the B-field from the windings:</u> $B_{n,coil\_2}$, $B_{t,coil\_2}$

Equation (8.26) and (8.27) describe the normal and tangential B-field components of the armature field. The normal field component is the component that crosses the air gap, hence the effective air gap (sum of magnet depth and air gap, ignoring effects from slots for the moment) appear in the equation. The tangential field component is similar, replacing the effective air gap with the slot opening.

$$B_{n,coil} = \frac{3}{2} \cdot \mu_0 \cdot \frac{NI_{ph,pk}}{2 \cdot (l_{gap} + l_{mag})} \cdot \frac{4}{\pi \cdot n} \cdot \sin\left(n \cdot \frac{\beta}{2}\right) \tag{8.26}$$

$$B_{t,coil} = -\frac{3}{2} \cdot \mu_0 \cdot \frac{NI_{ph,pk}}{w_{slot}} \cdot \frac{4}{\pi \cdot n} \cdot \sin\left(n \cdot \frac{\beta}{2}\right) \cdot \sin\left(n \cdot \frac{\gamma}{2}\right) \tag{8.27}$$

β is the coil pitch angle, and γ the slot opening angle ($\gamma = w_{slot}/r_{i,stator}$ in rad), w_{slot} the slot opening, and $r_{i,stator}$ the stator bore radius. With N_{ph}=50turns, rated current $I_{ph,pk}$ =7.07A$_{pk}$, l_{gap} and l_{mag} as above, $\beta = 2/3 \cdot \pi$, w_{slot}=0.0046m, $r_{i,stator}$=0.011m, and n=2 (to obtain the second harmonic), the second normal and tangential B-field component are: $B_{n,coil\_2}$=0.0319T, and $B_{t,coil\_2}$=0.0324T. These results are within 2% and 10% respectively of the equivalent Fourier component from the FE simulation (see Table 8.4), which is very acceptable.

8.8.3 Possibility of Affecting UMP by Design

The aim is to find a way to reduce the UMP in the three-tooth, two-pole motor, but without affecting the torque (equation (8.28)), nor increasing the physical space envelope.

$$Torque = \tfrac{1}{2} \cdot B_{gap} \cdot N_{ph} I_{pk} \cdot k_w \cdot r_{i,stator} \cdot 2 \cdot l_a \tag{8.28}$$

Keeping the torque constant is a balance between the magnetic loading B_{gap} and the electric loading $N_{ph}I_{pk}$, and the physical dimensions. Increasing the magnetic loading increases the stator iron losses, which is not desirable, whereas increasing the electric loading directly increases the 2nd harmonic of the armature field. Keeping B_{gap} and $N_{ph}I_{pk}$ and also the physical space envelope constant, only the air gap length l_{gap}, the magnet length l_{mag}, and the slot opening w_{slot} are left to change.

The **slot opening** only appears in the $B_{t,coil}$ component, and for small slot opening angles γ, $sin(n \cdot \gamma/2)$ can be approximated to $\approx n \cdot \gamma/2$, which cancels the slot opening out. This means that UMP is independent of the slot opening for small slots, and affecting $B_{t,coil}$ in any significant way with the slot opening is not practical.

For a fixed B_{gap} and a fixed magnet material (B_r, $\mu_{r,mag}$), the **magnet length** l_{mag} and the **air gap length** l_{gap} are proportional and cannot be varied independently. If the air gap increases the magnet thickness has to increase too. l_{mag} and l_{gap} both appear in the normal field component of the magnet and the windings.

$$B_{n,mag} \propto \frac{l_{mag}}{l_{mag} + l_{gap}}; \qquad B_{n,coil} \propto \frac{1}{l_{mag} + l_{gap}} \tag{8.29}$$

If B_{gap} and B_r are fixed, the magnet length and air gap length cannot be changed independently of each other, and hence the magnitude of $B_{n,mag}$ is independent of the choice of air gap length and magnet length. $B_{n,coil}$ is the only component, that will be reduced if the air gap and the magnet length are increased. A large air gap and a deep magnet help to keep the magnitude of the normal component of the coil low. However, given the space constraints in the pump, the magnet was chosen as deep as possible from the outset to reduce the rotor losses. Hence, UMP in the three-tooth, two-pole motor cannot be reduced by simple design changes.

Skewing the magnet or the stator poles has also been considered. But to affect the UMP force the 2nd harmonic needs to be reduced, which would require a skew angle of 180°, which is impractical. Other ideas like an **asymmetric air gap** or **notches in the middle of the teeth** were also considered, but without yielding any practical UMP benefit.

In summary, no design change has been identified, that would reduce the UMP significantly. It is appreciated that this discussion is in parts very simplistic, and there is plenty of room for more detailed analysis on how to reduce UMP in an inherently asymmetric three-tooth, two-pole motor, but project timescales and the need of the company for a working motor did not permit more time to be spent on it.

8.9 The Next Step

The only feasible and commercially acceptable solution for this application with its passive magnetic bearings is a motor without any inherent magnetic asymmetry. Hence, this was the end of the three-tooth motor for turbomolecular pumps. Unfortunately however, in practical terms it also was the end for SMC, mainly because the performance benefits were marginal and perceived not worth the risk, despite commercially interesting quotations.

The next chapter looks at alternative motor designs to avoid UMP altogether, and develops a six-tooth, four-pole motor for the use in turbomolecular pumps.

Chapter 9

Alternative Machine Design

Avoiding UMP (Mk5)

9.1 Introduction

After having built the three-tooth design into a magnetic levitated pump and identified the severe impact of the UMP force on the system, it was clear that the three-tooth design would never be a solution for turbomolecular pumps with passive magnetic bearings. A different motor topology was required that avoids significant UMP.

Furthermore, the objective of finding a low-cost replacement motor as part of a cost-down exercise had changed into a more general requirement of designing a new low-cost motor for the next generation of turbomolecular pumps. This meant a greater design freedom, as the constraints regarding retrofitting the motor were no longer part of the requirement.

A new marketing requirement identified the axial height of the turbo pump as critical, and hence the new motor needed to suit the selected pumping mechanism, by being axially as short as possible. Rotational speed and power requirements have stayed the same.

This chapter looks at some alternative design topologies to avoid UMP and then reports on the design, build and test of the chosen machine concept (Mk5). It is recognised that asymmetries caused by tolerances in dimensions or magnetisation will create some UMP, so phrases like 'avoid UMP' in this chapter refer to avoidance of intrinsic UMP in the design.

9.2 Design Topologies to Avoid UMP

9.2.1 Possible Tooth-Pole Combinations

The three-tooth motor had an inherent UMP problem due to its odd number of teeth causing an asymmetric magnetic circuit. To avoid asymmetry in the design an even number of teeth is required. For a three-phase motor the minimum number of teeth was therefore six.

With six teeth there were three winding configurations that avoid UMP. The first one was an overlapped, fully pitched winding as is used on the existing motor (Fig. 9.1a). This avoids UMP as there are no even harmonics present in the stator field. A fully-pitched winding has the greatest winding factor ($k_p=sin(180/2)=1$), but inserting the coils is difficult and expensive, and the endwindings are large. As axial length had become a critical parameter, an overlapped winding was not acceptable. Also, with respect to cost it was not a design that is easy or cost effective to produce.

The other possibility was to stay with non-overlapped windings. With six teeth and three phases, this meant two coils per phase. Using two coils per phase next to each other would create a similar asymmetric winding configuration to that of the three-tooth design, and still have an inherent UMP issue (Fig. 9.1b). Using opposite teeth per phase creates a symmetric winding and depending of the coil orientation either produces a two-pole field (Fig. 9.1c) or a four-pole field (Fig. 9.1d).

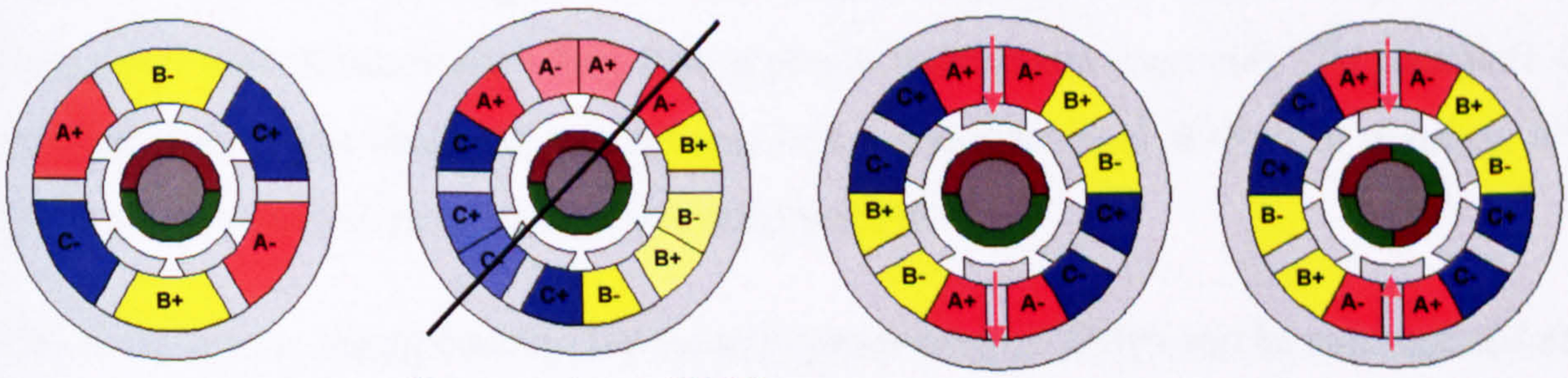

No good, due to UMP!

a) 6-teeth, 2-pole	b) 6-teeth, 2-pole	c) 6-teeth, 2-pole	d) 6-teeth, 4-pole
overlapped,	non-overlapped,	non-overlapped,	non-overlapped,
fully pitched winding	short pitched winding	short pitched winding	short pitched winding
best winding factor	poor copper utilisation	poor winding factor	better winding factor
k_w=1	Behaves like 3-tooth	k_w=0.5	k_w=0.866
large endwindings	design.	shorter endwindings	shorter endwindings
No UMP! **OK!**	**Has UMP!** **X**	**No UMP!** **OK!**	**No UMP!** **OK!**

Fig. 9.1 Possible winding configurations for a motor stator with 3 phases and 6 teeth

The two-pole winding has a very low winding factor as the coil pitch angle is down to 60° ($k_p=sin(60/2)=0.5$), which meant a poor copper utilization, whereas the four-pole configuration has a coil pitch angle of 120° ($k_p=sin(120/2)=0.866$), giving a 73% better copper utilization compared to the non-overlapped, two-pole winding.

The disadvantage of the four-pole winding is the required higher electrical frequency of 2kHz, and the associated risk of higher stator iron losses and switching losses in the drive due to the high frequency. However, existing turbopump drives of smaller pumps are operating at 1.5kHz, tested up to 20% overspeed (1.8kHz), so that the step to 2kHz was felt as a relatively low risk with regards to the drive. With regards to the stator iron losses, using thinner laminations will help to keep the iron losses to an acceptable level.

Hence, the chosen motor topology for the Mk5 motor was a non-overlapped, six-tooth, four-pole motor.

9.2.2 Further Concept Decisions

With regards to the SMC material it was decided to leave it for the moment. There were still many uncertainties with regards to the losses, especially with respect to damage done due to prototype machining. Only fully pressed parts could improve the situation and demonstrate the real properties, but only at large expense for the tooling necessary for prototyping. It was decided to take the lower cost, lower risk route and to use laminations for this motor.

Due to the high frequency a deep plastic bonded magnet was chosen to keep the rotor losses low. To keep the magnet assembly simple, a cylindrical magnet magnetised with four poles was chosen rather than four separate magnet-arc segments. To complete the magnetic circuit the four-pole magnet required a magnetic steel shaft. The magnets were protected as before with a carbon-fibre reinforced sleeve.

Hence the motor design concept for the next generation of TMPs can be summarised as:

- a laminated 6-tooth, 4-pole motor with non-overlapped windings, using a deep plastic-bonded, cylindrical 4pole magnet with a carbon fibre sleeve on a magnetic steel shaft.

9.3 The 6-Tooth, 4-Pole Machine Design

9.3.1 Initial Considerations

The performance requirements for this motor were the same as before with respect to rotational speed and output power, i.e. 100W at 60,000rpm (T=0.016Nm). However, physical size, especially the overall axial height became more important than efficiency during the conceptual design of the pump, and the motor was designed to achieve a short stack length of 15mm. The stator outer diameter was not as critical as the height, but if possible it should not exceed the diameter of the existing machine (54mm). Nevertheless, a smaller diameter would be better. As a starting point for the motor design a preferred stator outer diameter of 50mm was chosen.

All calculations were based on sinusoidal quantities, as this motor was going to be driven by a new sinusoidal, sensorless drive, which produces PWM-switched sinusoidal current waveforms in phase with the sinusoidal back EMF.

The magnetic loading of the machine, i.e. the peak radial air gap flux density B_{gap} was kept similar (=0.25T) to that in the previous machines. The peak flux density in the laminations was limited to 0.6T, which is a relatively low value for a 3% silicon-steel. But because an increase in iron loss was expected due to the two-times higher electrical frequency for the four-pole design, any increase in flux density would have made this worse.

The current density was increased compared to the existing motor. The permissible current density J_0 can vary a lot depending on the cooling conditions, class of insulation and type of enclosure. Small motors have typically a lower current density than large motors. All the motors used in turbomolecular pumps are rated for insulation class F (155°C), however the existing production motors have been limited to very low temperatures (i.e. 60-65°C) by a thermistor to prevent the impeller temperature exceeding 90-100°C. It was felt that it would be possible to allow the motor to run hotter and adjust the thermistor limit in the windings accordingly to prevent the impeller from overheating. The current density in the existing motor is about 2.8A/mm^2, whereas the SMC motors had current densities varying between 2.9 and 4.9A/mm^2. It was decided that the new motor will be potted, and for design purposes a current density of 4.5A/mm^2 was assumed.

Another constraint was the minimum shaft diameter. It needed to be at least 12mm to provide enough stiffness and avoid flexing of the shaft at full speed.

9.3.2 Basic Design Process – Sizing of the Machine

The fundamental design equation is the torque equation given below ((9.1) [109]), which is for a three-phase machine with sinusoidal or quasi-sinusoidal current waveforms, with sinusoidal or quasi-sinusoidal distribution of the magnet flux in the air gap, and with a 'real' winding, which includes winding factors and uses the fundamental component of the rectangular MMF wave.

$$T = \frac{3}{2} \cdot \frac{1}{2} \cdot \frac{4}{\pi} \cdot k_w \cdot N_{ph} \cdot I_{rms} \cdot \sqrt{2} \cdot B_{gap} \cdot \pi \cdot r_{i,stator} \cdot l_a \cdot \sin \beta \tag{9.1}$$

or simplified and with the torque angle $\beta = \pi/2$ for maximum torque

$$T = 3 \cdot k_w \cdot N_{ph} \cdot I_{pk} \cdot B_{gap} \cdot r_{i,stator} \cdot l_a \tag{9.2}$$

For a given torque T, winding factor k_w and a desired axial length l_a, the unknowns are the ampere-turns $N_{ph}I_{pk}$ and the inner stator diameter or radius $r_{i,stator}$.

The stator ID is typically between 50% and 65% of the stator OD, but can be as low as 40%. There are papers, which have investigated the optimal split ratio for brushless permanent magnet motors to minimise iron loss, or copper loss as a function of pole number and flux density ratio B_{gap}/B_{lam} [110, 111]. A split ratio of 55% was the final value in this design resulting in a stator ID of 27.5mm for a stator OD of 50mm.

As a result the minimum required ampere-turns $N_{ph}I_{pk\_min}$ to achieve the required torque can be calculated for the chosen stator ID by re-arranging (9.2).

$$N_{ph} I_{pk\_\min} = \frac{T}{3 \cdot k_w \cdot B_{gap} \cdot r_{i,stator} \cdot l_a} \tag{9.3}$$

This value needs to be smaller than the maximum allowable ampere-turn value (9.4), which is limited by the specified current density J_0 (in A_{rms}/mm^2), the expected slot fill factor k_{fill} and the slot area A_{slot} in the laminations. $N_{effslots\_ph}$ is the effective number of slots per phase (1 for this 6-tooth, 4-pole motor).

$$N_{ph} I_{pk\_\max} = J_0 \cdot \sqrt{2} \cdot k_{fill} \cdot A_{slot} \cdot N_{effslots\_ph} \tag{9.4}$$

The expected slot fill-factor depends on the stator construction and winding insertion method. A segmented stator allows a higher fill factor than a single piece lamination

stack. An expected fill factor of 28% was assumed for the single piece lamination stack. The segmented approach was not followed in this machine to lessen the technical risk associated with the untried nature of a segmented stack in this application.

Before the slot area can be calculated, the tooth width and the back iron thickness need to be defined. The tooth width w_{tooth} can be calculated for a given stator ID, number of teeth, and ratio of air gap to lamination flux density according to (9.5).

$$w_{tooth} = \frac{2\pi \cdot r_{i,stator}}{N_{teeth}} \cdot \frac{B_{gap}}{B_{lam}} \tag{9.5}$$

The back iron thickness is typically less than the tooth width. The aim is not to have a higher flux density in the back iron than in the teeth. As the flux splits into half when entering the back iron, the back iron thickness only needs to be half the tooth width. However, a lower flux density in the back iron would reduce the iron losses. Also, a thicker back iron helps to increase the natural frequency of the stack and reduces the likelihood of unwanted stator deformation and vibrations. A back iron depth of 75% of the tooth width was selected.

With the tooth width and back iron thickness determined, the available slot area A_{slot} for the windings can be estimated, and the maximum allowable ampere-turns calculated. If the maximum allowable ampere-turns is not greater than the necessary ampere-turns to achieve the required torque, then a different split-ratio and stator ID and/or back iron thickness need to be chosen and the steps repeated.

Regarding the rotor design, the magnet thickness l_{mag} is determined according to (9.6),

$$l_{mag} = \mu_{mag} \cdot \frac{B_{gap}}{\left(B_r - B_{gap}\right)} \cdot l_{gap} \tag{9.6}$$

where l_{gap} is the effective air gap length (i.e. sleeve thickness plus mechanical air gap), B_{gap} the desired air gap flux density and B_r and μ_{mag} are the remanence and relative permeability of the selected magnet material (plastic bonded NdFeB, B_r=0.59T, μ_{mag}=1.174, same values used in FE analysis). With the same effective air gap length of 3mm as in the other motors, the calculated magnet thickness came to 2.6mm. However, in the past plastic bonded magnets have underperformed slightly compared to calculations using data sheet values. To allow for a 'weaker magnet', a magnet length of 3mm was chosen instead (this is a 15% increase, in line with experience from previous tests). The resultant shaft diameter came to 15.5mm, which was significantly (29%)

larger than the minimum allowable shaft diameter of 12mm. If the calculated shaft diameter had not been larger than the given minimum, a larger stator ID would need to have been chosen, and the sizing of the machine repeated.

9.3.3 Target Back EMF, Turns per Phase and Wire Diameter

The target back EMF depends on the supply voltage. The motor will be run from a supply voltage of 24V+/-10%. The back EMF is typically chosen as large as possible without running out of volts so as to keep the current in the controller and drive to a minimum. Assuming full torque to be delivered at supply voltage minus 5%, plus a voltage drop of 5% in the drive and 10% across the motor inductance, the target line back EMF for this motor is about $13.7V_{rms}$ (phase back EMF $E_{ph,rms}$=$7.91V_{rms}$). With this back EMF value and the torque requirement the rated current can be calculated (9.7), and the number of turns determined (9.8) from the minimum required ampere-turns.

$$I_{rated,rms} = \frac{T \cdot \varpi_{mech}}{3 \cdot E_{ph,rms}} \qquad (9.7)$$

$$N_{ph} \geq \frac{N_{ph} I_{pk\_\min}}{I_{rated,rms} \cdot \sqrt{2}} \qquad (9.8)$$

The rated current came to $4.2A_{rms}$, and the required number of turns per phase was calculated as 20 (10turns per coil with two coils per phase).

Knowing the number of turns and the slot area, the wire diameter can be calculated. For high frequency application it is recommended that the wire diameter is about 4-5 times thinner than the skin depth to avoid increasing losses due to skin effect. For this motor 9 wires in parallel of 0.355mm diameter were specified (skin depth for copper at 2kHz δ=1.5mm). This gave a slot fill factor of 26.2%, compared to the design target of 28%, leading to a current density of $4.7A_{rms}/mm^2$, a slightly higher value than the initial design value of $4.5A_{rms}/mm^2$.

9.4 Verification and Refinement of the Design by FE Analysis

Having defined the main dimensions, a two-dimensional FE model has been set up to determine the flux densities in the stator under open-circuit, and under rated current, to validate the number of turns and back EMF calculation, estimate the inductance and model the torque. Fig. 9.2 shows the motor geometry with the dimensions given in Table 9.1.

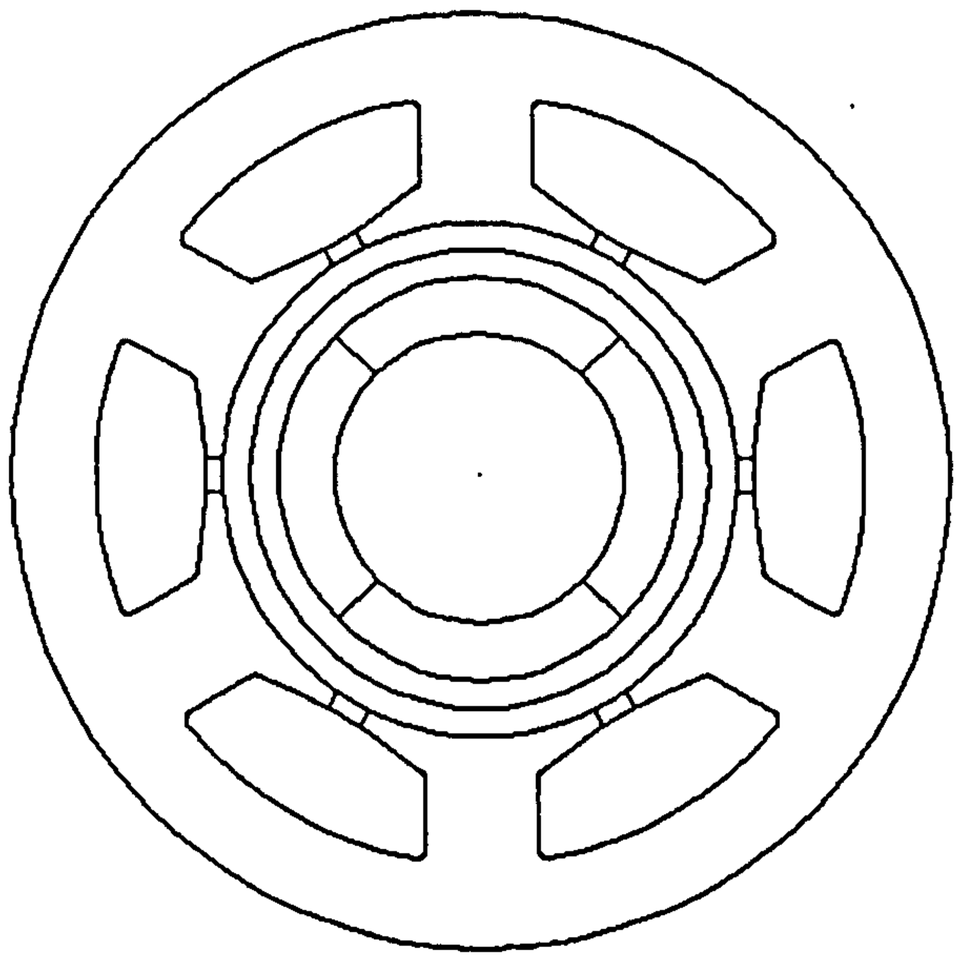

Fig. 9.2 Cross-section of 6-tooth, 4-pole motor (Mk5)

Parameter	Value
Stator OD	50.0 mm
Stator ID	27.5 mm
Sleeve OD	24.5 mm
Magnet OD	21.5 mm
Shaft OD	15.5 mm
Stack length	15.0 mm
Tooth width	6.0 mm
Back iron thickness	4.5 mm
Mechanical air gap	1.5 mm
Sleeve thickness	1.5 mm
Magnet thickness	3.0 mm
Slot opening	2.0 mm
Reactance slot depth	1.0 mm
Slot area	67.8 mm^2
Total lamination area	951.6 mm^2
Back iron area	643.2 mm^2
One tooth area	29.5 mm^2
One tooth tip area	21.9 mm^2

Table 9.1 Dimensions of 6-tooth, 4-pole motor (Mk5)

Open-Circuit Flux Plot and Back EMF

Fig. 9.3a shows the open-circuit flux density plot of the 4-pole motor, and Fig. 9.3b shows the corresponding back EMF waveform for half a rotor rotation. The modelled line-to-line back EMF is 13.77 V_{rms} for a stack length of 15mm and 20 turns per phase. From past experience with plastic bonded magnets and the fact that the magnet looses some strength in an axial magnetic short-circuit, an up to 15% lower back EMF compared to the model can be expected. To counteract the expected shortfall in back EMF, an axially longer magnet will be used in the final design (see section 9.7.2, Back EMF Measurements).

Full-Load Flux Plot and Torque

The full load flux density plot is shown in Fig. 9.4a, with both fields, i.e. the magnet field and the armature field, at right angles as to produce maximum torque. The resultant torque is shown in Fig. 9.4b. The peak flux densities, which were used to calculate the iron losses, are summarised in Table 9.2.

Armature-Reaction Flux Plot and Inductance

Fig. 9.5 shows the armature-reaction flux plot, with rated current of 4.2A_{rms}. The modelled line-to-line inductance is 52μH. However, this ignores the effects of the endwindings, and an increase of 20% to 30% in inductance is expected, leading to a value of 62 to 68μH.

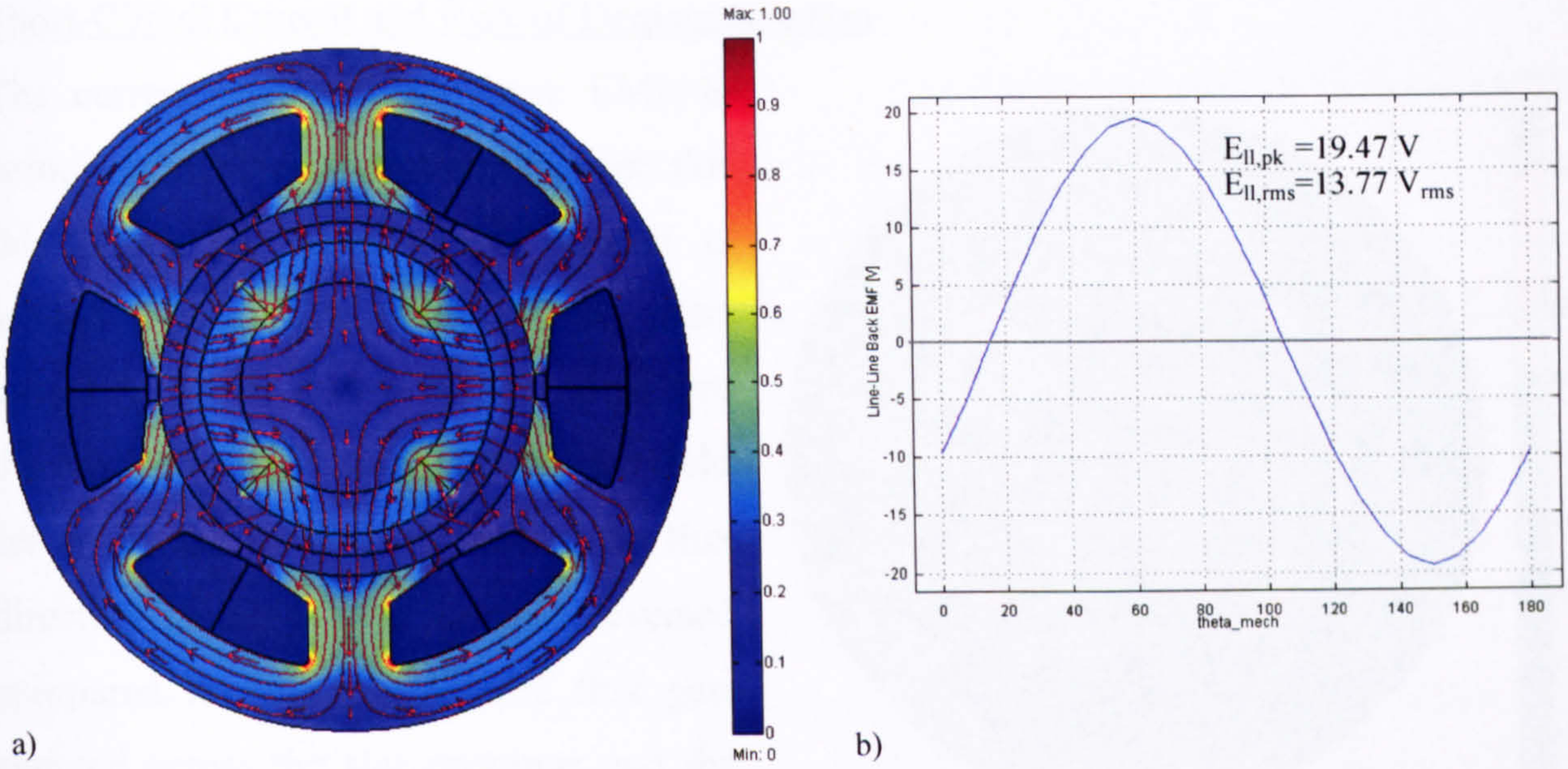

a) b)

Fig. 9.3 a) Open-circuit flux density plot of the 4-pole motor (Mk5); b) Line-line back EMF waveform

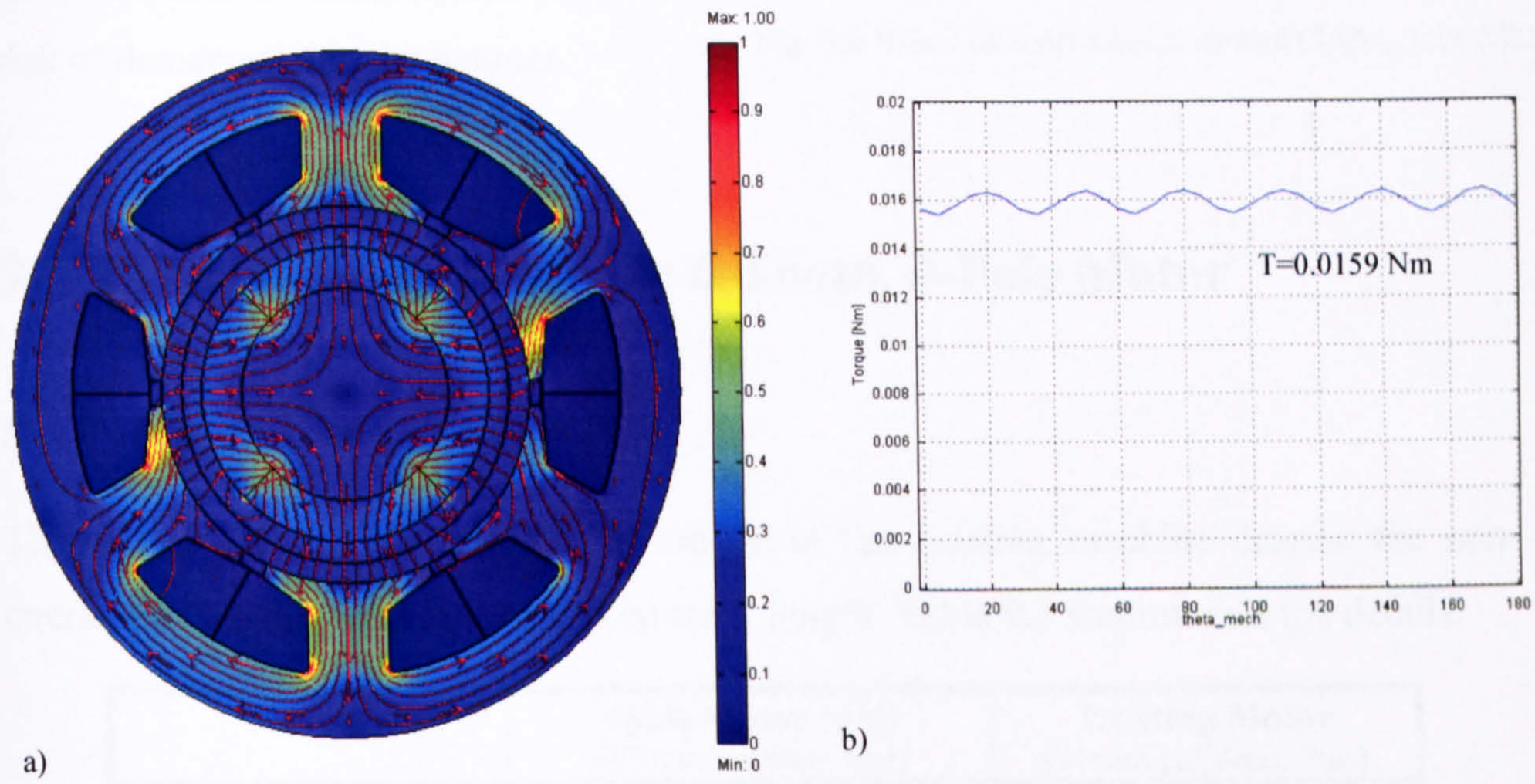

a) b)

Fig. 9.4 a) Full-load flux density plot with rated current, fields at 90°; b) Modelled torque (Mk5)

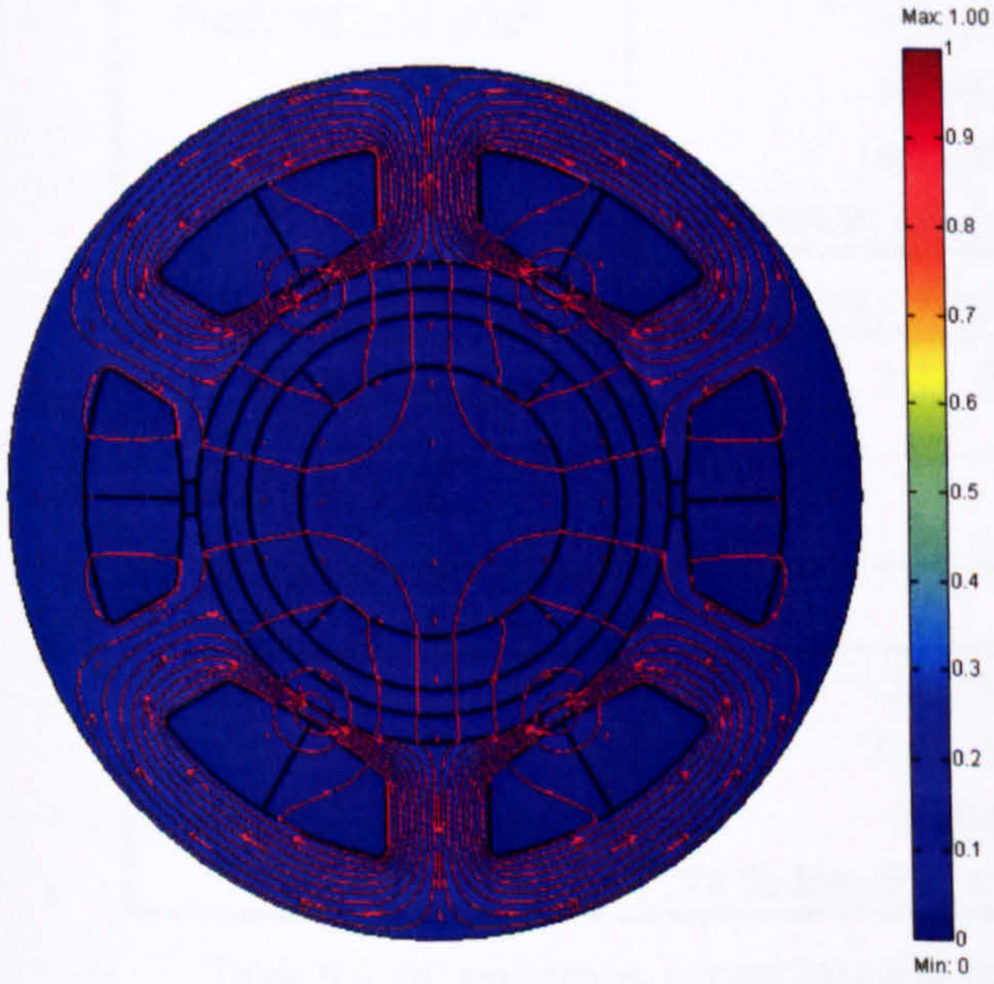

Fig. 9.5 Armature reaction flux density plot with rated current (Mk5)

Peak Flux Density:	Open-Circuit	Full-Load
air gap	0.26 T	0.26 T
back iron	0.38 T	0.39 T
tooth body	0.51 T	0.54 T
tooth tip	0.49 T	0.61 T

Table 9.2 Open-circuit and full-load peak flux densities of the 6-tooth, 4-pole motor (Mk5)

Short-Circuit Current and Risk of Demagnetisation

The current, at which the back EMF is zero, is called the short circuit current. For this motor the short circuit current is around $24A_{rms}$. The effect of the short circuit current is shown in Fig. 9.6, where the armature field totally opposes the field set up by the magnet. However, the flux direction in the magnet has not reversed compared to Fig. 9.3. All the flux gets shunted across the slot openings and the tooth tips start to saturate, but there is no risk of demagnetising the magnet.

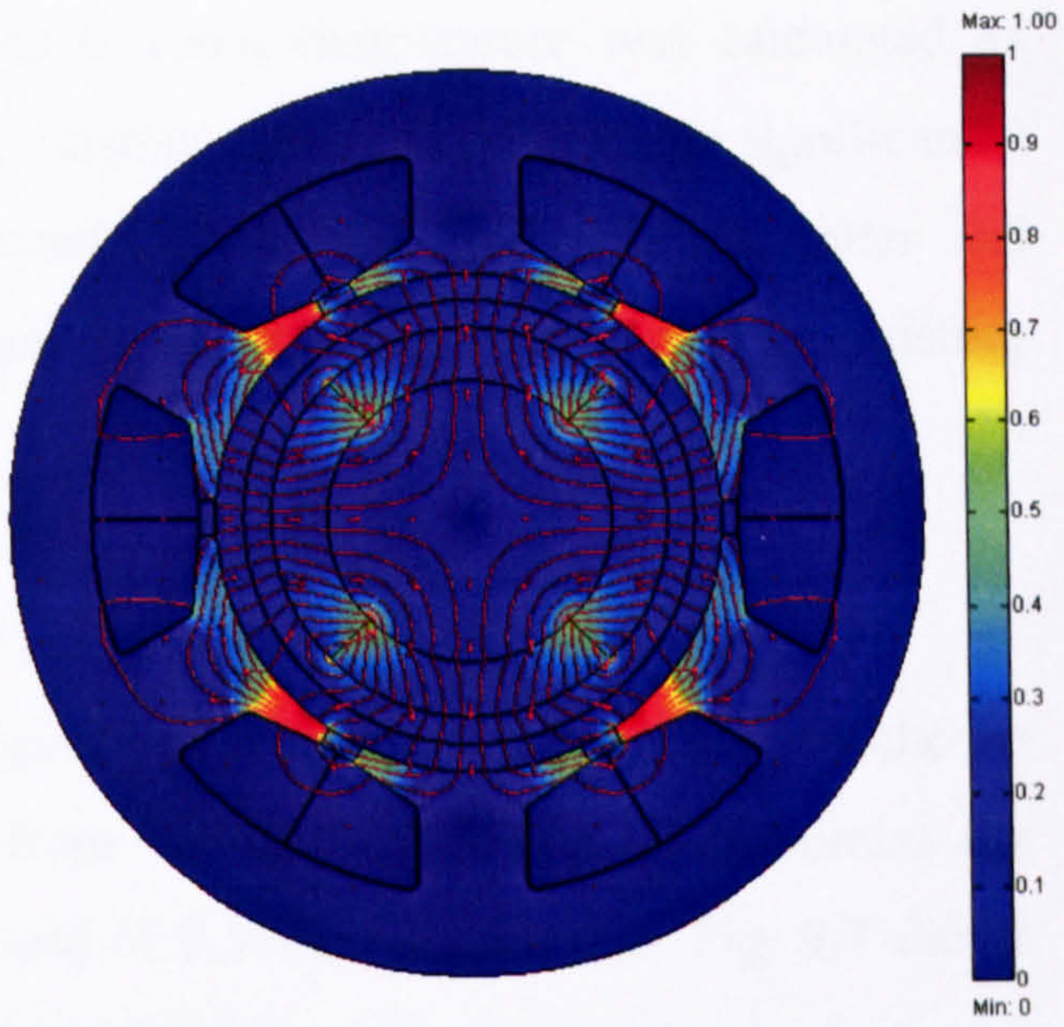

Fig. 9.6 Effect of short-circuit current ($24A_{rms}$) for Mk5

9.5 Predicted Losses for the 6-Tooth, 4-Pole Motor

9.5.1 Copper Loss

The copper loss in this machine is similar to the existing machine despite the non-overlapped winding and the short axial stack length. Table 9.3 summarizes the details.

	4pole Motor Mk5 (20turns per phase, Star)	**Existing Motor** (14turns per phase, Star)
DC Line-Line Resistance		
Predicted cold @20°C	**55 mΩ**	**55 mΩ**
hot @60°C	**64 mΩ**	
hot @80°C	**68 mΩ**	
	same as existing motor	
Copper Loss (based on same current but different winding temperature)		
with current of $5A_{rms}$, $T_{winding}$=80°C	**2.55 W**	
with current of $5A_{rms}$, $T_{winding}$=60°C		**2.35 W**
Copper Volume & Mass		
Slotfill	**26.7%**	**24.4 %**
Volume	**3.68 cm^3**	**14.32 cm^3**
Mass	**33.0 g**	**128.3 g**
	74 % less than existing motor	

Table 9.3 DC resistance, copper loss and copper volume for the 4-pole motor (Mk5)

With 9 wires in parallel of 0.355mm diameter, 20 turns per phase, and an average length per turn of 69mm, the line-to-line resistance at room temperature was calculated as 0.055Ω. This is the same resistance as in the existing motor, but due to the significantly reduced copper mass (74% less), it is expected that the windings will run hotter and therefore the copper loss will be slightly larger for the same current than in the existing motor.

9.5.2 Iron Loss Calculation

A significant increase in iron loss was the biggest risk when the 4-pole motor was chosen due to the increase in electrical frequency from 1000Hz to 2000Hz. To minimise the impact a lamination thickness of 0.2mm instead of 0.35mm was chosen. Fig. 9.7 shows the specific loss in W/kg for the lamination steel NO20 from Cogent.

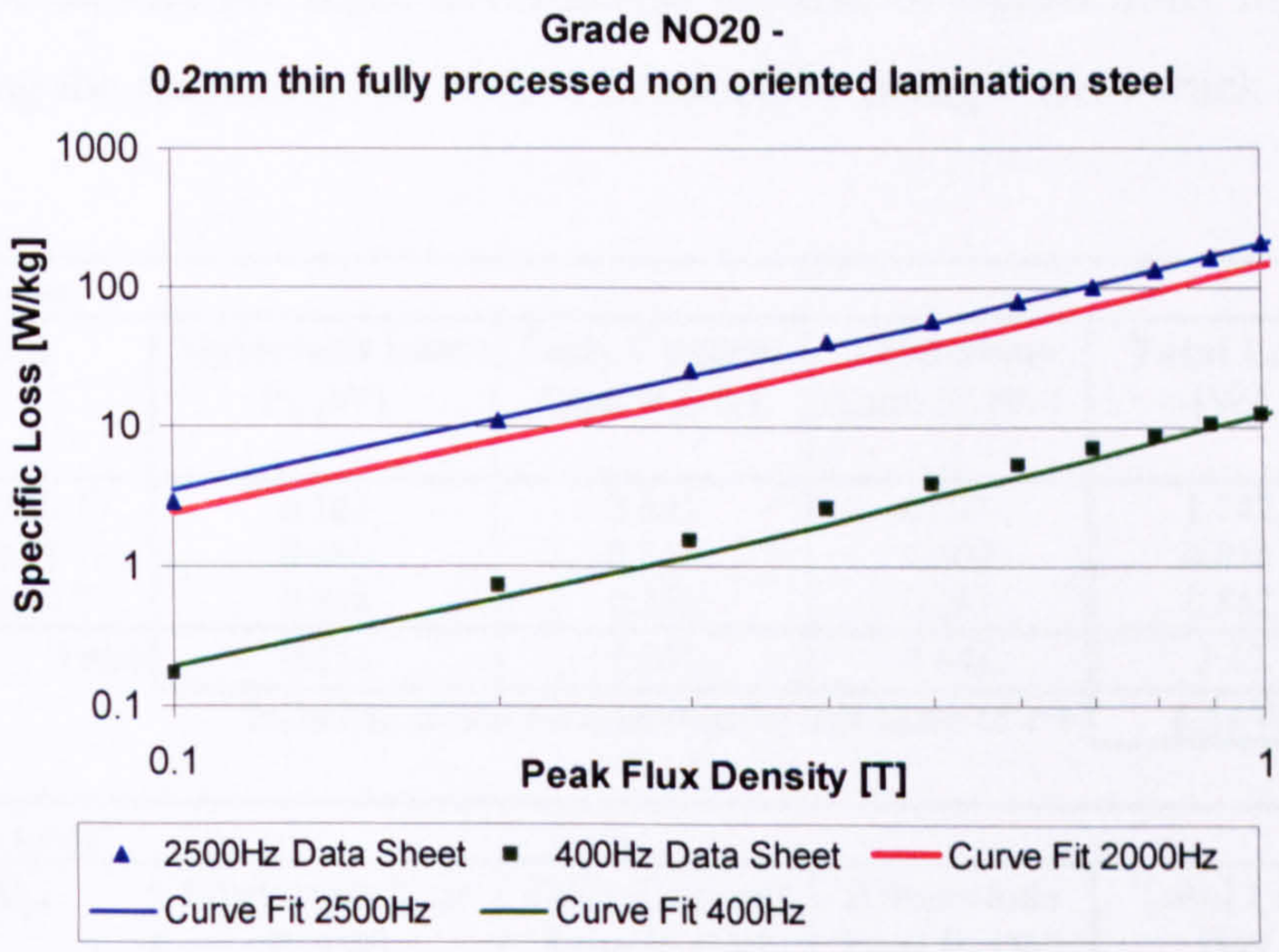

Fig. 9.7 Specific loss data in W/kg for Cogent lamination steel NO20 [112]

Specific Loss Data was available for frequencies of 400Hz and 2500Hz. With this data the coefficients for the loss equation given in (9.9) were established, and the loss data for 2000Hz calculated.

$$\frac{P}{mass} = k_h \cdot f \cdot B_{pk}{}^{n} + k_e \cdot f^2 \cdot B_{pk}{}^{2} + k_a \cdot f^{1.5} \cdot B_{pk}{}^{1.5} \quad \left[\frac{W}{kg}\right] \tag{9.9}$$

where B_{pk} is the peak flux density, n, k_h, k_e, and k_a are constants according to Table 9.4, and h stands for hysteresis, e for eddy-current and a for anomalous loss.

k_h	n	k_e	k_a
$1.1596 \cdot 10^{-2}$	2.9157	$1.6119 \cdot 10^{-5}$	$6.1625 \cdot 10^{-4}$

Table 9.4 Loss constants for Cogent NO20 lamination steel obtained through curve fitting

With the peak flux densities from Table 9.2 and the above constants the iron losses for no-load and full-load can be predicted according to equation (9.9) (see Table 9.5). For laminations it is common practice to multiply the loss data by a factor between 1.5 and 2 to account for an increase in losses due to insulation breakdown from stamping burrs and stacking, and due to differences in the test conditions compared to the real machine (effects of higher harmonics). For these thin laminations a correction factor of 2 had been assumed (worst case). The calculated iron losses for no-load are about 6.2W, and for full-load 7.1W. To account for rotating losses in the tooth tips and in part of the back iron, the tooth tip losses were multiplied by 2, and the back iron by 1.3 (30% of the back iron falls onto the joints with the teeth). Hence, the no-load iron losses came to 8.4W, and the full load iron losses to 10W. This is a similar value to the stator iron loss experienced in the two-pole machines discussed so far. Iron loss calculations are notoriously difficult and hence the uncertainties are high, nevertheless the risk of significantly higher iron losses due to doubling the frequency has been minimised by using 0.2mm thick laminations.

No-Load Iron Loss

	B_{pk}	Hysteresis Loss P_h [W]	Eddy Current Loss P_e [W]	Anomalous Loss P_a [W]	Total Loss [W]	Total Loss incl. rotating losses [W]
back iron	0.38 T	0.102	0.687	0.953	1.742	2.265
6 teeth	0.51 T	0.066	0.341	0.408	0.815	0.815
6 tooth-tips	0.49 T	0.044	0.233	0.285	0.562	1.124
	Total	0.212	1.261	1.646	3.12	4.20
a)				Including an empirical lamination loss factor of 2→	6.24 W	8.40 W

Full-Load Iron Loss

	B_{pk}	Hysteresis Loss P_h [W]	Eddy Current Loss P_e [W]	Anomalous Loss P_a [W]	Total Loss [W]	Total Loss incl. rotating losses [W]
back iron	0.39 T	0.110	0.724	0.991	1.825	2.373
6 teeth	0.54 T	0.078	0.382	0.444	0.904	0.904
6 tooth-tips	0.61 T	0.083	0.362	0.396	0.841	1.682
	Total	0.271	1.468	1.831	3.57	4.96
b)				Including an empirical lamination loss factor of 2 →	7.14 W	9.92 W

Table 9.5 Predicted iron loss for the 6-tooth, 4-pole motor (Mk5): a) No-load, b) Full-load

9.5.3 Current Waveform Simulation and Rotor Loss Calculation

The rotor loss depends on one hand on the rotor construction and the materials used and on the other hand on the space and time harmonics of the machine. The construction of the 6-tooth, 4-pole rotor is comparable to the SMC Mk1 machine as it uses a similar 'deep' plastic bonded magnet of 3mm magnet depth on a magnetic carbon steel shaft. Due to its short-pitched winding the 6-tooth, 4-pole motor has odd (except 3rd harmonics)

as well as even space harmonics similar to the 3-tooth motors. Due to the 4-pole design, the pole pitch is shorter, so the stator flux penetrates less far into the rotor, but at twice the frequency. The space harmonic loss comes to 0.005W or 2.6% of the total rotor losses (Table 9.6). Overall, space harmonics have made little contribution to the rotor loss in the other machines discussed, and this one is no exception.

The biggest difference is in the time harmonics, as this machine is driven by a sinusoidal PWM-inverter. Fig. 9.8 shows a simulated current waveform for 100W output power and its corresponding harmonic spectrum.

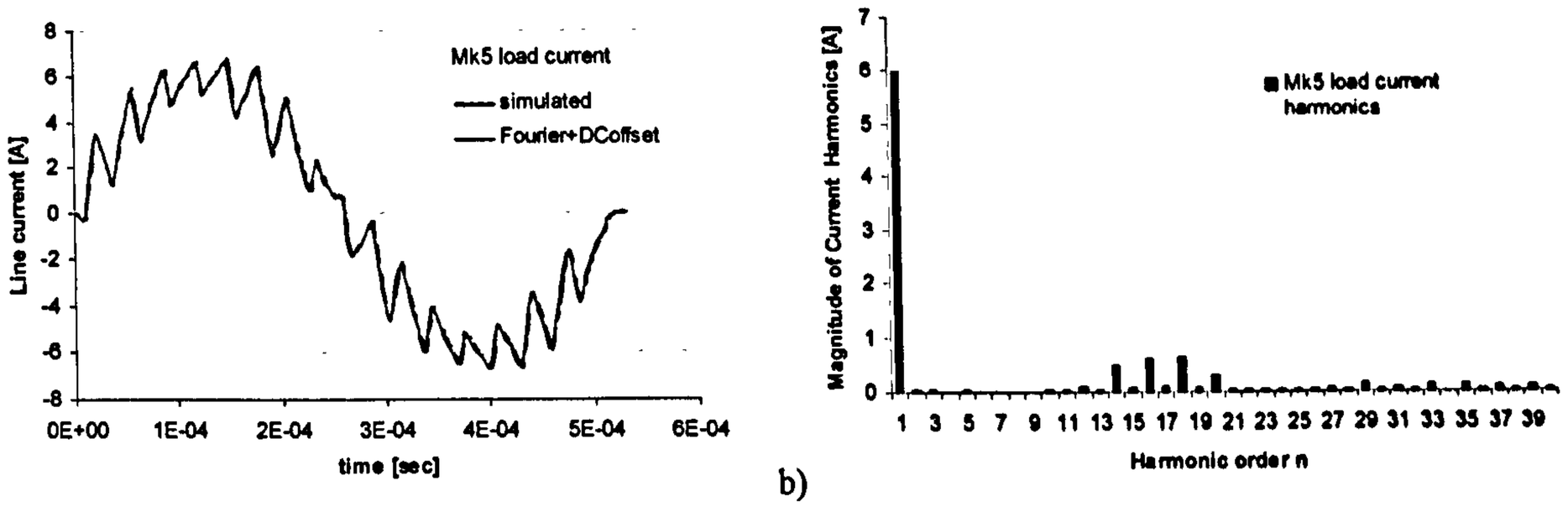

Fig. 9.8 Modelled Mk5 current for about 100W shaft output power: a) waveform, b) harmonic spectrum

Compared to the trapezoidal current waveforms of the previous drive (e.g. Fig. 6.8, page 111), there are no significant lower order harmonics, i.e. no 5^{th}, 7^{th}, (11^{th}, 13^{th}), which were responsible for the bulk of the rotor losses. The next largest harmonic after the fundamental is the $16^{th}/18^{th}$, which comes from the PWM frequency (16kHz, appearing as 32kHz ripple). As a consequence the rotor loss due to time harmonics is low with 0.18W (Table 9.6) in this machine compared with the other machines (Table 7.8, page 141), a further benefit for the turbomolecular pump. Nevertheless, the time harmonics are still the main source of the rotor losses, responsible for about 95% of the rotor loss.

The tooth ripple loss is like the space harmonic loss, also small enough to neglect, due to the use of deep plastic bonded magnets, which have a low conductivity, and a relatively small ratio of slot opening to tooth pitch due to the increase in stator inner diameter. All the rotor losses are summarised in Table 9.6.

6-tooth, 4-pole Motor Rotor Loss		
Space Harmonic Loss	**Time Harmonic Loss**	**Tooth Ripple Loss**
CFRE sleeve - *Deep plastic bonded NdFeB* magnet **0.000 W** Magnetic carbon steel shaft **0.005 W**	CFRE sleeve - Deep plastic bonded NdFeB magnet **0.017 W** Magnetic carbon steel shaft **0.166 W**	CFRE sleeve - Deep plastic bonded NdFeB *magnet* **0.000 W** Magnetic carbon steel shaft **0.004 W**
0.005 W	**0.183 W**	**0.004 W**
Total	**0.192 W**	

Table 9.6 Overview over the rotor losses for the 6-tooth, 4-pole machine (Mk5)

9.6 The Motor Built

Fig. 9.9 shows the motor in its unpotted and potted form. The laminations have been laser cut, and glued together. After the slot-liner has been inserted into the slots, the coils were hand-wound directly onto the teeth (work carried out by Mikroma SA, Poland). The slot fill looks just right; there is not much more space available for more turns or thicker wire. The quality of the motors was excellent, especially the small endwindings and the neat coil and phase lead connections.

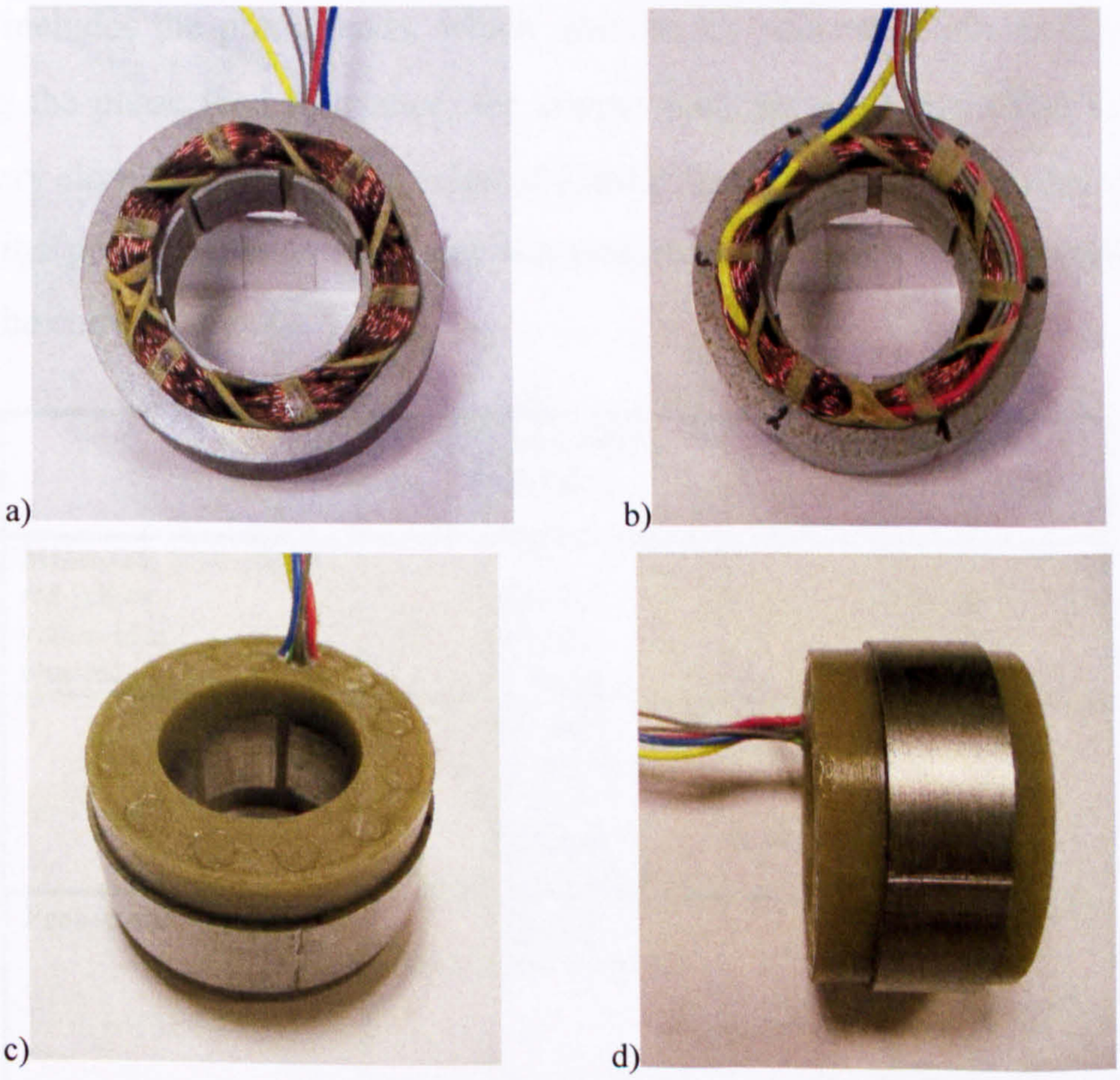

Fig. 9.9 Photos of the 6-tooth, 4-pole stator: a-b) unpotted, c-d) potted. Lamination OD=50mm, stack length=15mm, overall axial height (after potting)=29mm

The rotor parts can be seen in Fig. 9.10. The construction is very simple, consisting of a magnetic steel shaft, a cylindrical magnet, an aluminium end-ring and a carbon-fibre sleeve, all glued together.

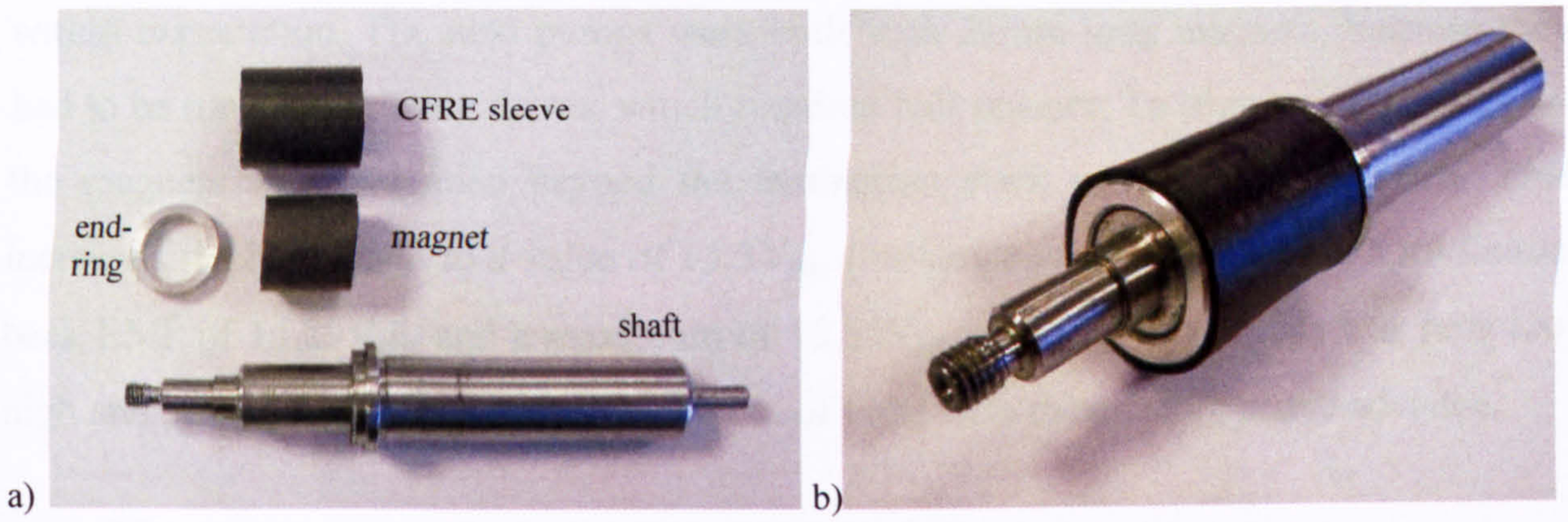

Fig. 9.10 Photos of the 6-tooth, 4-pole motor rotor: a) individual parts, b) assembled shaft

9.7 Testing of the 6-Tooth, 4-Pole Motor

9.7.1 Resistance & Inductance Values

The measured resistance and inductance values are summarised in Table 9.7. The DC resistance includes the phase leads, which account for approximately 4mΩ per phase. Subtracting the phase lead resistance, the copper winding resistance came to 52.5mΩ, which is very close to the predicted value of 55mΩ. The measured inductance also agrees well with the predicted value including the empirical correction for the neglected 3D-effects of the endwindings.

	DC Line-Line Resistance	**Line-Line Inductance@1kHz** Stator only
Measured: betw. phases red-yellow yellow-blue blue-red	 60.43 mΩ 60.14 mΩ 60.79 mΩ	 61.59 µH 61.09 µH 61.45 µH
Average	**60.5 mΩ** incl. ca. 8mΩ lead resistance → **52.5 mΩ** pure copper resistance	**61.4 µH**
Predicted:	**55 mΩ** pure copper resistance	**52 µH** plus 20%-30% for neglected endwinding 3D effects → **62-68 µH**

Table 9.7 Measured DC resistance and inductance values for the 6-tooth, 4-pole motor

9.7.2 Back EMF

The very first motor was built with a 16mm long magnet and the measured line-to-line back EMF came to 13.1V_{rms}. This was 5% lower than the predicted FE value, which was within expectation. The next pumps were built with 21mm long magnets, because they had to be run with existing drives, which required hall sensors. To trigger the hall sensors the magnets were extended beyond the lamination stack on one side by 5mm. This increased the back EMF to a value of 15.3V_{rms} (=average of 18 pumps, with a minimum back EMF of 14.89V_{rms} and a maximum of 15.55V_{rms}, see Fig. 9.11). This was now too high and pumps under load started to run out of volts with the existing phase advance.

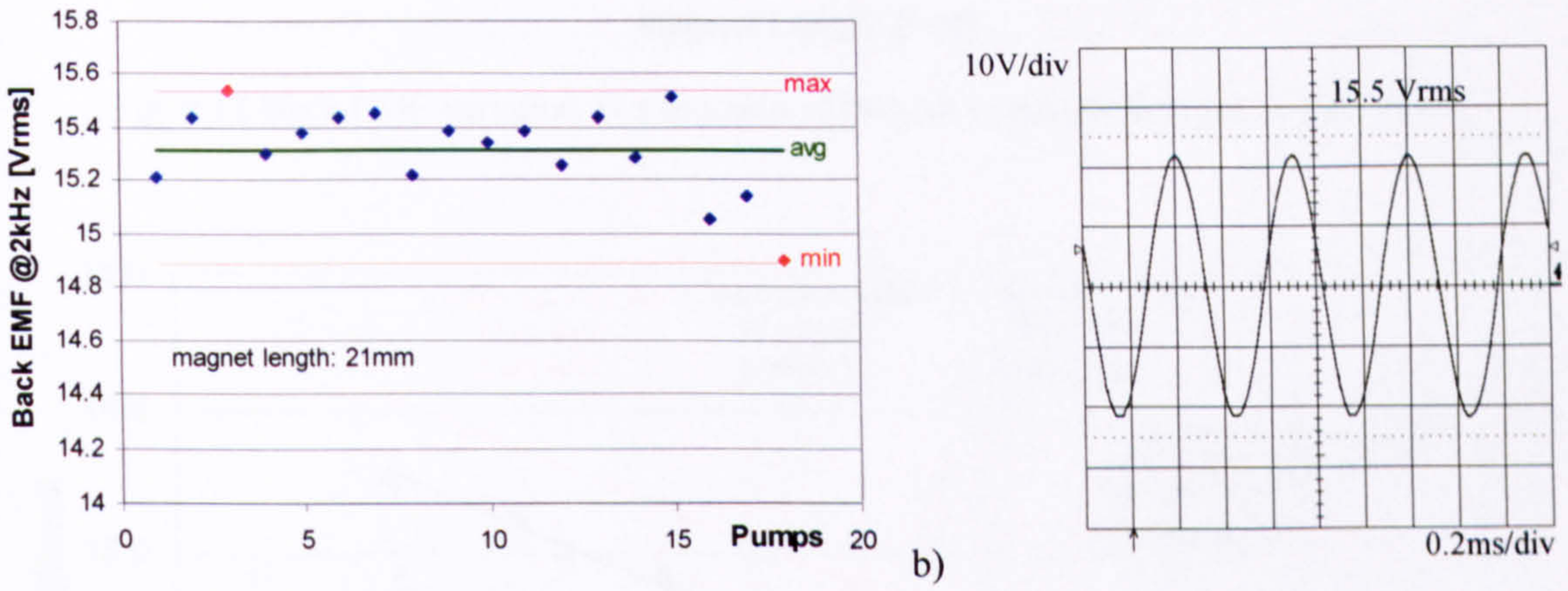

Fig. 9.11 a) Back EMF measurement of 18 pumps with 6-tooth, 4-pole motor b) typical waveform

To achieve a target back EMF of around 13.7V_{rms} (with the final sensorless drive), the back EMF as a function of magnet length was measured, using a dummy shaft between centres and an external motor to drive the shaft at low speed. Fig. 9.12 shows the back EMF results, calculated for rated speed. A magnet length of 17.5mm, with a 1.5mm overhang on the end of the shaft shoulder, and a 1mm overhang on the opposite end, has been chosen for the final design. The initial back EMF measurements of 5 pumps with 17.5mm magnets gave values between 13.4V_{rms} and 14.1V_{rms}, which is believed to represent the expected tolerance spread.

The back EMF also varies with temperature, and Fig. 9.13 shows the measured back EMF as a function of temperature. For this the shaft and magnet were heated up slowly and the back EMF measured at a few temperature points by spinning the shaft between centres. The temperature coefficient for the plastic bonded NdFeB magnets was determined as 0.09%/°C, which is close to the given data sheet value of 0.1%/°C. The variation with temperature needs to be taken into account for optimising the drive performance.

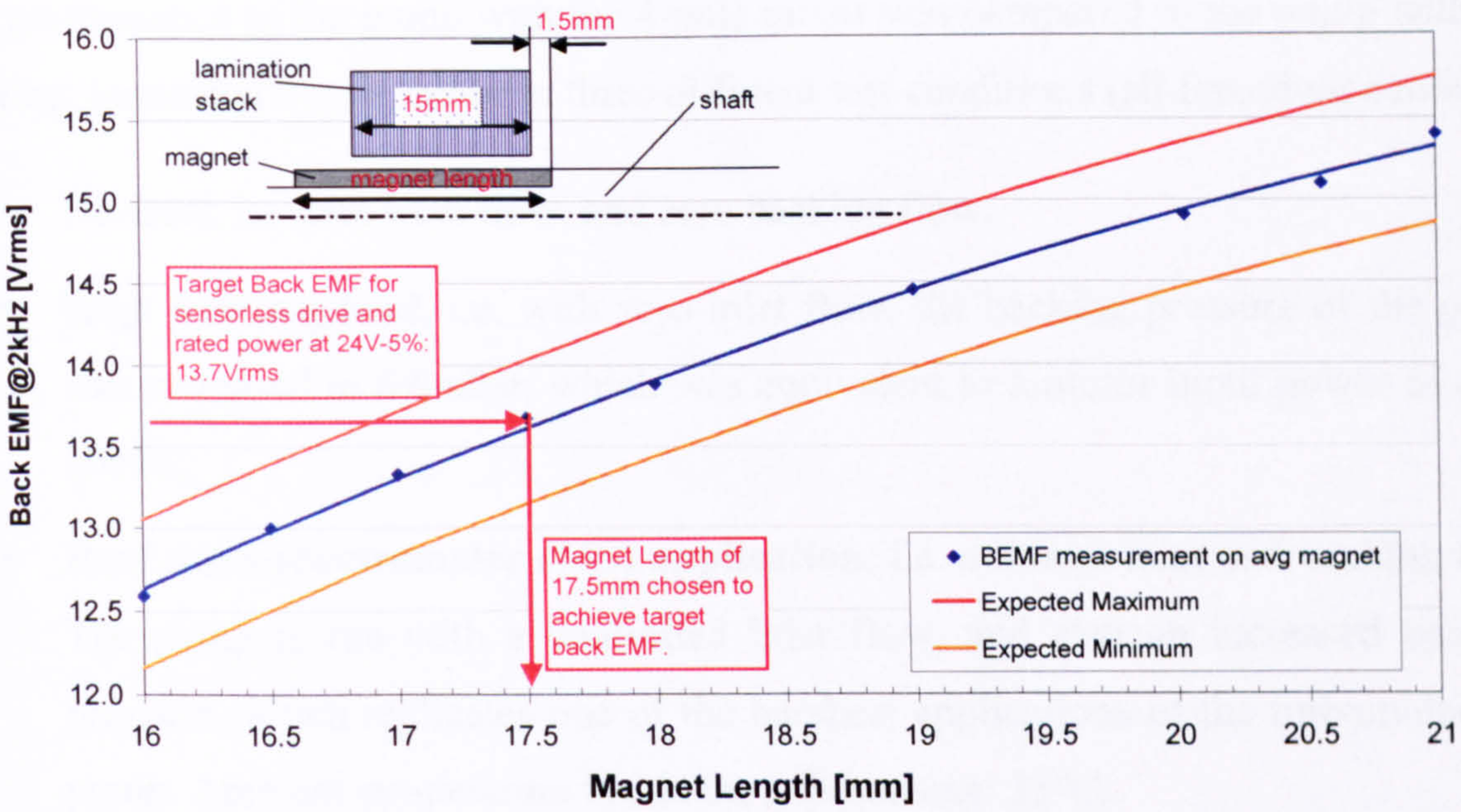

Fig. 9.12 Back EMF variation as a function of magnet length for 6-tooth, 4-pole motor

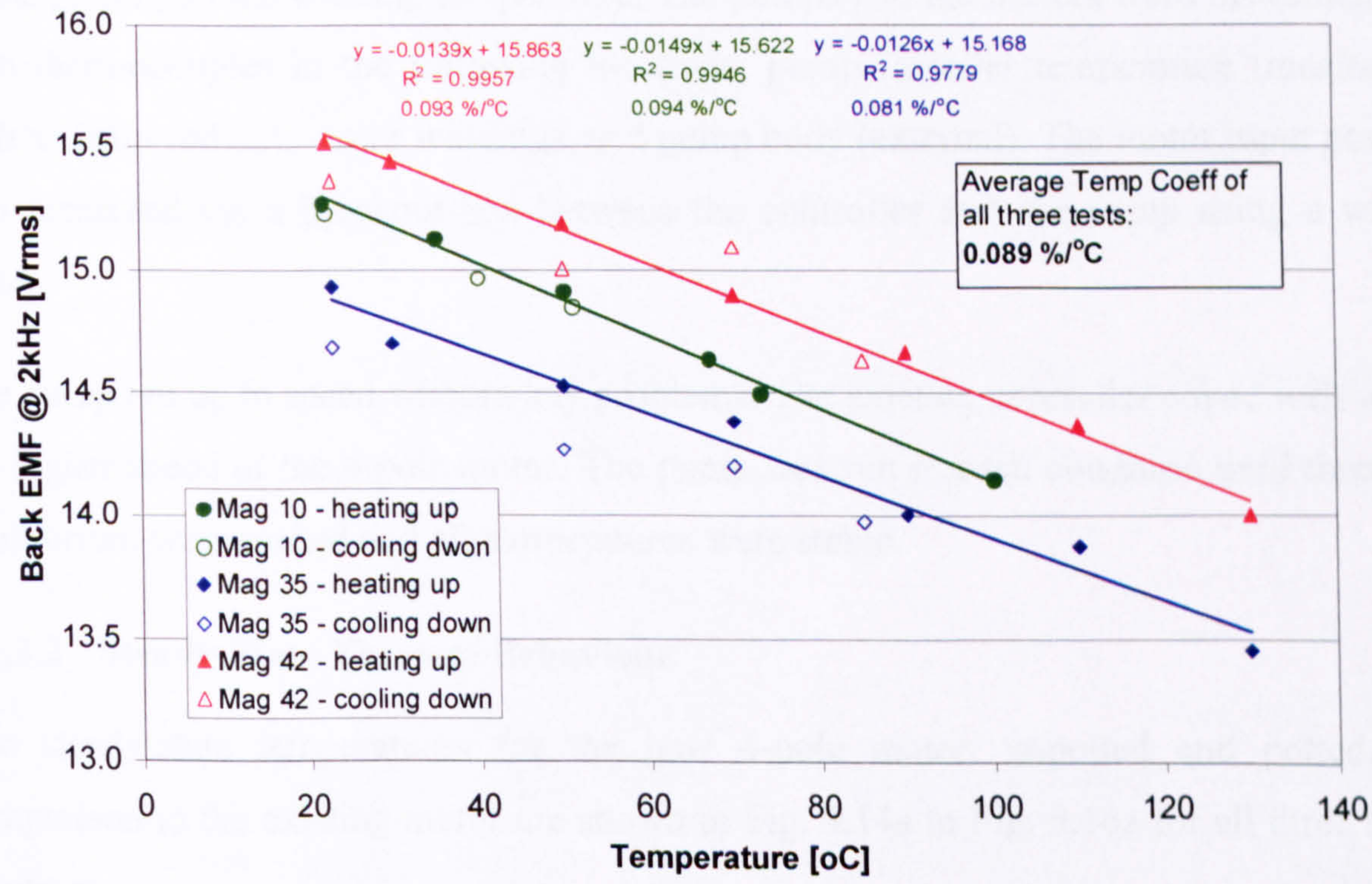

Fig. 9.13 Back EMF variation with temperature for plastic bonded NdFeB Bremag B10N-C

9.7.3 Thermal and Power Measurements

9.7.3.1 Test Conditions and Set-Up

The motor was built into an existing turbo pump, which was slightly modified to take the new smaller motor, and run with a standard controller (trapezoidal, PWM-inverter requiring Hall sensor input), adapted to reach 2kHz.

The performance of the pump with the 4-pole motor was compared to the pump with the existing, laminated 2-pole motor in three different test conditions (all forced air cooled):

- **No-load**, i.e. zero inlet flow, and zero backing flow.
- **High backing load**, i.e. with zero inlet flow, the backing pressure of the pump was increased to 6.6mbar, which was equivalent to a motor input power of circa 106W.
- **Real mass-spectrometer (MS) application**, i.e. a mixed inlet and backing load. The pump is run with a controlled inlet flow, and also an increased backing pressure, which replicates one of the harshest applications of the turbomolecular pump. Ambient temperature inside the MS housing: 35°C.

All three tests were carried out with an unpotted and potted 4-pole motor to see the effect of the potting on the winding temperature. The pumps and the motors were instrumented with thermocouples in the following locations: pump impeller temperature (measured with an infra-red t/c), motor windings, and pump body (external). The motor input power was measured via a breakout-box between the controller and the pump using a watt-meter.

The pump ran up to speed without any problems. The existing controller coped well with the higher speed of the 4-pole motor. The pump was run in each condition until thermal equilibrium was reached and all temperatures were stable.

9.7.3.2 Steady-State Thermal Behaviour

The steady-state temperatures for the new 4-pole motor, unpotted and potted, in comparison to the existing motor are shown in Fig. 9.14a to Fig. 9.16a for all three test-conditions.

Body and impeller temperature of the new motor were within 5°C of those measured with the existing motor, and therefore of no concern. The winding temperature, however, in the unpotted 4-pole motor was about 8-18°C hotter depending on load condition. It was expected that the motor would run hotter, as it had similar copper losses, but much less mass to dissipate the heat. Nevertheless, the maximum unpotted winding temperature corrected for an ambient temperature of 40°C reached only 90°C, which was well within the limit of a Class F (155°C) material rating. After potting the steady-state winding temperatures were similar to the measured winding temperatures in the existing motor.

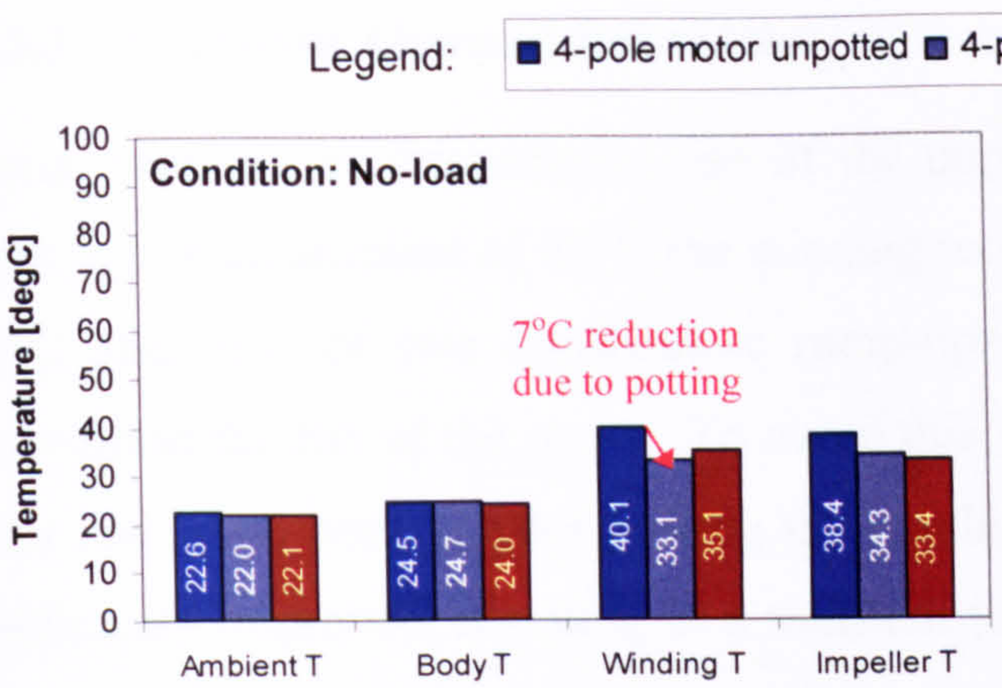

a)

	Motor Input Power [W]
4-pole motor unpotted	16.2
4-pole motor potted	16.5
Existing motor	15.5

b)

Fig. 9.14 Comparison of 4-pole motor (unpotted and potted) with the existing motor – Load Condition: No-load: a) temperatures, b) motor input power

Running Conditions: inlet pressure $p_1=1.2\cdot10^{-6}$mbar, backing pressure $p_2=1.1\cdot10^{-3}$mbar

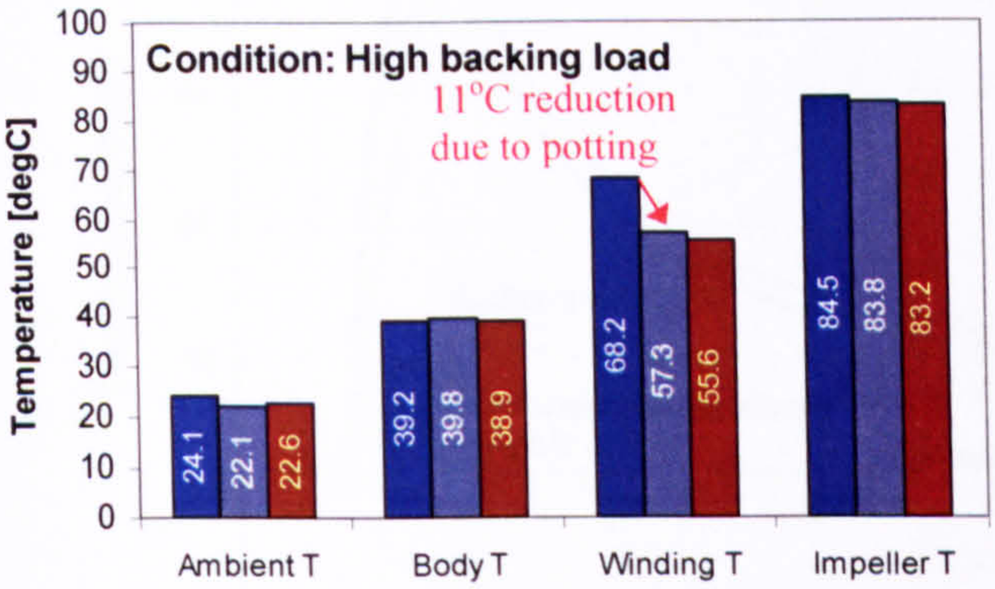

a)

	Motor Input Power [W]
4-pole motor unpotted	105.5
4-pole motor potted	107.6
Existing motor	106.6

b)

Fig. 9.15 Comparison of 4-pole motor (unpotted and potted) with the existing motor – Load Condition: High Backing Pressure: a) temperatures, b) motor input power

Running Conditions: inlet pressure $p_1=2.2\cdot10^{-6}$mbar, backing pressure $p_2=6.6$mbar

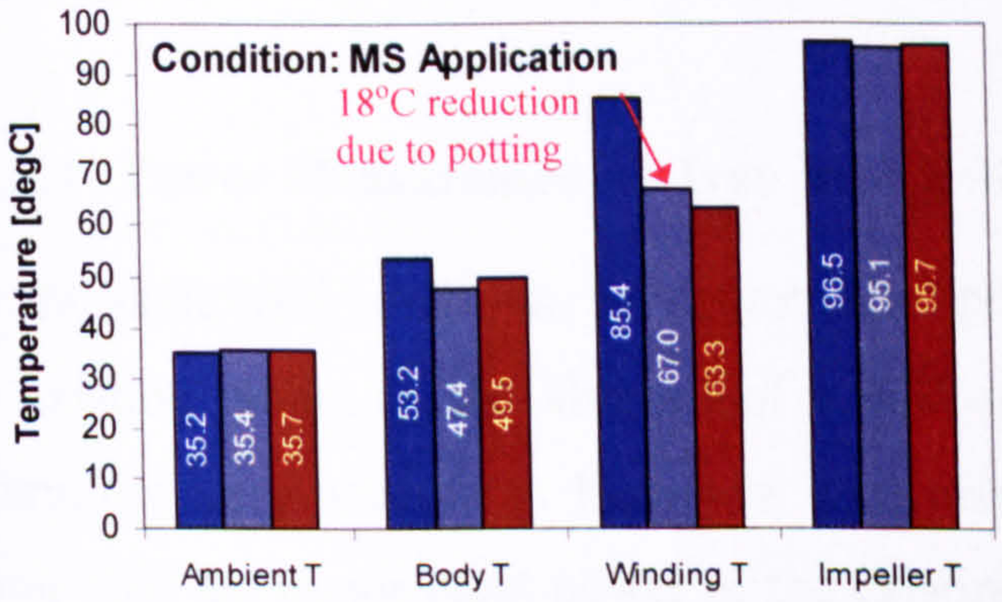

a)

	Motor Input Power [W]
4-pole motor unpotted	106.3
4-pole motor potted	105.2
Existing motor	106.9

b)

Fig. 9.16 Comparison of 4-pole motor (unpotted and potted) with the existing motor – Load Condition: Mass-Spectrometer Application: a) temperatures, b) motor input power

Running Conditions: inlet pressure $p_1=1.8\cdot10^{-3}$mbar, backing pressure $p_2=5$mbar

9.7.3.3 Transient Thermal Behaviour

During ramp-up the temperature rise of the unpotted winding was nearly 90°C, which meant that in an ambient of 40°C the winding would reach 130°C, and quickly exceeding 150°C after one or two consecutive ramp-ups. This was not acceptable and would compromise the life of the motor. To avoid this significant transient temperature rise the motor had to be potted. After potting the windings the transient thermal behaviour was significantly improved, resulting in a transient temperature rise of less than 20°C, which is identical to the existing motor (see Fig. 9.17).

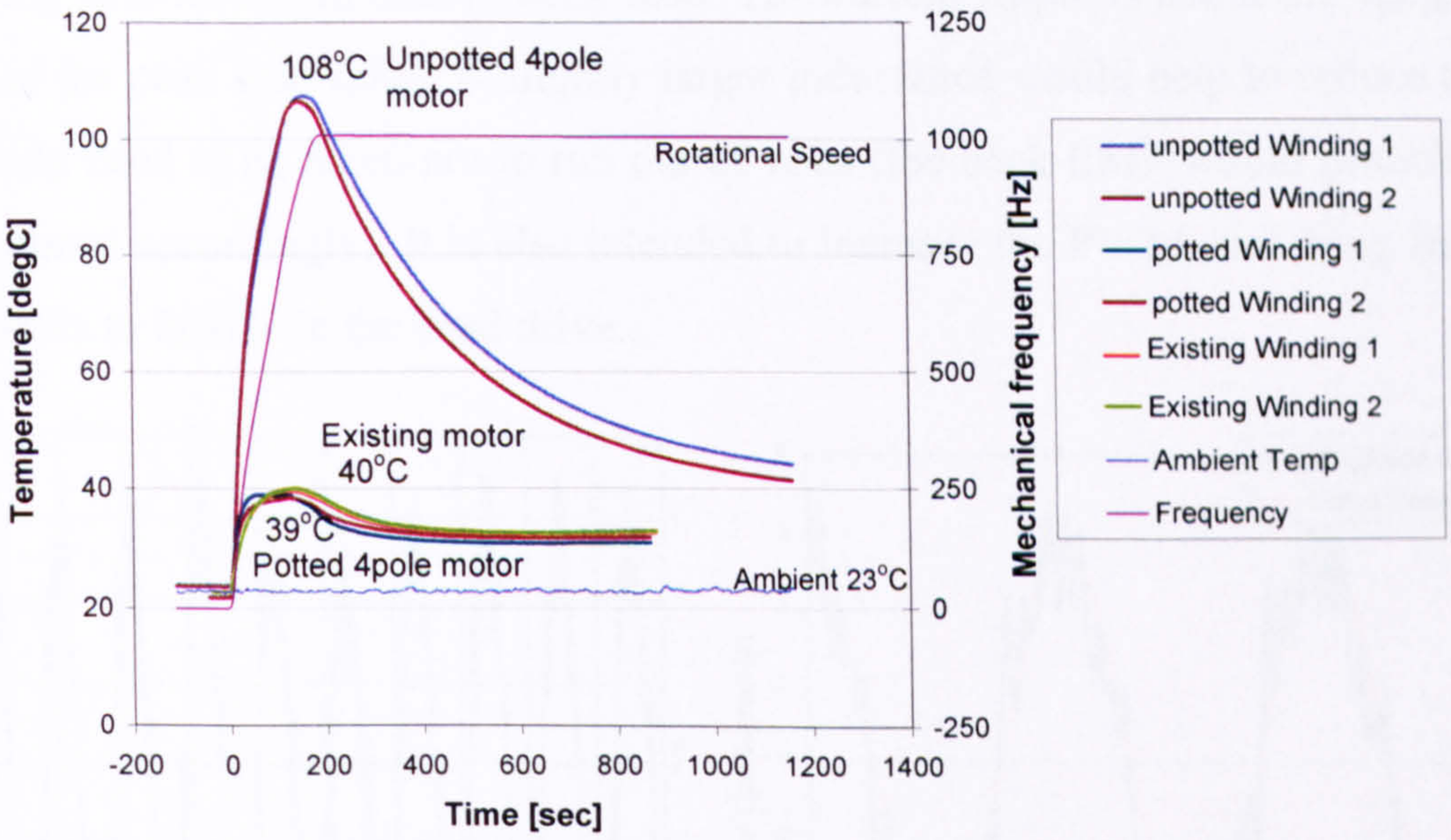

Fig. 9.17 Transient Thermal Behaviour of the 4-pole motor in comparison to the existing motor – Effect of potting the windings

9.7.3.4 Power Measurements – Iron Loss Estimation

For the same load condition, the motor input power of the 4-pole motor was similar to the existing motor. In the absence of a back-to-back rig, the motor losses cannot be determined very accurately. However, comparing the motor input power of the 4-pole motor with the motor input power of the existing motor under the same load conditions, the stator iron losses must be very similar, as there is hardly any difference in the total power measurements (within +/- 1W) (Fig. 9.14b to Fig. 9.16b). The no-load iron loss of the existing motor is about 7W. Hence, the no-load iron loss of the 4-pole motor might be about 8W (no-load input power was 1W more than the existing motor), which agrees well with the predicted iron loss of 6.2 to 8.4W.

9.7.4 Current Waveform with New Sensorless, Sinusoidal PWM-Inverter

The first prototypes of the new sensorless, sinusoidal PWM-inverter (which is a separate project carried out by a colleague at Edwards) have recently become available, and further characterisation and fine tuning of the system 'motor & drive' will need to be done in the future (which is beyond the scope and timescales of this thesis). However, to demonstrate that the 4-pole motor can be driven sensorless at 2kHz, a sample of a measured current waveform for about 100W system input power is shown in Fig. 9.18 together with a fitted sine-wave. The current waveform appears relatively spiky, but the underlying sine-wave can clearly been seen. The current ripple is about $2.5A_{pk\text{-}pk}$, which is 44% of the peak sine value. A slightly larger inductance would help to reduce this, but care would need to be taken not to run out of volts (the back EMF would probably have to be reduced accordingly). It is also intended to increase the PWM-switching frequency from 16kHz to 20kHz in the final drive.

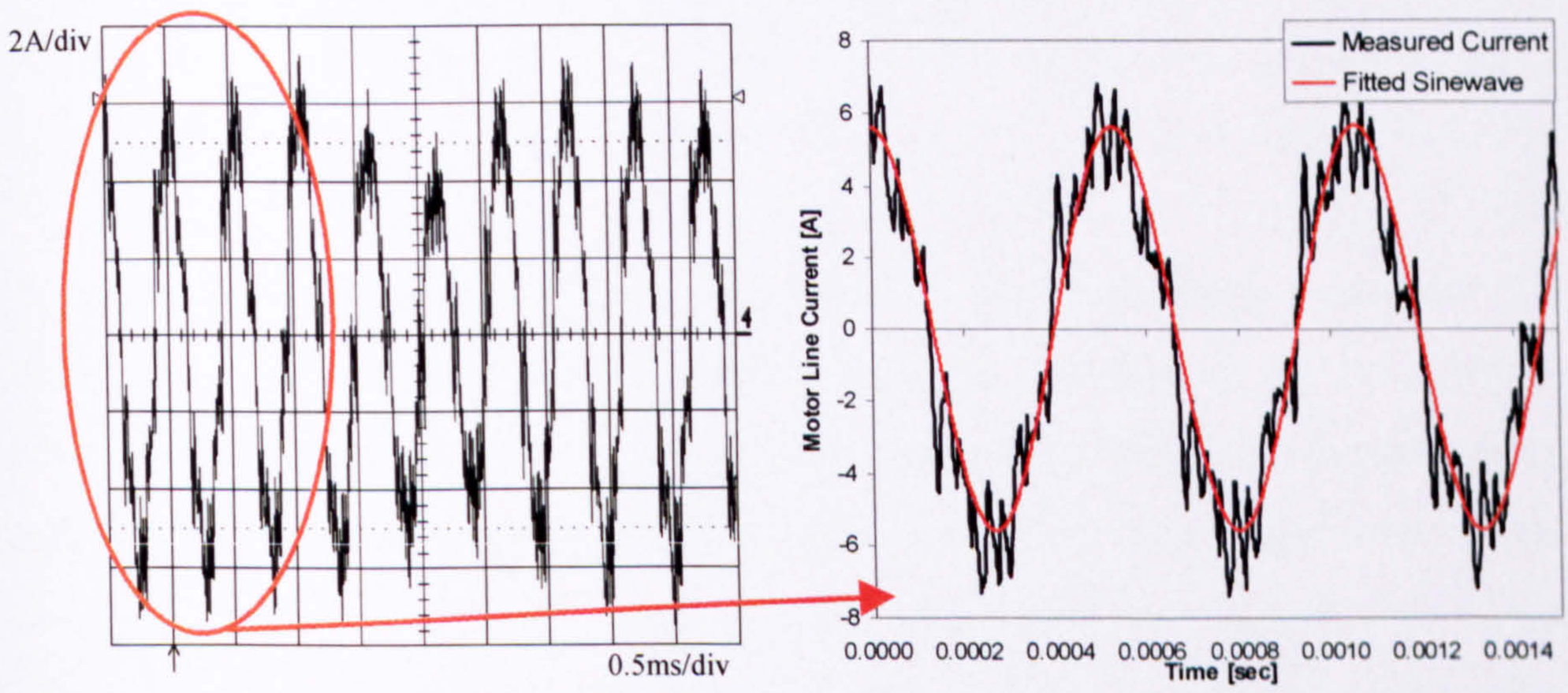

Fig. 9.18 Measured waveform of 6-tooth, 4-pole motor line current for 100W system input power, driven with the new sensorless, sinusoidal PWM-inverter: a) scope screen shot, b) zoomed in with fitted sine wave

9.8 Outlook

The 6-tooth, 4-pole motor has provided significant benefits over the previous motor designs. It has no inherent UMP and it is physically smaller than the existing motor. The lamination OD has reduced from 54mm to 50mm and the overall axial length including potted endwindings has gone down from 50mm to 29mm, which is a 42% reduction in total length. The motor losses are acceptable, only 1-2W higher, despite doubling the frequency. Thermally the motor is well within its limits under continuous operating conditions. Design calculations and predictions were very close with initial

measurements, avoiding several design iterations. Only minor adjustments had to be made to the magnet length to fine-tune the back EMF.

Due to the in-house design, it was possible to obtain quotes for the motor from several suppliers and a competitive price solution was found. As a result, this motor is a 'low-cost' motor in comparison to the existing one.

The motor has been approved to go into the next generation of turbomolecular pumps. So far around 20 motors have been built into alpha-pumps, and run successfully. It is still planned to build a purpose-built back-to-back rig, if project resources allow it. The benefit of doing this will be to characterise the motor with its final drive and to determine the motor and drive losses more accurately.

Chapter 10

Conclusions and Further Work

10.1 Evaluation of the EngD Project

10.1.1 Review of Objectives

The work presented in this thesis is the result of the Engineering Doctorate (EngD) carried out in collaboration with Edwards. The main objective of the company at the outset of this project was to develop their in-house capability of designing electrical machines in an attempt to break free from their dependency on a single supplier and the associated intellectual property issues. Design ownership and the resulting ability to source the motor from several subcontractors would allow a competitive price structure that should result in a cheaper machine. In addition the goal was to produce a simpler low-cost machine design that required no specialist skills with regards to the coil winding and insertion process, allowing freedom to choose from a greater selection of sub-contractors. This led to the initial design concept, using a segmented design with non-overlapped windings, where the stator segments were made either from laminations or Soft Magnetic Composites. The company initially choose to investigate the SMC route.

The **in-house design capability** has been developed and demonstrated with the design of the five prototypes. In particular the last motor, the 6-tooth, 4-pole motor (Mk5), was designed using analytical calculations and FE models, before being built. The measured performance agreed well with the predictions and only minor adjustments to the magnet length were required to achieve the target back EMF. The in-house design also gave the

company better control over the design, and has made answering 'what-if' scenarios much easier (like 'What happens if the axial length is reduced? ...if the diameter changes?' etc.).

However, the main advantage of owning the design was that Edwards could approach **several suppliers** for quotations to build the motor to Edward's drawings. This put Edwards in a very good position to negotiate a competitive price, which resulted in a **low-cost motor,** in comparison to the existing motor.

But low-cost in this case is a relative measure. The initial price, which was used for comparison, was very high due to being tied into one single UK supplier who could more or less charge what they wanted. The new prices varied largely, depending where the motor was being made, e.g. UK, East-Europe or China. The different labour cost rates in these countries allowed significant cost savings, despite the final motor design in itself not being as simple to make as it could have been had a segmented stack or even segmented SMC parts been used. Using a complete lamination stack, and therefore requiring in-situ hand-wound coils, is probably the only criticism of the 6-tooth motor (Mk5), as this makes the coil insertion more difficult, and requires some experience and skill in winding the motor.

Further objectives were to investigate the use of a **simple 3-tooth design in a turbomolecular pump,** the use of **Soft Magnetic Composites as a stator material** for a high-speed motor operating at 60,000rpm, and the use of **plastic bonded magnets** to reduce rotor losses. All of them were extensively investigated and a lot has been learned (see 10.2 Conclusions). Overall, the objectives set out at the beginning have been successfully achieved.

10.1.2 Review of the Industrial R&D Process

A characteristic of the EngD is that the company has a great influence in defining the direction of the research. Most industrial R&D projects are driven by a need to stay competitive in a highly cost sensitive market. Hence, they concentrate on cost reductions and continuous product development and incremental improvements to minimise risk and project timescales. The focus is on 'time to market' and not so much on academic detail.

For this project it meant that the use of SMC and the segmented design was dropped for the sake of getting a working product quicker and with less risk. Hence, going back to

laminations removed the uncertainties around the properties of the SMC. More thorough research would have probably continued with SMC, trying to understand and improve on the SMC properties in prototype parts, and testing pressed parts to demonstrate an improvement in the motor performance. This is an obvious direction for future work.

Also, in a real industrial environment it is often not possible to fully investigate the reasons why things have not worked out. There is a lot of pressure to move on quickly because of the necessity to get a product working, even if test and design methods are not fully developed. This is evident in the Chapters 2 to 4, with 'best guess', 'ad- hoc' decisions on the initial SMC prototypes, like changing from deep to thin plastic bonded magnets to rare earth magnets, or changing the length of the tooth tips. With proper design tools and the time taken, for example, the impact of the large inductance of the SMC Mk2 motor would have been known in advance. On the other hand without the building and testing of the different SMC motors none of the issues with damaged SMC properties through prototype machining, or the need to account for bulk eddy currents would have been identified, nor would the sensitivity of turbomolecular pumps to the inherent UMP force of the 3-tooth design have been found out.

What might have looked like research without a systematic or fully thought through approach, e.g. building several SMC motors without fully understanding the loss mechanisms and real material properties, is only the result of a more practical research in a real industrial environment, which is the difference of an EngD compared to a traditional PhD.

10.2 Conclusions and Recommendations

A 3-tooth SMC motor running at 60,000rpm in a vacuum pump application with passive magnetic bearings was something new that no-one had experience with. A lot has been learned through the building and testing of the SMC motors that has helped to form a better understanding of using SMC as a stator material, and of using a 3-tooth, 2-pole motor in a turbomolecular pump. The following conclusions can be made:

10.2.1 Bulk Eddy Currents – A Significant Source of Iron Losses in SMC's

Initial iron loss calculations based on the total loss per kg curves as provided in SMC material data sheets, underestimated the measured iron losses by 75% to 80%. This large

discrepancy was caused by the fact that bulk eddy currents were basically ignored or at least treated very inaccurately by using data measured on a standard ring sample and applying it without correction to any size and shape of the actual component.

An improved process for determining iron losses in SMC parts has been presented that takes account of the bulk eddy currents. It starts by separating the measured iron losses in the ring sample into the size-independent, material-specific hysteresis and in-grain eddy current losses and into the bulk eddy currents, which vary with the size and shape of the component. The material-specific, size-independent losses (hysteresis and in-grain) can then be calculated for the actual component if the peak flux densities are known. The bulk eddy current losses in the actual components are estimated using a 2D eddy-current time-harmonic FE model. The accuracy of the bulk eddy current loss calculation depends largely on the bulk conductivity of the component. To determine this accurately is in itself a challenge (see 10.2.2).

The bulk eddy current losses in the actual motor components were, at 55% to 62%, responsible for a significant portion of the total iron loss. Having considered the bulk eddy currents separately reduced the difference between predicted and measured iron loss to less than 20%. This is a significant improvement, given the uncertainty in the material data.

10.2.2 SMC Properties Adversely Affected by Prototype Machining

During the project it became evident that the SMC did not perform as expected. Several test results could not be explained unless the material properties of the SMC were different compared to the given data sheet values. Examples of this were: a) the large difference between measured and predicted iron losses, which even after taking the bulk eddy currents separately into account could only be accounted for if the bulk conductivity was much larger than anticipated, b) the fact that cutting off the long, thin tooth tips did not make much of a difference to the flux linkage, indicated that the thin SMC parts did not perform as expected, and c) the large discrepancy in back EMF prediction, which after accounting for weak magnets, pointed towards a lower permeability of the SMC.

Further investigations done by Höganäs on different wire-eroded rings showed a huge variation in conductivity values. Measurements carried out on the actual SMC back iron rings of the motors confirmed a larger bulk conductivity and reduced permeability

compared to the data sheet values. It became clear that the SMC properties were adversely affected by prototype machining using wire-erosion or mechanical cutting. Possible explanations are micro-cracks in the parts reducing the permeability and grain insulation damage increasing the bulk conductivity. At the time of this project the realisation of damaged properties was just emerging, and no-one knew or could predict the extent (see Section 10.3 Suggestions for Further Work).

It is therefore important to determine the bulk conductivity of the actual part as this influences the bulk eddy current loss significantly. However, it is difficult to measure the conductivity and permeability of the actual component unless it forms a ring. Without direct measurements of the SMC properties the only alternative is to build the machine and test it as a whole. In this way it is very difficult to isolate the SMC properties and distinguish between motor performance and material defects.

10.2.3 Inherent UMP in a 3-Tooth, 2-Pole Motor Not Neglectable in TMP's

The initial assumption, that UMP in these 3-tooth permanent magnet motors is small enough not to cause a problem due to the large air gap, has proven to be wrong. The pump was very noisy and produced high levels of transmitted vibration during run-up and the impeller assembly touched the emergency bearings each time for a couple of seconds when passing through the resonance frequency.

A practical and theoretical study followed quantifying the effects of the UMP with emphasis on this particular application, but also providing a more general understanding of UMP effects in permanent magnet machines. Finite Element Analysis using the Maxwell stress method has been used to calculate the force. The analysis has shown that only harmonics next to each other, i.e. harmonic fields whose pole pairs differ by one, contribute to a net radial force. The largest contribution came from the interaction of the fundamental field from the magnets with the second harmonic of the armature field.

A UMP force of about 4N has been calculated, which is a small force for a mechanical bearing, but for a passive magnetic bearing which has a much lower radial stiffness it turned out to be enough to take up the mechanical gap between the shaft and the bearing. The static UMP was determined experimentally for a known bearing stiffness by measuring the deflection of the impeller with a laser micrometer. The predicted and measured force / deflection agreed very well.

Without changing the bearing system no design change in the 3-tooth motor has been identified, that would reduce the inherent UMP significantly. Hence, the 3-tooth motor was abandoned for the use in turbomolecular pumps.

10.2.4 Rotor Loss Not the Main Heat Source in the Rotor of a TMP

For the life and reliability of the turbomolecular pump rotor temperature is a critical parameter, and Edwards thought that high impeller temperatures were mainly due to the motor rotor losses. Hence there was a lot of emphasis placed on minimising the motor rotor losses by design.

The work presented here has for the first time quantified the rotor losses theoretically using Finite Element Analysis. This has shown that the rotor losses are small, typically much less than 1W. The largest contribution comes from the time harmonics of the current waveform, and not from the space harmonics, even in the 3-tooth motor with its non-overlapped, short-pitched windings.

Thermal tests carried out at very low backing pressures ($1{\cdot}10^{-2}$ and $1{\cdot}10^{-4}$mbar), have shown that windage even at these low pressures cannot be neglected. The temperature rise due to the rotor loss of less than 1W accounted only for 11-15°C not enough to account on its own for the measured impeller temperatures of up to 100°C. The work on the rotor losses has helped to challenge the long standing assumptions that impeller temperature is mainly attributable to motor rotor losses and that windage, friction, and bearing drag is neglectable in a turbomolecular pump, which is clearly not the case.

10.2.5 Improve High-Speed Test Facilities to Measure Torque Directly

So far none of the pump motors have been directly tested for their torque capabilities, due to the fact that the operating speed is very high, and the torque is very small (i.e. a rated torque of 0.016Nm at 60,000rpm). Using a back-to-back rig as described in Chapter 2 was used for the first three SMC prototypes as an attempt to characterise the motor's performance and determine the losses. However, the biggest draw-back of the back-to-back rig was that the bearing and rig losses needed to be known, before the motor losses could be derived, which obviously puts great uncertainty on the loss data. A more direct measurement of the motor performance (output power) would be desirable.

10.2.6 Avoid Long, Thin Plastic Bonded Magnets

The use of plastic bonded magnets was suggested to help reduce the rotor losses because of the much lower conductivity compared with sintered rare earth magnets. However, there was some uncertainty about the performance of very thin plastic bonded magnets as used in Mk2 (l_{mag}=1.86mm, see Chapter 3). A significantly lower back EMF had been measured than predicted, even with a re-magnetised shaft.

Thin cylindrical magnets (i.e. thin wall thickness) are difficult to press and lower achievable material densities can be reasons for lower magnetic strength. In addition published magnet data is typically measured on a 5mm thick sample in the direction of magnetisation. Hence, any component with significantly less than 5mm thickness can deviate from the expected performance. It is recommended that magnets with a thickness of less than 2mm are avoided, especially when a large air gap is present, as a much lower magnetic performance is likely to be the result.

10.2.7 Efficient Development Depends on Clear Understanding of Real Motor Requirements

During the project it became clear that the motor requirements were ill defined. The main reason was that no-one really understood what was actually important for the customer, e.g. Is efficiency a real requirement or a 'nice to have'? Can some phase advance in the drive be allowed? What is the real limit of the stator winding temperature? Is the stator winding temperature limit unnecessarily low, conflicting with the requirement for a small motor? What level of UMP is tolerable?

Without clear specifications it was difficult to decide whether a design was acceptable or not. A lot of time was spent discussing whether a change in parameter or some performance trade-off was allowable. However, the work has helped to identify the weak points in the requirements and has challenged and shaped some of the company's ideas; for example, allowing some phase advance, and negotiating an increase in the maximum stator winding temperature in Mk5, or quantifying the rotor losses and removing them as the main source for impeller heating. More work needs to be done to understand the customer's requirements better and hence formulate them into a clearer motor specification.

10.3 Suggestions for Further Work

The result of this research project has been the successful design of the 6-tooth, 4-pole motor and its acceptance for the use in turbomolecular pump applications. However, the original idea of a segmented design possibly using SMC should not be forgotten as a low-cost alternative. Especially when considering the possibility that the labour-rate in these so-called low-cost countries might also increase over the next few years. In these circumstances long-term further cost reductions are only achievable by replacing the manual coil insertion with automatic processes. This leads to the following suggestions for further work:

1. **Design of a segmented, laminated stator for the 6-tooth, 4-pole motor:** The non-overlapped coils would make it easy to split the stator into six equal segments. Small modifications to the shape of the slots and teeth might be necessary to aid automatic coil winding directly onto the teeth.

2. **Re-design of the 6-tooth, 4-pole motor using the latest SMC material:** Due to the high frequency of 2kHz very thin laminations were required. With careful design and SMC material properties optimised for low conductivity it is believed that equal or better motor performance could be achieved. Using SMC and a segmented design approach would allow the coils to be either wound separately or directly onto the teeth, making the assembly simple and cost-effective.

Typically a lot of testing is required to validate the motor design. However, the back-to-back rig had its own uncertainties, as it required knowing the rig losses and assumed the two motors having the same losses. A better way to characterise the motors is required, if possible independent of the arrangement in the pump. Also better modelling tools to improve the accuracy of the inductance calculation and to represent the 3D features of the SMC component more accurately could be of benefit and help to optimise a stator design. Hence other suggestions for future work are:

3. **Design and build a high-speed (60,000rpm) dynamometer rig,** which allows torque measurement of the motor under test, either direct in-line or as reaction torque from the stator.

4. **Use 3D FE modelling** to more accurately model the 3D flux path in SMC components and the axial short circuit on the magnet-shaft shoulder. Also to improve the inductance calculation by modelling the coils and endwindings more realistically.

Other areas, which are not directly related to the motor design, but would benefit from further investigations, are:

5. **Finding better ways of prototyping SMC:** understanding better the effects and the extent to which SMC is damaged by machining or wire-erosion, and finding alternative ways of prototyping the material without having to invest in full press tooling.

6. **Increase damping and/or stiffness of magnetic bearing in TMP** so that the simple 3-tooth, 2-pole motor could be used. The inherent UMP was only noticeable during run-up, exciting a resonance. If the effect of the resonance vibration could be damped out, than the 3-tooth, 2-pole motor could still be a valid simple motor topology for TMP's.

7. **Develop thermal model of the turbopump** to understand better the real requirements with regards to maximum motor stator and motor rotor temperatures.

Appendix A

Machine Details - Overview

The following tables summarise the most important parameters of all the motors discussed in this thesis. They allow the reader to find quickly information and to easily compare the different designs. Detailed discussion of the motors is covered in the following chapters:

Existing Motor	→ Chapter 1
SMC Mk1.1	→ Chapter 2, 5, 6
SMC Mk2	→ Chapter 3, 5, 6
SMC Mk3	→ Chapter 4, 5, 6
SMC Mk4	→ Chapter 7
Mk5 – 6tooth, 4pole	→ Chapter 9

General Requirements and Characteristics								
Parameter		**Unit**	**Existing Motor**	**SMC Mk1.1**	**SMC Mk2**	**SMC Mk3**	**SMC Mk4**	**Mk5 4pole motor**
Rotational speed (mechanical)	n	rpm	60,000	60,000	60,000	60,000	60,000	60,000
	f_{mech}	Hz	1000	1000	1000	1000	1000	1000
Continuous rated power	P_{rated}	W	100	100	100	100	100	100
Continuous rated torque	T_{rated}	Nm	0.0159	0.0159	0.0159	0.0159	0.0159	0.0159
Stator outside diameter	$d_{o.s}$	mm	54	54	54	54	54	50
Maximum overall axial height incl. endwindings and Hall sensor board		mm	<40	<40	<40	<40	<40	<30
Number of phases		-	3	3	3	3	3	3
Number of poles	2p	-	2	2	2	2	2	4
Number of pole pairs	p	-	1	1	1	1	1	2
Electrical frequency	f_{elec}	Hz	1000	1000	1000	1000	1000	2000
DC supply voltage	V_{dc}	V	24	24	24	24	24	24
Drive topology	-	-	PWM trapezoidal current	PWM trapezoidal current	PWM trapezoidal current	PWM trapezoidal current	PWM trapezoidal current	PWM Sinusoidal current

Table A.1 General Requirements and Motor Characteristics

Stator Material								
Parameter		**Unit**	**Existing Motor**	**SMC Mk1.1**	**SMC Mk2**	**SMC Mk3**	**SMC Mk4**	**Mk5 4pole motor**
Type		-	Laminations	SMC	SMC	SMC	SMC	Laminations
Material		-	Electrical Steel M330-35-A5	Somaloy 500 + 0.5% Kenolube, 600MPa	Somaloy 500 +0.5% Kenolube, 600MPa	Somaloy 500 + 0.5% Kenolube, 600MPa	Somaloy 700 + 0.5% Kenolube, 800MPa	Electrical Steel NO20, 3% Si
Lamination thickness		mm	0.35	-	-	-	-	0.2
Grain diameter		mm	-	0.1	0.1	0.1	0.2	-
Grain radius	a	mm	-	0.05	0.05	0.05	0.1	-
Permeability	μ_r	-	2000	445	445	445 (455)	575 (350)	2000
Density	ρ	g/cm^3	7.65	7.18	7.18	7.18	7.4	7.65
Bulk Conductivity (data sheet)	σ	S/m	2.27E+6	20000	20000	20000	2500	1.923E+6
(measured)			-	22115	22115	22115	13550	-
Grain (Iron) Conductivity	σ_g	S.m	-	1.04E+7	1.04E+7	1.04E+7	1.04E+7	-
Specific Core Loss		W/kg	Table A.4	Table A.3	Table A.3	Table A.3	Table A.3	Table A.4

Table A.2 Stator Material

Specific Core Loss SMC (W/kg)												
Somaloy500+0.5%Kenolube, 600MPa, 30min at 500°C [23]												
		Frequency [Hz]										
Induction [T]		50	60	100	200	300	400	500	600	700	800	900	1000
	0.5	2.0	2.3	4.0	8.2	12.7	17.4	22.4	27.6	33.1	38.9	44.9	51.2
	1	6.6	8.0	13.5	28.1	43.7	60.3	78.0	96.7	116.5	137.3	159.2	182.1
	1.5	12.9	15.6	26.7	56.8	90.2	127.1	167.2	210.8	257.7	307.9	361.5	418.5
Somaloy700+0.5%Kenolube, 800MPa, 30min at 500°C [23]												
		Frequency [Hz]										
Induction [T]		50	60	100	200	300	400	500	600	700	800	900	1000
	0.5	1.6	1.9	3.2	6.6	10	14	18	23	27	32	36	41
	1	4.9	5.9	10	21	33	46	60	75	91	105	122	142
	1.5	9.6	12	20	44	71	101	130	164	200	238	278	312

Table A.3 SMC Specific Core Loss Data

Specific Core Loss Laminations (W/kg)												
M330-35-A5 – Electrical Steel, Non-Oriented, Fully Processed [26]												
		Frequency [Hz]										
Induction [T]		50		100	200		400					1000	2500
	0.5	0.39	-	0.92	2.30	-	6.16	-	-	-	-	24.9	107
	1	1.19	-	2.96	7.83	-	22.3	-	-	-	-	98.4	476
	1.5	2.93	-	7.13	18.6	-	54.7	-	-	-	-	-	-
NO20 – Electrical Steel, Thin Non-Oriented Grade, Si 3%, Al 0.4% [112]												
		Frequency [Hz]										
Induction [T]		50					400						2500
	0.3	0.14	-	-	-	-	1.49	-	-	-	-	-	24.4
	0.5	0.32	-	-	-	-	3.8	-	-	-	-	-	58.4
	1.0	0.95	-	-	-	-	12.2	-	-	-	-	-	205

Table A.4 Lamination Specific Core Loss Data

Rotor Material									
Parameter		**Unit**	**Standard Rotor**	**Splitflow Rotor**	**SMC Mk1.1**	**SMC Mk2**	**SMC Mk3**	**SMC Mk4**	**Mk5 4pole motor**
Shaft			Stainless Steel 303S31	Carbon Steel 817-M40T	Carbon Steel 817-M40T	Carbon Steel 817-M40T	Carbon Steel 817-M40T	Stainless Steel 303S31	Carbon Steel 817-M40T
Conductivity	σ	S/m	1.4E+6	5E+6	5E+6	5E+6	5E+6	1.4E+6	5E+6
Permeability	μ_r	-	1	100	100	100	100	1	100
Carrier			Mild Steel EN2A	N/A	N/A	N/A	N/A	N/A	N/A
Conductivity	σ	S/m	5E+6	-	-	-	-	-	-
Permeability	μ_r	-	100	-	-	-	-	-	-
Magnet			Sintered $SmCo_5$ VACOMAX 200	Sintered $SmCo_5$ VACOMAX 200	Plastic bonded NdFeB VACOBOND NC 76/64	Plastic bonded NdFeB VACOBOND NC 76/64	Sintered NdFeB VACODYM 677HR	Plastic bonded NdFeB EPN71/63	Plastic bonded NdFeB Bremag B10C
Conductivity	σ	S/m	1.8E+6	1.8E+6	5E+3	5E+3	7E+5	5E+3	5E+3
Remanence	Br	T	1.01	1.01	0.66	0.66	1.18	0.7	0.6
Coercivity	H_{cB}	kA/m	755	755	382	382	915	430	400
Intrinsic Coercivity	H_{cJ}	kA/m	1500	1500	660	660	2400	740	1100
Permeability	μ_r	-	1.0645	1.0645	1.375	1.375	1.026	1.295	1.194
Temp. Coefficient B_r		%/°C	-0.04	-0.040	-0.090	-0.090	-0.085	-0.070	-0.100
Sleeve			Stainless Steel 303S42	CFRE	CFRE	CFRE	CFRE	CFRE	CFRE
Conductivity	σ	S/m	1.4E+6	0	0	0	0	0	0
Permeability	μ_r	-	1	1	1	1	1	1	1

Table A.5 Rotor Materials

Stator Dimensions								
Parameter		**Unit**	**Existing Motor**	**SMC Mk1.1**	**SMC Mk2**	**SMC Mk3**	**SMC Mk4**	**Mk5 4pole motor**
Stator outside diameter	$d_{o,s}$	mm	54	54	54	54	54	50
Stator inside diameter	$d_{i,s}$	mm	22.43	22	22	22	22	27.5
Stator slot ground diameter		mm	42	42	44	44	45	41
Stator axial length (or tooth tip length)	l_a	mm	27.1	31	31	14	19	15
Number of slots / teeth		-	6	3	3	3	3	6
Slot area	A_{slot}	mm^2	101.5	155.6	186.4	186.4	252.5	68 0
Tooth depth (in radial direction)		mm	7	7	8	8	7.5	5.5
Tooth width		mm	4	14	14	14	8	6
Tooth axial length	l_{tooth}	mm	27.1	20	20	14	16	15
Tooth cross section area		mm^2	108.40	237.94	237.94	174.97	114.27	90.00
Tooth spacing factor	sf_{tooth}	-	1	0.548	0.548	0.893	0.752	1
Back iron thickness		mm	6	6	5	5	4.5	4.5
Back iron axial length	l_{back}	mm	27.1	36	36	36	38	15
Back iron cross section area		mm^2	162.6	216	180	180	171	67.6
Back iron spacing factor	sf_{back}	-	1	1.161	1.161	2.571	2.000	1
Reactance slot opening	w_{slot}	mm	2	2	2	2	4.6	2
Stator lamination weight	m_{iron}	g	252	307	280	246	238	108

Table A.6 Stator Dimensions

Rotor Dimensions									
			Standard Rotor	Splitflow Rotor	SMC Mk1.1	SMC Mk2	SMC Mk3	SMC Mk4	Mk5 4pole motor
Number of poles		-	2	2	2	2	2	2	4
Pole arc		deg_{mech} deg_{elec}	127 127	127 127	180 180	180 180	180 180	180 180	90 180
Construction		-	10 rectangular slabs (5 per pole)	10 rectangular slab (5 per pole)	cylindrical magnet	cylindrical magnet	cylindrical magnet	cylindrical magnet	cylindrical magnet
Magnetisation direction		-	radial	radial	diametrical	diametrical	diametrical	diametrical	diametrical
Magnet OD		mm	-	-	16.32	16.32	16.32	16.32	21.5
Magnet ID		mm	-	-	10.1	12.6	12.6	10.5	15.5
Magnet thickness		mm	1.35	1.35	3.11	1.86	1.86	2.91	3
Magnet width		mm	3	3	-	-	-	-	-
Magnet axial length		mm	32.5	32.5	35 (2x17.5)	35 (2x17.5)	19	23	17.5
Shaft diameter		mm	10	13.665	10.0	12.5	12.5	10.4	15.5
Carrier OD		mm	13.665	-	-	-	-	-	-
Carrier thickness		mm	1.8325	-	-	-	-	-	-
Sleeve OD		mm	20	18.95	18.95	18.95	18.95	18.95	24.5
Sleeve thickness		mm	1.84	1.315	1.315	1.315	1.315	1.315	1.5
Mechanical air gap		mm	1.215	1.74	1.525	1.525	1.525	1.525	1.5
Effective air gap (mech. air gap + sleeve thickness		mm	1.215	3.055	2.84	2.84	2.84	2.84	3

Table A.7 Rotor Dimensions

Winding Details								
Parameter		Unit	Existing Motor	SMC Mk1.1	SMC Mk2	SMC Mk3	SMC Mk4	Mk5 4pole motor
Winding configuration		-	star	delta	delta	delta	delta	star
Number of phases		-	3	3	3	3	3	3
Coil arrangement		-	fully pitched	short pitched	short pitched	short pitched	short pitched	short pitched
Coil pitch angle	β	deg_{mech} deg_{elec}	180 180	120 120	120 120	120 120	120 120	60 120
Winding factor	k_p	-	1	0.866	0.866	0.866	0.866	0.866
Number of coils per phase		-	2	1	1	1	1	2
Number of turns per coils		-	7	27	49	34	50	10
Number of turns per phase	N_{ph}	-	14	27	49	34	50	20
Number of strands in parallel	a	-	9	4	4	5	3	9
Number of effective slots per phase (to calculate fill factor)		-	1	0.5	0.5	0.5	0.5	1
Copper skin depth at f_{elec} (σ_{cu}=5.6E+7 S/m)	δ	mm	2.13	2.13	2.13	2.13	2.13	1.50
Copper wire diameter	d_{wire}	mm	0.5	0.5	0.5	0.5	0.5	0.355
Wire area (1 strand)	A_w	mm^2	0.196	0.196	0.196	0.196	0.196	0.099
Copper cross section per turn (parallel strands together)	$A_{cu,turn}$	mm^2	1.767	0.785	0.785	0.982	0.589	0.891
Copper cross section per phase	A_{cu}	mm^2	24.74	21.21	38.48	33.38	29.45	17.82
Slot fill factor	k_{fill}	%	24.4	27.3	41.3	35.8	23.3	26.2
Avg. length of one turn	l_{turn}	mm	193	70.1	78.0	76.4	72.5	68.8
Copper volume	V_{cu}	cm^3	14.32	4.46	9.00	7.65	6.41	3.68
Copper mass (ρ=8.96g/cm^3)	m_{cu}	g	128.3	40.0	80.7	68.6	57.4	33.0
Rated Current ($P_{rated}/E_{LL,rms}/\sqrt{3}$)	$I_{rated,LL}$	A_{rms}	4.08	4.00	4.11	3.88	3.88	4.21
Rated Phase Current	$I_{rated,ph}$	A_{rms}	4.08	2.31	2.37	2.24	2.24	4.21
Current Density	J	A_{rms}/mm^2	2.31	2.94	3.02	2.28	3.80	4.73

Table A.8 Winding Details

Peak Flux Densities under Open-Circuit (Magnet Only)								
Parameter		**Unit**	**Existing Motor**	**SMC Mk1.1**	**SMC Mk2**	**SMC Mk3**	**SMC Mk4**	**Mk5 4pole motor**
Peak flux density in air gap	B_{gap}	T	0.23	0.27	0.16	0.42	0.24	0.26
Peak flux density in back iron		T	0.45	0.44	0.22	0.28	0.21	0.38
Peak flux density in tooth body		T	0.58	0.61	0.33	0.57	0.62	0.51
Peak flux density in tooth tip		T	0.38	0.50	0.26	0.66	0.40	0.49

Table A.9 Peak Flux Densities under Open-Circuit (Magnet Only)

Motor Parameters								
Parameter		**Unit**	**Existing Motor**	**SMC Mk1.1**	**SMC Mk2**	**SMC Mk3**	**SMC Mk4**	**Mk5 4pole motor**
Measured Line-Line Resistance at 20-25°C (phase lead resistance taken into account and subtracted)	$R_{LL,20}$	mΩ	54.5	33.5	63.0	40.0	76.0	52.5
Line-Line Resistance at 60°C	$R_{LL,60}$	mΩ	63.0	38.7	72.8	46.2	87.9	60.7
Measured Line-Line Inductance	L_{LL}	μH	109	130	379	127	252	61
Measured Line-Line Back EMF at rated speed	$E_{LL,rms}$	V_{rms}	14.14	14.42	(12.58) demag 14.03	14.89	14.90	13.70
Rated Current $P_{rated}/E_{LL\ rms}/\sqrt{3}$	$I_{rated,LL}$	A_{rms}	4.08	4.00	4.11	3.88	3.88	4.21
Copper Loss $1.5\ R_{LL,60}\ I_{rated,LL}^2$	P_{cu}	W	1.57	0.93	1.84	1.04	1.98	1.61
Total Stator Iron Loss (No Load) (predicted)	P_{stator}	W	7.0	26.4	7.1	11.8	5.4	6.3
Total Rotor Loss (predicted)	P_{rotor}	W	0.82 / 0.73 (Stand./Splitf).	0.51	1.58	1.11	0.52	0.19

Table A.10 Motor Parameters: Resistance, Inductance, Back EMF and Losses

Appendix B

Conductivity and Permeability of the Actual SMC Back Iron Rings

B.1 Background

During the testing of the SMC motors it became clear that the material properties of the SMC components were not as quoted in the data sheets. Further investigation revealed that prototyping SMC by wire erosion or mechanical machining affected the properties in a negative manner, leading to a higher conductivity and reduced permeability.

The conductivity has a direct influence on the bulk eddy current losses as discussed in Chapter 5 and hence it is important to know the true properties of the actual components to predict the iron loss more accurately.

This section describes the methods used and presents the actual conductivity and permeability data obtained for Somaloy500 and Somaloy700 prototype parts. The measured conductivity values have subsequently been used to calculate the bulk eddy current losses (Chapter 5 and Chapter 7).

B.2 Test Specimens

The tests have been carried out on one SMC Mk3 back iron ring made out of Somaloy500, and two SMC Mk4 back iron rings made out of Somaloy700. Table B.1 lists the material specifications and average dimensions. The back iron rings do not form a ring of constant cross sectional area due to the cut out for the teeth. This has been taken into account in form of an equivalent height for the ring based on the same volume (Fig. B.1).

Ring Sample Material	Height [mm]	OD [mm]	ID [mm]	Thick ness [mm]	Mean Circum-ference *l* [mm]	Equivalent Height [mm]	Cross Section Area *A* [mm^2]	Weight [g]	Density [g/cm^3]
Somaloy500 + 0.5% Kenolube, compacted at 600MPa, heat treated at 500°C for 30min in air	18.00	54.00	44.00	5.00	49.00	16.5	82.5	88.72	7.19
Somaloy700 + 0.5% Kenolube, compacted at 800MPa, heat treated at 500°C for 30min in air	19.00	54.02	45.04	4.49	49.53	17.4	78.13	91.81	7.36

Table B.1 Geometric data of back iron ring samples

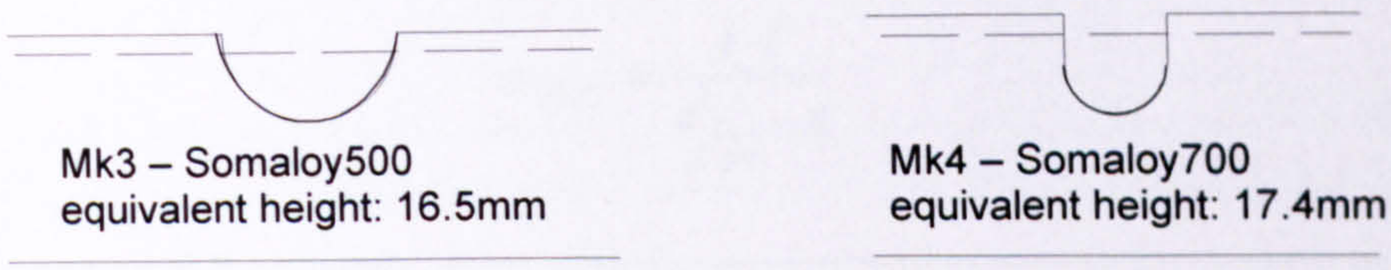

Fig. B.1 Shape of tooth cut-outs in back iron ring samples and equivalent height

B.3 Conductivity Measurements

B.3.1 Test Method

For the conductivity measurement the SMC ring forms the secondary winding of a transformer (Fig. B.2).

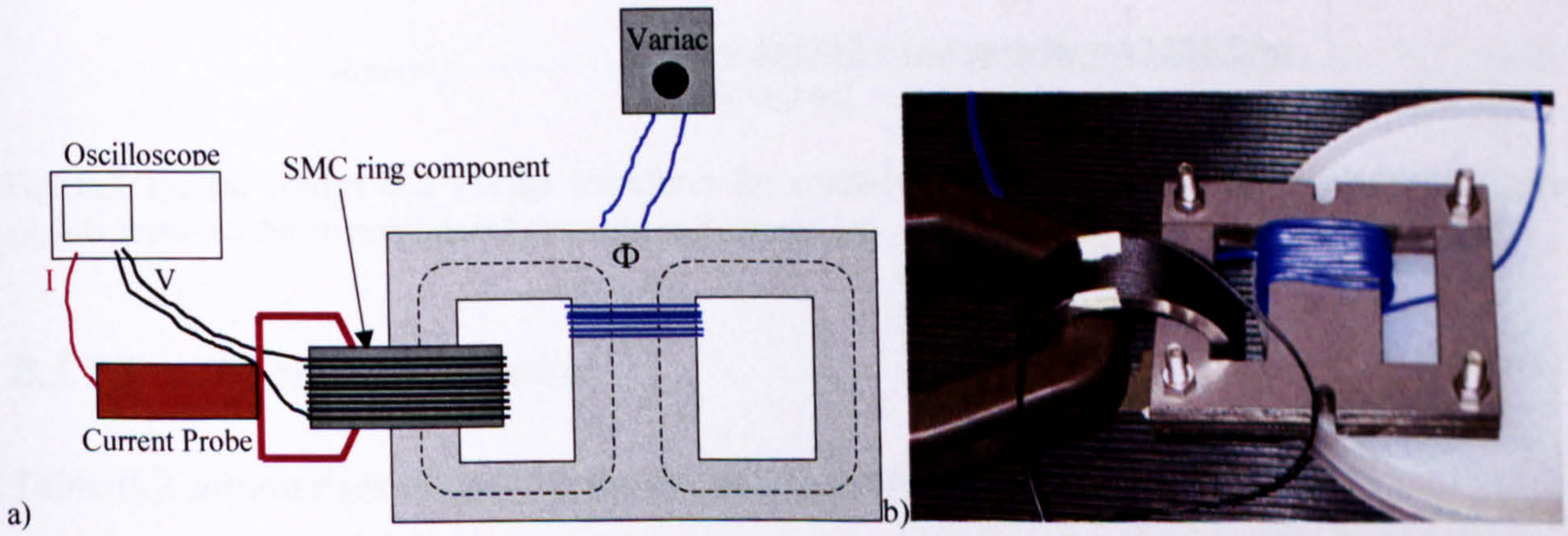

Fig. B.2 Schematic test set-up for conductivity measurement and photo of test arrangement

The changing flux from the primary side induces a voltage e in the ring, which causes a current i to flow in the ring.

$$e = -\frac{d\Phi}{dt} \tag{B1}$$

$$i = \frac{e}{R_{SMC}} \tag{B2}$$

R_{SMC} is the resistance of the SMC ring, defined as

$$R_{smc} = \frac{l}{\sigma_{SMC} \cdot A} = \frac{e}{i} \tag{B3}$$

where l is the mean circumference of the ring sample, and A is the cross section area of the ring. The current can be measured with a clamp-on current probe and the voltage e' can be picked up with turns wound around the outside of the ring (e' is the voltage measured across N turns; N=15 for Mk3 Somaloy500 back iron ring, and N=16 for Mk4 Somaloy700 back iron). Fig. B.3 shows an example of a current and voltage waveform. The conductivity can then be calculated using rms-values for current and voltage:

$$\sigma_{SMC} = \frac{i \cdot l}{e'/N \cdot A} \tag{B4}$$

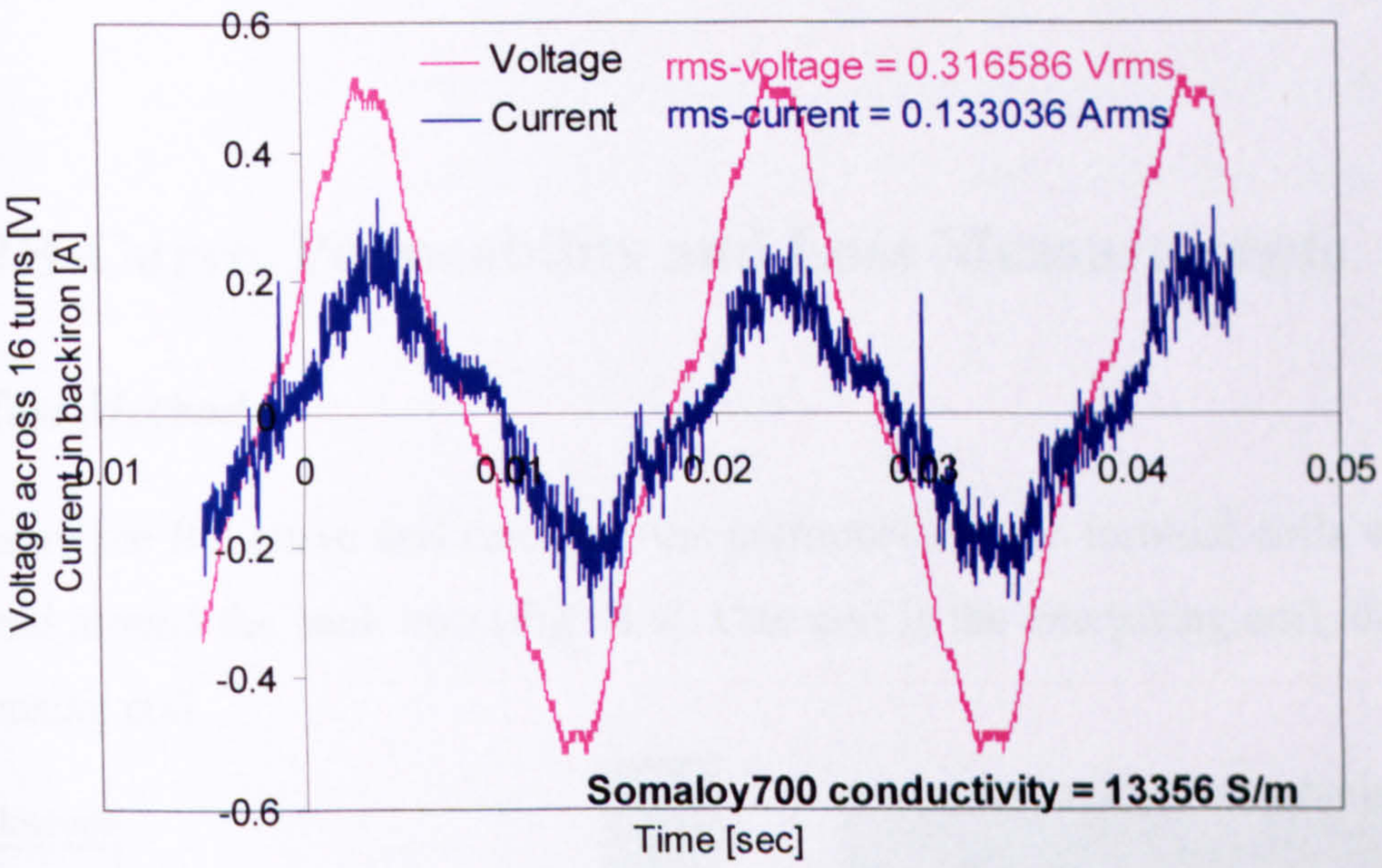

Fig. B.3 Typical current and voltage waveform for conductivity measurement (ideally sinusoidal, here slightly distorted due to non-linear behaviour and saturation)

B.3.2 Results and Conclusions

Table B.2 summarises the results for the conductivity measurements.

- Somaloy700 has a lower conductivity, i.e. higher resistivity, than Somaloy500 by a factor of about 2, which will help to reduce the eddy current losses.
- There is a large variation between the conductivity of the two Somaloy700 rings, with an average between the two rings of 11581 S/m and a spread of +/- 15.5% about this average. According to Höganäs, Somaloy700 is more difficult to prototype and suffers to a greater extent during prototype machining than Somaloy500, resulting in a larger spread and a relative larger increase in conductivity compared to its data sheet values (Somaloy700: 2500 S/m, Somaloy500: 20,000 S/m).

Ring sample	Current i [A_{rms}]	Voltage e' [V_{rms}]	Conductivity σ [S/m]
Somaloy500	0.212	0.277	21477
Ring 1	0.327	0.413	22146
	0.463	0.577	22429
	0.565	0.705	22408
			Average: 22115 S/m
Somaloy700	0.133	0.317	13356
Ring 1	0.188	0.447	13397
			Average: 13376 S/m
Somaloy700	0.129	0.421	9747
Ring 2	0.176	0.580	9626
	0.222	0.718	9840
	0.261	0.834	9930
			Average: 9786 S/m
			Average of both rings: 11581 S/m

Table B.2 Conductivity results for Somaloy500 (Mk3) and Somaloy700 (Mk4)

B.4 BH-Curve, Permeability and Loss Measurements

B.4.1 Test Method

To measure the BH curve and calculate the permeability two toroidal coils with N turns are wound around the back iron (Fig. B.4). One coil is the energising coil, the other coil is the sensing coil.

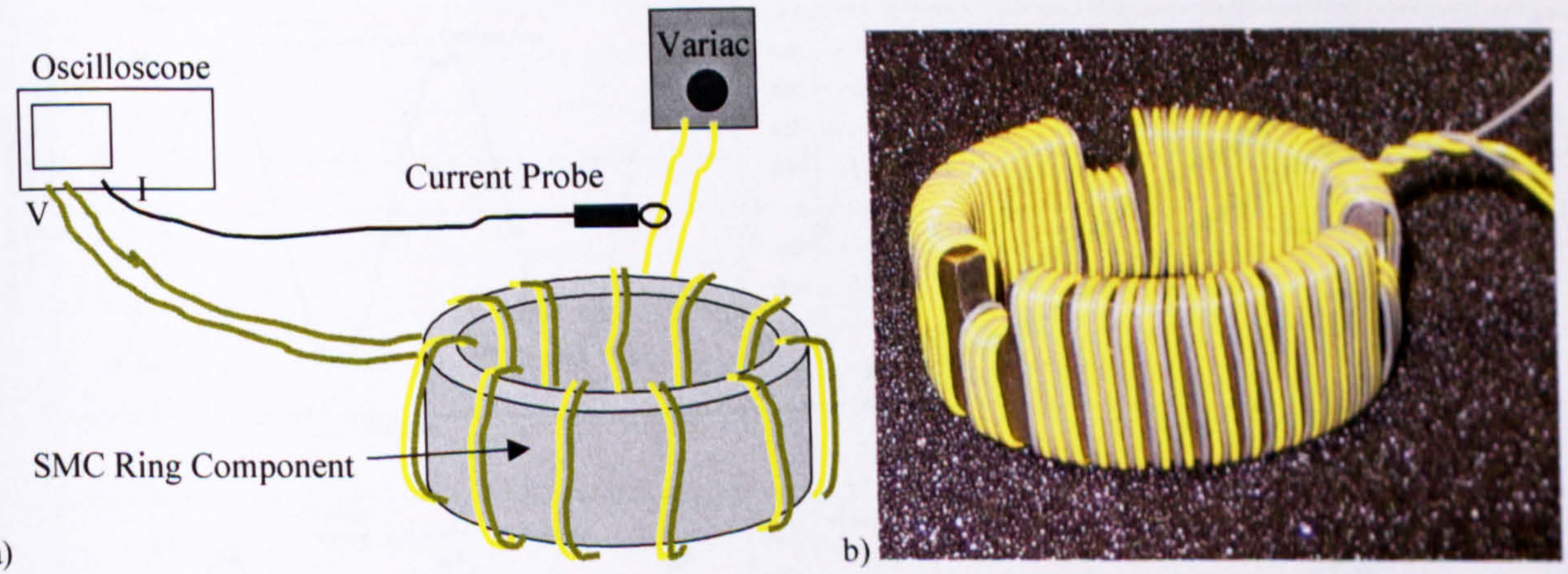

Fig. B.4 Schematic test set-up for permeability measurement and photo of test piece

Turns around back iron: Somaloy®700, ring 1 N=66 for both energising and sensing coil,
Somaloy®700, ring 2 N=64 " " " " " " ,
Somaloy®500, ring 1 N=62 " " " " " "

The energising coil is setting up a magneto-motive force (MMF) in the SMC ring, which is proportional to the current applied. This current can be measured with a current probe, and the H-field can be calculated as follows:

$$MMF = \oint H \bullet dl = N \cdot I \qquad \rightarrow \qquad H(t) = \frac{N \cdot I(t)}{l} \tag{B5}$$

where l is the mean circumference of the SMC ring. This MMF drives a flux around the ring, which links the turns of the sensing coil. This changing flux linkage creates a voltage, which can be measured with the sensing coil.

$$e = -\frac{d\Psi}{dt} = -\frac{N \cdot d\Phi}{dt} \tag{B6}$$

The flux is obtained by integrating the voltage waveform, and the flux density can be calculated by taking the cross section area A of the back iron into account.

$$\Phi(t) = \frac{-\int e \cdot dt}{N}; \qquad and \qquad B(t) = \frac{\Phi(t)}{A} \tag{B7), (B8}$$

Hysteresis loops are obtained by plotting B(t) as a function of H(t). The enclosed area of the hysteresis loops is a measure of the iron losses. The 'tip' of the BH loops defines the BH curve. Permeability values are calculated from these maximum B and H values.

$$\mu_r = \frac{B}{\mu_0 \cdot H} \tag{B9}$$

Typical current and voltage waveforms with corresponding BH-loops are shown in Fig. B.5.

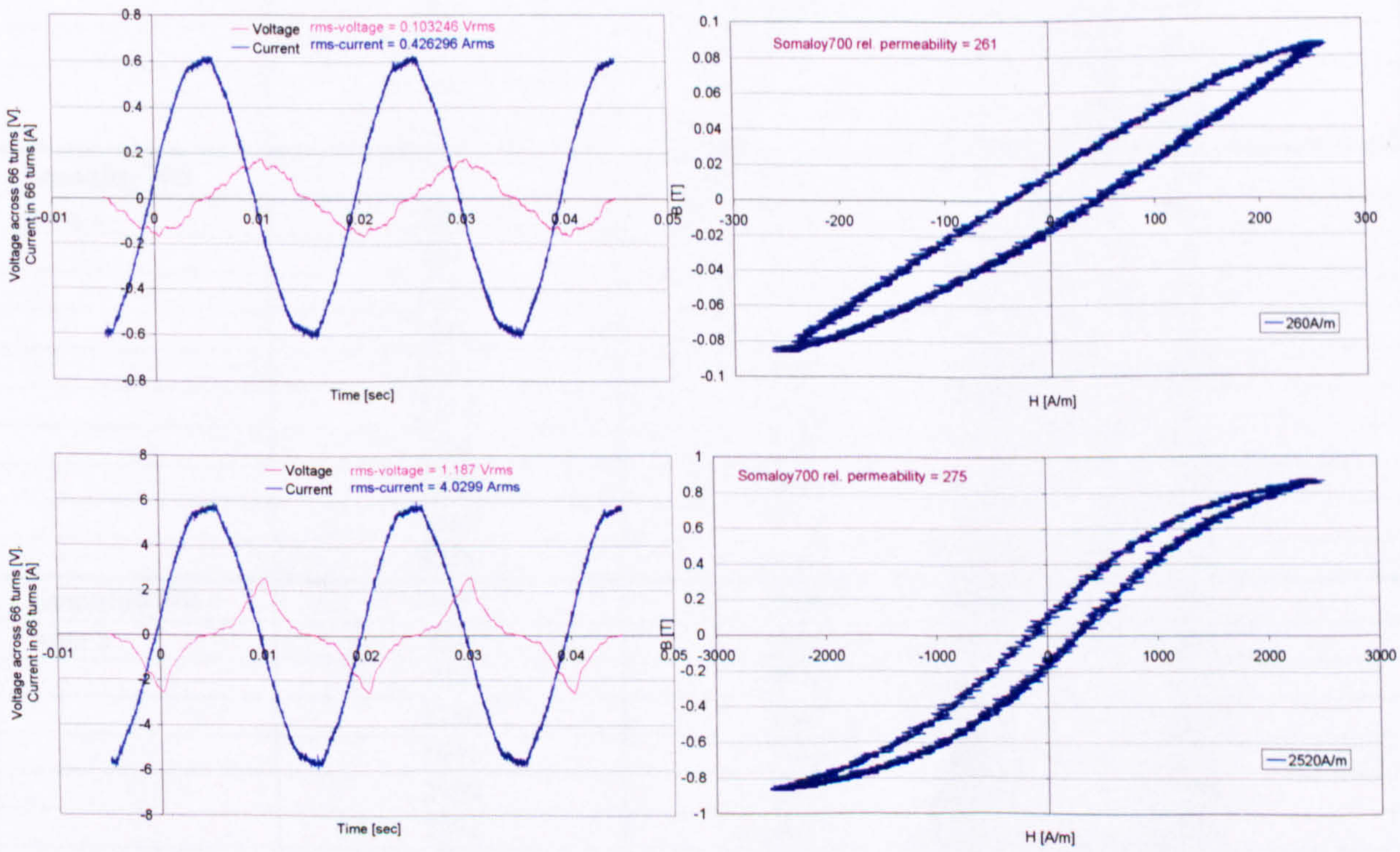

Fig. B.5 Example voltage and current waveforms and corresponding BH-curves for Somaloy700 (Mk4 back iron) at two different energising levels (260A/m and 2520A/m)

B.4.4 Results and Conclusions

BH curve and Relative Permeability

The results are tabulated in Table B.3, and graphically shown in Fig. B.6 (BH curve) and Fig. B.7 (relative permeability as a function of flux density). All measurements were carried out at a frequency of 50Hz.

- The peak permeability for Somaloy500 is around 450, which is more or less its data sheet value, and surprisingly good for a wire-eroded part.

- The peak permeability for Somaloy700 is with 350 much lower than expected (data sheet value of 600), even lower than Somaloy500. It is believed that this reduction is caused by prototype machining. Somaloy700 is more severely affected by wire-erosion than Somaloy500.

Ring sample	Mag. Field Strength H [A/m]	Mag. Field Density B [T]	Rel. Permeability μ_r [-]
Somaloy500	231	0.10	340
Ring 1	535	0.29	434
	812	0.46	453
	1139	0.62	433
	1353	0.72	422
	1850	0.84	359
	2354	0.92	312
	2996	1.05	278
	3726	1.11	238
	4355	1.18	216
	5003	1.24	198
Somaloy700	265	0.09	261
Ring 1	587	0.24	332
	822	0.37	355
	1227	0.53	346
	1280	0.57	352
	1611	0.68	338
	2215	0.81	292
	2520	0.87	275
	3210	0.96	237
	4410	1.12	202
	5210	1.17	179
Somaloy700	189	0.06	241
Ring 2	524	0.19	283
	778	0.31	314
	1190	0.47	316
	1601	0.63	311
	2109	0.74	279
	2791	0.87	248
	4984	1.07	171

Table B.3 Permeability results for Somaloy500 and Somaloy700

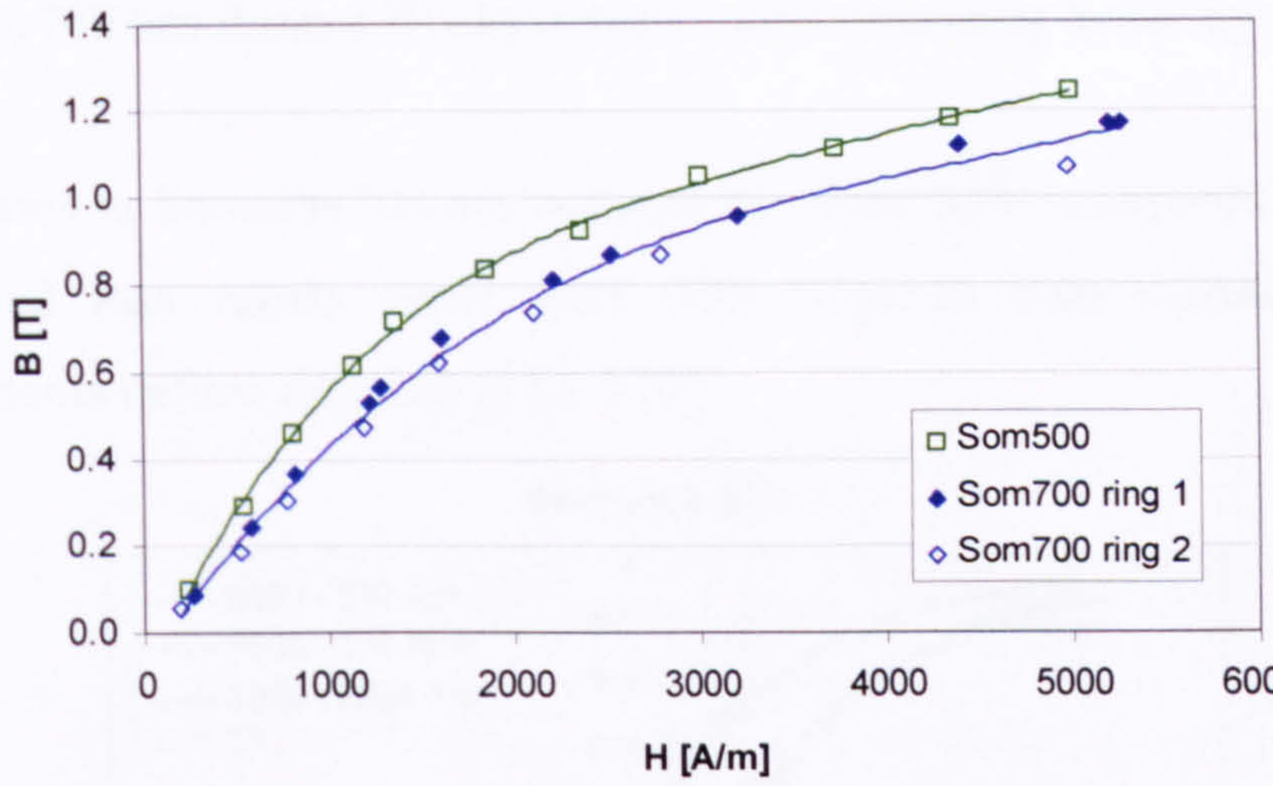

Fig. B.6 Measured BH curve for Somaloy500 and Somaloy700 on wire-eroded back iron rings

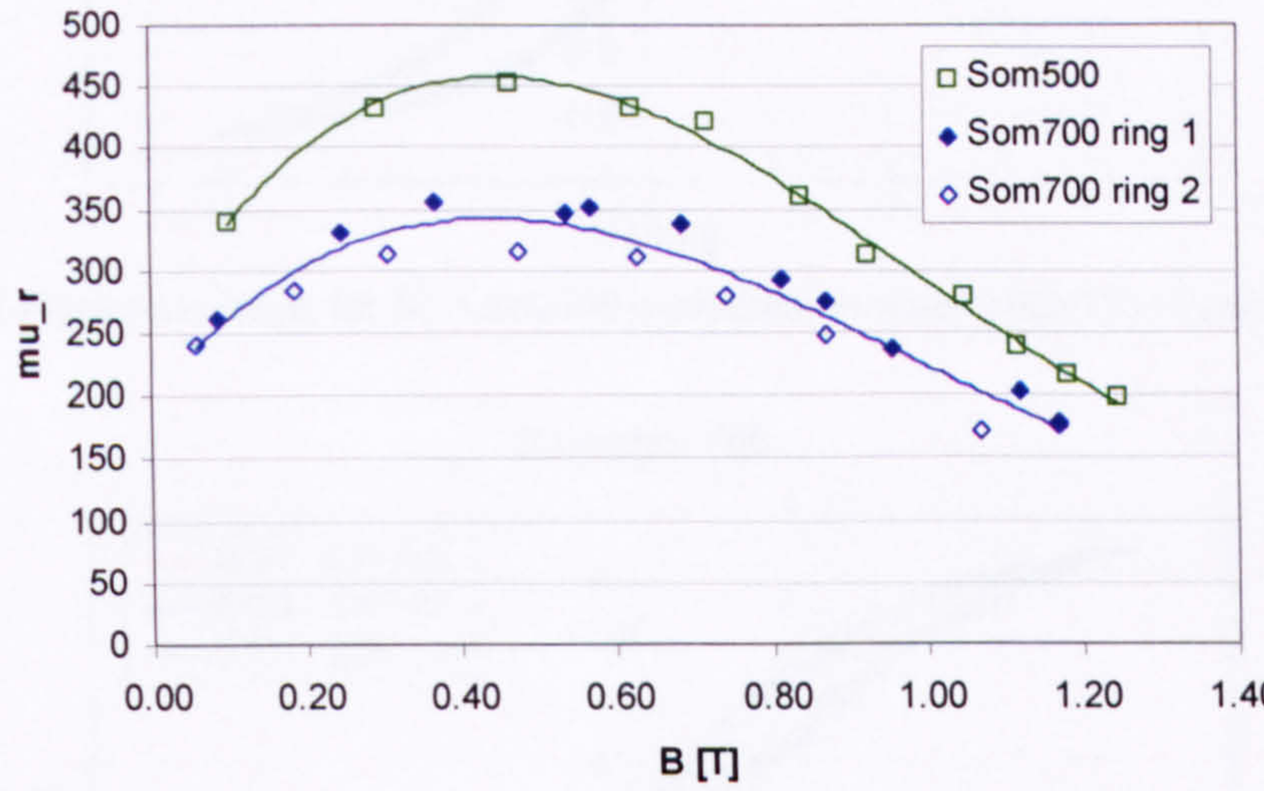

Fig. B.7 Measured relative permeability for Somaloy500 and Somaloy700 on wire-eroded back iron rings

Hysteresis Loops and Iron Loss at 50Hz

Fig. B.8 and Fig. B.9 show three hysteresis loops for Somaloy500 and Somaloy700 respectively. The enclosed area of the hysteresis loops is a measure of the iron losses, and the values are summarised in Table B.4 and plotted in Fig. B10.

Ring sample	Mag. Field Strength H_{max} [A/m]	Mag. Field Density B_{max} [T]	Iron Loss @50Hz P_{iron} [W/kg]
Somaloy®700	260	0.085	0.071
Ring 1	560	0.24	0.459
	2520	0.88	4.621
From Höganäs	-	0.5	1.670
report [113]:	-	1	5.370
Somaloy®500	230	0.097	0.102
Ring 1	534	0.29	0.742
	2354	0.91	6.518
From Höganäs	-	0.5	2.500
Report [114]:	-	1	8.300

Table B.4 Measured iron loss for Somaloy500 and Somaloy700 wire-eroded back iron rings

- Somaloy700 has thinner BH hysteresis loops indicating lower hysteresis losses (at 50Hz).
- The losses in Somaloy700 are reduced by about 35% compared to Somaloy500. Measured loss values agree well with Höganäs own measurements on the components before shipping [113, 114].

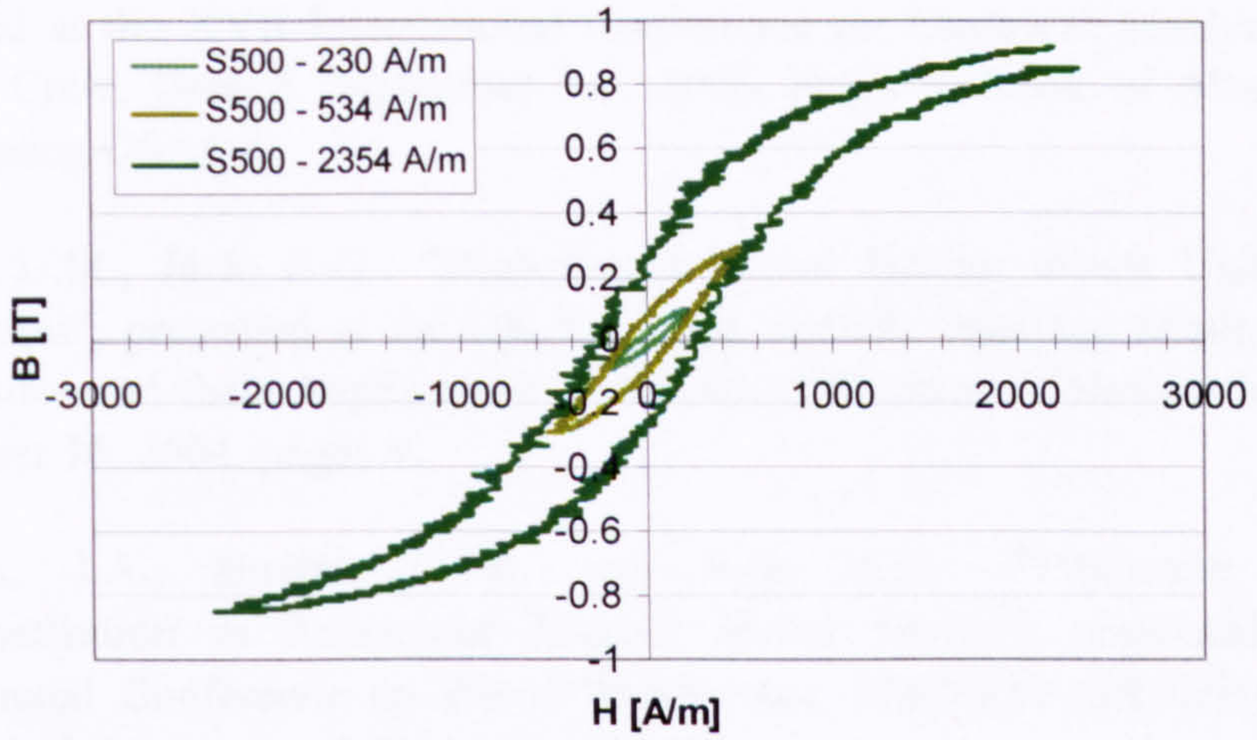

Fig. B.8 BH-Hysteresis loops for Somaloy500 measured on wire-eroded back iron ring of Mk3

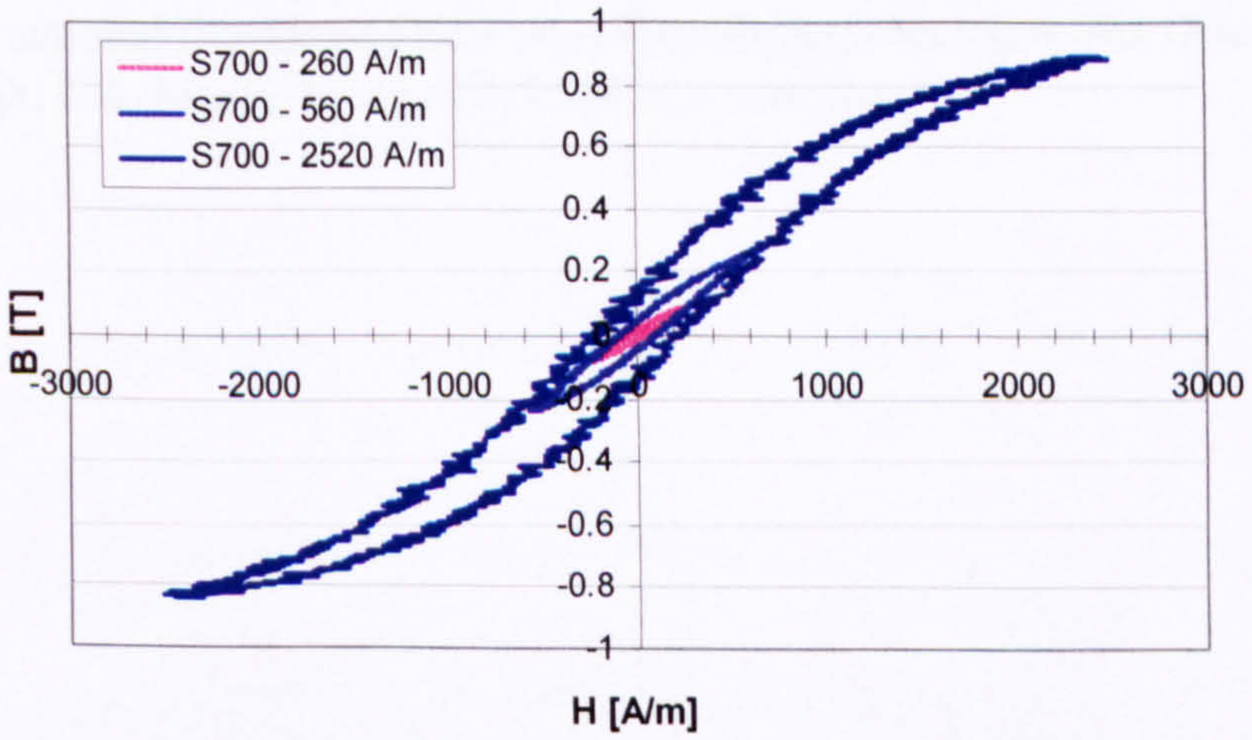

Fig. B.9 BH-Hysteresis loops for Somaloy700 measured on wire-eroded back iron ring of Mk4

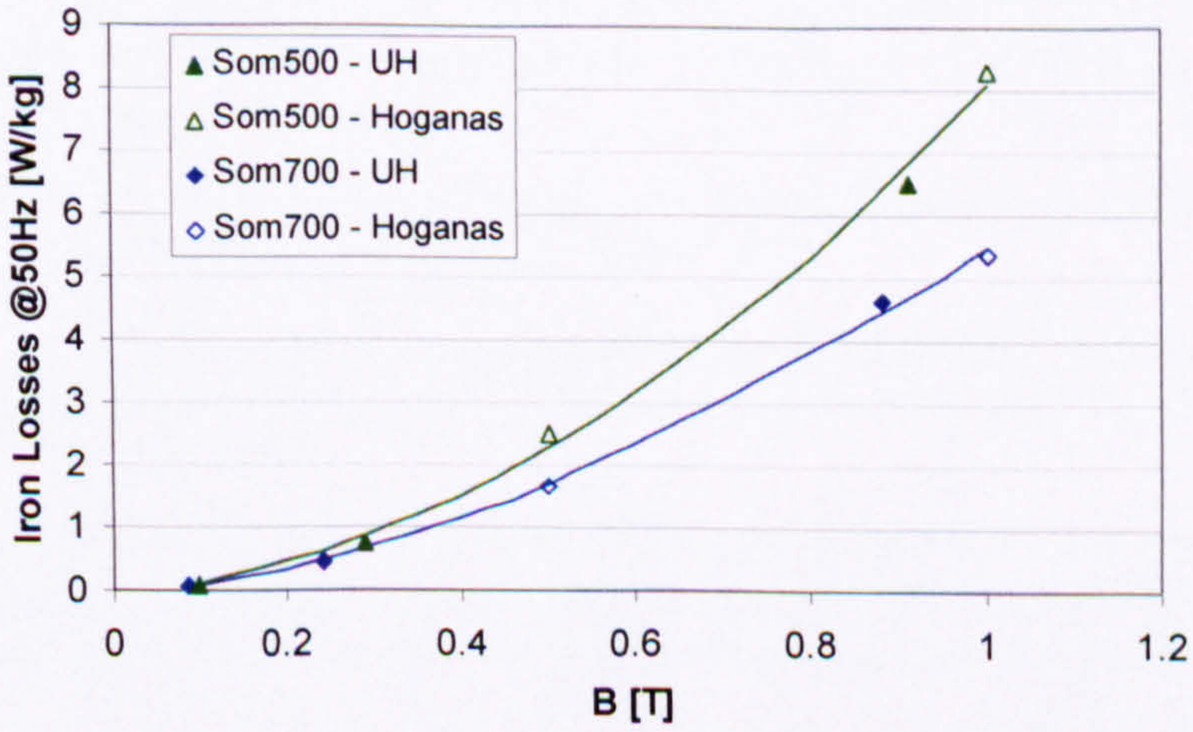

Fig. B.10 Measured iron loss for Somaloy500 and Somaloy700 at 50Hz on back iron rings of Mk3 and Mk4

List of Publications

[1] Hoefer, U.M., Jack, A.G., and Mecrow, B.C., "Unbalanced Magnetic Pull in High-Speed Brushless Permanent Magnet Motors – Experimental Observations and Results", presented at the XVII International Conference on Electrical Machines (ICEM 2006), Chania, Crete, Greece, September 2-5, 2006, pages 5, Book of Abstracts pp.116-117, Oral Session OSA1-4.

[2] Hoefer, U.M., Jack, A.G., "High Speed Motor Design Issues Using Soft Magnetic Composites", presented at the UK Magnetic Society One-Day Seminar 'Soft Magnetic Composites and their Applications in Electrical Machines', Newcastle upon Tyne, UK, November 16, 2004, pages 4.

[3] Haylock, J.A., Hoefer, U.M., and Jack, A.G., "Predicting and Preventing Demagnetisation in Permanent Magnet Motor Drives", presented at the 3rd IET International Conference on Power Electronics, Machines and Drives (PEMD 2006), Dublin, Ireland, April 4-6 2006, pp. 474-478.

[4] Mecrow, B.C., Jack, A.G., Haylock, J.A., Hoefer, U.M., and Dickinson, P.G., "Simplifying the Manufacturing Process for Electrical Machines", presented at the 2nd IET International Conference on Power Electronics, Machines and Drives (PEMD 2004), Edinburgh, UK, March 31-April 2, 2004, pp. 169-174.

List of References

[1] Gaede, W., "Die Molekularluftpumpe (The Molecular Air Pump)", *Annalen der Physik*, vol. 41, pp. 337-380, 1913.

[2] Becker, W., "Eine neue Molekularpumpe (A new Molecular Pump)", *Vakuum-Technik*, vol. 7, pp. 149-152, 1958.

[3] Henning, J., "Thirty Years of Turbomolecular Pumps: A Review and Recent Developments", *Journal of Vacuum Science and Technology A*, vol. 6, pp. 1196-1201, 1988.

[4] Harris, N., *Modern Vacuum Practice*, McGraw-Hill, 1989, 0-07-707099-2.

[5] Wutz, M., Adam, H., and Walcher, W., *Theorie und Praxis der Vakuumtechnik*, 4th revised Ed., Braunschweig/Wiesbaden, F. Vieweg & Sohn, 1988, 3-528-24884-X.

[6] Roth, A., *Vacuum Technology*, 3rd updated and enlarged Ed., Amsterdam, Elsevier Science B.V., 1990, 0-444-88010-0.

[7] "Gaede's First Experiment on Molecular Drag Pumping", Picture taken from the Internet: http:/avs.org/pdf/timeline.pdf, 27th Sept. 2006, document created by AVS Research: Perham Foundation, Revision date: May 2003

[8] "pump cross sections based on B75304000 and B7350000," BOC Edwards drawings.

[9] Conrad, A. and Gutperlet, R., "Einfluss verschiedener Antriebsarten auf das Betriebsverhalten von Turbomolekularpumpen (Influence of Different Kinds of Driving Systems over the Operating-Properties of Turbomolecular Pumps)", *Vakuum-Technik*, vol. 37, pp. 41-47, 1988.

[10] Mecrow, B. C., Jack, A. G., Haylock, J. A., Hoefer, U., and Dickinson, P. G., "Simplifying the Manufacturing Process for Electrical Machines," presented at 2nd IEE International Conference on Power Electronics, Machines and Drives, Edinburgh, UK, 2004, pp. 169-174.

[11] Hoefer, U., "Evaluation of Motor Technologies - SMC versus Segmented Laminations for the 'Miniom Pump'", Edwards Ltd., internal R&D Technical Report, April 2002.

[12] Fritts, C. E., US-patent No:874,908, "Apparatus or Means for the Production, Transmission, and Distribution of Electric Currents", filed in 1886, patent granted in 1907

[13] Hanejko, F. G., Phan, H. G., Rutz, H. G., and Stuart, T. L., "Powder Metallurgy Materials for AC Magnetic Applications," presented at PM^{2}TEC, Washington D.C., 1996, pp. 11pages.

[14] Jansson, P., "Advances in Soft Magnetic Composites Based on Iron Powder," presented at Soft Magnetic Materials, Barcelona, Spain, 1998

[15] Jansson, P., "A Rapidly Expanding Range of Materials - Iron Powders for AC Applications," presented at International Symposium on AC Application of P/M Soft Magnetic Materials, 1999

[16] Nord, G., Hultman, L., and Jack, A. G., "Design Concepts for Electrical Machines Using Soft Magnetic Composite Materials," presented at SMMA 2003 Fall Technical Conference: New Technologies for the Motors and Drives Industry, Nashville, USA, 2003

[17] Dickinson, P. G.,"Application of Soft Magnetic Composites in Electrical Machines",Thesis submitted for Doctor of Philosophy,School of Electrical, Electronic and Computer Engineering, University of Newcastle upon Tyne, 2002

[18] Jack, A. G., Mecrow, B. C., Dickinson, P. G., Stephenson, D., Burdess, J. S., Fawcett, N., and Evans, J. T., "Permanent-Magnet Machines with Powdered Iron Cores and Prepressed Windings", *IEEE Transactions on Industry Applications*, vol. 36, pp. 1077-1083, 2000.

[19] Jack, A. G., Dickinson, P. G., Mecrow, B. C., Jansson, P., and Hultman, L., "A Scoping Study for Universal Motors with Soft Magnetic Composite Stators," presented at International Conference on Electrical Machines (ICEM), Espoo, Finland, 2000, pp. 613-617.

[20] Guo, Y., Zhu, J. G., Watterson, P. A., and Wu, W., "Development of a PM Transverse Flux Motor with Soft Magnetic Composite Core", *IEEE Transactions on Energy Conversion*, vol. 21, pp. 426-434, 2006.

[21] Persson, M., Nord, G., Pennander, L.-O., Atkinson, G., and Jack, A. G., "Development of Somaloy Components for a BLDC Motor in a Scroll Compressor Application," presented at PM2006, Busan, Korea, 2006

[22] Hultman, L., Andersson, O., and Jack, A. G., "The SMC Technology - From Idea to Reality," presented at 2003 SAE World Conference, Detroit, USA, 2003, pp. 9.

[23] "SMC-Datasheet for Somaloy 500 & 700", Höganäs Material Data provided on request, by e-mail or from the Internet www.hoganas.com (data sheet restricted access - password required), 2002 - 2006.

[24] "VACOBOND NI (Injection) / VACOBOND NC (Compression) Polymer Bonded Magnets on Nd-Fe-B Base," Vacuumschmelze GmbH & Co. KG, Material Info Leaflet, 2000.

[25] Hanselman, D., *Brushless Permanent Magnet Motor Design*, 2nd Ed., Magna Physics Publishing, 2006, 1-881855-15-5.

[26] "Electrical Steel - Non Oriented - Fully Processed," Cogent Power Ltd, Material Brochure, 2002.

[27] "Rotating Electrical Machines - Part2: Methods for Determining Losses and Efficiency of Rotating Electrical Machinery from Tests (excluding Machines for Traction Vehicles)", *Brithish Standard BS EN 60034-2*, 1999.

[28] *Femlab - Model Library, version 2.1: Electromagnetic Models, page 2-37,*

[29] "Rare-Earth Permanent Magnets VACODYM-VACOMAX," Vacuumschmelze GmbH & Co.KG, Company Brochure PD-002, 2000.

[30] Hendershot jr, J. R. and Miller, T. J. E., *Design of Brushless Permanent-Magnet Motors*, Magna Physics Publications, 1994, 1-881855-03-1.

[31] Safi, S. K., Acarnley, P. P., and Jack, A. G., "Analysis and Simulation of the High-Speed Torque Performance of Brushless DC Motor Drives", *IEE Proc.-Electrical Power Applications*, vol. 142, No. 3, pp. 191-200, 1995.

[32] Lawler, J. S., Bailey, J. M., McKeever, J. W., and Pinto, J., "Limitations of the Conventional Phase Advance Method for Constant Power Operation of the Brushless DC Motor," presented at IEEE Southeast Conference 2002, Columbia SC, 2002, pp. 174-180.

[33] El-Rafaie, A. M. and Jahns, T. M., "Optimal Flux Weakening in Surface PM Machines Using Concentrated Windings," presented at IEEE Industry Applications Conference, 39th IAS annual meeting, Seattle, 2004, pp. 1038-1047.

[34] Reinap, A., Martinez-Munoz, D., and Alaküla, M., "Iron Loss Calculation in a Claw-pole Structure," presented at Nordic Workshop on Power and Industrial Electronics, NORPIE'04, Trondheim, Norway, 2004, pp. 6.

[35] Lange, A., Canders, W.-R., and Mosebach, H., "Investigation of Iron Losses of Soft Magnetic Powder Components for Electrical Machines," presented at International Conference on Electrical Machines (ICEM), Espoo Finland, 2000, pp. 1521-1525.

[36] Granberg, P. and Krogen, Ö. "Soft Magnetic Composites: Materials with Tuneable Magnetic Properties," presented at PM2000, Kyoto, Japan, 2000, pp. 4.

[37] Gilbert, I., Bull, S., Evans, T., Jack, A. G., Stephenson, D., and De Sa, A., "Effects of Processing upon the Properties of Soft Magnetic Composites for Low Loss Applications", *Journal of Materials Science*, vol. 39, pp. 457-461, 2004.

[38] *SMC-Handbook I-VII*, Höganäs AB, 2006,

[39] Pennander, L.-O., "Difference between Cut and Pressed SMC Parts," personal communication per e-mail, 2007.

[40] Nord, G., Pennander, L.-O., and Jack, A. G., "Loss Calculations for Soft Magnetic Composites," presented at 16th International Conference on Electrical Machines (ICEM2004), Cracow, Poland, 2004, pp. 6.

[41] Bertotti, G., Boglietti, A., Chiampi, M., Chiarabaglio, D., Fiorillo, F., and Lazzari, M., "An Improved Estimation of Iron Losses in Rotating Electrical Machines", *IEEE Transactions on Magnetics*, vol. 27, pp. 5007-5009, 1991.

[42] Atallah, K., Zhu, Z. Q., and Howe, D., "An Improved Method for Predicting Iron Losses in Brushless Permanent Magnet DC Drives", *IEEE Transactions on Magnetics*, vol. 28, pp. 2997-2999, 1992.

[43] Beckley, P., "Modern Steels for Transformers and Machines," in *Power Engineering Journal*, 1999, pp. 190-200.

[44] Markovic, M. and Perriard, Y., "An Analytical Determination of Eddy-Current Losses in a Configuration with a Rotating Permanent Magnet", *IEEE Transactions on Magnetics*, vol. 43, pp. 3380-3386, 2007.

[45] Roshen, W., "Iron Loss Model for Permanent-Magnet Synchronous Motors", *IEEE Transactions on Magnetics*, vol. 43, pp. 3428-3434, 2007.

[46] Stoll, R. L., *The Analysis of Eddy Currents*, Clarendon Press, Oxford, 1974, 0-19-859311-2.

[47] "FEMLAB Electromagnetics Module", Version 3.1i, COMSOL AB 1994-2005

[48] Abu Sharkh, S. M., Harris, M. R., and Taghizadeh Irenji, N., "Calculation of Rotor Eddy-Current Loss in High-Speed PM Alternators," presented at International Conference on Electrical Machines and Drives, EMD97, Cambridge, UK, 1997, pp. 170-174.

[49] Bottauscio, O., Pellegrino, G., Guglielmi, P., Chiampi, M., and Vagati, A., "Rotor Loss Estimation in Permanent Magnet Machines with Concentrated Windings", *IEEE Transactions on Magnetics*, vol. 41, pp. 3913-3915, 2005.

[50] Ishak, D., Zhu, Z. Q., and Howe, D., "Eddy-Current Loss in the Rotor Magnets of Permanent-Magnet Brushless Machines having a Fractional Number of Slots per Pole", *IEEE Transactions on Magnetics*, vol. 41, pp. 2462-2469, 2005.

[51] Toda, H., Xia, Z., Wang, J., Atallah, K., and Howe, D., "Rotor Eddy-Current Loss in Permanent Magnet Brushless Machines", *IEEE Transactions on Magnetics*, vol. 40, pp. 2104-2106, 2004.

[52] Zhu, Z. Q., Ng, K., Schofield, N., and Howe, D., "Improved Analytical Modelling of Rotor Eddy Current Loss in Brushless Machines Equipped with Surface-Mounted Permanent Magnets", *IEE Proc.-Electrical Power Applications*, vol. 151, pp. 641-650, 2004.

[53] Zhu, Z. Q., Ng, K., Schofield, N., and Howe, D., "Analytical Prediction of Rotor Eddy Current Loss in Brushless Machines equipped with Surface-Mounted Permanent

Magnets. II. Accounting for Eddy Current Reaction Field," presented at ICEMS 2001. Proceedings of the Fifth International Conference on Electrical Machines and Systems, Shenyang, China, 2001, pp. 810-813.

[54] Zhu, Z. Q., Ng, K., Schofield, N., and Howe, D., "Analytical Prediction of Rotor Eddy Current Loss in Brushless Machines equipped with Surface-Mounted Permanent Magnets. I. Magnetostatic Field Model," presented at ICEMS 2001. Proceedings of the Fifth International Conference on Electrical Machines and Systems, Shenyang, China, 2001, pp. 806-809.

[55] Zhou, F., Shen, J., Fei, W., and Lin, R., "Study of Retaining Sleeve and Conductive Shield and their Influence on Rotor Loss in High-Speed PM BLDC Motors", *IEEE Transactions on Magnetics*, vol. 42, pp. 3398-3400, 2006.

[56] Deng, F., "Commutation-Caused Eddy-Current Losses in Permanent-Magnet Brushless DC Motors", *IEEE Transactions on Magnetics*, vol. 33, pp. 4310-4318, 1997.

[57] Deng, F. and Nehl, T. W., "Analytical Modeling of Eddy-Current Losses Caused by Pulse-Width-Modulation Switching in Permanent-Magnet Brushless Direct-Current Motors", *IEEE Transactions on Magnetics*, vol. 34, pp. 3728-3736, 1998.

[58] Polinder, H. and Hoeijmakers, M. J., "Effect of a Shielding Cylinder on the Rotor Losses in a Rectifier-Loaded PM Machine," presented at Proceedings of World Congress on Industrial Applications of Electrical Energy and 35th IEEE-IAS Annual Meeting., Rome, Italy, 2000, pp. 163-170.

[59] Mecrow, B. C., Jack, A. G., and Masterman, J. M., "Determination of Rotor Eddy Current Losses in Permanent Magnet Machines," presented at 6th International Conference on Electrical Machines and Drives, IEE, Oxford, UK, 1993, pp. 299-304.

[60] Stoll, R. L. and Hanson, D. J., "Modelling Tooth-Ripple Losses in the Solid Pole Faces of Synchronous Machines Using Reversible Permeability," presented at 6th International Conference on Electrical Machines & Drives, Oxford, UK, 1993, pp. 463-467.

[61] Drubel, O. and Stoll, R. L., "Tooth Ripple Losses in Salient Pole Synchronous Machines," presented at International Conference on Electric Machines and Drives, IEMD, Seattle, WA, 1999, pp. 649-652.

[62] Fam, W. Z., "Direct Measurement of the Fundamental and Harmonic Tooth-Ripple Losses in Solid Poles, Part 1: Theory", *IEEE Transactions on Power Apparatus and Systems*, vol. 90, pp. 597-601, 1971.

[63] Reid, R. C., Prausnitz, J. M., and Poling, B. E., *The Properties of Gases & Liquids*, 4th Ed.,

[64] Pennander, L.-O., "Material Data for X-SMC-11: Loss, BH curve," per email, Höganäs AB, March, 2004.

[65] Siew, C.-C., "Free-Free Frequency as a Function of Shaft Diameter and Motor Axial Length," Edwards Internal Rotor Dynamic Analysis, 2004.

[66] Alger, P. L., *Induction Machines - Their Behaviour and Uses*, 2nd Ed., Gordon and Breach Science Publishers, 1970 (2nd edition) (1st edition 1951),

[67] Timar, P. L., *Noise and Vibration of Electrical Machines*, Elsevier Science Publishers, 1989, 0-444-98896-3.

[68] Zhu, Z. Q., Ng, K., and Howe, D., "Design and Analysis of High-Speed Brushless Permanent Magnet Motors," presented at EMD97, 1997, pp. 381-385.

[69] Gray, A. and Pertsch, J. G., "Critical Review of the Bibliography on Unbalanced Magnetic Pull in Dynamo-Electric Machines", *American Institute of Electrical Engineers, A.I.E.E.*, vol. 37, pp. 1417-1424, 1918.

[70] Rosenberg, E., "Magnetic Pull in Electric Machines", *American Institute of Electrical Engineers, A.I.E.E.*, vol. 37, pp. 1425-1469, 1918.

[71] Stiel, W., "Experimental Investigations on the Torques of 3-Phase Asynchronous Motors with Squirrel-Cage Rotors of Different Slot Numbers", *Forschungsarbeiten des Ingenieurwesens (V.D.I.) (in German)*, pp. 2-64, 1919.

[72] Fritze, H., "Noise in Electrical Machines", *Archiv fuer Elektrotechnik (in German)*, vol. 10, pp. 73-95, 1921.

[73] Chapman, F. T., "The Production of Noise and Vibration by certain Squirrel-Cage Induction Motors", *I.E.E*, vol. 61, pp. 39-48, 1923.

[74] Von Kaehne, P., "Unbalanced Magnetic Pull in Rotating Electric Machines - Survey of Published Work", The Electrical Research Association, ERA, Leatherhead, UK report ref Z/T142, 1963.

[75] Arkkio, A., Antila, M., Pokki, K., Simon, A., and Lantto, E., "Electromagnetic Force on a Whirling Cage Rotor", *IEE Proc.-Electrical Power Applications*, vol. 147, pp. 353-360, 2000.

[76] Binns, K. J. and Dye, M., "Identification of Principal Factors Causing Unbalanced Magnetic Pull in Cage Induction Motors", *IEE Proc.-Electrical Power Applications*, vol. 120, pp. 349-354, 1973.

[77] Frosini, L. and Pennacchi, P., "Detection and Modelling of Rotor Eccentricity in Electrical Machines - an Overview," presented at IMechE, 8th International Conference on Vibrations in Rotating Machinery, University of Wales, Swansea, UK, 2004, pp. 501-510.

[78] Dorrell, D. G., "Experimental Behaviour of Unbalanced Magnetic Pull in 3-Phase Induction Motors with Eccentric Rotors and the Relationship with Tooth Saturation", *IEEE Transactions on Energy Conversion*, vol. 14(3), pp. 304-309, 1999.

[79] Schirle, N. and Lieu, D. K., "History and Trends in the Development of Motorized Spindles for Hard Disk Drives", *IEEE Transactions on Magnetics*, vol. 32, pp. 1703-1708, 1996.

[80] Kim, U. and Lieu, D. K., "Effects of Magnetically Induced Vibration Force in Brushless Permanent-Magnet Motors", *IEEE Transactions on Magnetics*, vol. 41, pp. 2164-2172, 2005.

[81] Bi, C., Liu, Z. J., and Low, T. S., "Effects of Unbalanced Magnetic Pull in Spindle Motors", *IEEE Transactions on Magnetics*, vol. 33, pp. 4080-4082, 1997.

[82] Yoon, T., "Magnetically Induced Vibration in a Permanent-Magnet Brushless DC Motor with Symmetric Pole-Slot Configuration", *IEEE Transactions on Magnetics*, vol. 41, pp. 2173-2179, 2005.

[83] Hartmann, A. and Lorimer, W., "Undriven Vibration in Brushless DC Motors", *IEEE Transactions on Magnetics*, vol. 37, pp. 789-792, 2001.

[84] Hwang, S.-M., Kim, K.-T., Jeong, W.-B., Jung, Y.-H., and Kang, B.-S., "Comparison of Vibration Sources between Symmetric and Asymmetric HDD Spindle Motors with Rotor Eccentricity", *IEEE Transactions on Industry Applications*, vol. 37, pp. 1727-1731, 2001.

[85] Jang, G. H., Yoon, J. W., Park, N. Y., and Jang, S. M., "Torque and Unbalanced Magnetic Force in a Rotational Unsymmetric Brushless DC Motor", *IEEE Transactions on Magnetics*, vol. 32, pp. 5157-5159, 1996.

[86] Bi, C., Liu, Z. J., and Low, T. S., "Analysis of Unbalanced Magnetic Pull in Hard Disk Drive Spindle Motors using a Hybrid Method", *IEEE Transactions on Magnetics*, vol. 32, pp. 4308-4310, 1996.

[87] Bi, C., Jiang, Q., and Lin, S., "Unbalanced Magnetic Pull induced by the EM Structure of PM Spindle Motor," presented at the 8th International Conference on Electrical Machines & Systems, 2005, pp. 183-187.

[88] Liu, Z. J., Bi, C., Lin, H., Yang, J. P., and Jabbar, M. A., "Electromagnetic Design of Permanent Magnet Motors for High Speed Applications," presented at the 9th International Conference on Electrical Machines and Drives, 1999, pp. 45-48.

[89] Kim, K.-T., Kim, K.-S., Hwang, S.-M., Kim, T.-J., and Jung, Y.-H., "Comparison of Magnetic Forces for IPM and SPM Motor with Rotor Eccentricity", *IEEE Transactions on Magnetics*, vol. 37, pp. 3448-3451, 2001.

[90] Stephens, L. S. and Casemore, M. A., "Influence of Stator Slot Geometry and Rotor Eccentricity on Field Distribution in Cylindrical Magnetic Actuators", *IEEE Transactions on Magnetics*, vol. 38, pp. 1348-1356, 2002.

[91] Frosini, L., Mimmi, G., Negri, A., and Rottenbacher, C., "Vibration Monitoring for Detecting Rotor Eccentricity in Brushless Motors," presented at the 5th International Conference on Acoustical and Vibratory Surveillance Methods and Diagnostic Techniques, Senlis, France, 2004, pp. 10.

[92] Zhu, W., Pekarek, S., and Fahimi, B., "On the Effect of Stator Excitation on Radial and Tangential Flux and Force Densities in a Permanent Magnet Synchronous Machine," presented at IEMDC'05, IEEE International Conference on Electric Machines and Drives, San Antonio (Texas), USA, 2005, pp. 346-353.

[93] Zhu, W., Fahimi, B., and Pekarek, S., "Optimal Excitation of Permanent Magnet Synchronous Machines via Direct Computation of Electromagnetic Force Components," presented at IEMDC'05, IEEE International Conference on Electric Machines and Drives, San Antonio (Texas), USA, 2005, pp. 918-925.

[94] Ishak, D., Zhu, Z. Q., and Howe, D., "Unbalanced Magnetic Forces in Permanent Magnet Brushless Machines with Diametrically Asymmetric Phase Windings," presented at Industry Application Conference, 2005. Fourtieth IAS Annual Meeting, 2005, pp. 1037-1043.

[95] Ito, M., Tajima, F., and Kanazawa, H., "Evaluation of Force Calculating Methods", *IEEE Transactions on Magnetics*, vol. 26, pp. 1035-1038, 1990.

[96] Mueller, W., "Comparison of Different Methods of Force Calculation", *IEEE Transactions on Magnetics*, vol. 26, pp. 1058-1061, 1990.

[97] Marinescu, M. and Marinescu, N., "Numerical Computation of Torques in Permanent Magnet Motors by Maxwell Stresses and Energy Method", *IEEE Transactions on Magnetics*, vol. 24, pp. 463-466, 1988.

[98] Benhama, A., Williamson, A. C., and Reece, A. B. J., "Force and Torque Computation from 2D and 3D Finite Element Field Solutions", *IEE Proc.-Electrical Power Applications*, vol. 146, pp. 25-31, 1999.

[99] Carter, G. W., "Maxwell's Stresses in the Magnetic Field (chapter 9.17), Consequences of the Maxwell Stress Theory (chapter 9.18)," in *The Electromagnetic Field in its Engineering Aspectes*, 2nd ed. New York: American Elsevier Publishing Company Inc., 1967, pp. 201-210.

[100] Hammond, P., "Magnetic Field Stress (section 7.5.4)," in *Applied Electromagnetism*, 1st ed. Oxford: Pergamon Press Ltd., 1971, pp. 191-193.

[101] Brewster, B. D., "Permanent Magnet Bearing Design and Analysis", file: pmbrng6.exe, version 6, Edwards Ltd., in-house software

[102] Waye, A., "Influence of Axial Offset on Radial Stiffness of Passive Magnetic Bearings in EXT Turbomolecular Pumps", Edwards Ltd., internal R&D Technical Report, 20 July 2005.

[103] Church, A. H., *Mechanical Vibrations*, 2nd Ed., New York, London, John Wiley and Sons, Inc., 1963,

[104] Thomson, W. T., *Theory of Vibration with Applications*, 3rd Ed., London, Allen & Unwin, 1989, 0044450695.

[105] Zhu, Z. Q., Howe, D., and Chan, C. C., "Improved Analytical Model for Predicting the Magnetic Field Distribution in Brushless Permanent-Magnet Machines", *IEEE Transactions on Magnetics*, vol. 38, no.1, pp. 229-238, 2002.

[106] Zhu, Z. Q., Howe, D., Bolte, E., and Ackermann, B., "Instaneaneous Magnetic Field Distribution in Brushless Permanent Magnet DC Motors, Part I: Open-Circuit Field", *IEEE Transactions on Magnetics*, vol. 29, no.1, pp. 124-135, 1993.

[107] Zhu, Z. Q. and Howe, D., "Instaneaneous Magnetic Field Distribution in Brushless Permanent Magnet DC Motors, Part II: Armature-Reaction Field", *IEEE Transactions on Magnetics*, vol. 29, no.1, pp. 136-142, 1993.

[108] Zhu, Z. Q. and Howe, D., "Instaneaneous Magnetic Field Distribution in Brushless Permanent Magnet DC Motors, Part III: Effect of Stator Slotting", *IEEE Transactions on Magnetics*, vol. 29, no.1, pp. 143-151, 1993.

[109] Miller, T. J. E., *Brushless Permanent-Magnet and Reluctance Motor Drives*, Clarendon Press, Oxford, 1989, 0-19-859369-4.

[110] Ede, J. D., Zhu, Z. Q., and Howe, D., "Optimal Split Ratio for High-Speed Permanent Magnet Brushless DC Motors," presented at the 5th International Conference on Electrical Machines and Systems, ICEMS, Shenyang, China, 2001, pp. 909-912.

[111] Pang, Y., Zhu, Z. Q., and Howe, D., "Analytical Determination of Optimal Split Ratio for Permanent Magnet Brushless Motors", *IEE Proc.-Electrical Power Applications*, vol. 153, pp. 7-13, 2006.

[112] "Electrical Steel - Thin Non Oriented," Cogent Power Ltd, Material Brochure, 2003-04.

[113] "Component Properties of Somaloy700 Wire-Eroded Motor Parts for Edwards", Höganäs AB, Technical Service Report - CSI 200412008, 25.January 2005.

[114] "Component Properties of Somaloy500 Wire-Eroded Motor Parts for Edwards", Höganäs AB, Technical Service Report - CSI 200304073, 20.May 2003.